

ผลกระทบของสัณฐานรูพรุนต่อการดูดซับของของไหลในคาร์บอนที่มีรูพรุน:  
การศึกษาโดยใช้แบบจำลอง มอนติ คาร์โล

นายนิคม กลมเกลี้ยง

วิทยานิพนธ์นี้เป็นส่วนหนึ่งของการศึกษาตามหลักสูตรปริญญาวิศวกรรมศาสตรดุษฎีบัณฑิต  
สาขาวิชาวิศวกรรมเคมี  
มหาวิทยาลัยเทคโนโลยีสุรนารี  
ปีการศึกษา 2555

**EFFECTS OF PORE MORPHOLOGY ON THE  
ADSORPTION OF FLUID IN POROUS CARBONS:  
MONTE CARLO SIMULATION STUDY**

**Nikom Klomkliang**

**A Thesis Submitted in Partial Fulfillment of the Requirements for the  
Degree of Doctor of Philosophy in Chemical Engineering  
Suranaree University of Technology  
Academic Year 2012**

**EFFECTS OF PORE MORPHOLOGY ON THE ADSORPTION  
OF FLUID IN POROUS CARBONS: MONTE CARLO  
SIMULATION STUDY**

Suranaree University of Technology has approved this thesis submitted in partial fulfillment of the requirements for the Degree of Doctor of Philosophy.

Thesis Examining Committee

---

(Dr. Terasut Sookkumnerd)

Chairperson

---

(Prof. Dr. Chaiyot Tangsathitkulchai)

Member (Thesis Advisor)

---

(Asst. Prof. Dr. Atichat Wongkoblap)

Member

---

(Dr. Supunee Junpirom)

Member

---

(Asst. Prof. Dr. Ratanawan Kiattikomol)

Member

---

(Prof. Dr. Sukit Limpijumnong)

Vice Rector for Academic Affairs

---

(Assoc. Prof. Ft. Lt. Dr. Kontom Chamniprasart)

Dean of Institute of Engineering

นิคม กลมเกลี้ยง : ผลกระทบของลักษณะรูพรุนต่อการดูดซับของของไหลในคาร์บอนที่มีรูพรุน: การศึกษาโดยใช้แบบจำลอง มอนติ คาร์โล (EFFECTS OF PORE MORPHOLOGY ON THE ADSORPTION OF FLUID IN POROUS CARBONS: MONTE CARLO SIMULATION STUDY) อาจารย์ที่ปรึกษา : ศาสตราจารย์ ดร.ชัยยศ ตั้งสติย์กุลชัย, 200 หน้า.

ในวิทยานิพนธ์นี้แสดงถึงผลการศึกษาผลกระทบของลักษณะรูพรุนต่อพฤติกรรมการดูดซับของของไหลในคาร์บอนที่มีรูพรุนโดยใช้แบบจำลอง มอนติ คาร์โล งานวิจัยนี้สามารถแบ่งออกได้เป็นสามส่วน โดยที่ส่วนแรก ทำการศึกษาพฤติกรรมการดูดซับของสารอะโรมาติกไฮโดรคาร์บอน ได้แก่ เบนซีน โทลูอิน และไซลีน (BTX) การจำลองแบบแกรนด์คานอนิคัล มอนติ คาร์โล (GCMC) ถูกประยุกต์ใช้เพื่อตรวจสอบการดูดซับของเบนซีนบนแบบจำลองของแข็งอย่างง่ายของพื้นผิวกราฟีน เพื่อให้เข้าใจถึงผลกระทบของแบบจำลองของของไหลต่าง ๆ ต่อไอโซเทอร์มของการดูดซับ (adsorption isotherm) ซึ่งพบว่า ไอโซเทอร์มของการดูดซับ และความร้อนของการดูดซับ (isosteric heat) ที่ได้จากผลของการจำลองนั้นสอดคล้องเป็นอย่างดีกับผลการทดลองที่อุณหภูมิต่าง ๆ นอกจากนี้ พบว่า ลำดับสัมพรรคภาพ (affinity) ของการดูดซับในรูพรุนทรงกระบอกเหมือนกันกับกรณีของพื้นผิว และรูพรุนที่มีรูปทรงเป็นแบบสลิต ลำดับสัมพรรคภาพดังกล่าวคือ เบนซีน น้อยกว่า โทลูอิน และน้อยกว่าไซลีน ตามลำดับ และพบว่ารูปทรงของพื้นผิวไม่มีผลต่อลำดับการบรรจุ (packing) โมเลกุลของของไหล (เบนซีน มากกว่า โทลูอิน และมากกว่าไซลีน ตามลำดับ)

ในส่วนที่สอง รูพรุนที่เชื่อมต่อกันซึ่งมีโครงสร้างและรูปทรงเรขาคณิตแบบต่าง ๆ คือ รูพรุนรูปทรงอย่างง่ายแบบสลิต รูพรุนเดี่ยวรูปทรงแบบสลิตที่ถูกปิดท้ายข้างหนึ่ง รูพรุนแบบรูทึบสองมีขนาดต่างกันเชื่อมต่อกัน และแบบรูปขวด ได้ถูกจำลองขึ้นเพื่อศึกษาถึงไอโซเทอร์มของการดูดซับ วงรอบฮิสเทอรีซิส (hysteresis loop) และการเปลี่ยนสมดุลวัฏภาค (equilibrium phase transition) ของอาร์กอน และเบนซีน โดยใช้การจำลองแบบบิน แกรนด์คานอนิคัล มอนติ คาร์โล (Bin-GCMC) เพื่อศึกษาไอโซเทอร์มของการดูดซับและวงรอบฮิสเทอรีซิส ในขณะเดียวกันได้ใช้วิธีการที่เรียกว่า ความหนาแน่นกลาง (Mid-Density scheme) เพื่อประยุกต์ใช้ในการหาจุดเปลี่ยนสมดุลวัฏภาคในรูพรุน พบว่า ปรากฏการณ์ยับยั้งรูพรุน (pore blocking) และการเกิดโพรงในรูพรุน (cavitation) ถูกควบคุมโดยขนาดของคอกขวด และไม่ขึ้นอยู่กับความยาวของคอกขวด เมื่อขนาดของคอกขวดเล็กกว่าค่าวิกฤตแล้ว การเกิดโพรงในรูพรุนนั้นเป็นกลไกที่มีบทบาทเหนือกว่า แต่ถ้าขนาดของคอกขวดใหญ่กว่าแล้ว ปรากฏการณ์ยับยั้งรูพรุนจะเป็นกลไกที่มีบทบาทเหนือกว่าแทน สำหรับการศึกษากการเปลี่ยนสมดุลวัฏภาคในรูพรุนที่เกิดปรากฏการณ์การยับยั้งรูพรุนและการเกิดโพรงในรู

พรุนนั้น พบว่า การเปลี่ยนสมคุณวิภาคในรูพรุนมีสามระยะ โดยที่ระยะแรกเป็นการเปลี่ยนลำดับที่สอง ซึ่งเกิดขึ้นในคอขวดและใกล้กับเส้นแขนงของการคายซับ ในขณะที่ระยะที่สามเป็นระยะที่เกี่ยวข้องกับโพรง (ตัวขวด) ซึ่งเป็นการเปลี่ยนแบบลำดับที่หนึ่งและเกิดขึ้นใกล้กับเส้นแขนงของการดูดซับ ส่วนระยะที่สองนั้น เป็นระยะที่เชื่อมระหว่างทั้งสองระยะที่อธิบายข้างต้นแล้วเข้าด้วยกันและอยู่ระหว่างเส้นแขนงของการดูดซับและการคายซับ

การดูดซับของน้ำในแบบจำลองของรูพรุนรูปขวดที่เปิดออกสู่บรรยากาศและในถ่านกัมมันต์ ได้ถูกศึกษาในส่วนสุดท้ายนี้ พบว่า มีพฤติกรรมไม่ปกติสำหรับการดูดซับน้ำในคาร์บอนที่มีรูพรุนที่พบในงานวิจัยนี้มีอยู่สองพฤติกรรม พฤติกรรมแรกคือ พฤติกรรมที่ไม่ปกติของการไม่ขึ้นอยู่กับอุณหภูมิของการดูดซับน้ำในถ่านกัมมันต์ โดยพฤติกรรมนี้เกิดขึ้นในช่วงของอุณหภูมิที่ใกล้กับจุดหลอมเหลวของน้ำ กล่าวคือ การดูดซับน้ำที่อุณหภูมิต่ำนั้นมีค่าน้อยกว่ากรณีที่อุณหภูมิสูง อีกปรากฏการณ์ที่ไม่ปกติของน้ำที่ถูกสังเกตเห็นคือ ปรากฏการณ์ปิดกั้นรูพรุน (pore blockage) ในรูพรุนรูปขวด ซึ่งปรากฏการณ์นี้ไม่ถูกพบในกรณีของของไหลอย่างง่าย เช่น อาร์กอน



สาขาวิชาวิศวกรรมเคมี

ปีการศึกษา 2555

ลายมือชื่อนักศึกษา \_\_\_\_\_

ลายมือชื่ออาจารย์ที่ปรึกษา \_\_\_\_\_

ลายมือชื่ออาจารย์ที่ปรึกษาร่วม \_\_\_\_\_

NIKOM KLOMKLIANG : EFFECTS OF PORE MORPHOLOGY ON THE  
ADSORPTION OF FLUID IN POROUS CARBONS: MONTE CARLO  
SIMULATION STUDY. THESIS ADVISOR : PROF. CHAIYOT  
TANGSATHITKULCHAI, Ph.D., 200 PP.

PORE MORPHOLOGY/ADSORPTION/POROUS CARBON/MONTE CARLO  
SIMULATION

The study of effects of pore morphology on the adsorption behavior of fluid in porous carbons using a Monte Carlo (MC) simulation method is presented in this thesis. This research is divided into three parts. The first part is focused on the adsorption behaviors of aromatic hydrocarbons such as benzene, toluene, and xylene (BTX). A grand canonical Monte Carlo (GCMC) simulation is applied to investigate the adsorption of benzene on a simple solid model of a graphene surface to see whether the different fluid models can affect the adsorption isotherm. It is found that the adsorption isotherm and isosteric heat obtained by simulation results are in good agreement with experimental data at various temperatures. In addition, the order of adsorption affinity in a cylindrical pore is the same as that for a surface and slit-pore ( $B < T < X$ ) and the packing order is not affected by the surface curvature ( $B > T > X$ ).

In the second part, connected pores with different pore structures and geometries, single slit-pore, single slit-pore closed at one end, two pores connected and bottle-pore are used to study the adsorption isotherm, hysteresis loop and equilibrium phase transition of argon and benzene. A *Bin* grand canonical Monte Carlo (*Bin*-GCMC) simulation is introduced to investigate the adsorption isotherm

and hysteresis loop whereas the Mid-Density scheme is applied to determine the equilibrium phase transition in the pores. Pore blocking and cavitation are dictated by the size of the neck, and are somewhat insensitive to the neck length. When the neck size is smaller than some critical value, cavitation is the dominant mechanism; otherwise pore blocking is the mechanism for evaporation. The equilibrium phase transition in pores having pore blocking and cavitation is determined. We found that it has three stages; the first stage is exhibited second-order like transition indicated in the neck and closed to desorption branch while third stage is associated with the cavity exhibited as first-order transition and closed to adsorption branch. The second stage joining the other two stages and it falls between the adsorption and desorption branches.

The adsorption of water in a bottle pore model exposed to bulk and activated carbon is studied in the final part. There are two unusual behaviors for water adsorption in porous carbons found in this work. One is the unusual temperature dependence of water adsorption in activated carbon which is happened in the range of temperature where closed to melting point of water. The water uptake at low temperatures is lower than that at high temperatures. The other observation of water is that pore blockage in bottle-pore is occurred for water adsorption which is not found that for simple fluid like argon.

School of Chemical Engineering

Academic Year 2012

Student's Signature \_\_\_\_\_

Advisor's Signature \_\_\_\_\_

Co-Advisor's Signature \_\_\_\_\_

## **ACKNOWLEDGEMENTS**

I would like to express my appreciation to my thesis examining committee for their wonderful questions and guidance. I am most grateful to my thesis advisor, Prof. Dr. Chaiyot Tangsathitkulchai, and co-advisor, Asst. Dr. Atichat Wongkoblaph for their supporting information and invaluable advice and encouragement that have helped me pass through my difficult times. Also my deep appreciation is extended to Prof. Dr. Doung Dang Do who is a great supervisor during my research time at the University of Queensland (UQ), Australia.

I would like to thank all of the lecturers at the school of Chemical Engineering, Suranaree University of Technology (SUT) for their good attitude and advice. I would also like to thank all of my friends who are graduate students in the school of Chemical Engineering, SUT, who shared the experience of graduate student life.

I would like to express my honest gratefulness to everyone in my family, especially my parents for their love and care.

Finally, I acknowledge the support from the Office of the Commission on Higher Education of Thailand in the form of Ph.D. scholarship throughout my study. I am also grateful to the invaluable help of everyone I may have forgotten to mention here.

Nikom Klomkliang



# TABLE OF CONTENTS

	<b>Page</b>
ABSTRACT (THAI).....	I
ABSTRACT (ENGLISH).....	III
ACKNOWLEDGEMENTS.....	V
TABLE OF CONTENTS.....	VI
LIST OF TABLES.....	XIII
LIST OF FIGURES.....	XIV
SYMBOLS AND ABBREVIATIONS.....	XXIX
<b>CHAPTER</b>	
<b>I INTRODUCTION</b> .....	1
1.1 Significance of the Problem.....	1
1.2 Research Objectives.....	5
1.3 Scope and Limitations .....	6
1.4 References.....	8
<b>II THEORY</b> .....	13
2.1 Gas adsorption and Hysteresis.....	13
2.2 Fluid Models.....	17
2.3 Solid Models.....	21
2.4 Fluid-Fluid Interaction Energy .....	22
2.5 Fluid-Solid Interaction Energy.....	24

## TABLE OF CONTENTS (Continued)

	<b>Page</b>
2.5.1 Infinite Surface and Slit-Pore.....	24
2.5.2 Infinite Cylindrical Pore.....	26
2.5.3 Finite Slit-Pore.....	26
2.5.4 Finite Cylindrical Pore .....	29
2.6 The Conventional Monte Carlo Simulation.....	30
2.6.1 Canonical Monte Carlo Simulation.....	31
2.6.2 Grand Canonical Monte Carlo Simulation.....	33
2.7 The <i>Bin</i> Monte Carlo Simulation.....	35
2.7.1 <i>Bin</i> Grand Canonical Monte Carlo Simulation .....	35
2.7.2 <i>Bin</i> Canonical Monte Carlo Simulation.....	37
2.8 Outputs from GCMC.....	38
2.9 The Mid-Density Scheme .....	41
2.10 References.....	42
<b>III ADSORPTION OF BENZENE ON GRAPHITIZED</b>	
<b>THERMAL CARBON BLACK.....</b>	<b>48</b>
3.1 Abstract.....	48
3.2 Introduction.....	49
3.3 Literature Review.....	49
3.4 Simulation.....	52
3.5 Results and Discussion .....	53

## TABLE OF CONTENTS (Continued)

	<b>Page</b>
3.5.1 Adsorption at 293 K .....	53
3.5.2 Structure of Adsorbed Benzene.....	60
3.5.3 Adsorption at Wider Temperature Range.....	69
3.6 Conclusions.....	73
3.7 References.....	74
<b>IV ADSORPTION OF BTX ON GRAPHITIC</b>	
<b>SURFACE AND IN PORES.....</b>	<b>78</b>
4.1 Abstract.....	78
4.2 Introduction .....	79
4.3 Literature Review.....	79
4.4 Simulation.....	80
4.5 Results and Discussion .....	81
4.5.1 Adsorption on Graphitized Surface .....	81
4.5.2 Adsorption on Graphitized Pores .....	85
4.6 Conclusions.....	93
4.7 References.....	94
<b>V HYSTERESIS AND EQUILIBRIUM TRANSITION</b>	
<b>OF ARGON AND BENZENE ADSORPTIONS IN</b>	
<b>FINITE SLIT PORES.....</b>	<b>100</b>
5.1 Abstract.....	100

## TABLE OF CONTENTS (Continued)

	<b>Page</b>
5.2	Introduction.....100
5.3	Literature Review.....101
5.4	Simulation.....102
5.5	Results and Discussion .....104
5.5.1	Acceptance Ratio for Ar Adsorption on a Surface and in an Infinitely Long Slit-Pore.....104
5.5.2	GCMC and <i>Bin</i> -GCMC Simulations for Benzene on Surface and in an Infinitely Long Slit-Pore.....107
5.5.3	Simulations with the Mid-Density Scheme.....108
5.5.4	The Effect of Pore Width.....110
5.5.5	The Effect of Pore Length.....111
5.5.6	The Effect of Temperature.....116
5.6	Conclusions.....118
5.7	References.....119
<b>VI</b>	<b>HYSTERESIS AND EQUILIBRIUM TRANSITION OF ARGON ADSORPTION IN SLIT-SHAPED INK-BOTTLE PORES.....123</b>
6.1	Abstract.....123
6.2	Introduction.....124

## TABLE OF CONTENTS (Continued)

	<b>Page</b>
6.3 Literature Review.....	125
6.4 Simulation.....	128
6.5 Results and Discussion .....	131
6.5.1 Simple Slit Pores.....	131
6.5.1.1 Equilibrium Transition.....	132
6.5.2 Finite Slit-Pore with One Closed End.....	134
6.5.2.1 Equilibrium Transition.....	136
6.5.3 Two Connected Pores Exposed to Bulk.....	137
6.5.3.1 Equilibrium Transition.....	140
6.5.4 Ink-Bottle Pore.....	142
6.5.4.1 Pore Blocking .....	142
6.5.4.2 Cavitation.....	144
6.5.4.3 Equilibrium Transition.....	150
6.6 Conclusions.....	153
6.7 References.....	154
<b>VII ADSORPTION OF WATER IN ACTIVATED</b>	
<b>CARBON AND BOTTLE PORE MODEL .....</b>	<b>160</b>
7.1 Abstract.....	160
7.2 Introduction.....	161
7.3 Literature Review.....	162

## TABLE OF CONTENTS (Continued)

	<b>Page</b>
7.4 Simulation.....	164
7.5 Experimental Work.....	165
7.5.1 Preparation of Activated Carbon.....	165
7.5.2 Characterization of Activated Carbon.....	166
7.5.2.1 BET Surface Area and Pore Size Distribution.....	166
7.5.2.2 Boehm Titration.....	167
7.5.3 Water Adsorption Measurement.....	167
7.6 Experimental Data and Simulation Results.....	168
7.6.1 Porous Characterizations of Activated Carbons .....	168
7.6.2 Adsorption of Water in Activated Carbon.....	170
7.6.3 Simulation Results for Water Adsorption.....	171
7.6.4 Water Adsorption in an Bottle Pore at 298 K.....	174
7.7 Conclusions.....	177
7.8 References.....	178
<b>VIII CONCLUSIONS AND RECOMMENDATIONS .....</b>	<b>181</b>
8.1 Conclusions.....	181
8.1.1 Benzene, Toluene and Xylene on Graphitic Surface and in Pores .....	181

## TABLE OF CONTENTS (Continued)

	<b>Page</b>
8.1.2 Hysteresis and Equilibrium Transition of Argon and Benzene in Slit-Shaped Ink-Bottle Pores .....	182
8.1.3 Water Adsorption in Activated Carbon and Bottle Pore Model .....	183
8.2 Recommendations for Future Work.....	184
<b>APPENDIX LIST OF PUBLICATIONS</b> .....	186
<b>BIOGRAPHY</b> .....	200

## LIST OF TABLES

Table	Page
2.1 Potential parameters of benzene for three potential models.....	19
2.2 Potential parameters for benzene, toluene and xylene.....	20
2.3 Potential parameters for TIP4P/2005 model (Abascal and Vega, 2005).....	21
2.4 Ensembles in Monte Carlo simulation.....	31
2.5 The FORTRAN code for the main program of conventional GCMC and <i>Bin</i> -GCMC.....	37
2.6 The FORTRAN code for the main program of conventional CMC and <i>Bin</i> -CMC.....	39
4.1 Monolayer coverage concentration of BTX adsorption on GTCB at 298 K.....	84
4.2 Pore volume at different physical pore widths of slit-pore.....	87
7.1 Potential model parameters of surface functional group.....	165
7.2 Physical properties and Boehm titration results of activated carbon.....	169
7.3 Melting point of water.....	171



## LIST OF FIGURES

Figure	Page
2.1 Schematic described of different types of pore sizes.....	13
2.2 The IUPAC classification of isotherms.....	15
2.3 The IUPAC classification of hysteresis loop.....	16
2.4 Graphitized structure-less model for (a) a slit-pore and (b) cylindrical pore.....	22
2.5 Graphitized atomistic model for (a) a slit-pore and (b) cylindrical pore.....	22
2.6 Configuration of a finite strip.....	28
2.7 The adsorbate is inside the finite cylindrical pore.....	30
2.8 Periodic boundary conditions and minimum image applied in bulk phase.....	33
2.9 Periodic boundary condition applied in confined space, here is adsorption phase.....	35
2.10 The adsorption phase is divided into bins, for example in this figure there are 4 bins.....	36
2.11 Schematic representation of the hysteresis loop during adsorption enclosed by the stable and metastable states. The vertical dashed line is the equilibrium phase transition.....	42

## LIST OF FIGURES (Continued)

Figure	Page
3.1 Schematic showing: (a) the two angles defining the benzene orientation on the surface, (b) perpendicular benzene rotated $0^\circ$ , and (c) perpendicular benzene rotated $30^\circ$ . $\mathbf{n}$ is the normal unit vector through the benzene ring.....	54
3.2 Adsorption isotherm of benzene on GTCB at 293 K; comparison between the GCMC simulation results using the TraPPE-UA-9 model with and without surface mediation and experimental data from Isirikyan and Kiselev (Isirikyan and Kiselev, 1961). $F$ is the surface mediation factor. $R^2$ is R-squared error.....	54
3.3 Adsorption isotherm of benzene on GTCB at 293 K; comparison between the GCMC simulation results using (a) the OPLS-AA model and (b) the TraPPE-EH model with and without surface mediation and experimental data from Isirikyan and Kiselev (Isirikyan and Kiselev, 1961). $F$ is the surface mediation factor. $R^2$ is R-squared error.....	56
3.4 Adsorption isotherm of benzene on GTCB at 293 K obtained by GCMC by using the TraPPE-UA-9 model (with $F = 0.9$ ), the OPLS-AA model (with $F = 1.0$ ), and the TraPPE-EH model (with $F = 0.9$ ); the experimental data are from Isirikyan and Kiselev (Isirikyan and Kiselev, 1961). (a) Surface excess vs bulk pressure and (b) surface excess vs relative pressure. $R^2$ is R-squared error.....	58

## LIST OF FIGURES (Continued)

Figure	Page
3.5 (a) Isothermic heat vs loading for benzene adsorption on GTCB at 293 K; comparison with the GCMC simulation results (structure-less model) using the TraPPE-UA-9 model ( $F = 0.9$ ), the OPLS-AA model ( $F = 1.0$ ), and the TraPPE-EH model ( $F = 0.9$ ) and (b) their percent deviation; the experimental data are from Isirikyan and Kiselev (Isirikyan and Kiselev, 1961).....	59
3.6 Total, benzene-benzene, and benzene-solid isothermic heats vs loading for benzene adsorption on GTCB at 293 K; comparison with the GCMC simulation results (structure-less model) using the TraPPE-EH model ( $F = 0.9$ ); the experimental data are from Isirikyan and Kiselev (Isirikyan and Kiselev, 1961).....	60
3.7 (a) Local density distribution vs distance from the graphite surface and (b) electrostatic interaction vs pressure at 293 K for the TraPPE-EH model at points A, B, C, and D.....	61
3.8 Local density distribution vs distance from the graphite surface at 293 K for 10,000 Pa for the TraPPE-UA-9 model ( $F = 0.9$ ) and the OPLS-AA model ( $F = 1.0$ ).....	63
3.9 Local density distribution vs distance from the graphite surface at 293 K for the TraPPE-EH model at points D, E, and F.....	64
3.10 Local density distribution vs distance from the graphite surface at 293 K for the TraPPE-EH model at points F, G, H, and I.....	65

## LIST OF FIGURES (Continued)

Figure	Page
3.11 (a) Local density distribution vs distance from the surface to the centre of mass and the angle $\theta$ and (b) top view of the snapshot of benzene molecules adsorbed on a graphite surface at 293 K and point B.....	66
3.12 (a) Local density distribution vs distance from the surface to the centre of mass and the angle $\theta$ and (b) top view of the snapshot of benzene molecules adsorbed on a graphite surface (molecules in purple colours are those in second layer) at 293 K and point D.....	67
3.13 (a) Local density distribution vs distance from the surface to the centre of mass and the angle $\theta$ and (b) top view of the snapshot of benzene molecules adsorbed on a graphite surface (molecules in purple and blue colours are those in second and third layer, respectively) at 293 K and point E.....	68
3.14 Local density distribution vs distance from the surface to the centre of mass and the angle $\theta$ at 293 K and point H.....	68
3.15 Local density distribution vs distance from the surface to the centre of mass and the angle $\Phi$ at 293 K and point H.....	69
3.16 Adsorption isotherms for benzene on GTCB at various temperatures; comparison between the GCMC simulation results using the TraPPE-EH model and experimental data from Pierotti and Smallwood (1966) and Belyakov et al. (1968).....	70

## LIST OF FIGURES (Continued)

Figure	Page
3.17	Local density distribution vs distance from the graphite surface at 273 and 343 K using the TraPPE-EH model for $30 \mu\text{mol}/\text{m}^2$ .....71
3.18	Local distribution vs distance from the surface to the centre of mass and the angle $\theta$ at 343 K for $30 \mu\text{mol}/\text{m}^2$ .....71
3.19	Local density distribution vs distance from the surface to the centre of mass and the angle $\Phi$ at 343 K for $30 \mu\text{mol}/\text{m}^2$ .....72
3.20	Isosteric heat vs loading for benzene adsorption on GTCB at 293 and 343 K: comparison between GCMC simulation results (structure-less model) using the TraPPE-EH model with surface mediation ( $F = 0.9$ ) and experimental data from Isirikyan and Kiselev (Isirikyan and Kiselev, 1961) and Belyakova and co-workers (Belyakov et al., 1968).....73
4.1	(a) Adsorption isotherms and (b) isosteric heats of benzene and toluene on GTCB at 293 K using the TraPPE-UA model and the adjustment parameters, $k_{sf}$ and the surface mediation factor $F$ as described in the text. (c) Toluene adsorption isotherms on GTCB at 293 K obtained from the TraPPE-UA and OPLS-AA models. The simulations are compared with experimental data from Avgul et al. (1959) and Isirikyan and Kiselev (1961). $k_{sf}$ is the binary interaction parameter .....82

## LIST OF FIGURES (Continued)

Figure	Page
4.2 Adsorption isotherms of BTX on GTCB at 298 K using the TraPPE-UA model without adjusting $k_{sf}$ and $F$ . (a) Surface excess per mole vs relative pressure; (b) surface excess per unit mass vs relative pressure .....	83
4.3 Isothermic heats of BTX on GTCB at 298 K using the TraPPE-UA model without adjusting $k_{sf}$ and $F$ . (a) Total isothermic heat. (b) fluid-fluid and fluid-solid isothermic heats. SE is surface excess at any loadings. $SE_M$ is monolayer coverage concentration.....	84
4.4 Local density distributions as a function of distance from a graphite surface to the centre of a benzene ring in BTX at 298 K and a loading of $20 \mu\text{mol}/\text{m}^2$ using the TraPPE-UA model without adjusting $k_{sf}$ and $F$ .....	85
4.5 Adsorption/desorption isotherms of BTX at 298 K using the TraPPE-UA model without adjusting $k_{sf}$ and $F$ on graphitized slit-pore width of $20 \text{ \AA}$ . (a) Pore density per mole vs relative pressure; (b) pore density per unit mass vs relative pressure. The pore density is based on accessible pore volume.....	87
4.6 Adsorption/desorption isotherms for BTX at 298 K on graphitized slit-pores of 8, 16 and $20 \text{ \AA}$ width. (a) Pore density per mole vs $P/P_0$ ; (b) pore density per unit mass vs relative pressure. The pore density is based on the physical pore volume.....	89

## LIST OF FIGURES (Continued)

Figure	Page
4.7	Local density distributions as a function of distance from a pore wall to the centre of benzene ring for BTX at 298 K and $P/P_0 = 1.0$ on graphitized slit-pore width range between 8 and 30 Å.....90
4.8	Local density distributions as a function of distance from a pore wall to the centre of the benzene ring and the angle $\theta$ (3D) and top view of the snapshot of molecules adsorbed of BTX at 298 K and $P/P_0 = 1.0$ on graphitized slit-pore width of 8 Å; (a) B, (b) T, and (c) X.....91
4.9	Local density distributions as a function of distance from a pore wall to the centre of the benzene ring and the angle $\theta$ (3D) and top view of the snapshot of molecules adsorbed for monolayer of BTX at 298 K and $P/P_0 = 1.0$ on graphitized slit-pore width of 20 Å; (a) B, (b) T, and (c) X.....92
4.10	Adsorption/desorption isotherms for BTX at 298 K on graphitized cylindrical pore width range between 18 and 30 Å. (a) Pore density per mole vs relative pressure; (b) pore density per unit mass vs relative pressure. The pore density is based on physical pore volume.....93
4.11	(a) Local density distributions as a function of distance from a pore wall to the centre of benzene ring and (b) snapshots of molecules adsorbed of BTX at 298 K and $P/P_0$ of 1.0 using the TraPPE-UA model without adjusting $k_{sf}$ and $F$ on graphitized cylindrical pore width of 30 Å.....94

## LIST OF FIGURES (Continued)

Figure	Page
5.1 Schematic diagram of a slit-pore of finite length in the $y$ -direction; the pore is connected to the bulk gas phase at each end in the $y$ -direction. Periodic boundary conditions are applied in the $x$ -direction .....	103
5.2 Ar adsorption isotherms on graphitized thermal carbon black (GTCB) at 87.3 K: comparison between GCMC and <i>Bin</i> -GCMC schemes with different displacement/acceptance ratios; the experimental data are taken from Avgul and Kiselev, 1970. The saturation vapour pressures of 101.300 and 88.500 kPa are taken from the experimental data and the simulation, respectively (Do and Do, 2005).....	105
5.3 Isothermic heats of Ar adsorption on GTCB at 87.3 K comparison between GCMC and <i>Bin</i> -GCMC schemes at different displacement acceptance ratios; the experimental data is taken from Avgul and Kiselev (1970) .....	106
5.4 Argon adsorption-desorption isotherms in infinitely long slit-pore of width 2 nm at 87.3 K: comparison between GCMC and <i>Bin</i> -GCMC schemes at different displacement/acceptance ratios.....	106
5.5 (a) $C_6H_6$ adsorption isotherms on GTCB at 293 K and (b) $C_6H_6$ adsorption-desorption isotherms in an infinitely long slit-pore of width of 3 nm at 298 K comparing the GCMC and <i>Bin</i> -GCMC schemes. The $P_0$ of 10.052 and 9.800 kPa are taken from the experimental data and simulation, respectively (Isirikyan and Kiselev, 1961; Rai and Siepmann, 2007).....	107



## LIST OF FIGURES (Continued)

Figure	Page
5.6 (a) GCMC adsorption-desorption isotherm of Ar and showing the equilibrium phase transition obtained by the Mid-Density scheme using CMC+GCMC and (b) <i>Bin</i> -GCMC adsorption and desorption isotherms for Ar and the equilibrium phase transition obtained by the Mid-Density scheme using <i>Bin</i> -CMC+ <i>Bin</i> -GCMC in an infinitely long slit-pore of width 2 nm at 87.3 K. Vertical dashed lines show the equilibrium transition.....	109
5.7 <i>Bin</i> -GCMC adsorption-desorption isotherms of (a) Ar at 87.3 K and (b) C <sub>6</sub> H <sub>6</sub> at 298 K, and the equilibrium phase transition obtained by the Mid-Density scheme using <i>Bin</i> -CMC+ <i>Bin</i> -GCMC in an infinitely long slit-pore of different pore widths. The coexistence pressure of Ar in the 3 nm pore is compared with results obtained by the gauge-cell method and Mid-Density scheme from Liu and co-workers (Liu et al., 2011). Vertical dashed lines show the equilibrium phase transition.....	111
5.8 <i>Bin</i> -GCMC adsorption-desorption isotherms for (a) Ar at 87.3 K and (b) C <sub>6</sub> H <sub>6</sub> at 298 K, and the equilibrium phase transition obtained by the Mid-Density scheme using <i>Bin</i> -CMC+ <i>Bin</i> -GCMC in a finite slit-pore of width 3 nm with different pore lengths expressed in units of <i>H</i> the pore width. Dashed lines with crosses show the equilibrium phase transition.....	114

## LIST OF FIGURES (Continued)

Figure	Page
5.9 Snapshots from <i>Bin</i> -CMC of Ar at the mid-density $\rho_{av}^*$ and 87.3 K in pores of 3 nm width with lengths from 2 to 16 times the pore width ( $H$ ).....	115
5.10 Snapshots from <i>Bin</i> -CMC of C <sub>6</sub> H <sub>6</sub> at the mid-density $\rho_{av}^*$ and 298 K in pores of 3nm width with lengths from 2 to 16 times the pore width ( $H$ ).....	115
5.11 Snapshot of C <sub>6</sub> H <sub>6</sub> at the metastable desorption branch corresponding to point A in Figure 5.8b.....	116
5.12 <i>Bin</i> -GCMC adsorption-desorption isotherms for (a) Ar in pores of length 48nm and width 3 nm and (b) C <sub>6</sub> H <sub>6</sub> in pores of length 6nm, and the equilibrium phase transition obtained by the Mid-Density scheme using <i>Bin</i> -CMC+ <i>Bin</i> -GCMC at different temperatures. Dashed with crosses indicate the equilibrium phase transition.....	117
5.13 Snapshots from <i>Bin</i> -CMC of Ar at the mid-density $\rho_{av}^*$ in pores of width 3 nm with length 16 times the pore width.....	118
6.1 Schematic diagram of a slit-shaped pores of finite length in the $y$ -direction; the pore is connected to the bulk gas phase at two ends in the $y$ -direction. Periodic boundary conditions are applied in the $x$ -direction. (a) Finite simple slit pore, (b) finite slit pore with one closed end, (c) two connected pores exposed to bulk, and (d) ink-bottle pore (one cavity with one neck).....	129

## LIST OF FIGURES (Continued)

Figure	Page
6.2 Division of bins in simulation box, for example, (a) there are 10 bins with equal size for a simple slit-pore and (b) there are 13 bins with equal size for an ink-bottle pore. The number of bins depended on the width of simulation box which we evaluate the width in $z$ -direction of bins approximately of 0.2 nm and equally.....	130
6.3 Adsorption and desorption isotherms of argon in infinite and finite pores at 87.3 K. The vertical dash line indicates the equilibrium phase transition in infinite pore. The dotted line indicates the equilibrium phase transition in finite pore (both end exposed to gas reservoir).....	131
6.4 Snapshot of argon along adsorption and desorption branches in finite slit pore at 87.3 K for 3 nm pore width and 10 nm pore length.....	133
6.5 Snapshot of argon at the equilibrium phase transition state (point C1 in Figure 6.4) output from the Mid-Density scheme at 87.3 K for 3.0 nm pore width and 10nm pore length.....	134
6.6 Adsorption and desorption isotherms of argon in finite slit pore (both ends are exposed to gas reservoir) and finite slit pore with one closed end at 87.3 K. The dotted line along the cross symbol indicates the equilibrium phase transition in the pores.....	134

## LIST OF FIGURES (Continued)

Figure	Page
6.7	Snapshot of argon along adsorption and desorption branches in slit pore with one closed end at 87.3 K for 3 nm pore width and 10 nm pore length.....136
6.8	Adsorption and desorption isotherms of argon in the two connected pores exposed to bulk at 87.3 K. The dotted line is the equilibrium phase transition in the pores.....138
6.9	Snapshot of argon along the adsorption and desorption branches output from the <i>Bin</i> -GCMC at 87.3 K for the two connected pores exposed to bulk. Desorption by receding of pressure as menisci is investigated.....139
6.10	Snapshot of argon at the equilibrium phase transition state output from the Mid-Density scheme at 87.3 K for the two connected pores exposed to bulk.....141
6.11	Adsorption and desorption isotherms of argon in the ink-bottle pore at 87.3 K. The dotted line is the equilibrium phase transition in the pores.....143
6.12	Snapshot of argon along the adsorption and desorption branches output from the <i>Bin</i> -GCMC at 87.3 K for the ink-bottle pore corresponding to Figure 6.11 (bottom graph). Pore blocking is investigated.....144

## LIST OF FIGURES (Continued)

Figure	Page
6.13 Adsorption and desorption isotherms of argon in the ink-bottle pore at 87.3 K. The dotted line along the cross symbol indicates the equilibrium phase transition in the pores. The square symbol indicates the desorption scanning curve. The cross symbol indicates the output from the Mid-Density scheme ( <i>Bin</i> -CMC+ <i>Bin</i> -GCMC). The equilibrium transition in pores having cavitation.....	146
6.14 Snapshot of argon along the adsorption and desorption branches output from the <i>Bin</i> -GCMC at 87.3 K for the ink-bottle pore corresponding to top graph of Figure 6.12. Cavitation is investigated .....	148
6.15 Snapshot of argon along the desorption branches output from the <i>Bin</i> -GCMC at 87.3 K for the ink-bottle pore corresponding to bottom graph of Figure 6.13. Cavitation is investigated.....	149
6.16 Snapshot of argon at the equilibrium phase transition state (point K1-K4 in Figure 6.12) output from the Mid-Density scheme at 87.3 K for the ink-bottle pore.....	150
6.17 Snapshot of argon at the equilibrium phase transition state output from the Mid-Density scheme at 87.3 K for the ink-bottle pore corresponding to top graph of Figure 6.11.....	152

## LIST OF FIGURES (Continued)

Figure	Page
6.18	Snapshot of argon at the equilibrium phase transition state (point Q1-Q3 in Figure 6.14) output from the Mid-Density scheme at 87.3 K for the ink-bottle pore.....153
7.1	(a) Side view of surface functional group of phenol used in simulation and (b) functional group configuration.....165
7.2	Thermal history during the preparation of activated carbon (one-step method).....166
7.3	$N_2$ Adsorption isotherms at 77 K on the activated carbon.....170
7.4	Water vapor adsorption isotherms in the original and modified activated carbons at different temperatures obtained from IGA.....171
7.5	Adsorption isotherms of water at different temperatures in slit-pore of 30 Å width with hydrophilic surface obtained from GCMC.....173
7.6	Isostatic heat of water adsorption in 30 Å width of slit-pore with introducing phenol group on the solid surface.....173
7.7	Snapshot of water onto slit-pore of 30 Å width with hydrophilic surface: (a) $x$ - $y$ - $z$ plane and (b) $y$ - $z$ plane. All of carbon, oxygen and hydrogen atoms of phenol group are indicated in red. Oxygen and hydrogen atoms of water molecule are indicated in gray and black, respectively.....174

**LIST OF FIGURES (Continued)**

<b>Figure</b>		<b>Page</b>
7.8	Adsorption isotherm and snapshot onto a bottle-pore of (a) water at 298 K and (b) argon at 87.3 K. The snapshots of water are located only for oxygen atom.....	176
7.9	Isosteric heat of water in the bottle pore at 298 K.....	177



## SYMBOLS AND ABBREVIATIONS

$F$	=	Surface mediation factor [-]
$H$	=	Physical pore width [ $\text{\AA}$ ]
$H'$	=	Accessible pore width [ $\text{\AA}$ ]
$k_B$	=	Boltzmann's constant [J/K]
$k_{sf}$	=	Binary interaction parameter [-]
$L$	=	Length of simulation box [ $\text{\AA}$ ]
$N$	=	Number of particle [-]
$q$	=	Partial charge on Coulombs site [e]
$q_{isos}$	=	Isosteric heat [J/mol]
$r$	=	Separation of interaction sites [ $\text{\AA}$ ]
$T$	=	Temperature [K]
$U$	=	Interaction energy [J]
$\varepsilon$	=	Lennard-Jones well-depth [J]
$\varepsilon_0$	=	Permittivity of a vacuum [ $\text{C}^2/\text{J}\cdot\text{m}$ ]
$\sigma$	=	Lennard-Jones collision diameter [ $\text{\AA}$ ]
$\rho$	=	Average local density [ $\text{mol}/\text{m}^3$ ]
$\rho_s$	=	Surface density of carbon atoms [ $\text{\AA}^{-2}$ ]
$\Delta$	=	Carbon layer separation [ $\text{\AA}$ ]
$\Gamma$	=	Surface adsorption [ $\text{mol}/\text{m}^2$ ]



# CHAPTER I

## INTRODUCTION

### 1.1 Significance of the Problem

Porous carbons are widely used in adsorption processes for separation, purification, and catalysis purposes, because of their large micropore and mesopore volumes and the high surface area. The adsorption and phase behavior of fluids in carbon pores has been studied extensively. Like any industrial process, a good design and optimization of industrial adsorption processes rely upon the theoretical understanding of their underlying phenomena. To design the adsorption processes, it is important to understand the thermodynamic equilibrium. The amount of adsorbent needed in an adsorber is determined by the equilibrium data, and the selection of an effective adsorbent depends on its adsorption isotherm. The heat of adsorption yields valuable insights into the mechanism of adsorption. It is a critical thermodynamic property for the design of adsorption processes because it can be used to estimate the heat released or consumed during the adsorption or desorption processes.

Experimental observations alone cannot allow us to understand the adsorption behaviors of fluid in porous solids; this is due to the wide range of pore size varied from micropores to mesopores and their peculiar morphologies. Therefore, a computer simulation for adsorption of fluid is now commonplace with application ranging from elucidating the structures and properties of fluid to the study of systems involving hazardous or difficult to synthesize adsorbates. The principal computational methods widely used nowadays are a molecular dynamics (MD) and a Monte Carlo

statistical mechanics (MC) (Allen and Tildesley, 1987). The success of these tools in prediction the adsorption isotherm depends on the appropriate choice of intermolecular potential models. There are many fluid-fluid interaction models available in the literature; one of the simplest equations is the Lennard-Jones (LJ) 12-6 equation. This is an empirical equation, contained two parameters the collision diameter,  $\sigma$ , and energy well depth,  $\epsilon$ . These parameters are usually obtained from the fitting of the simulation results against some appropriate macroscopic quantities. The popular use of the LJ 12-6 equation rather than other equation in adsorption problems is that it is consistent with the usage of the well-known Steele 10-4-3 equation for calculating the fluid-solid interaction energy. Even with this very simple form of LJ 12-6, there are many different sets of molecular parameters available in the literature for a specific adsorbate. Some were obtained by using the second virial coefficient, while some were obtained from the matching between the simulation results and fluid properties such as gas viscosity, liquid radial density distribution, spectroscopic data, and the vapor-liquid equilibrium (VLE), etc.

Hysteresis associated with capillary condensation in porous materials have been the subject of immense interest over 100 years (Horikawa et al., 2011), especially the mechanics behind the hysteresis and its dependence on the pore topology, the pore parameters (such as pore width and length), and temperature. It is reported that the adsorption in simple mesopores always exhibits hysteresis when temperature is less than the critical hysteresis temperature and pore size is greater than a critical value (Morishige, 2008; Morishige and Tateishi, 2003) and the characteristics of hysteresis loop depend on the material examined, the adsorbate and the temperature (Kruk and Jaroniec, 2003; Morishige and Tateishi, 2003). Thus, for a

given adsorbate and temperature, the adsorption and desorption branches of the isotherm depend on the material properties: the pore size distribution, the pore shape and connectivity (Fan et al., 2011; Grant and Jaroniec, 2012; Horikawa et al., 2004; Lu and Schüth, 2006; Nguyen et al., 2011; Reichenbach et al., 2011). No matter what the properties are, the existence of the hysteresis is attributed to the metastable states of the adsorbed layer along the adsorption branch and those of the liquid condensates along the desorption branch (Neimark and Vishnyakov, 2000).

The adsorption of simple fluid such as argon, krypton, nitrogen, methane, and carbon dioxide on porous carbons has been studied which is useful as a basic understand for more complex fluids, however, the adsorption of complex fluids still needs to be implemented. Among these complex fluids, aromatic hydrocarbons, benzene, toluene, and xylene (BTX) are interesting for sciences and engineers; this is due to that they are hazardous organic compounds emitted from the chemical and petrochemical industries. It has been reported that these aromatic hydrocarbons are neurotoxic and consequently cause diseases of the nervous system and sterility (White and Proctor, 1997). Stricter environmental regulations require that aromatics must be removed before the effluents can be safely discharged into the environment. Among the various available technologies, adsorption is the simplest mean to achieve this goal due to its low energy consumption. While an activated carbon (AC), silica gel, and zeolite are the possible candidate adsorbents, AC is preferable because of its non-polar surface and high surface area. To understand the basic interaction between BTX and graphitic walls better, physisorption of the simplest aromatic hydrocarbon, benzene, on a graphite (or graphitized thermal carbon black) surface has been studied both experimentally (Avgul et al., 1958; Avgul et al., 1959; Belyakov et al., 1968;

Berezin et al., 1972; Berezin et al., 1970; Carrott et al., 2000; Davis and Pierce, 1966; Isirikyan and Kiselev, 1961; Isirikyan and Kiselev, 1963; Pierce and Ewing, 1967; Pierotti and Smallwood, 1966) and theoretically (Do and Do, 2006; Matties and Hentschke, 1996a; Matties and Hentschke, 1996b; Vernov and Steele, 1991a; Vernov and Steele, 1991b). The fundamental understanding of this adsorbate-adsorbent interaction is the basic step to better design for adsorption of aromatic hydrocarbons in pores whose walls are graphitic; such as activated carbon (Lai et al., 2010; Yun et al., 1999), carbon nanotubes (Masenelli-Varlot et al., 2002; Terzyk et al., 2009) and ordered solids with hexagonal pores (Morishige, 2011a; Morishige, 2011b; Wang et al., 2011).

Water adsorption on porous carbons is also widely studied in the literature because water adsorption in porous carbons is significantly different from that of simple fluids such as argon, nitrogen, carbon dioxide, and hydrocarbons. The main source differences come from the strong water-water interactions as hydrogen bond, the weak water-carbon interactions, and the formation of hydrogen bond with oxygenated groups on carbon surface. Thus, the adsorption of simple fluids in porous carbon cannot be used to describe the behavior of water in the corresponding materials.

Activated carbons can be prepared from a wide variety of precursors, thus their amorphous pore structure is the most difficulty for pore characterization. However, molecular simulation offers the possibility of studying the effects of pore structure and geometry on the adsorption of fluid in order to better understand in adsorption behavior of different adsorbates in activated carbon. This research will play more attention on the effects of pore morphology and structure of porous carbons on

the mechanism of adsorption-desorption especially hysteresis loop. The adsorption of complex fluids, BTX and water on carbon surfaces is also a challenge issue in this study, the simulation results will be used to describe the adsorption mechanism of these fluids. To achieve these; a Grand Canonical Monte Carlo (GCMC) simulation is used as a tool in this study.

## 1.2 Research Objectives

The aim of this research work is to study the effects of pore morphology on the adsorption of fluid in porous carbons by using Monte Carlo simulation. This is achieved through the following specific objectives.

1. To develop the GCMC method to study benzene adsorption on graphitized surface using different models of benzene and compare the simulation results with experimental data to test whether which model can describe well the adsorption behavior of benzene.
2. To develop the GCMC method to study BTX adsorption on graphitic surface as well as in pores whose shape is either slit or cylinder to study the effect of pore structure on the adsorption mechanism of aromatic hydrocarbons with different sites of methyl group.
3. To develop the *Bin*-GCMC and Mid-Density scheme methods to investigate the adsorption hysteresis loop and the equilibrium phase transition, respectively, in slit pores for argon and benzene.
4. To develop the *Bin*-GCMC and Mid-Density scheme methods to investigate hysteresis loop and determine the equilibrium phase transition, respectively, in slit-shaped ink-bottle pores for argon.

5. To investigate polar fluid of water adsorption in either activated carbon or ink-bottle pore using *Bin*-GCMC simulation to study the effect of pore morphology on adsorption of polar fluid and compare the results with those obtained for non-polar fluid of argon.

### 1.3 Scope of Works

The present research is focused on Monte Carlo simulation to study the effects of pore morphology on the adsorption of fluid in porous carbons. The study is separated into three main parts.

Aromatic hydrocarbons such as benzene, toluene, and xylene (BTX) are used in the first part of this work in order to study the adsorption on graphitic surface and in pores. To study the accuracy of the fluid models, we develop the GCMC simulation to investigate benzene adsorption on graphite surface at different temperatures and compare the simulation results obtained from different fluid models with experimental data. Furthermore, the adsorption of BTX on graphitic surface, slit- and cylindrical pores is investigated to study the affinity and packing.

In the second part, Slit-shaped ink-bottle pores are used to study the adsorption of non-polar gases, argon and benzene, using *Bin*-GCMC. The acceptance probability of the *Bin*-GCMC is based on local density which is more effective rather than the conventional GCMC. Slit-shaped ink-bottle pores consisting of simple slit-pore, single slit-pore closed at one end, two pores connected and bottle-pore with a cavity connected to one neck are used in this part. All of the pores considered in this part are of a finite length and are connected to a bulk reservoir so that they mimic real materials for which confined fluid is always in contact with the external gas phase.

Not only the different of the pore structures is addressed in this part but their length and width are also varied. For a bottle pore, the desorption occurs either through pore blocking effects or cavitations depending on the pore width. In addition, a mechanism behind the hysteresis loop which is the equilibrium phase transition in pores is determined by using the Mid-Density scheme.

In the final part of this work, effects of pore morphology on the adsorption of polar fluid in porous carbons are carried out using the *Bin*-GCMC method. The solid models used are a single slit-pore and bottle-pore considering as finite length exposed to bulk reservoirs. Here, water is used as a representation for polar molecule while argon is that for non-polar molecule. The adsorption of polar and non-polar fluids in a bottle pore is investigated and compare to each other. In addition, evidence from experiment will be done in this work for water adsorption in activated carbon prepared from coconut shell with physical heat treatment in a fixed-bed, Boehm titration and ASAP2010 Micromeritics are used to measure surface functional groups and physical properties, respectively. Water adsorption isotherm is measured by using an intelligent gravimetric analyzer (IGA) and its observation is explained by GCMC simulation qualitatively.

In order to complete the whole goal, we divide the whole works into eight chapters; CHAPTER I presents the significance of the problem and the specific objectives. CHAPTER II represents the theory involving in this work, for example, the conventional Monte Carlo simulation and the *Bin* Monte Carlo simulation are taken into account to investigate the adsorption and isosteric heat of fluid in adsorbent. To determine the equilibrium phase transition in pores the Mid-Density scheme which is the consequence of *Bin*-CMC and *Bin*-GCMC simulations is

described in this chapter as well. Results and discussion corresponding to each specific objective are presented in CHAPTER III to VII. The last CHAPTER VIII presents conclusions and recommendations for future work. The publications of this work are listed in an APPENDIX.

## 1.4 References

- Allen, M.P. and Tildesley, T.P. (1987). Computer simulation of liquids. **Japanese Journal of Applied Physics Part 2-Letters**. 35: L405-L407.
- Avgul, N.N., Berezin, G.I., Kiselev, A.V. and Korolev, A.Y. (1958). Heat of adsorption of hydrocarbons by carbon blacks of different degrees of graphitization. **Kolloidnyi Zhurnal**. 20: 298-304.
- Avgul, N.N., Berezin, G.I., Kiselev, A.V. and Lygina, I.A. (1959). Heats of adsorption of toluene and various isoparaffins and naphthenes on graphitized carbon black. **Russian Chemical Bulletin**. 8: 764-773.
- Belyakov, L.D., Kiselev, A.V. and Kovaleva, N.V. (1968). Gas-chromatographic determination of isotherms and heats of adsorption of water, benzene and methanol vapours on graphitised carbon black. **Russian Journal of Physical Chemistry**. 42: 1204-1208.
- Berezin, G.I., Kiselev, A.V., Sagatelyan, R.T. and Sinitsyn, V.A. (1972). A thermodynamic evaluation of the state of the benzene and ethanol on a homogeneous surface of a nonspecific adsorbent. **Journal of Colloid and Interface Science**. 38: 335-340.



- Berezin, G.I., Kiselev, A.V. and Sinitsyn, V.A. (1970). Adsorption of benzene and n-hexane on graphitised carbon black. **Russian Journal of Physical Chemistry**. 44: 408-411.
- Carrott, P.J.M., Carrott, M., Cansado, I.P.P. and Nabais, J.M.V. (2000). Reference data for the adsorption of benzene on carbon materials. **Carbon**. 38: 465-474.
- Davis, B.W. and Pierce, C. (1966). A study of stepwise adsorption. **The Journal of Physical Chemistry**. 70: 1051-1058.
- Do, D.D. and Do, H.D. (2006). Adsorption of benzene on graphitized thermal carbon black: Reduction of the quadrupole moment in the adsorbed phase. **Langmuir**. 22: 1121-1128.
- Fan, C.Y., Do, D.D. and Nicholson, D. (2011). On the cavitation and pore blocking in slit-shaped ink-bottle pores. **Langmuir**. 27: 3511-3526.
- Grant, S.M. and Jaroniec, M. (2012). Effect of cosolvent organic molecules on the adsorption and structural properties of soft-templated ordered mesoporous alumina. **Journal of Colloid and Interface Science**. 367: 129-134.
- Horikawa, T., Do, D.D. and Nicholson, D. (2011). Capillary condensation of adsorbates in porous materials. **Advances in Colloid and Interface Science**. 169: 40-58.
- Horikawa, T., Hayashi, J. and Muroyama, K. (2004). Controllability of pore characteristics of resorcinol-formaldehyde carbon aerogel. **Carbon**. 42: 1625-1633.

- Isirikyan, A.A. and Kiselev, A.V. (1961). The absolute adsorption isotherms of vapors of nitrogen, benzene and n-hexane, and the heats of adsorption of benzene and n-hexane on graphitized carbon blacks. I. Graphitized thermal blacks. **The Journal of Physical Chemistry**. 65: 601-607.
- Isirikyan, A.A. and Kiselev, A.V. (1963). Isotherms and heats of adsorption of nitrogen, benzene, and n-hexane vapours on graphitised carbon blacks. III. Thermodynamic quantities. **Russian Journal of Physical Chemistry**. 37: 957-961.
- Kruk, M. and Jaroniec, M. (2003). Argon adsorption at 77 K as a useful tool for the elucidation of pore connectivity in ordered materials with large cage-like mesopores. **Chemistry of Materials**. 15: 2942-2949.
- Lai, M.H., Shih, Y.L., Chen, Y.H., Shu, S.H. and Chung, T.W. (2010). Equilibrium isotherms of the adsorption of pyrolysis gases from polymer products. **Journal of Chemical and Engineering Data**. 55: 723-727.
- Lu, A.H. and Schüth, F. (2006). Nanocasting: A versatile strategy for creating nanostructured porous materials. **Advanced Materials**. 18: 1793-1805.
- Masenelli-Varlot, K., McRae, E. and Dupont-Pavlovsky, N. (2002). Comparative adsorption of simple molecules on carbon nanotubes: Dependence of the adsorption properties on the nanotube morphology. **Applied Surface Science**. 196: 209-215.
- Matties, M.A. and Hentschke, R. (1996a). Molecular dynamics simulation of benzene on graphite. 1. Phase behavior of an adsorbed monolayer. **Langmuir**. 12: 2495-2500.

- Matties, M.A. and Hentschke, R. (1996b). Molecular dynamics simulation of benzene on graphite. 2. Phase behavior of adsorbed multilayers. **Langmuir**. 12: 2501-2504.
- Morishige, K. (2008). Adsorption hysteresis in ordered mesoporous silicas. **Adsorption**. 14: 157-163.
- Morishige, K. (2011a). Freezing and melting of Kr in hexagonally shaped pores of turbostratic carbon: Lack of hysteresis between freezing and melting. **Journal of Physical Chemistry C**. 115: 2720-2726.
- Morishige, K. (2011b). Layer-by-layer freezing of Kr confined in hexagonal pores with crystalline carbon walls. **Journal of Physical Chemistry C**. 115: 12158-12162.
- Morishige, K. and Tateishi, N. (2003). Adsorption hysteresis in ink-bottle pore. **Journal of Chemical Physics**. 119: 2301-2306.
- Neimark, A.V. and Vishnyakov, A. (2000). Gauge cell method for simulation studies of phase transitions in confined systems. **Physical Review E**. 62: 4611-4622.
- Nguyen, P.T.M., Do, D.D. and Nicholson, D. (2011). On the cavitation and pore blocking in cylindrical pores with simple connectivity. **The Journal of Physical Chemistry B**. 115: 12160-12172.
- Pierce, C. and Ewing, B. (1967). Localized adsorption on graphite surfaces. **Journal of Physical Chemistry**. 71: 3408-3413.
- Pierotti, R.A. and Smallwood, R.E. (1966). The adsorption of benzene on homogeneous substrates. **Journal of Colloid and Interface Science**. 22: 469-481.

- Reichenbach, C., Kalies, G., Enke, D. and Klank, D. (2011). Cavitation and pore blocking in nanoporous glasses. **Langmuir**. 27: 10699-10704.
- Terzyk, A.P., Gauden, P.A., Furmaniak, S., Wesolowski, R.P., Harris, P.J.F. and Kowalczyk, P. (2009). Adsorption from aqueous solutions on opened carbon nanotubes-organic compounds speed up delivery of water from inside. **Physical Chemistry Chemical Physics**. 11: 9341-9345.
- Vernov, A. and Steele, W.A. (1991a). Computer-simulations of benzene adsorbed on graphite. 1. 85 K. **Langmuir**. 7: 3110-3117.
- Vernov, A. and Steele, W.A. (1991b). Computer-simulations of benzene adsorbed on graphite. 2. 298 K. **Langmuir**. 7: 2817-2820.
- Wang, Y., Nguyen, P.T.M., Sakao, N., Horikawa, T., Do, D.D., Morishige, K. and Nicholson, D. (2011). Characterization of a new solid having graphitic hexagonal pores with a GCMC technique. **Journal of Physical Chemistry C**. 115: 13361-13372.
- White, R.F. and Proctor, S.P. (1997). Solvents and neurotoxicity. **Lancet**. 349: 1239-1243.
- Yun, J.H., Choi, D.K. and Kim, S.H. (1999). Equilibria and dynamics for mixed vapors of BTX in an activated carbon bed. **AIChE. Journal**. 45: 751-760.

## CHAPTER II

### THEORY

#### 2.1 Gas Adsorption and Hysteresis

Gas adsorption is a widely used technique to investigate the morphology of porous materials. In discussions of adsorption in these materials it is customary to distinguish between micropores and mesopores, broadly speaking, the capillary condensation phenomena are observed in the latter, while in the former, isotherms do not exhibit this transition, and micropore filling (and cooperative filling) is the dominant mechanism. It is noted that real materials contain pores ranging from micropores to macropores, and there are ranges of pore sizes where an overlap between these two mechanisms of adsorption occurred as shown in Figure 2.1.

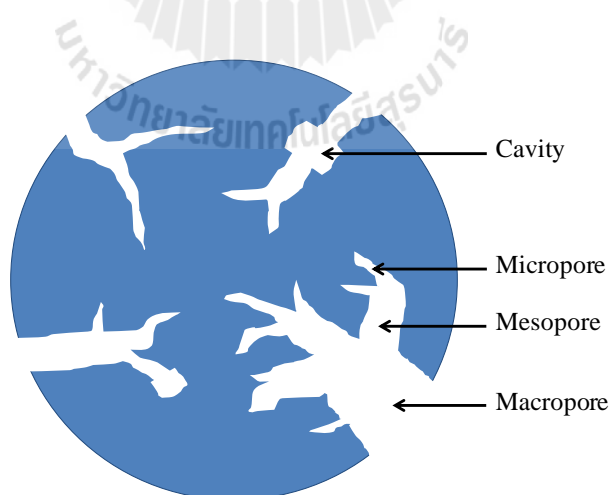


**Figure 2.1** Schematic described of different types of pore sizes

The mechanism of adsorption of simple gases in mesoporous materials begins with the formation of a monolayer on the surface followed by multilayer formation (unless the temperature is low enough, adsorption on higher layers occurs before the lower layers are completed and this is due to the molecular thermal energy) and finally by capillary condensation. At temperatures below the critical point, the amount of gas adsorbed in a porous material increases with increasing relative pressure. Isotherms are classified into six types according to the International Union of Pure and Applied Chemist (IUPAC) classification. Figure 2.2 shows the six main adsorption isotherm types. All adsorption isotherms should be categorized by one or a combination of two or more of these isotherms. The detail of each isotherm is outlined below.

Type I isotherm. This isotherm is the Langmuir type, showing a monolayer coverage adsorption. The adsorbents are dominated by microporous structure. The majority adsorption occurs at relative pressure below 0.1 and usually complete at the relative pressure approximately 0.5.

Type II isotherm. It involves the BET adsorption mechanism, monolayer coverage is followed by multi-layering at high relative pressures.

Type III isotherm. This class of isotherm exhibits a characteristic of weak adsorbate-adsorbent interactions leading to a low capacity of the uptake at low relative pressures. This behavior usually occurs in the adsorption of water on activated carbon because of the non-polar nature of the carbon surface. However, the presence of the oxygenated surface functional groups of activated carbon may act as the primary sites for water to adsorb on, and then this adsorbed molecule further acts as the secondary site for the other water molecules to adsorb on by hydrogen bonding.

The growing of the water cluster around the oxygenated group leads to rapid uptake at higher relative pressures.

Type IV isotherm. The general behavior of this isotherm is the same as type II isotherm, but this type exhibits a limit uptake when the pressure approaches the saturation pressure. The hysteresis loop is generally associated with the filling and emptying of the mesopores by capillary condensation.

Type V isotherm. This isotherm type is the same as the type III, the differences are the limit uptake and the presence of hysteresis loop. The water adsorption isotherm on activated carbon may be classified as type V.

Type VI isotherm. This isotherm shape is due to the complete formation of monolayer before the progression to a subsequent layer.

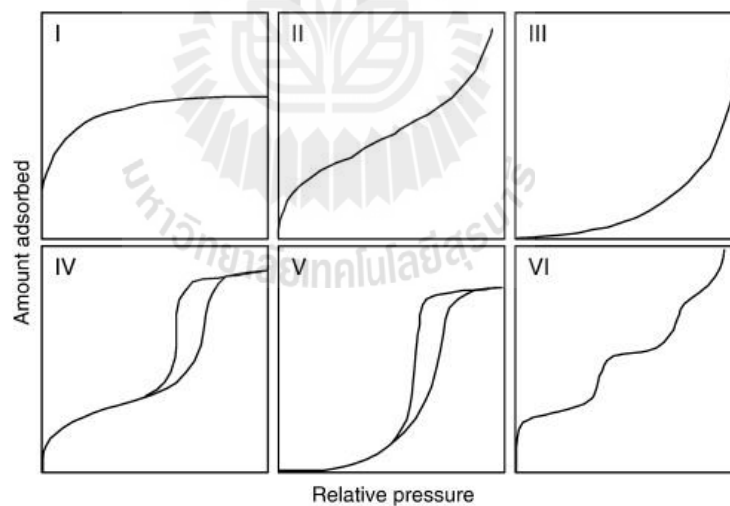


**Figure 2.2** The IUPAC classification of isotherms

Type IV and V, show a hysteresis loop associated with the filling and emptying of the mesopores by capillary condensation and evaporation, respectively. There have been many studies reporting different isotherms, many of which exhibit a

hysteresis loop. These hysteresis loops were subsequently classified into four types by IUPAC, and these are shown in Figure 2.3. The shapes of the adsorption hysteresis loop have been attributed to particular pore shapes. Type H1 loop, which is narrow with very steep and parallel adsorption and desorption branches, is associated with adsorbents with a narrow and uniform pore distribution such as MCM-41 (Kresge et al., 1992), SBA-15 (Zhao et al., 1998) etc., both of which have open-ended pores. Type H2 hysteresis loop has a broad loop with a gradual uptake on adsorption and a very steep desorption branch and it is typically observed with porous materials having networks of interconnected pores of progressive sizes and shapes. Type H3 and H4 do not terminate in a plateau at relative pressure, and thus, the limiting desorption boundary curve is not easy to define. Type H3 loop is associated with solids having aggregates of platy particles or solids containing slit-shaped pores, and type H4 loop is observed for solids having narrow slit-shaped pores, such as activated carbons.

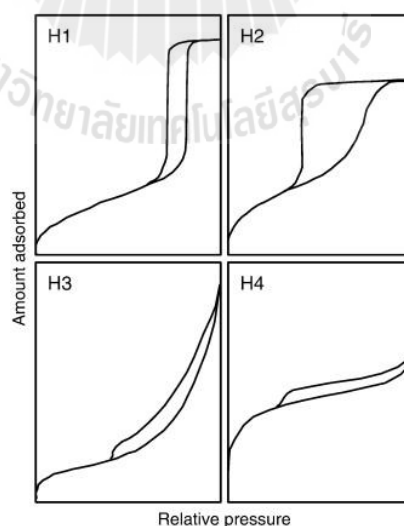


**Figure 2.3** The IUPAC classification of hysteresis loop



## 2.2 Fluid Models

The single-site Lennard Jones (LJ) 12-6 and Steele 10-4-3 potential energy equations have been shown to give a good description of adsorption of small pseudo-spherical molecules on surfaces and in pores. For argon, the molecular parameters are  $\varepsilon/k_B = 119.8$  K and  $\sigma = 0.3405$  nm (Do and Do, 2005b; Hauschild and Prausnitz, 1993).

For benzene model, high-level *ab initio* quantum mechanical calculations have been computed for dimers (Zhao and Truhlar, 2005), trimers (Tauer and Sherrill, 2005), and tetramers (Tauer and Sherrill, 2005), but their applications in condensed phases and larger systems are limited because of the long computation times required. As an alternative, empirical potentials (or force fields) are generally obtained by deriving their molecular parameters and partial atomic charges from fitting simulation results to the experimental data such as the liquid density, heat of vaporization and vapour-liquid equilibrium. Most of the general force fields, such as AMBER (Cornell et al., 1996), OPLS (Jorgensen and McDonald, 1998), and CHARMM (Feller and MacKerell, 2000), are fitted to the experimental data at ambient conditions and their application to other temperatures has not been tested, while the anisotropic OPPE force field (Ahunbay et al., 2005; Contreras-Camacho et al., 2004), and the exp-6 force field for benzene (Errington and Panagiotopoulos, 1999) are limited because the C–H bond are neglected and no electrostatic interactions are accounted for. The better empirical potential models for benzene come from the TraPPE family, TraPPE-6 (Wick et al., 2000), TraPPE-UA-9 (Wick et al., 2002) and TraPPE-EH (Rai and Siepmann, 2007). These models provide more accurate liquid and vapour densities,

vapour pressures, and heats of vaporization over a wide range of temperatures than the other models.

From an assessment of the various potential models for benzene that are currently available in the literature, we selected three models and tested them for their description of benzene adsorption on a graphite surface. The first model is TraPPE-UA-9 model with 6 LJ sites and 3 charges that account for quadrupole moment. The 6 dispersive sites lie at the centres of the carbon atoms and the C–C bond length is 1.40 Å. The positive partial charge (+2.42 e) is put at the centre of the benzene ring, and two negative partial charges (−1.21 e) are placed at a distance of 0.785 Å on both sides of the ring along a normal to the ring. The second model is the OPLS-AA model, which was proposed originally by Jorgensen and Severance (Jorgensen and Severance, 1990), and was tested by Rai and Siepmann (Rai and Siepmann, 2007) who showed that it gives a good description of the vapor-liquid equilibria (VLE) data at room temperature. This model has 12 dispersive sites and 12 partial charge sites at the centres of the carbon atoms and hydrogen atoms. The C–C and C–H bond lengths are 1.40 and 1.08 Å, respectively. Finally, the new TraPPE-EH model proposed by Rai and Siepmann is also studied in the present work. Again this model has 12 dispersive sites and 12 partial charge sites centered on the carbon and hydrogen atoms; the C–C and C–H bond lengths are 1.392 and 1.08 Å, respectively, but differ from the TraPPE-EH model in the values of the parameters. The parameters of these three models are listed in Table 2.1.

**Table 2.1** Potential parameters of benzene for three potential models

model	group	$\sigma$ (Å)	$\epsilon/k_B$ (K)	$q$ (e)
TraPPE-UA-9 (Wick et al., 2002)	CH	3.74	48.00	-
	$z = 0$			+2.420
	$z = \pm 0.785$ Å			-1.210
OPLS-AA (Jorgensen and Severance, 1990)	C	3.55	35.22733	-0.115
	H	2.42	15.09743	+0.115
TraPPE-EH (Rai and Siepmann, 2007)	C	3.60	30.70	-0.095
	H	2.36	25.45	+0.095

It has been found in our previous work (Klomkliang et al., 2012) that the TraPPE-UA models (Wick et al., 2002) comprising six LJ sites and three charged sites can describe the experimental data for fluid benzene reasonably well, and we will employ this model here to study BTX adsorption on graphitic surface and in pores. The six LJ sites are at the centres of the carbon atoms of the aromatic ring with a C(aro)–C(aro) bond length of 1.40 Å. For toluene and xylene (only *p*-xylene is taken in this work), additional dispersive sites are located at the centre of mass of the carbon atom of the methyl group and C(aro)–CH<sub>3</sub> bond length is 1.54 Å. A positive partial charge (+2.42 e) is placed at the centre of the benzene ring, and two negative partial charges (–1.21 e each) on both sides of the ring are placed at a distance of 0.785 Å normal to the ring to account for the quadrupole. Since toluene has a dipole, we investigate the effects of dipole by using the OPLS-AA model (Jorgensen and Nguyen, 1993). The molecular parameters of these models are listed in Table 2.2.

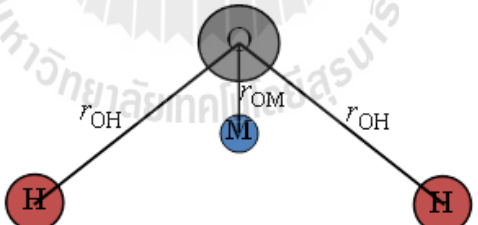
**Table 2.2** Potential parameters for benzene, toluene and xylene

model	group	$\sigma$ (Å)	$\epsilon/k_B$ (K)	$q$ (e)	
TraPPE-UA (Wick et al., 2002)	CH	3.74	48.00	-	
	C	3.88	21.00	-	
	CH <sub>3</sub>	3.75	98.00	-	
	$z = 0$			+2.420	
	$z = \pm 0.785$ Å			-1.210	
	<b>bond length</b>				
	C(aro)-C(aro)		1.40 Å		
	C(aro)-CH <sub>3</sub>		1.54 Å		
OPLS-AA (Jorgensen and Nguyen, 1993)	C	3.55	35.227	-0.115	
	H	2.42	15.097	+0.115	
	CH <sub>3</sub>	3.80	85.513	+0.115	
	<b>bond length</b>				
		C(aro)-C(aro)		1.40 Å	
		C(aro)-H		1.08 Å	
	C(aro)-CH <sub>3</sub>		1.51 Å		

There are many different models of water have been proposed; they can be classified by the number of points used to define the model (atoms plus dummy sites), whether the structure is rigid or flexible, and whether the model includes polarization effects. We believe that a good prediction of vapor-liquid equilibria (VLE) is a prerequisite for adsorption studies (Do et al., 2005; Do and Do, 2005a; Do and Do, 2005c; Do and Do, 2005d; Do et al., 2004). Therefore, we shall consider the TIP4P/2005 model (Abascal and Vega, 2005) to represent with only dispersive and Coulombic forces. The molecular parameters of this model are listed in Table 2.3. There are four interaction sites. Three of them are placed at the oxygen and hydrogen atom positions, respectively. The other site, often called the M site, is coplanar with

the O and H sites and is located at the bisector of the H–O–H angle. The O–H distance and H–O–H angle are 0.9572 Å and 104.52°, respectively. The total potential energy of the system is the sum of the pair interactions between molecules. The intermolecular pair potential has two contributions, a Lennard-Jones term and an electrostatic interaction. An important feature of the model is that the oxygen site carries no charge, but contributes to the LJ term. Conversely, the H and M sites are charged, but do not contribute to the LJ term.

**Table 2.3** Potential parameters for TIP4P/2005 model (Abascal and Vega, 2005)

group	$\sigma$ (Å)	$\epsilon/k_B$ (K)	$q$ (e)
O	3.1589	93.2	-
M	-	-	-1.1128
H	-	-	+0.5564
$r_{OH} = 0.9572$ Å			
$r_{OM} = 0.1546$ Å			
$\angle HOH = 104.52^\circ$			
			

## 2.3 Solid Models

The surface of solid models can be modeled as a structure-less surface and atomistic model as shown in Figure 2.4 and 2.5, respectively. In the atomistic model of a slit-pore, the solid surface is assumed to consist of four graphene layers, and these layers are stacked on top of each other with an interlayer spacing of 0.3354 nm. The carbon-carbon bond length in a graphene layer is 0.142 nm. The layers themselves are

rather weakly bound to each other (weak longrange Van der Waals type interaction). For the atomistic model of cylindrical pore, the carbon-carbon bond length is the same as in the slit-pore. If the cylindrical pore is modeled as a multiwall carbon nanotube the interlayer distance is also the same as in case of slit-pore.

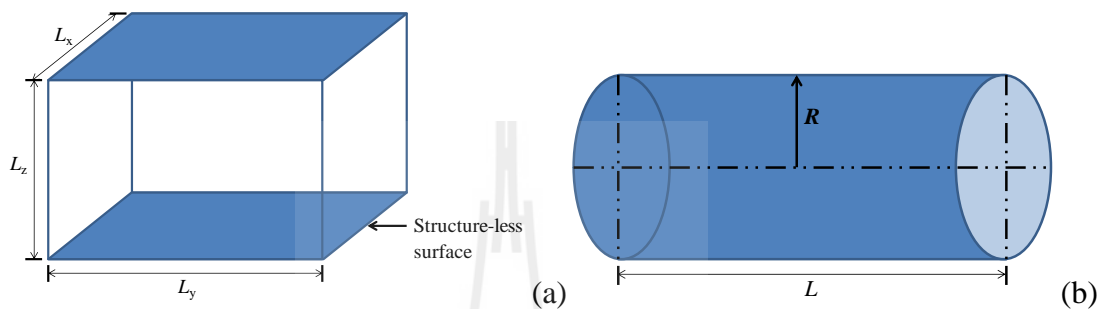


**Figure 2.4** Graphitized structure-less model for (a) a slit-pore and (b) cylindrical pore

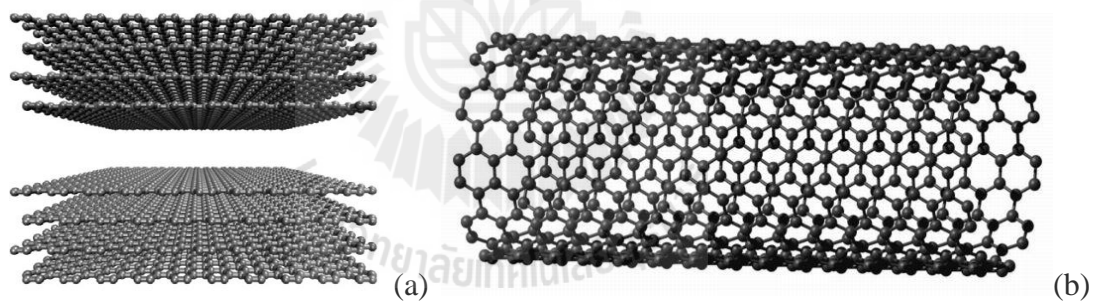


**Figure 2.5** Graphitized atomistic model for (a) a slit-pore and (b) cylindrical pore

## 2.4 Fluid-Fluid Interaction Energy

The commonly accepted single-site LJ 12-6 and Steele 10-4-3 potential energy equations work well for small pseudo-spherical molecules. However, for large molecules, such as benzene, single-site models are not suitable. Here we consider benzene to be a hexagonal molecule composed of at least 6 sites. For a polyatomic

molecule with  $M$  LJ site centres, the potential energy of interaction between a site  $a$  on a molecule  $i$  with a site  $b$  on a molecule  $j$  can be calculated using the following LJ 12-6 equation:

$$U_{i,j}^{(a,b)} = \sum_{a=1}^M \sum_{b=1}^M 4\varepsilon_{i,j}^{(a,b)} \left[ \left( \frac{\sigma_{i,j}^{(a,b)}}{r_{i,j}^{(a,b)}} \right)^{12} - \left( \frac{\sigma_{i,j}^{(a,b)}}{r_{i,j}^{(a,b)}} \right)^6 \right] \quad (2.1)$$

where  $r_{i,j}^{(a,b)}$  is the separation distance between the LJ site  $a$  on molecule  $i$  and the LJ site  $b$  on molecule  $j$ ,  $\sigma_{i,j}^{(a,b)}$  and  $\varepsilon_{i,j}^{(a,b)}$  are the cross collision diameter and the cross well-depth of the interaction energy, respectively. The cross parameters,  $\sigma_{i,j}^{(a,b)}$  and  $\varepsilon_{i,j}^{(a,b)}$  can be determined by the Lorentz-Berthelot mixing rules:  $\sigma_{i,j}^{(a,b)} = (\sigma_{i,j}^{(a,a)} + \sigma_{i,j}^{(b,b)})/2$  and  $\varepsilon_{i,j}^{(a,b)} = (\varepsilon_{i,j}^{(a,a)} \varepsilon_{i,j}^{(b,b)})^{1/2}$ . The interaction energy due to the electrostatic force between a charge  $\alpha$  on a molecule  $i$  and a charge  $\beta$  on a molecule  $j$  can be calculated from the Coulomb law of electrostatic interaction

$$U_{q_i^{\alpha}, q_j^{\beta}}^{(\alpha, \beta)} = \sum_{\alpha=1}^{M_q} \sum_{\beta=1}^{M_q} \frac{1}{4\pi\varepsilon_0} \frac{q_i^{\alpha} q_j^{\beta}}{r_{i,j}^{(\alpha, \beta)}} \quad (2.2)$$

where  $M_q$  is the number of charges on the molecule,  $\varepsilon_0$  is the permittivity of free space [ $\varepsilon_0 = 10^7/(4\pi c^2) = 8.8543 \times 10^{-12} \text{ C}^2\text{J}^{-1}\text{m}^{-1}$ ,  $c$  is the speed of light],  $r_{i,j}^{(\alpha, \beta)}$  is the distance between two charges  $\alpha$  and  $\beta$  on molecules  $i$  and  $j$ , respectively,  $q_i^{\alpha}$  is the value of charge  $\alpha$  on molecule  $i$ , and  $q_j^{\beta}$  is the value of charge  $\beta$  on molecule  $j$ . In the present work, surface mediation is taken into account because of the surface influence on the interaction among adsorbed molecules close to the surface (Do and Do, 2006). This is

done empirically by reducing the contribution of each benzene molecule in the intermolecular fluid-fluid interaction energy by a factor  $F$  whenever that molecule is in the first layer.

## 2.5 Fluid-Solid Interaction Energy

Solid surface as atomistic model is able to be applied for both infinite and finite pore lengths by accounting or untaken, respectively the periodic boundary conditions. The potential between adsorbate and carbon atoms of solid is calculated by using LJ 12-6 equation and/or Coulombic electrostatic interaction, while the structure-less surface has to be accounted a particular equation by the following sections.

### 2.5.1 Infinite Surface and Slit-Pore

To calculate adsorbate-adsorbent interaction, we employ a model which the GTCB surface was modelled as a structure-less surface with infinitely long length, and therefore the adsorbate-adsorbent potential energy can be calculated from the Steele 10-4-3 equation (Steele, 1973). For a polyatomic molecule with  $M$  LJ site centres, the interaction potential energy between molecule  $i$  and the homogeneous flat solid substrate can be calculated from

$$U_{i,s} = \sum_{a=1}^M 4\pi\varepsilon_i^{(a,s)} \rho_s [\sigma_i^{(a,s)}]^2 \left[ \frac{1}{5} \left( \frac{\sigma_i^{(a,s)}}{z_i^a} \right)^{10} - \frac{1}{2} \left( \frac{\sigma_i^{(a,s)}}{z_i^a} \right)^4 - \frac{[\sigma_i^{(a,s)}]^4}{6\Delta(z_i^a + 0.61\Delta)^3} \right] \quad (2.3)$$

where  $z_i^a$  is the distance of site  $a$  of molecule  $i$  from the graphite surface,  $\varepsilon_i^{(a,s)}$  and  $\sigma_i^{(a,s)}$  are the adsorptive-graphite interaction potential well-depth and intermolecular



collision diameter respectively,  $\rho_s$  is the surface density (taken as  $38.2 \text{ nm}^{-2}$  in this work), and  $\Delta$  is the spacing between the two adjacent graphite layers (0.3354 nm).

The parameters are calculated by combining the parameters for a carbon atom in graphene with the appropriate adsorbate parameters using the Lorentz-Berthelot mixing rules. The well-depth of interaction energy for the adsorbate-adsorbent interaction was adjusted with the binary interaction parameter,  $k_{sf}$ , to give agreement between the experimental Henry constant and GCMC simulations, where  $\epsilon_i^{(a,s)} = (1 - k_{sf}) \sqrt{\epsilon_i^{(a,a)} \epsilon_i^{(s,s)}}$ . The molecular parameters for a carbon atom in the graphene layer are  $\sigma_i^{(s,s)} = 0.34 \text{ nm}$  and  $\epsilon_i^{(s,s)} / k_B = 28 \text{ K}$ . For the structure-less model and the atomistic model, we assume that the binary interaction parameter,  $k_{sf}$  is the same for all the interaction sites on a molecule; the values  $-0.120$ ,  $-0.060$  and  $-0.036$  were found for TraPPE-UA-9, OPLS-AA and TraPPE-EH models, respectively for benzene adsorption on graphite surface. For a slit pore, the adsorbate molecule interacts with both walls, so the fluid-solid potential energy  $U_{sf}$  is calculated from:

$$U_{sf} = U_{i,s}(z) + U_{i,s}(H - z) \quad (2.4)$$

where  $H$  is the physical pore width, defined as the distance between the plane passing through all carbon atoms in the outermost layer of one wall and the corresponding plane at the opposite wall.

### 2.5.2 Infinite Cylindrical Pore

For a sufficiently long cylindrical pore and structure-less surface, the end effects are neglected and the fluid-solid potential energy can be calculated using the following equation (Tjatjopoulos et al., 1988);

$$U_{i,s} = \sum_{a=1}^M 4\pi^2 \varepsilon_i^{(a,s)} \rho_s [\sigma_i^{(a,s)}]^2 [I_6 - I_3] \quad (2.5)$$

The functions  $I_3$  and  $I_6$  are given by

$$I_3 = \frac{3}{4} \left( \frac{\sigma_i^{(a,s)}}{R} \right)^4 \left[ 1 - \left( \frac{r_i^a}{R} \right)^2 \right]^4 F_{\text{Hyp}} \left[ -\frac{3}{2}; -\frac{3}{2}; 1; \left( \frac{r_i^a}{R} \right)^2 \right] \quad (2.6)$$

$$I_6 = \frac{63}{128} \left( \frac{\sigma_i^{(a,s)}}{R} \right)^{10} \left[ 1 - \left( \frac{r_i^a}{R} \right)^2 \right]^{-10} F_{\text{Hyp}} \left[ -\frac{9}{2}; -\frac{9}{2}; 1; \left( \frac{r_i^a}{R} \right)^2 \right] \quad (2.7)$$

where  $r_i^a$  is the distance of site  $a$  of molecule  $i$  to the centre axis of the cylindrical pore, and  $R$  is radius of the pore and  $F_{\text{Hyp}}[a, b, c, d]$  is a hypergeometric function. The cross molecular parameters are estimated using the Lorentz-Berthelot mixing rules.

### 2.5.3 Finite Slit-Pore

The interaction between a site at  $(y_i^a, z_i^a)$  and a graphene strip as a structure-less surface which is finite in the  $y$ -direction and infinite in the  $x$ -direction (see Figure 2.6) is calculated from the Bojan-Steele equation (Bojan and Steele, 1988; Bojan and Steele, 1989; Bojan and Steele, 1993):

$$U_{i,s} = \sum_{a=1}^M 2\pi\varepsilon_i^{a,s} \rho_s (\sigma_i^{a,s})^2 \left\{ \left[ U_{rep}(y_i^{a,+}, z_i^a) - U_{rep}(y_i^{a,-}, z_i^a) \right] - \left[ U_{att}(y_i^{a,+}, z_i^a) - U_{att}(y_i^{a,-}, z_i^a) \right] \right\} \quad (2.8)$$

where

$$y_i^{a,+} = \frac{L}{2} - y_i^a; \quad y_i^{a,-} = -\frac{L}{2} - y_i^a \quad (2.9)$$

The repulsive and attractive terms on the right hand side of Eq. (2.8) are given by:

$$U_{rep}(y, z) = \frac{y}{\sqrt{y^2 + z^2}} \left\{ \frac{1}{5} \left( \frac{\sigma_i^{a,s}}{z} \right)^{10} + \frac{1}{10} \frac{(\sigma_i^{a,s})^{10}}{z^8 (y^2 + z^2)} + \frac{3}{40} \frac{(\sigma_i^{a,s})^{10}}{z^6 (y^2 + z^2)^2} + \frac{1}{16} \frac{(\sigma_i^{a,s})^{10}}{z^4 (y^2 + z^2)^3} + \frac{7}{128} \frac{(\sigma_i^{a,s})^{10}}{z^2 (y^2 + z^2)^4} \right\} \quad (2.10)$$

$$U_{att}(y, z) = \frac{y}{\sqrt{y^2 + z^2}} \left\{ \frac{1}{2} \left( \frac{\sigma_i^{a,s}}{z} \right)^4 + \frac{1}{4} \frac{(\sigma_i^{a,s})^4}{z^2 (y^2 + z^2)} \right\} \quad (2.11)$$

where  $\varepsilon_i^{a,s}$  and  $\sigma_i^{a,s}$  are the adsorptive-graphite interaction potential well-depth and intermolecular collision diameter respectively, and  $\rho_s$  is the surface density (38.2 nm<sup>-2</sup>).

The cross parameters,  $\sigma_i^{a,s}$  and  $\varepsilon_i^{a,s}$  can be determined from the Lorentz-Berthelot

mixing rules:  $\sigma_i^{a,s} = (\sigma_i^{a,a} + \sigma^{s,s})/2$  and  $\varepsilon_i^{a,s} = (\varepsilon_i^{a,a} \varepsilon^{s,s})^{1/2}$ .

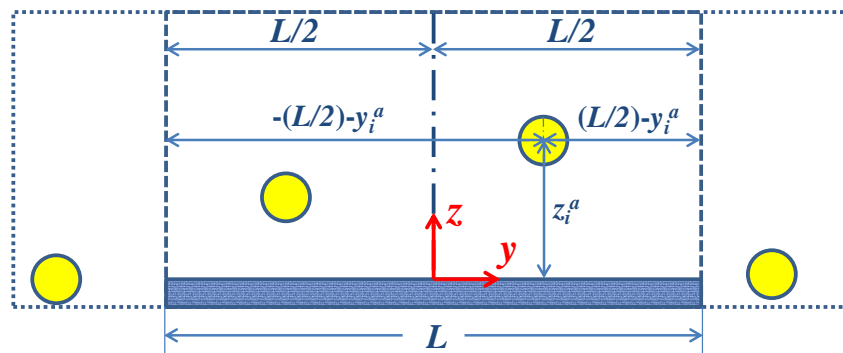


**Figure 2.6** Configuration of a finite strip

The potential equation energy in Eqs. (2.8) to (2.11) is valid for any positions around the strip, except  $z_i^a \rightarrow 0$ , and in such cases we use the following Taylor series expansion:

$$\begin{aligned}
\frac{U_{i,s}}{2\pi K \rho_s} = & \sum_{a=1}^M \varepsilon_i^{a,s} (\sigma_i^{a,s})^2 \left( \left\{ \frac{63}{1280} \left[ \left( \frac{\sigma_i^{a,s}}{y_i^{a,-}} \right)^{10} - \left( \frac{\sigma_i^{a,s}}{y_i^{a,+}} \right)^{10} \right] \right. \right. \\
& - \frac{3}{16} \left[ \left( \frac{\sigma_i^{a,s}}{y_i^{a,-}} \right)^4 - \left( \frac{\sigma_i^{a,s}}{y_i^{a,+}} \right)^4 \right] \left. \right\} \\
& - \left( \frac{z_i^a}{\sigma_i^{a,s}} \right)^2 \left\{ \frac{231}{1024} \left[ \left( \frac{\sigma_i^{a,s}}{y_i^{a,-}} \right)^{12} - \left( \frac{\sigma_i^{a,s}}{y_i^{a,+}} \right)^{12} \right] \right. \\
& - \frac{5}{16} \left[ \left( \frac{\sigma_i^{a,s}}{y_i^{a,-}} \right)^6 - \left( \frac{\sigma_i^{a,s}}{y_i^{a,+}} \right)^6 \right] \left. \right\} \\
& + \left( \frac{z_i^a}{\sigma_i^{a,s}} \right)^4 \left\{ \frac{1287}{2048} \left[ \left( \frac{\sigma_i^{a,s}}{y_i^{a,-}} \right)^{14} - \left( \frac{\sigma_i^{a,s}}{y_i^{a,+}} \right)^{14} \right] \right. \\
& - \frac{105}{256} \left[ \left( \frac{\sigma_i^{a,s}}{y_i^{a,-}} \right)^8 - \left( \frac{\sigma_i^{a,s}}{y_i^{a,+}} \right)^8 \right] \left. \right\} \\
& - \left( \frac{z_i^a}{\sigma_i^{a,s}} \right)^6 \left\{ \frac{45045}{32768} \left[ \left( \frac{\sigma_i^{a,s}}{y_i^{a,-}} \right)^{16} - \left( \frac{\sigma_i^{a,s}}{y_i^{a,+}} \right)^{16} \right] \right. \\
& - \frac{63}{128} \left[ \left( \frac{\sigma_i^{a,s}}{y_i^{a,-}} \right)^{10} - \left( \frac{\sigma_i^{a,s}}{y_i^{a,+}} \right)^{10} \right] \left. \right\} \\
& + \left( \frac{z_i^a}{\sigma_i^{a,s}} \right)^8 \left\{ \frac{85085}{32768} \left[ \left( \frac{\sigma_i^{a,s}}{y_i^{a,-}} \right)^{18} - \left( \frac{\sigma_i^{a,s}}{y_i^{a,+}} \right)^{18} \right] \right. \\
& \left. - \frac{1155}{2048} \left[ \left( \frac{\sigma_i^{a,s}}{y_i^{a,-}} \right)^{12} - \left( \frac{\sigma_i^{a,s}}{y_i^{a,+}} \right)^{12} \right] \right\} + O(z / \sigma_i^{a,s})^{10} \Big)
\end{aligned} \tag{2.12}$$

where  $K = 1$  for positive values of  $y_i^{a,+}$  and  $y_i^{a,-}$ ,  $K = -1$  for negative values of  $y_i^{a,+}$

and  $y_i^{a,-}$ .

### 2.5.4 Finite Cylindrical Pore

In order to account for the pore end of a finite cylindrical pore as a structure-less surface (see Figure 2.7), the fluid-solid potential energy between an

adsorbate and a single wall finite cylindrical pore is obtained from the following equation (a detailed derivation is given in ref. (Nguyen et al., 2011)):

$$U_{fs} = 4\varepsilon_{fs}\rho_s R \sum_{n=3,6} a_n \sigma_{fs}^{2n} \int_0^{2\pi} I(\theta, r, z, n, R, L) d\theta \quad (2.13)$$

where  $R$  is the pore radius,  $L$  is the pore length,  $r$  is the radial distance from the pore center to the adsorbate,  $z$  is the axial distance from the middle of the pore to the adsorbate, and  $a_n$  is a constant ( $a_3=-1$  and  $a_6=1$ ).

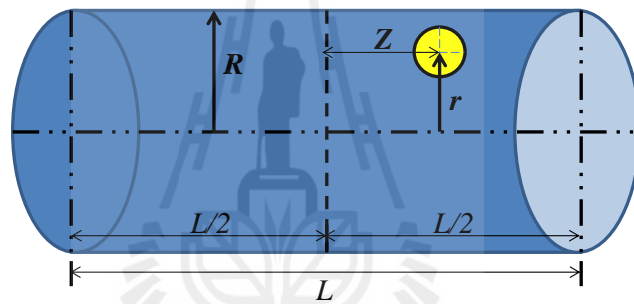


**Figure 2.7** The adsorbate is inside the finite cylindrical pore.

## 2.6 The Conventional Monte Carlo Simulation

Monte Carlo simulation is a powerful tool to study molecular simulation that combined with statistical thermodynamics, allows calculation the properties of fluids from the interaction of its constituent particles in both bulk phase and confined space. Using Monte Carlo simulation, the properties of systems such as density, pressure, energy, etc., are usually determined with the selection of an ensemble. An ensemble is defined as a set of a large number of systems in different quantum states but sharing the same macroscopic properties.

In Monte Carlo there are four main ensembles (Allen and Tildesley, 1987): canonical, isobaric-isothermal, grand canonical and Gibbs ensembles. A brief description of them is presented in Table 2.4.

**Table 2.4** Ensembles in Monte Carlo simulation

ensemble	description	applications
Grand canonical Monte Carlo simulation (GCMC)	The chemical potential ( $\mu$ ), volume (V), and temperature (T) are constant.	To use in adsorption.
Canonical Monte Carlo simulation (CMC)	The number of molecules (N), volume (V), and temperature (T) are constant.	To estimate pressure when the density of fluid is known.
Isobaric-isothermal Monte Carlo simulation (NPT)	The number of molecules (N), pressure (P), and temperature (T) are constant.	To use in case where the experiments are performed under conditions of pressure and temperature controlled.
Gibbs ensemble Monte Carlo simulation (GEMC)	There are two versions of this ensemble the CMC and NPT.	To use in conditions where there is phase coexistence.

There are two ensembles used in this work CMC and GCMC, we have described these ensembles by the following:

### 2.6.1 Canonical Monte Carlo Simulation

In this ensemble, the number of molecules (N), volume of simulation box (V), and temperature (T) are fixed. N particles are addressed in the simulation box and they are moved randomly one by one to minimize the total potential energy interaction between all particles (and all particles with solid in case of a confined space) of the system. The displacement of a particle from a position in where its

potential energy is  $U_{old}$ , to another position of potential energy  $U_{new}$ , is accepted with the following probability;

$$P = \min \left\{ 1, \exp \left( -\frac{(U_{new} - U_{old})}{k_B T} \right) \right\} \quad (2.14)$$

where  $k_B$  is Boltzmann constant. To apply this ensemble for bulk phase or confined space to calculate fluid properties such as density, pressure and chemical potential, it is necessary to make the simulation box being at least ten times of the colloid diameter of fluid and need to apply periodic boundary conditions. In Figure 2.8, how to apply the periodic boundary condition is that all particles in the simulation box (dark box) are calculated the distance between particles. For example particle number 1 in the dark box, if the distance of particle 1 with others in the dark box is greater than half of box length ( $L/2$ ), the distance between particle will be deducted by:

$$\begin{aligned} d_{12} &= |d_1 - d_2|; \text{ if } d_{12} > L/2, \quad d_{12} = |d_{12} - L/2| \\ d_{13} &= |d_1 - d_3|; \text{ if } d_{13} > L/2, \quad d_{13} = |d_{13} - L/2| \\ d_{14} &= |d_1 - d_4|; \text{ if } d_{14} > L/2, \quad d_{14} = |d_{14} - L/2| \\ d_{15} &= |d_1 - d_5|; \text{ if } d_{15} > L/2, \quad d_{15} = |d_{15} - L/2| \\ d_{16} &= |d_1 - d_6|; \text{ if } d_{16} > L/2, \quad d_{16} = |d_{16} - L/2| \end{aligned}$$

From Figure 2.8, the distance of  $d_{13}$ ,  $d_{14}$ ,  $d_{15}$ , and  $d_{16}$  in the dark box is greater than half of box length, so the distance is deducted to be in the circle which is equivalent to particle 1 interacts with particles 3, 5, and 6 in the other boxes as minimum image conventions. The new  $d_{14}$  is still larger than the radius of the circle, the radius of the circle in Figure 2.8 equals to radius cut off which is the value of



significant distance interaction between molecules, if the distance between particles is greater than radius cut off the potential energy has no significance.

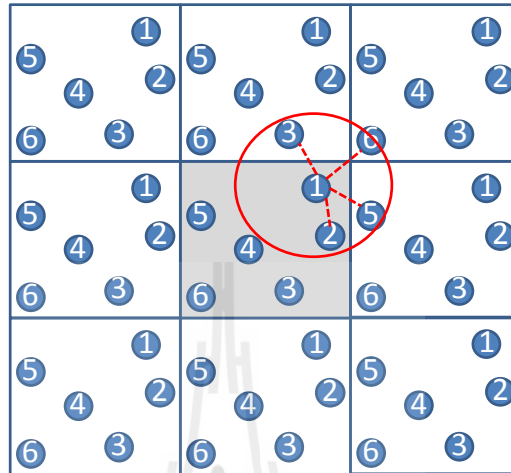


**Figure 2.8** Periodic boundary conditions and minimum image applied in bulk phase

### 2.6.2 Grand Canonical Monte Carlo Simulation

This ensemble looks for the calculation of the number of particles of a system where chemical potential ( $\mu$ ), volume ( $V$ ), and temperature ( $T$ ) are fixed. The calculation scheme for this ensemble is given by three main types of trial moves: insertion, deletion, and displacement move of particles. The insertion step is carried out by inserting a particle in the simulation box at a random position and calculating its total potential with the existing particles in the box, and the solid (in case that adsorption is simulated). The inserted particle is kept in the simulation box with the following probability otherwise it would be rejected.

$$P = \min \left\{ 1, \frac{V}{\Lambda^3(N+1)} \exp \left[ \frac{\mu - U(N+1) + U(N)}{k_B T} \right] \right\} \quad (2.15)$$

where  $V$  is the volume of the simulation box,  $N$  is numbers of particle,  $\mu$  is chemical potential and  $\Lambda$  is the thermal de Broglie wavelength which is calculated by:

$$\Lambda = \sqrt{\frac{h^2}{2\pi \cdot MW \cdot k_B \cdot T}} \quad (2.16)$$

To remove a particle from the simulation box a particle is randomly selected which its total potential energy is calculated, the selected particle is removed with the following probability:

$$P = \min \left\{ 1, \frac{\Lambda^3 N}{V} \exp \left[ -\frac{\mu + U(N-1) - U(N)}{k_B T} \right] \right\} \quad (2.17)$$

The displacement move step is performed in the same manner as in the CMC. The fractions of attempted displacement move, insertion, and deletion used in this work are equal probability, hence in each cycle of calculation, the fraction number is randomly selected and if it falls in the range of 0 to  $< 1/3$ , the system is allowed to conduce insertion. When the fraction is in the range of  $1/3$  to  $< 2/3$  and  $2/3$  to 1, the system is allowed to conduce deletion and displacement move, respectively. When the system is attempted with high and enough number of cycles, the system will raise the equilibrium.

Figure 2.9 shows adsorption of fluid in pore and periodic boundary conditions is applied in the direction parallel to the solid surface. For example, the distance between particle 2 and 1 and 3 in the dark box is greater than half of box length, so the distance is reduced to be which is within the cycle.

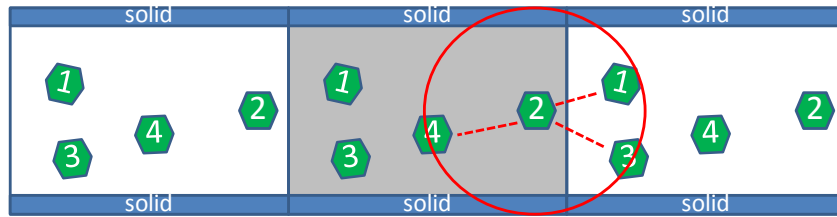


**Figure 2.9** Periodic boundary condition applied in confined space, here is adsorption phase.

## 2.7 The *Bin* Monte Carlo Simulation

### 2.7.1 *Bin* Grand Canonical Monte Carlo Simulation

To simulate the adsorption isotherm we used the conventional GCMC scheme (Allen and Tildesley, 1987), and the *Bin*-GCMC scheme (Fan et al., 2011), the latter is described briefly here. The adsorption space is divided into bins as shown in Figure 2.10 and a bin (say bin  $K$ ) is randomly selected for particle insertion at a random position, after which a randomly selected particle is displaced within that bin. Then, a randomly selected particle in the same bin is deleted, followed by a displacement of a randomly selected particle. The probabilities of acceptance of the displacement move, insertion and deletion are given by Eqs. (2.18), (2.19) and (2.20), respectively.

$$\text{Displacement: } P = \min \left\{ 1, \exp \left( -\frac{\Delta U}{k_B T} \right) \right\} \quad (2.18)$$

$$\text{Insertion: } P = \min \left\{ 1, \frac{V_K}{\Lambda^3 (N_K + 1)} \exp \left[ \frac{\mu - U(N_K + 1) + U(N_K)}{k_B T} \right] \right\} \quad (2.19)$$

$$\text{Deletion: } P = \min \left\{ 1, \frac{\Lambda^3 N_K}{V_K} \exp \left[ -\frac{\mu + U(N_K - 1) - U(N_K)}{k_B T} \right] \right\} \quad (2.20)$$

where  $\Delta U$  in Eq. (2.18) is the different energy between  $U_{\text{new}}$  and  $U_{\text{old}}$ ,  $[U(N_{K+1})+U(N_K)]$  in Eq. (2.19) is the interaction energy of the inserted particle in bin  $K$  with the existing particles of all bins and solid,  $[U(N_K-1)-U(N_K)]$  in Eq. (2.20) is the interaction energy of the deleted particle with the remaining particles and solid,  $V_K$  and  $N_K$  are volume and number of particles in bin  $K$ , respectively,  $k_B$  is the Boltzmann constant,  $T$  is the temperature,  $\mu$  is the chemical potential, and  $\Lambda$  is the thermal de Broglie wavelength. It should be noted that the probabilities of insertion and deletion depend on the local density, rather than the overall average density as in the conventional GCMC. Table 2.5 shows the computer program in FORTRAN for the main program of the *Bin*-GCMC comparison to the conventional GCMC developed in this work.

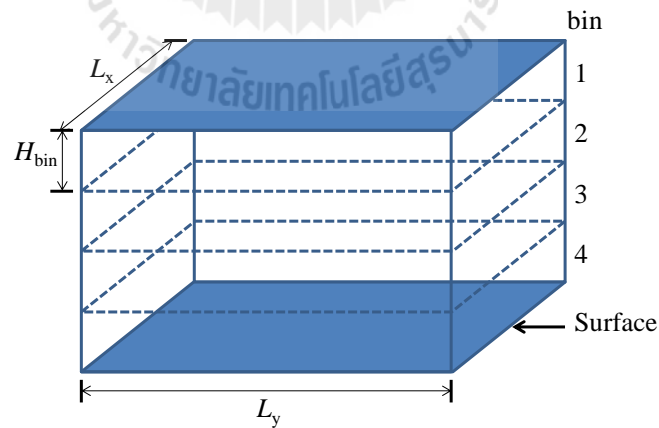


**Figure 2.10** The adsorption phase is divided into bins, for example in this figure there are 4 bins.

**Table 2.5** The FORTRAN code for the main program of conventional GCMC and *Bin-GCMC*

Conventional GCMC	<i>Bin-GCMC</i>
<pre> do iEqui = 1, NCycle do iMove = 1, 1000 call random_number(rdm)  if (rdm &lt;= 1.0D0/3.0D0) then  call Insertion (Temp, UFF, UC, UFS, V, mu)  else if (rdm &gt; 1.0D0/3.0D0 .AND. rdm &lt;= 2.0D0/3.0D0) then  call Deletion (Temp, UFF, UC, UFS, V, mu)  else  call MoveParticle (NMove, NAccpt, DeltaRx, DeltaRy, DeltaRz, Temp, UFF, UC, UFS, V)  end if  end do !do iMove = 1, 1000 end do !do iEqui = 1, NCycle </pre>	<pre> do iEqui = 1, DispMove do iBin = 1, NoMuBin!there are NoMuBin bins. call random_number(rdm) BinK = Select (NoMuBin)! BinK is selected  if (rdm &lt;= 0.50D0) then  call Insertion (Temp, UFFbin, UCbin, UFSbin, Vbin, UFF, UC, UFS, V, mu, BinK)  call MoveRotateParticle (NMove, NAccpt, DeltaRx, DeltaRy, DeltaRz, Temp, UFFbin, UCbin, UFSbin, Vbin, UFF, UC, UFS, V, BinK)  call Deletion (Temp, UFFbin, UCbin, UFSbin, Vbin, UFF, UC, UFS, V, mu, BinK)  call MoveRotateParticle (NMove, NAccpt, DeltaRx, DeltaRy, DeltaRz, Temp, UFFbin, UCbin, UFSbin, Vbin, UFF, UC, UFS, V, BinK)  else  call Deletion (Temp, UFFbin, UCbin, UFSbin, Vbin, UFF, UC, UFS, V, mu, BinK)  call MoveRotateParticle (NMove, NAccpt, DeltaRx, DeltaRy, DeltaRz, Temp, UFFbin, UCbin, UFSbin, Vbin, UFF, UC, UFS, V, BinK)  call Insertion (Temp, UFFbin, UCbin, UFSbin, Vbin, UFF, UC, UFS, V, mu, BinK)  call MoveRotateParticle (NMove, NAccpt, DeltaRx, DeltaRy, DeltaRz, Temp, UFFbin, UCbin, UFSbin, Vbin, UFF, UC, UFS, V, BinK)  end if  end do !do iBin = 1, NoMuBin end do !do iEqui = 1, DispMove </pre>

### 2.7.2 *Bin* Canonical Monte Carlo Simulation

*Bin*-canonical Monte Carlo simulation proposed by Fan and co-workers (Fan et al., 2011) briefly described here. The system is divided into bins. There are two moves in this scheme: displacement move and swapping a particle between two

randomly selected bins, say bin  $K$  and bin  $L$ . For the swapping move, a particle is selected at a random position in bin  $K$  and removed and as part of the same move, a particle is inserted at a random position in bin  $L$ . After this, displacement moves are made in both bins such that the displaced particles are not allowed to cross the boundaries between bins to ensure that microscopic reversibility is satisfied, otherwise they would have different maximum displacement lengths. The probability to delete a particle in bin  $K$  and to insert a particle in bin  $L$  is given by Eq. (2.21).

$$P = \min \left\{ 1, \frac{(N_K / V_K)}{(N_L + 1) / V_L} \exp \left( - \frac{[U(N_L + 1) - U(N_L)] - [U(N_K) - U(N_K - 1)]}{k_B T} \right) \right\} \quad (2.21)$$

A related method, devised to overcome the sampling problem in non-uniform systems was proposed earlier by Finn and Monson (Finn and Monson, 1988) in which moves of different lengths were permitted throughout the whole simulation box, but no division into bins was implemented. Table 2.6 shows the computer program in FORTRAN for the main program of the *Bin*-CMC comparison to the conventional CMC developed in this work.

## 2.8 Outputs from GCMC

Outputs from either the conventional GCMC or *Bin*-GCMC are calculated in the same way, for example: The average surface excess for an open surface was calculated from

$$\Gamma_{av} = \frac{\langle N \rangle - \rho_b V_{acc}}{2A} \quad (2.22)$$

**Table 2.6** The FORTRAN code for the main program of conventional CMC and *Bin*-CMC

Conventional CMC	<i>Bin</i> -CMC
<pre> do iEqui = 1, NCycle do iMove = 1, 1000  call MoveParticle (NMove, NAccpt, DeltaRx, DeltaRy, DeltaRz, Temp, UFF, UC, UFS, V)  end do !do iMove = 1, 1000 end do !do iEqui = 1, NCycle </pre>	<pre> do iEqui = 1, DispMove do iBin = 1, NoMuBin!there are NoMuBin bins. BinK = Select (NoMuBin)! BinK is selected BinL = Select (NoMuBin)! BinL is selected if (BinL == BinK) then if (BinL == 1) then BinL = BinL + 1 else if (BinL == NoMuBin) then BinL = BinL - 1 else BinL = BinL + 1 end if end if  call SwapDelIns (Temp, UFFbin, UCbin, UFSbin, Vbin, UFF, UC, UFS, V, BinK, BinL, mu) call MoveRotateParticle (NMove, NAccpt, DeltaRx, DeltaRy, DeltaRz, Temp, UFFbin, UCbin, UFSbin, Vbin, UFF, UC, UFS, V, BinK) call MoveRotateParticle (NMove, NAccpt, DeltaRx, DeltaRy, DeltaRz, Temp, UFFbin, UCbin, UFSbin, Vbin, UFF, UC, UFS, V, BinL) call SwapDelIns (Temp, UFFbin, UCbin, UFSbin, Vbin, UFF, UC, UFS, V, BinL, BinK, mu) call MoveRotateParticle (NMove, NAccpt, DeltaRx, DeltaRy, DeltaRz, Temp, UFFbin, UCbin, UFSbin, Vbin, UFF, UC, UFS, V, BinL) call MoveRotateParticle (NMove, NAccpt, DeltaRx, DeltaRy, DeltaRz, Temp, UFFbin, UCbin, UFSbin, Vbin, UFF, UC, UFS, V, BinK)  end do !do iBin = 1, DispMove end do !do iEqui = 1, NCycle </pre>

For the case of adsorption in pores, the pore density is defined by the excess quantity

$$\rho_{pore}^{EXC} = \frac{\langle N \rangle - \rho_b V}{V} \quad (2.23)$$

where  $\rho_b$  is the bulk molecular density,  $A$  is surface area of one wall of the simulation box, and  $\langle N \rangle$  is the ensemble average of the number of particles in the pore. The volume,  $V$ , in Eq. (2.23) can be taken either as the accessible pore volume ( $V_{acc}$ ) or as the physical pore volume ( $V_{phy}$ ). If the accessible volume (which is adsorbate-dependent) is used, the pore density gives a measure of how dense the adsorbed phase is. To compare the adsorptive capacities of different adsorbates, the volume  $V$  is taken to be the physical volume because the experimental data are expressed as the amount adsorbed per unit mass of solid adsorbent and the mass of the solid is related to the physical volume (which does not depend on adsorbate).

A thermodynamic quantity of interest that can be readily obtained from the GCMC simulations is the isosteric heat. Using the fluctuation theory, it is calculated from (Nicholson and Parsonage, 1982)

$$q_{isos} = \frac{\langle U \rangle \langle N \rangle - \langle UN \rangle}{\langle N^2 \rangle - \langle N \rangle \langle N \rangle} + k_B T \quad (2.24)$$

where  $\langle \rangle$  is the ensemble average,  $N$  is the number of particles, and  $U$  is the configuration energy of the system.

In order to study the variation of density from the surface, the local density of the centre of benzene ring is defined as:

$$\rho(z) = \frac{\langle \Delta N_{z+\Delta z} \rangle}{L_x L_y \Delta z} \quad (2.25)$$



where  $\langle \Delta N_{z+\Delta z} \rangle$  is the ensemble average of the number of molecules whose benzene ring centres are located in the segment having boundaries  $z$  and  $z + \Delta z$ .

## 2.9 The Mid-Density Scheme

GCMC simulation has been widely used as a standard method to simulate equilibrium isotherms of fluids in porous structures because it mimics the conditions of an adsorption experiment in which the temperature, volume and chemical potential (equivalent to the pressure of the bulk phase) are specified. Simulation of an adsorption system with a GCMC is started with either an empty box or a box full of particles. We increase the chemical potential and use the configuration of the previous chemical potential as the starting configuration for the determination of the next equilibrium point. This will give the adsorption branch. For the latter, we decrease the chemical potential and repeat the same procedure to obtain the desorption branch. Under conditions when the system exhibits a hysteresis, the adsorption and desorption branches are distinct, and the hysteresis loop is enclosed by stable and metastable states as shown in Figure 2.11. The equilibrium phase transition is shown in the same figure as a vertical dashed line separated between dilute stable state branch and dense stable state branch. It is this equilibrium transition that we aim to determine.

The Mid-Density scheme proposed recently by Liu and co-workers (Liu et al., 2011) was used to determine the equilibrium phase transition which has not previously been studied in detail in this type of pore model of this thesis. For a given chemical potential in the hysteresis loop, say  $\mu^*$ , the system exists in either a low density state ( $\rho_L$ ) or a high density state ( $\rho_H$ ), from which we calculate the average density,  $\rho_{av}$ , as the arithmetic average. The Mid-Density scheme starts with a

canonical simulation of a system with this average density; the initial configuration can be constructed by randomly inserting molecules into the empty box until the average density is achieved. This system is then relaxed canonically, followed by a grand canonical simulation at the chemical potential  $\mu^*$ . The final state from this simulation is taken to be the stable state. In this work, we have exploited the efficient sampling of the *Bin*-GCMC scheme to obtain the hysteresis loop, and *Bin*-CMC combined with *Bin*-GCMC in the Mid-Density scheme to find the path of the equilibrium transition.

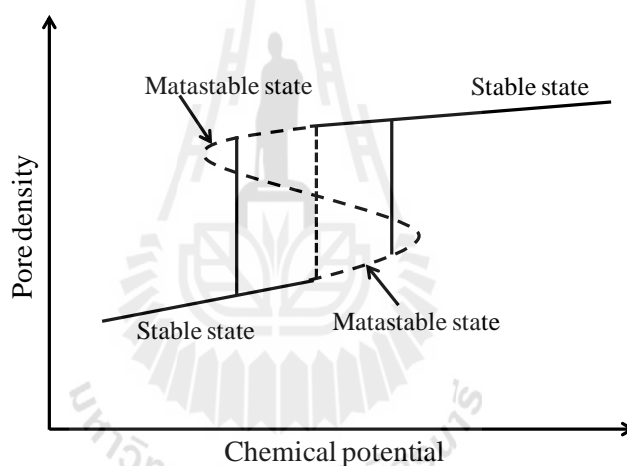


**Figure 2.11** Schematic representation of the hysteresis loop during adsorption enclosed by the stable and metastable states. The vertical dashed line is the equilibrium phase transition.

## 2.10 References

Abascal, J.L.F. and Vega, C. (2005). A general purpose model for the condensed phases of water: TIP4P/2005. **The Journal of Chemical Physics**. 123: 234505.

- Ahunbay, M.G., Perez-Pellitero, J., Contreras-Camacho, R.O., Teuler, J.M., Ungerer, P., Mackie, A.D. and Lachet, V. (2005). Optimized intermolecular potential for aromatic hydrocarbons based on anisotropic united atoms. III. Polyaromatic and naphthenoaromatic hydrocarbons. **Journal of Physical Chemistry B**. 109: 2970-2976.
- Allen, M.P. and Tildesley, T.P. (1987). Computer simulation of liquids. **Japanese Journal of Applied Physics Part 2-Letters**. 35: L405-L407.
- Bojan, M.J. and Steele, W.A. (1988). Computer simulation of physisorption on a heterogeneous surface. **Surface Science**. 199: L395-L402.
- Bojan, M.J. and Steele, W.A. (1989). Computer-simulation of physisorbed Kr on a heterogeneous surface. **Langmuir**. 5: 625-633.
- Bojan, M.J. and Steele, W.A. (1993). Computer-simulation of physical adsorption on stepped surfaces. **Langmuir**. 9: 2569-2575.
- Contreras-Camacho, R.O., Ungerer, P., Boutin, A. and Mackie, A.D. (2004). Optimized intermolecular potential for aromatic hydrocarbons based on anisotropic united atoms. I. Benzene. **Journal of Physical Chemistry B**. 108(37): 14109-14114.
- Cornell, W.D., Cieplak, P., Bayly, C.I., Gould, I.R., Merz, K.M., Ferguson, D.M., Spellmeyer, D.C., Fox, T., Caldwell, J.W. and Kollman, P.A. (1996). A second generation force field for the simulation of proteins, nucleic acids, and organic molecules (vol. 117, pg. 5179, 1995). **Journal of the American Chemical Society**. 118: 2309-2309.

- Do, D.D., Do, H.D. (2005). Adsorption of quadrupolar, diatomic nitrogen onto graphitized thermal carbon black and in slit-shaped carbon pores: Effects of surface mediation. **Adsorption Science & Technology**. 23: 267-288.
- Do, D.D. and Do, H.D. (2005a). Adsorption of argon on homogeneous graphitized thermal carbon black and heterogeneous carbon surface. **Journal of Colloid and Interface Science**. 287: 452-460.
- Do, D.D. and Do, H.D. (2005b). Effects of potential models in the vapor-liquid equilibria and adsorption of simple gases on graphitized thermal carbon black. **Fluid Phase Equilibria**. 236: 169-177.
- Do, D.D. and Do, H.D. (2005c). Effects of potential models in the vapor-liquid equilibria and adsorption of simple gases on graphitized thermal carbon black. **Fluid Phase Equilibria**. 236: 169-177.
- Do, D.D. and Do, H.D. (2005d). Effects of surface heterogeneity on the adsorption of nitrogen on graphitized thermal carbon black. **Molecular Simulation**. 31: 651-659.
- Do, D.D. and Do, H.D. (2006). Adsorption of benzene on graphitized thermal carbon black: Reduction of the quadrupole moment in the adsorbed phase. **Langmuir**. 22: 1121-1128.
- Do, D.D., Do, H.D. and Kaneko, K. (2004). Effect of surface-perturbed intermolecular interaction on adsorption of simple gases on a graphitized carbon surface. **Langmuir**. 20: 7623-7629.
- Errington, J.R. and Panagiotopoulos, A.Z. (1999). New intermolecular potential models for benzene and cyclohexane. **Journal of Chemical Physics**. 111: 9731-9738.

- Fan, C.Y., Do, D.D. and Nicholson, D. (2011). New Monte Carlo simulation of adsorption of gases on surfaces and in pores: A concept of multibins. **Journal of Physical Chemistry B**. 115: 10509-10517.
- Feller, S.E. and MacKerell, A.D. (2000). An improved empirical potential energy function for molecular simulations of phospholipids. **Journal of Physical Chemistry B**. 104: 7510-7515.
- Finn, J.E. and Monson, P.A. (1988). Adsorption equilibria in an isobaric ensemble. **Molecular Physics**. 65: 1345-1361.
- Hauschild, T. and Prausnitz, J.M. (1993). Monte-Carlo calculations for methane and argon over a wide-range of density and temperature, including the 2-phase vapor-liquid region. **Molecular Simulation**. 11: 177-185.
- Jorgensen, W.L. and McDonald, N.A. (1998). Development of an all-atom force field for heterocycles: Properties of liquid pyridine and diazenes. **THEOCHEM-Journal of Molecular Structure**. 424: 145-155.
- Jorgensen, W.L. and Nguyen, T.B. (1993). Monte Carlo simulations of the hydration of substituted benzenes with OPLS potential functions. **Journal of Computational Chemistry**. 14: 195-205.
- Jorgensen, W.L. and Severance, D.L. (1990). Aromatic-aromatic interactions: Free energy profiles for the benzene dimer in water, chloroform, and liquid benzene. **Journal of the American Chemical Society**. 112: 4768-4774.
- Klomkliang, N., Do, D.D., Nicholson, D., Tangsathitkulchai, C. and Wongkoblaph, A. (2012). Multilayer adsorption of benzene on graphitised thermal carbon black: The importance of quadrupole and explicit hydrogen in the potential model. **Chemical Engineering Science**. 69: 472-482.

- Kresge, C.T., Leonowicz, M.E., Roth, W.J., Vartuli, J.C. and Beck, J.S. (1992). Ordered mesoporous molecular sieves synthesized by a liquid-crystal template mechanism. **Nature**. 359: 710-712.
- Liu, Z.J., Herrera, L., Nguyen, V.T., Do, D.D. and Nicholson, D. (2011). A Monte Carlo scheme based on mid-density in a hysteresis loop to determine equilibrium phase transition. **Molecular Simulation**. 37: 932-939.
- Nguyen, P.T.M., Do, D.D. and Nicholson, D. (2011). On the hysteresis loop of argon adsorption in cylindrical pores. **The Journal of Physical Chemistry C**. 115: 4706-4720.
- Nicholson, D. and Parsonage, N. (1982). **Computer Simulation and the Statistical Mechanics of Adsorption**. Academic Press, London.
- Rai, N. and Siepmann, J.I. (2007). Transferable potentials for phase equilibria. 9. explicit hydrogen description of benzene and five-membered and six-membered heterocyclic aromatic compounds. **Journal of Physical Chemistry B**. 111: 10790-10799.
- Steele, W.A. (1973). Physical interaction of gases with crystalline solids. 1. Gas-solid energies and properties of isolated adsorbed atoms. **Surface Science**. 36: 317-352.
- Tauer, T.P. and Sherrill, C.D. (2005). Beyond the benzene dimer: An investigation of the additivity of pi-pi interactions. **Journal of Physical Chemistry A**. 109: 10475-10478.
- Tjatjopoulos, G.J., Feke, D.L. and Mann, J.A. (1988). Molecule micropore interaction potentials. **Journal of Physical Chemistry**. 92: 4006-4007.

- Wick, C.D., Martin, M.G. and Siepmann, J.I. (2000). Transferable potentials for phase equilibria. 4. United-atom description of linear and branched alkenes and alkylbenzenes. **Journal of Physical Chemistry B**. 104: 8008-8016.
- Wick, C.D., Siepmann, J.I., Klotz, W.L. and Schure, M.R. (2002). Temperature effects on the retention of n-alkanes and arenes in helium-squalane gas-liquid chromatography: Experiment and molecular simulation. **Journal of Chromatography A**. 954: 181-190.
- Zhao, D., Huo, Q., Feng, J., Chmelka, B.F. and Stucky, G.D. (1998). Nonionic triblock and star diblock copolymer and oligomeric surfactant syntheses of highly ordered, hydrothermally stable, mesoporous silica structures. **Journal of the American Chemical Society**. 120: 6024-6036.
- Zhao, Y. and Truhlar, D.G. (2005). Multicoefficient extrapolated density functional theory studies of pi-pi interactions: The benzene dimer. **Journal of Physical Chemistry A**. 109: 4209-4212.

# CHAPTER III

## ADSORPTION OF BENZENE ON GRAPHITIZED THERMAL CARBON BLACK

### 3.1 Abstract

Grand Canonical Monte Carlo (GCMC) simulation was used to study multilayer adsorption of benzene on graphitized thermal carbon black over a range of temperature between 273 and 373 K. Three potential models for benzene were compared: TraPPE-UA-9, OPLS-AA and TraPPE-EH, in order to study their capability to correctly describe the adsorption isotherms and isosteric heats. In the sub-monolayer region, there is no difference between the simulation results obtained with the three models, which all describe the experimental data well. However, in the multilayer region only the TraPPE-EH model, that includes the quadrupole moment and explicit modelling of the hydrogen, is able to describe the experimental data accurately; the other two models significantly under-predict the data. The TraPPE-EH model was then used to investigate the microscopic behaviour of the adsorbed phase: the local density distribution and the orientation of various layers, particularly the change in orientation of benzene in the first layer with increase in loading from sub-monolayer to multi-layer. It was found that the orientation of benzene molecules in the first layer is affected by the presence of molecules in the higher layers, but that most benzene molecules remain in an orientation parallel to the surface, which is favoured by the interaction with the surface, while a smaller population takes  $60^\circ$  and



vertical orientations to the surface which maximizes the entropy. The ratio of the number of molecules having parallel orientation to that having  $60^\circ$  and vertical orientations decreases in higher layers due to the weaker influence of the adsorbate-adsorbent interaction. Detailed study of the orientation shows that most slant and vertical molecules have two of their hydrogen atoms closer to the surface.

### **3.2 Introduction**

Benzene adsorption has been widely studied in the past because it is typical of many aromatic toxic organic compounds that are present in gas and/or liquid effluents from many chemical and petrochemical industries. The key step in an adsorption process is the choice of a solid adsorbent, and activated carbon is often the solid of choice because the graphitic nature of the pore walls offers two distinct advantages over other solid adsorbents: it is both hydrophobic and has high atom density (greater affinity for the adsorptive). The fundamental understanding of this adsorbate and graphite surface interaction is the basic step to better design of adsorption systems for benzene in pores whose walls are graphitic; for example activated carbon (Lai et al., 2010; Yun et al., 1999).

### **3.3 Literature Review**

Early experimental studies of adsorption of benzene on graphite or graphitized thermal carbon black (GTCB) were made by Kiselev and co-workers (Avgul et al., 1958; Berezin et al., 1972; Berezin et al., 1970; Isirikyan and Kiselev, 1961; Isirikyan and Kiselev, 1963); they measured adsorption isotherms at ambient temperatures, with a volumetric apparatus and isosteric heats with a calorimetric device for a number of carbon blacks. As long as the carbon blacks were sufficiently well

graphitized, the experimental data were in perfect agreement with each other because the benzene molecules form a perfect hexagonal tessellation on the graphene surface. Following this early work of Kiselev, adsorption over a wider range of temperature (273-373 K), above and below the bulk freezing point of 278.7 K has been carried out by a number of workers (Belyakov et al., 1968; Davis and Pierce, 1966; Pierce and Ewing, 1967; Pierotti and Smallwood, 1966).

In recent years, with the advances of the computer simulation, molecular simulation has also been used to study benzene adsorption on graphite. Vernov and Steele (Vernov and Steele, 1991a; Vernov and Steele, 1991b) used Monte Carlo simulation to investigate the structures and energies of benzene adsorption on graphite at 85 and 298 K. They found that the heat of adsorption was nearly constant in the sub-monolayer region, in agreement with the calorimetric data of Isirikyan and Kiselev (Isirikyan and Kiselev, 1961). This constant heat is attributed to cancellation between the increase in the benzene-benzene interaction and the decrease in the benzene-adsorbent interaction; which changes as the orientation of benzene molecules changes with increased loading in the sub-monolayer region. The structure of the second layer was found to be less ordered than that of the first layer, as a result of the weaker interactions of the benzene molecules in the second layer. Matties and Hentschke (Matties and Hentschke, 1996a; Matties and Hentschke, 1996b) used molecular dynamics to study the structure of the benzene adsorbate in the first and higher layers on the basal plane of graphite over a wide range of temperature (60-320 K). Their results showed that ordering beyond the nearest neighbours decreases rapidly with coverage, and is virtually non-existent for second and higher layers. However, since molecular dynamics does not yield adsorption isotherms or heats their

simulation results cannot be tested against experimental data. More detailed study of isotherms, heats and the structure of adsorbed benzene on graphite using grand canonical Monte Carlo (GCMC) simulation was presented by Do and Do (Do and Do, 2006). They investigated the performance of various potential models for benzene that were available up to 2006, the united atom models TraPPE-UA-6 (Wick et al., 2000) and TraPPE-UA-9 (Wick et al., 2002) and the all atom model OPLS-AA (with 12 dispersive sites and 12 partial charges) (Jorgensen and Severance, 1990), for their suitability in correctly describing the experimental adsorption isotherm and the heat of adsorption, and found that the TraPPE-UA-9 gave the better results. From the simulation data, they found that at very low loadings, most benzene molecules adopt an orientation parallel to the surface which is the most energetically favourable position. When the loading is increased within the sub-monolayer coverage, some benzene molecules adopt a slant configuration, due to the quadrupolar interactions between benzene molecules. However, the work by Do and Do was restricted to the sub-monolayer region, and therefore a molecular simulation of benzene adsorption on GTCB beyond the first layer is desirable to assess the ability of the potential models to describe the isotherm and isosteric heat and to explore how molecules in higher layers affect the orientation of molecules in the first layer. Furthermore, a new potential model was recently proposed by Rai and Siepmann (Rai and Siepmann, 2007), TraPPE-EH, which includes twelve dispersive sites (carbon and hydrogen atoms) and twelve partial charges on these atoms, and it is of interest to test its capability to describe benzene adsorption. These authors compared this new model with previous potential models for benzene, and have found that this model and OPLS-AA are significantly more accurate than the 6-site model (TraPPE-UA-6) and

the 9-site model (TraPPE-UA-9) for the description of vapour-liquid equilibria at 298.15 K. The OPLS-AA model performed well at 298.15 K (where it was fitted) but its performance degraded rapidly with increasing temperature. Interestingly the better models are the ones that account explicitly for the hydrogen atoms.

In this paper, we re-investigate the performance of various benzene potential models, particularly the ones that account explicitly for the hydrogen atoms, and examine whether this can describe the adsorption of benzene in the multi-layer regions, despite the small value of the well-depth of interaction energy of hydrogen atom. Physically we expect the presence of hydrogen atoms will affect packing when loadings are high (i.e. when molecules are packed close to each other), and expect the potential models, such as TraPPE-EH and OPLS-AA to perform better in the dense adsorbed layer. We then study the structure of benzene to see whether the higher layers change the orientation of benzene molecules in the first dense layers.

### 3.4 Simulation

The conventional Grand Canonical Monte Carlo (GCMC) simulation is applied in this work. For modelling an open surface, we used a slit pore wide enough to behave as two independent surfaces (10 nm width). The graphitized atomistic and structure-less surface models are used as an infinitely long length. The long range corrections are not required in the present work due to the box length is more than 10 times the collision diameter that taken as  $80 \times 80 \times 80 \text{ \AA}^3$  in the case of structure-less model. We also consider carefully to make the graphene layers to be continuous in the case of infinite surface, therefore, the box length of the atomistic model is  $76.68 \times 78.72 \times 80 \text{ \AA}^3$  (which is  $L_x \times L_y \times L_z$ , respectively).

To more understand the variation in the molecular orientation, we consider the orientational local density, which is calculated from (Klochko et al., 1999)

$$\rho(z, \theta) = \frac{\langle \Delta N_{z+\Delta z, \theta+\Delta \theta} \rangle}{L_x L_y \Delta z \sin \theta \Delta \theta} \quad (3.1)$$

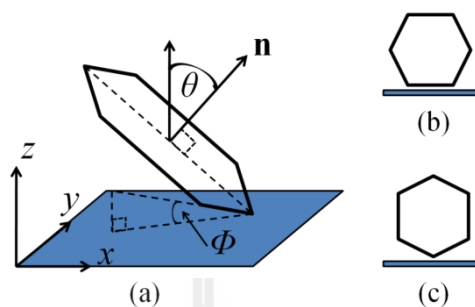
where  $\langle \Delta N_{z+\Delta z, \theta+\Delta \theta} \rangle$  is the ensemble average of the number of benzene molecules whose centres of mass are located in the segment having boundaries between  $z$  and  $(z + \Delta z)$  and an angle between  $\theta$  and  $(\theta + \Delta \theta)$ . We describe the orientation of a benzene molecule with two angles  $\theta$  and  $\Phi$  as shown in Figure 3.1a. The angle  $\theta$  is defined as the angle between the normal vector of benzene ring ( $\mathbf{n}$ ) and the vertical  $z$  axis, while  $\Phi$  is defined as the angle between the vector passing through two adjacent carbon atoms and the horizontal surface. An angle  $\theta$  of 0 means that the molecule lies parallel to the pore surface and a value  $\theta$  of 90° means that the molecule is perpendicular to the pore surface. Due to the hexagonal shape of benzene, the range of  $\Phi$  is from 0 to 30°. An angle of 0 means that the benzene molecule has one side parallel to the surface (Figure 3.1b), and an angle of 30° indicates that benzene take a vertical orientation as shown in Figure 3.1c. Any other angle falling between 0 and 30° are shown in Figure 3.1a.

## 3.5 Results and Discussion

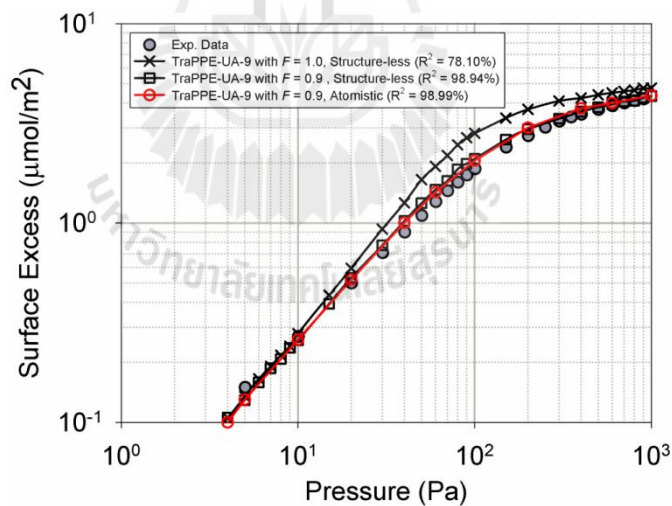
### 3.5.1 Adsorption at 293 K

Figure 3.2 shows the simulated adsorption isotherm from structure-less model and atomistic model at 293 K obtained using the TraPPE-UA-9 model in the sub-monolayer region; the results agree with the experimental data of Isirikyan and

Kiselev (Isirikyan and Kiselev, 1961), when the surface mediation (Do and Do, 2006) is accounted for.



**Figure 3.1** Schematic showing: (a) the two angles defining the benzene orientation on the surface, (b) perpendicular benzene rotated  $0^\circ$ , and (c) perpendicular benzene rotated  $30^\circ$ .  $\mathbf{n}$  is the normal unit vector through the benzene ring.



**Figure 3.2** Adsorption isotherm of benzene on GTCB at 293 K; comparison between the GCMC simulation results using the TraPPE-UA-9 model with and without surface mediation and experimental data from Isirikyan and Kiselev (Isirikyan and Kiselev, 1961).  $F$  is the surface mediation factor.  $R^2$  is R-squared error.

The mediation of the TraPPE-UA-9 potential between the benzene molecules by 3-body interaction through the adsorbent was accounted for empirically by reducing these interactions by 10% ( $F = 0.9$ ) when two benzene molecules are in the first layer, i.e. their pairwise interaction is mediated by the surface. Without mediation, the simulation results over-predict the experimental data when the first layer is close to completion. This raises the question of whether surface mediation is required when we consider the more complex OPLS-AA and TraPPE-EH potential models for benzene. The results are shown in Figure 3.3, and it is interesting to see that the OPLS-AA model does not require surface mediation to describe the adsorption isotherm correctly because of the effective parameters of this model, but it does not mean that surface mediation is not required at other temperatures. While a reduction of 10% ( $F = 0.9$ ) is required for the TraPPE-EH model, which is similar to the TraPPE-UA-9 model. Thus except for the difference in surface mediation, all three models give a good description of the data in the sub-monolayer region (the monolayer concentration is  $4.2 \mu\text{mol}/\text{m}^2$ ). The TraPPE-UA-9 and OPLS-AA are comparable in the adsorption of benzene on graphite surface that is different from what have been allowed in our early publication that is due to the number of cycles was not sufficient in our early work for OPLS-AA because of its 12 dispersive sites and 12 partial charges. In addition, the simulation results using the structure-less model and the atomistic model with the same binary interaction parameter,  $k_{sf}$  and the surface mediation factor,  $F$  give almost the same results due to benzene is a big molecule. Therefore, we would like to study benzene adsorption on GTCB for the next sections by using the structure-less model because of simulation time consuming.

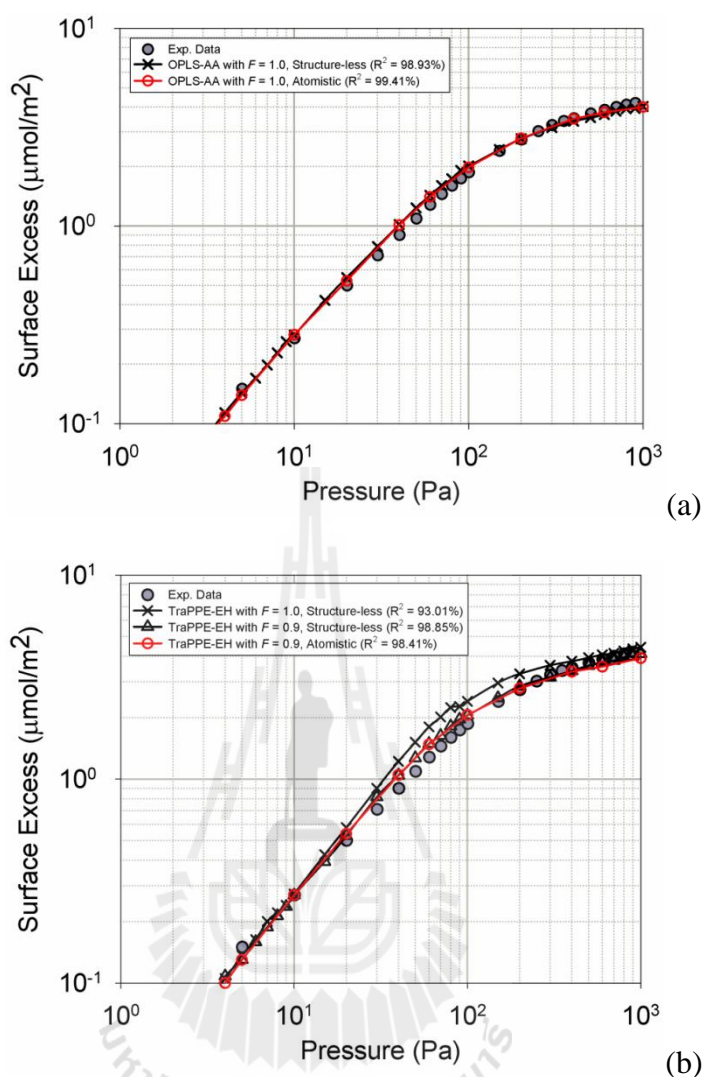


**Figure 3.3** Adsorption isotherm of benzene on GTCB at 293 K; comparison between the GCMC simulation results using (a) the OPLS-AA model and (b) the TraPPE-EH model with and without surface mediation and experimental data from Isirikyan and Kiselev (Isirikyan and Kiselev, 1961).  $F$  is the surface mediation factor.  $R^2$  is R-squared error.

We now investigate the performance of the three potential models for their description of the multi-layer region. The simulated results are shown in Figure 3.4 for a wide range of pressure over which five layers of benzene are adsorbed. As the



surface excess versus bulk pressure, all these potential models describe the data in the sub-monolayer region quite well, but only the TraPPE-EH model is capable of describing the data well, up to five adsorbed layers of benzene. The surface excess of the experimental data, TraPPE-UA-9 and TraPPE-EH is also plotted as a function of relative pressure by taking vapor pressure ( $P_0$ ) from the literature of Isirikyan and Kiselev (Isirikyan and Kiselev, 1961), Wick and co-workers (Wick et al., 2002), and Rai and Siepmann (Rai and Siepmann, 2007), respectively. The vapour pressure of the OPLS-AA was not mentioned in the literature. As can be seen in this figure, the TraPPE-EH is still the best fit in monolayer coverage and multilayer coverage.

To support the statement that the TraPPE-EH potential is a better model, we test their performance in the description of the isosteric heat. The simulation results are shown in Figure 3.5, together with the experimental data obtained from the calorimetric measurements. Over the range of two layers where the heat data are available, we can draw the conclusion that the TraPPE-EH, as a whole, is the best model for the description of the isotherm and heat data as we can see from the percentage deviation in Figure 3.5b.

To see the contributions of the benzene-solid and benzene-benzene interactions toward the isosteric heat, we plot these contributions in Figure 3.6 as a function of loading for the TraPPE-EH model. In the sub-monolayer region, the increase in the benzene-benzene interactions compensates for the decrease in the benzene-solid interaction, resulting in a relatively constant isosteric heat in this region (although we note a modest increase of the isosteric heat in the sub-monolayer region).

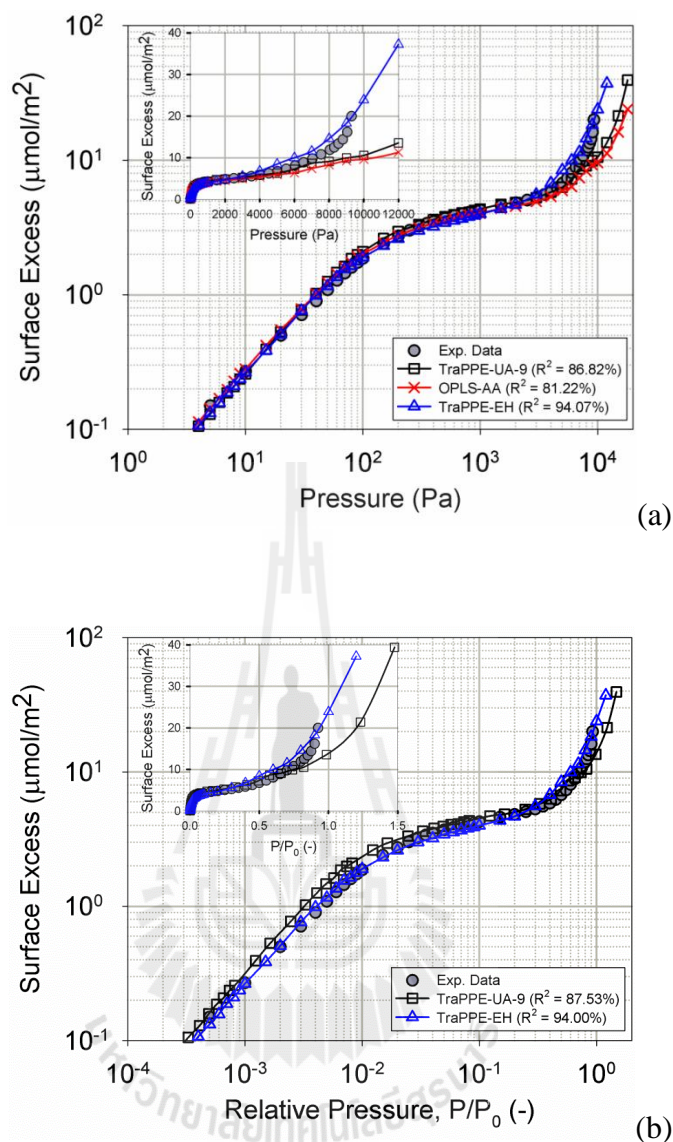


**Figure 3.4** Adsorption isotherm of benzene on GTCB at 293 K obtained by GCMC by using the TraPPE-UA-9 model (with  $F = 0.9$ ), the OPLS-AA model (with  $F = 1.0$ ), and the TraPPE-EH model (with  $F = 0.9$ ); the experimental data are from Isirikyan and Kiselev (Isirikyan and Kiselev, 1961). (a) Surface excess vs bulk pressure and (b) surface excess vs relative pressure.  $R^2$  is R-squared error.

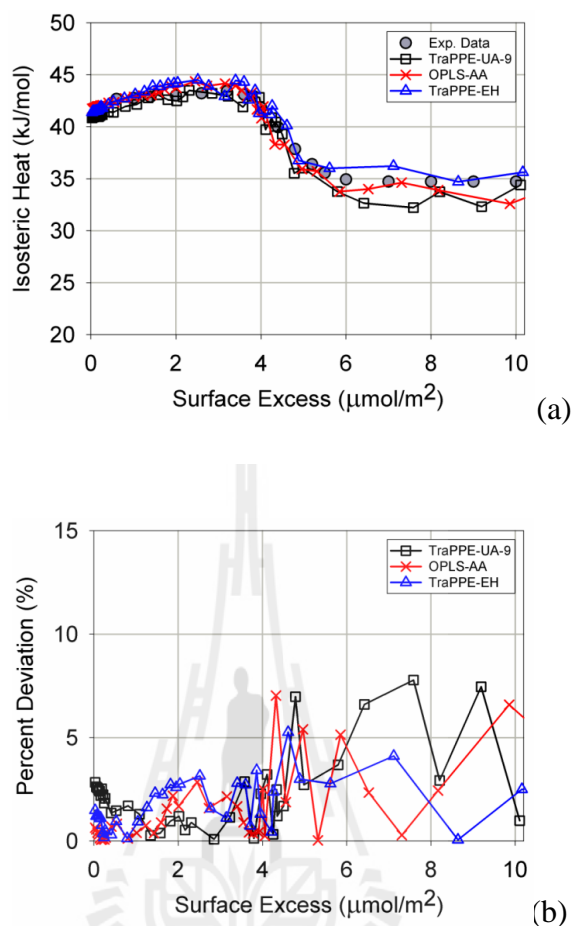


**Figure 3.5** (a) Isosteric heat vs loading for benzene adsorption on GTCB at 293 K; comparison with the GCMC simulation results (structure-less model) using the TraPPE-UA-9 model ( $F = 0.9$ ), the OPLS-AA model ( $F = 1.0$ ), and the TraPPE-EH model ( $F = 0.9$ ) and (b) their percent deviation; the experimental data are from Isirikyan and Kiselev (Isirikyan and Kiselev, 1961).

The benzene-adsorbent interaction diminishes in the second layer because molecules are further away from the surface, while the adsorbate interaction increases only slightly giving a constant isosteric heat, of 35 kJ/mol, compared to 42 kJ/mol in the sub-monolayer region. The isosteric heat in the second layer of

35 kJ/mol is close to the heat of liquefaction of benzene (34 kJ/mol), but this does not mean that the second layer is a liquid phase. The Fluid-Fluid (FF) interaction of the second layer is less than that in the bulk liquid because each molecule has fewer neighbours, and this is only partially compensated by the small Fluid-Solid (FS) interaction. This is further supported when we study the structure of benzene molecules in the next section.

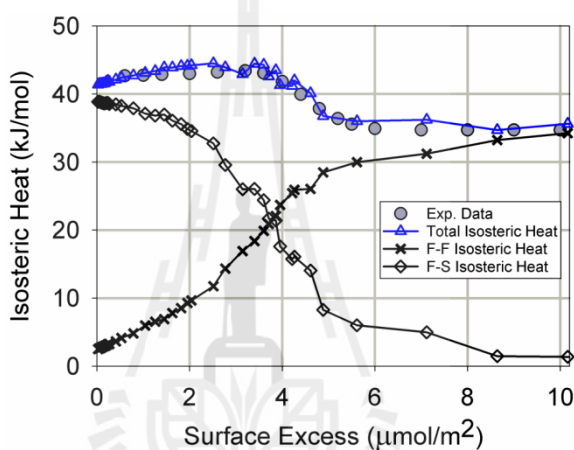


**Figure 3.6** Total, benzene-benzene, and benzene-solid isosteric heats vs loading for benzene adsorption on GTCB at 293 K; comparison with the GCMC simulation results (structure-less model) using the TraPPE-EH model ( $F = 0.9$ ); the experimental data are from Isirikyan and Kiselev (Isirikyan and Kiselev, 1961).

### 3.5.2 Structure of Adsorbed Benzene

Since the TraPPE-EH gives the best description of the isotherm and the isosteric heat of adsorption, we shall use it to study the structure of the adsorbed layer. Figures 3.7-3.10 show the local density distributions for the centre of mass of benzene with respect to the distance from the graphite surface at 293 K.

First, we analyze the structure of benzene molecules in the sub-monolayer region, and then later show how the presence of higher layers disturbs this structure because of the FF interactions from higher layers. The chosen isotherm points are shown in the inset of Figure 3.7, where A and B represent points well below the monolayer coverage and C and D are points just before and after the completion of the first layer. At points A and B, the surface is 10% and 50% covered with benzene molecules, respectively. The first layer is about 3.44 Å from the graphite surface. At very low loadings there is a single peak indicating that all molecules have the same orientation parallel to the surface, as will be shown later. However, at point C a shoulder develops which then evolves into two minor peaks in the local density distribution at point D (Figure 3.7).

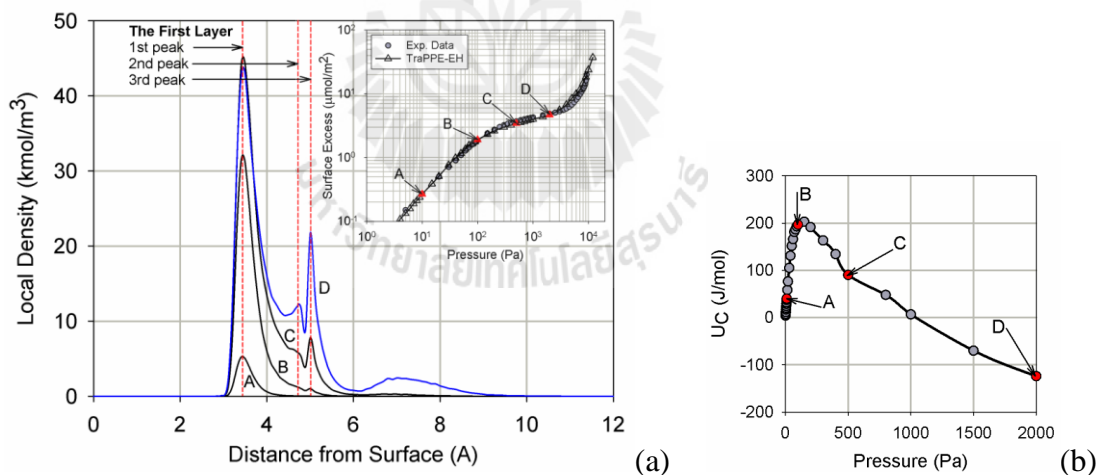


**Figure 3.7** (a) Local density distribution vs distance from the graphite surface and (b) electrostatic interaction vs pressure at 293 K for the TraPPE-EH model at points A, B, C, and D.

These peaks do not result from the formation of another layer, but rather reflect the change in the orientation of some molecules, such that their centres of mass shift further away from the surface. These minor peaks are at 4.7 and 5 Å. The peak at 4.7 Å is associated with molecules having a slant configuration and the peak at 5 Å corresponds to those having a vertical configuration. These configurations are not energetically favoured by the adsorbate-adsorbent interaction, but are favoured by the increase in the fluid-fluid interaction energy by having more benzene molecules closer to the surface. This is supported by the plot of the fluid-fluid energy contributed by the electrostatic interactions (Figure 3.7b). However, it can be seen that the majority of molecules in the first layer remain parallel to the surface because the area under the first peak at 3.44 Å is still the largest. Thus at the completion of the first layer we have three configurations, parallel, slant and vertical. This interesting conclusion is slightly different from the conclusions derived from our earlier work using the TraPPE-UA-9 model (Do and Do, 2006) in that only the parallel and slant configurations were observed, with a much smaller population taking the vertical orientation (see Figure 3.8). This can be attributed to the fact that the TraPPE-UA-9 model has no explicit hydrogen atoms, which occupy significant space when the packing is dense. Interestingly, although the OPLS-AA model has explicit hydrogen atoms, it does not show vertical orientations (see dotted line in Figure 3.8). However, since this model does not give an accurate description of the isotherm; we take the view that the local density distribution derived from the TraPPE-EH model is superior.

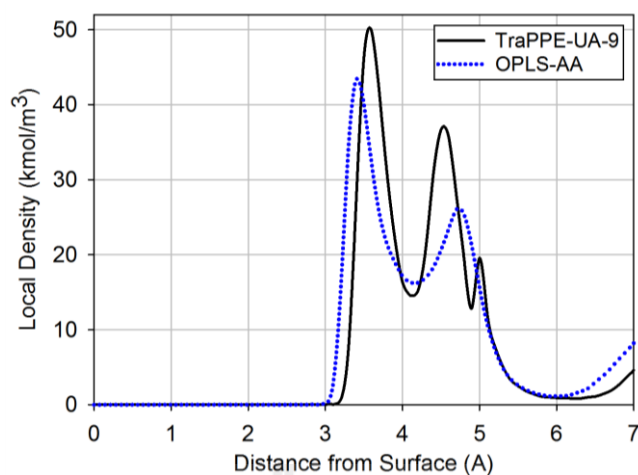


**Figure 3.8** Local density distribution vs distance from the graphite surface at 293 K for 10,000 Pa for the TraPPE-UA-9 model ( $F = 0.9$ ) and the OPLS-AA model ( $F = 1.0$ ).

It is also interesting to observe that the minor peaks become higher when the second layer starts to form (point D), i.e. more benzene molecules in the first layer then adopt the slant and vertical configurations with the increase in the concentration of the second layer although the majority still remain in the parallel orientation.

When the loading increases from the onset of the second layer to the third layer (points D to F in the inset of Figure 3.9), the positions of the major and two minor peaks of the first layer are unchanged, but the peak position of the second layer moves from 7 to 8 Å and becomes more delocalised. This is due to the presence of third layer, coupled with the thermal motion of molecules in the second layer. At point F, the third layer occurs at 11.3 Å, and we note that although the positions of the minor peaks of the first layer do not change, the density of the major peak of the first layer is increased at the expense of the two minor peaks, indicating that some

molecules re-orientate themselves to the energetically favoured parallel configuration. This also maximises the quadrupolar interaction if benzene molecules lie in offset positions when higher layers are present. This is shown in Figure 3.7b where we show the enhancement in the electrostatic (quadrupole) interactions.

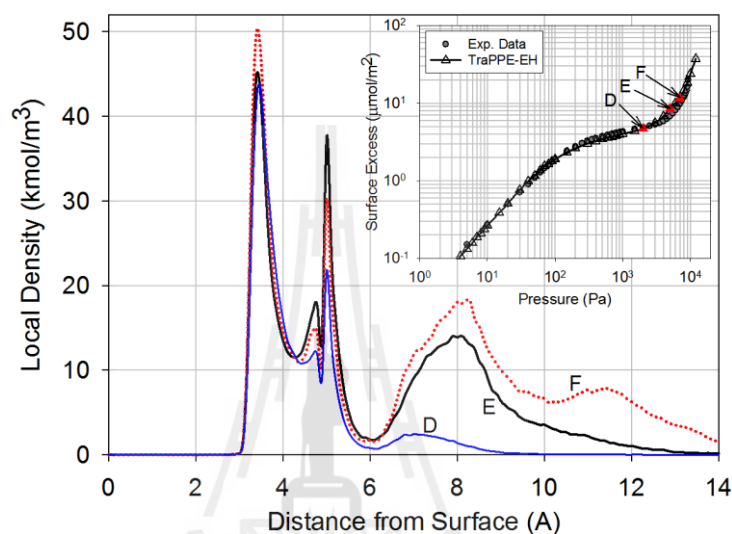


**Figure 3.9** Local density distribution vs distance from the graphite surface at 293 K for the TraPPE-EH model at points D, E, and F.

When the loading is further increased the concentration at the fourth layer distance increases (Figure 3.10) (point H). The position of the first two layers remains unchanged, but the the third layer becomes more diffuse. This is similar to the redistribution of the second layer when the third layer forms (at distances between 10 and 16 Å from the surface). Thus we can draw a general conclusion that the presence of a layer only affects the adjacent layer underneath. When the pressure is increased further to point I (about 6 layers are formed above the surface), the layering



structure of the third and fourth layers disappears and the adsorbate has the uniform structure of a bulk liquid phase (Figure 3.10).

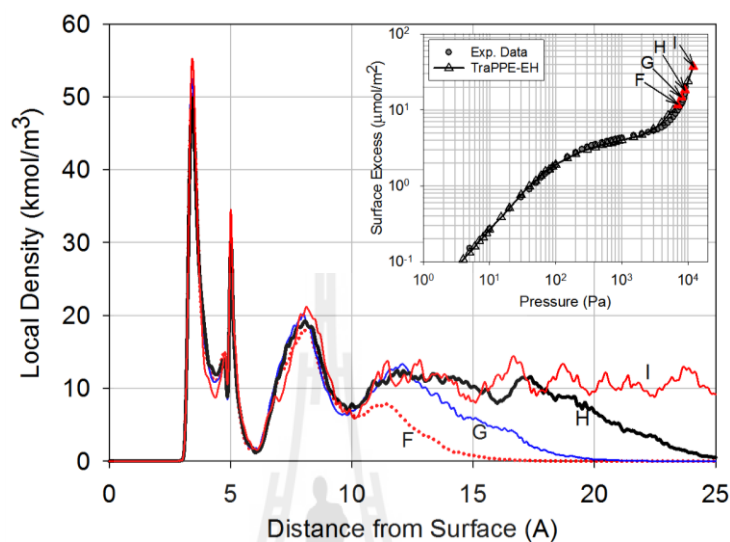


**Figure 3.10** Local density distribution vs distance from the graphite surface at 293 K for the TraPPE-EH model at points F, G, H, and I.

To study in detail the orientation of molecules, the orientation density distributions versus the distance and  $\theta$  are presented in Figure 3.11-3.14. It is seen that at very low loadings (for example, point B) benzene molecules lie flat on the surface, with a peak at zero degrees. This orientation is expected at low loadings because it is the most energetically favorable position. This observation is also supported by the snapshot as shown in Figure 3.11.

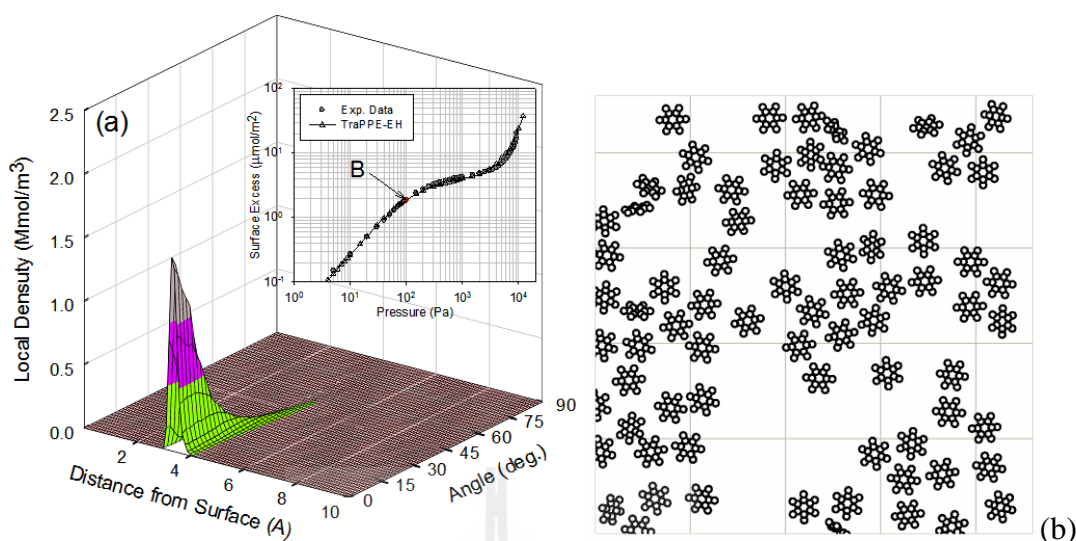


**Figure 3.11** (a) Local density distribution vs distance from the surface to the centre of mass and the angle  $\theta$  and (b) top view of the snapshot of benzene molecules adsorbed on a graphite surface at 293 K and point B.

When the loading is increased to point D (just after the formation of the first layer and at the onset of the second layer), we see the beginning of the formation of a second layer at 7 Å from the surface (Figure 3.12). At this coverage, most molecules in this layer are parallel to the surface, but some molecules in the first layer have orientations other than parallel, including slant and vertical orientations. It is seen that the slant peak at 4.7 Å from the surface is associated with molecules having  $\theta$  about 60° to the surface. When loading is increased to point E (Figure 3.13), the second layer continues to fill but the peak shifts further away from the surface (from 7 to be 8 Å), because as molecules fill the second layer they adopt orientations away from parallel. We note that the second layer is beginning to form before the first layer is complete, and the third layer also starts before the completion of the second layer as shown by the snapshot in Figure 3.13b as is usual in physical adsorption processes.

When loading is increased to point H (Figure 3.14), there is an adsorbate thickness equivalent to about 5 layers above the surface and there is no preference for any orientation, suggesting a liquid-like structure above the second layer.

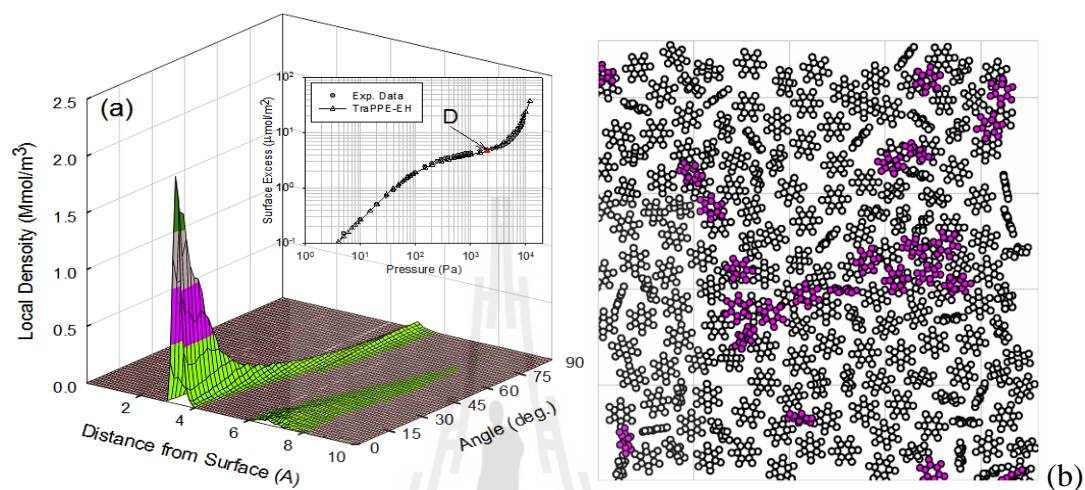


**Figure 3.12** (a) Local density distribution vs distance from the surface to the centre of mass and the angle  $\theta$  and (b) top view of the snapshot of benzene molecules adsorbed on a graphite surface (molecules in purple colours are those in second layer) at 293 K and point D.

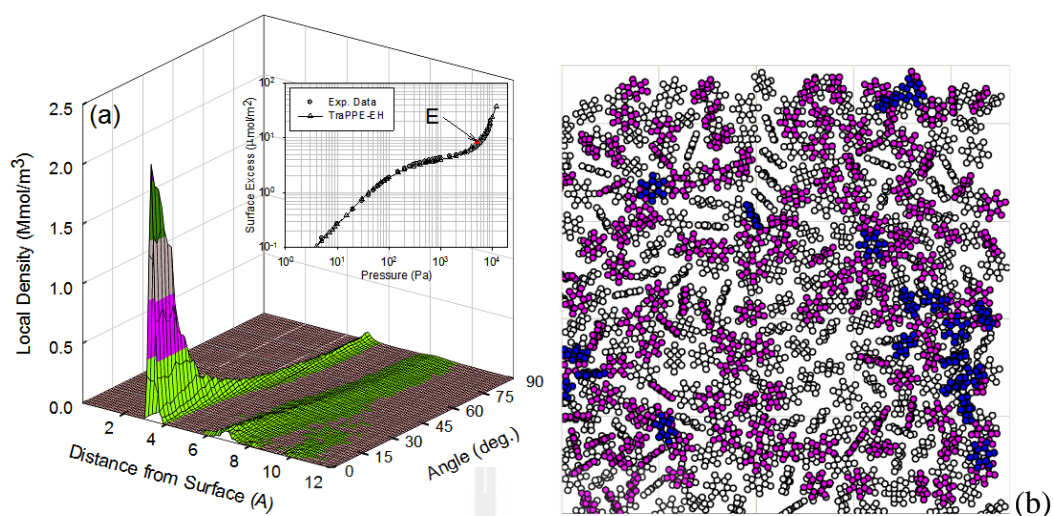


**Figure 3.13** (a) Local density distribution vs distance from the surface to the centre of mass and the angle  $\theta$  and (b) top view of the snapshot of benzene molecules adsorbed on a graphite surface (molecules in purple and blue colours are those in second and third layer, respectively) at 293 K and point E.

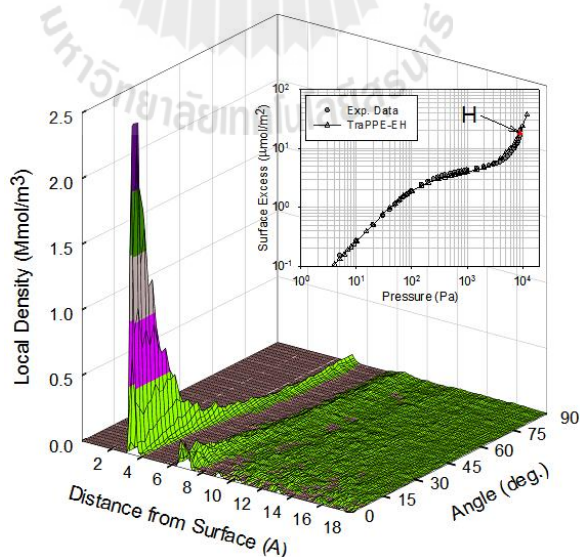


**Figure 3.14** Local density distribution vs distance from the surface to the centre of mass and the angle  $\theta$  at 293 K and point H.

Figure 3.15 shows the orientational local density distribution as a function of distance and  $\Phi$ . The peaks *J*, *K*, and *L* in this figure are associated with the first layer and the two minor peaks *K* and *L* are for molecules having slant and vertical orientations where the centre of mass is further away from the surface (see the earlier discussion of Figure 3.7). In Figure 3.15, we see that most slant and vertical benzene molecules have  $\Phi$  equal to 0, meaning that one side of the molecule lies parallel to the surface (i.e. with two hydrogen atoms close to the surface).

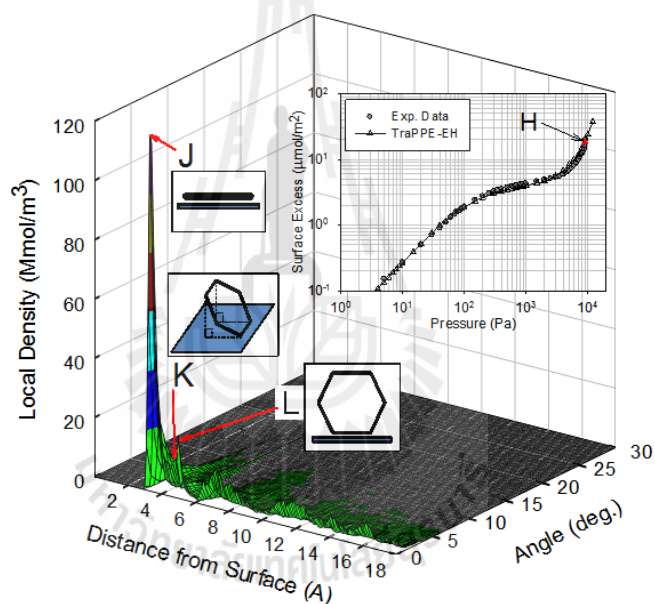


**Figure 3.15** Local density distribution vs distance from the surface to the centre of mass and the angle  $\Phi$  at 293 K and point H.

### 3.5.3 Adsorption at Wider Temperature Range

To further test the TraPPE-EH model description of multilayer adsorption, we have carried out simulations at 273 K (below the bulk phase triple point of 278.7 K). In Figure 3.16, we compare simulation results using this model

(including surface mediation with a factor  $F = 0.9$ , used earlier for a temperature of 293 K) with experimental data over a range of temperatures from 273 up to 373 K. The agreement between simulation and experiment (data of Pierotti and Smallwood (Pierotti and Smallwood, 1966) at 288 K, 303 K and 323 K, and of Belyakova and co-workers (Belyakov et al., 1968) at 343 K and 373 K) is good over the whole 50 K range. The potential model tends to slightly overestimate the adsorption, but there is no particular trend with temperature.

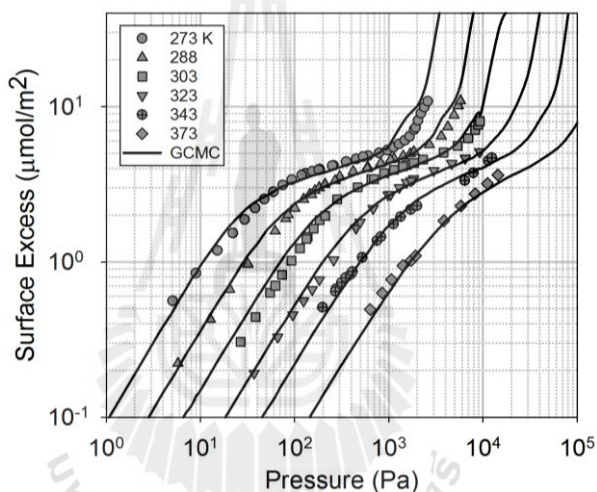


**Figure 3.16** Adsorption isotherms for benzene on GTCB at various temperatures; comparison between the GCMC simulation results using the TraPPE-EH model with surface mediation ( $F = 0.9$ ) and experimental data from Pierotti and Smallwood (Pierotti and Smallwood, 1966) and Belyakova and co-workers (Belyakov et al., 1968).

To illustrate the difference in the structure of the adsorbed film as temperature is increased, we show, in Figure 3.17, the local density distributions for 273 K and 343 K. The structure of the first layer remains unchanged (although lower

in density), but the structure of the second layer starts to disappear and to become more uniform and liquid-like, which can also be seen from the orientation density distributions of Figures 3.18 and 3.19 for 343 K.

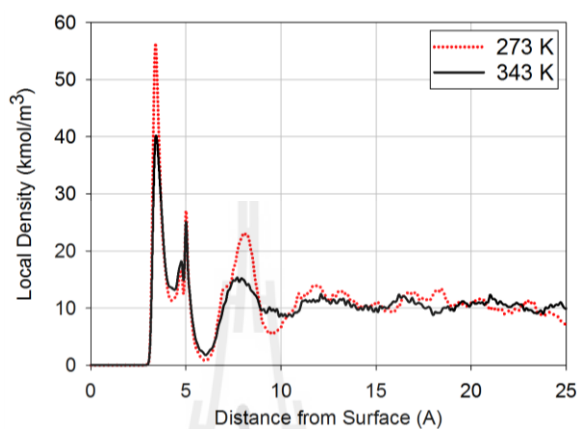


**Figure 3.17** Local density distribution vs distance from the graphite surface at 273 and 343 K using the TraPPE-EH model for  $30 \mu\text{mol}/\text{m}^2$ .

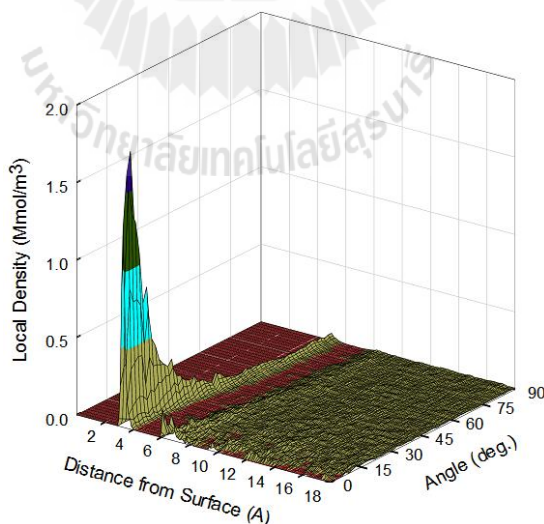


**Figure 3.18** Local distribution vs distance from the surface to the centre of mass and the angle  $\theta$  at 343 K for  $30 \mu\text{mol}/\text{m}^2$ .

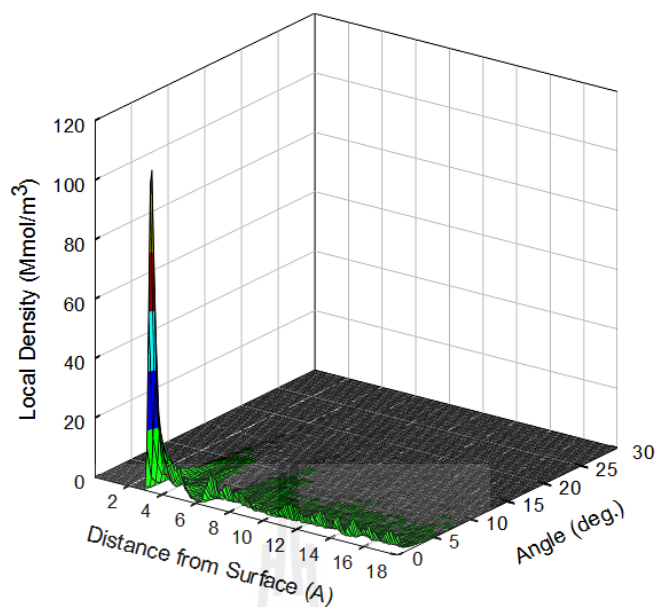


**Figure 3.19** Local density distribution vs distance from the surface to the centre of mass and the angle  $\Phi$  at 343 K for  $30 \mu\text{mol}/\text{m}^2$ .

Finally, in Figure 3.20, we show the temperature dependence of the isosteric heat, at 293 K and 343 K. The experimental data at 293 K are taken from Isirikyan and Kiselev (Isirikyan and Kiselev, 1961), and those at 343 K are from Belyakova and co-workers (Belyakov et al., 1968). The excellent agreement between simulation and experiment reinforces our conclusion that the TraPPE-EH potential is the best model to describe the adsorption of benzene on graphite. A weak temperature dependence of the isosteric heat is also noted in this figure.



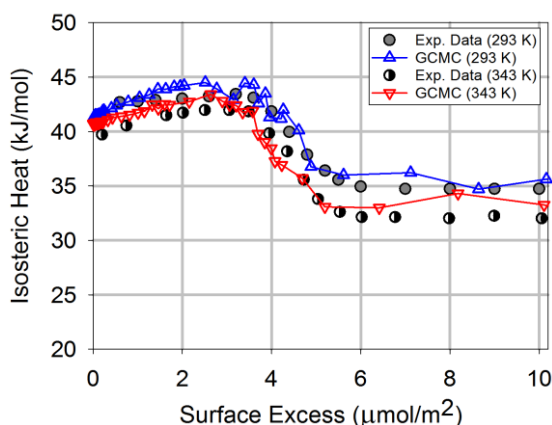


**Figure 3.20** Isosteric heat vs loading for benzene adsorption on GTCB at 293 and 343 K: comparison between GCMC simulation results (structure-less model) using the TraPPE-EH model with surface mediation ( $F = 0.9$ ) and experimental data from Isirikyan and Kiselev (Isirikyan and Kiselev, 1961) and Belyakova and co-workers (Belyakov et al., 1968).

### 3.6 Conclusions

This study of benzene adsorption on a graphite surface at various temperatures in both the submonolayer and the multilayer regions provides a detailed picture of the molecular behaviour of this system. Of the various potential models for benzene tested, we have found that the TraPPE-EH model is the most suitable, and the GCMC simulation results for adsorption isotherms and isosteric heats are in excellent agreement with experimental data taken from the literature.

The GCMC simulation allows us to probe the structure of the adsorbed phase using local density distributions plots. The molecular orientation in the lower layers is influenced by the presence of molecules in higher layers. Most benzene molecules in the first layer adopt an orientations parallel to the surface plane but there are two

minor populations having slant and vertical orientations. The slant orientation has an azimuthal angle of about  $60^\circ$  to the surface. The parallel configuration is energetically favorable in term of benzene-adsorbent interaction. The slant orientation optimises the quadrupole interactions and together with the vertical configuration is entropically favoured over the parallel orientation as temperature increases. However, the ratio of the number molecules adopting parallel orientation to that having slant and vertical orientations decreases in higher layers due to the weaker influence of the adsorbent interaction. We find that most slant and vertical molecules optimise the balance between energy and entropy when one side of the molecule lies parallel to the surface (i.e. two hydrogen atoms are closer to the surface)

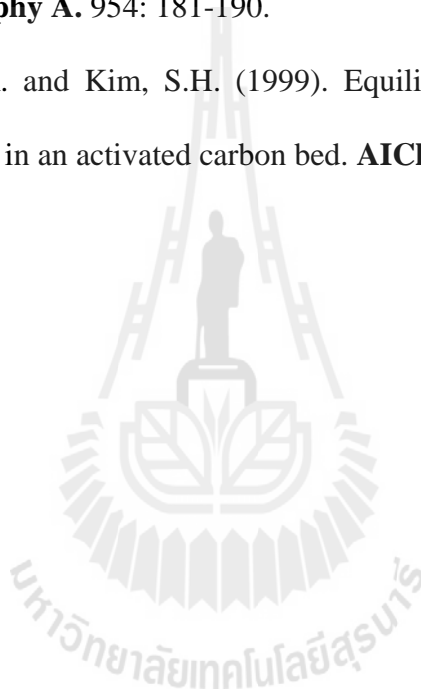
### 3.7 References

- Avgul, N.N., Berezin, G.I., Kiselev, A.V. and Korolev, A.Y. (1958). Heat of adsorption of hydrocarbons by carbon blacks of different degrees of graphitization. **Kolloidnyi Zhurnal**. 20: 298-304.
- Belyakov, L.D., Kiselev, A.V. and Kovaleva, N.V. (1968). Gas-chromotographic determination of isotherms and heats of adsorption of water, benzene and methanol vapours on graphitised carbon black. **Russian Journal of Physical Chemistry**. 42: 1204-1208.
- Berezin, G.I., Kiselev, A.V., Sagatelyan, R.T. and Sinitsyn, V.A. (1972). A thermodynamic evaluation of the state of the benzene and ethanol on a homogeneous surface of a nonspecific adsorbent. **Journal of Colloid and Interface Science**. 38: 335-340.

- Berezin, G.I., Kiselev, A.V. and Sinitsyn, V.A. (1970). Adsorption of benzene and n-hexane on graphitised carbon black. **Russian Journal of Physical Chemistry**. 44: 408-411.
- Davis, B.W. and Pierce, C. (1966). A study of stepwise adsorption. **The Journal of Physical Chemistry**. 70: 1051-1058.
- Do, D.D. and Do, H.D. (2006). Adsorption of benzene on graphitized thermal carbon black: Reduction of the quadrupole moment in the adsorbed phase. **Langmuir**. 22: 1121-1128.
- Isirikyan, A.A. and Kiselev, A.V. (1961). The absolute adsorption isotherms of vapors of nitrogen, benzene and n-hexane, and the heats of adsorption of benzene and n-hexane on graphitized carbon blacks. I. Graphitized thermal blacks. **The Journal of Physical Chemistry**. 65: 601-607.
- Isirikyan, A.A. and Kiselev, A.V. (1963). Isotherms and heats of adsorption of nitrogen, benzene, and n-hexane vapours on graphitised carbon blacks. III. Thermodynamic quantities. **Russian Journal of Physical Chemistry**. 37: 957-961.
- Jorgensen, W.L. and Severance, D.L. (1990). Aromatic-aromatic interactions: Free energy profiles for the benzene dimer in water, chloroform, and liquid benzene. **Journal of the American Chemical Society**. 112: 4768-4774.
- Klochko, A.V., Brodskaya, E.N. and Piotrovskaya, E.M. (1999). Computer simulations of dependence of adsorption characteristics of ethane on the size of graphite micropores. **Langmuir**. 15: 545-552.

- Lai, M.H., Shih, Y.L., Chen, Y.H., Shu, S.H. and Chung, T.W. (2010). Equilibrium isotherms of the adsorption of pyrolysis gases from polymer products. **Journal of Chemical and Engineering Data**. 55: 723-727.
- Matties, M.A. and Hentschke, R. (1996a). Molecular dynamics simulation of benzene on graphite. 1. Phase behavior of an adsorbed monolayer. **Langmuir**. 12: 2495-2500.
- Matties, M.A. and Hentschke, R. (1996b). Molecular dynamics simulation of benzene on graphite. 2. Phase behavior of adsorbed multilayers. **Langmuir**. 12: 2501-2504.
- Pierce, C. and Ewing, B. (1967). Localized adsorption on graphite surfaces. **Journal of Physical Chemistry**. 71: 3408-3413.
- Pierotti, R.A. and Smallwood, R.E. (1966). The adsorption of benzene on homogeneous substrates. **Journal of Colloid and Interface Science**. 22: 469-481.
- Rai, N. and Siepmann, J.I. (2007). Transferable potentials for phase equilibria. 9. explicit hydrogen description of benzene and five-membered and six-membered heterocyclic aromatic compounds. **Journal of Physical Chemistry B**. 111: 10790-10799.
- Vernov, A. and Steele, W.A. (1991a). Computer-simulations of benzene adsorbed on graphite. 1. 85 K. **Langmuir**. 7: 3110-3117.
- Vernov, A. and Steele, W.A. (1991b). Computer-simulations of benzene adsorbed on graphite. 2. 298 K. **Langmuir**. 7: 2817-2820.

- Wick, C.D., Martin, M.G. and Siepmann, J.I. (2000). Transferable potentials for phase equilibria. 4. United-atom description of linear and branched alkenes and alkylbenzenes. **Journal of Physical Chemistry B**. 104: 8008-8016.
- Wick, C.D., Siepmann, J.I., Klotz, W.L. and Schure, M.R. (2002). Temperature effects on the retention of n-alkanes and arenes in helium-squalane gas-liquid chromatography: Experiment and molecular simulation. **Journal of Chromatography A**. 954: 181-190.
- Yun, J.H., Choi, D.K. and Kim, S.H. (1999). Equilibria and dynamics for mixed vapors of BTX in an activated carbon bed. **AIChE. Journal**. 45: 751-760.



# CHAPTER IV

## ADSORPTION OF BTX ON A GRAPHITIC SURFACE AND IN PORES

### 4.1 Abstract

Grand canonical Monte Carlo simulation has been carried out at ambient temperature to investigate the adsorption of benzene, toluene and xylene (BTX) on a graphite surface and in graphitic slit and cylindrical pores. Particular emphasis has been paid to the effects of the confined space on the affinity and packing density. Simulation results for adsorption on a graphite surface were tested against the experimental data to validate the potential models used in the description of adsorption. Our extensive simulation has shown that on an open graphite surface, where there is no restriction in the packing, xylene has the highest affinity and adsorbed amount at a given reduced pressure and benzene is the lowest, due to the additional interaction of the methyl groups with the surface. In a confined space the order of the affinity remains the same, but the packing (hence the amount adsorbed per unit physical pore volume) is affected by the geometry of the space. It was found that benzene has the highest packing density, whether it is expressed in terms of mole or mass.

## 4.2 Introduction

Benzene, toluene and xylene (BTX) are hazardous organic compounds that are emitted from chemical and petrochemical industries. These toxic compounds have to be removed from the effluents before release to the environment. As mentioned previously in CHAPTER I, adsorption is preferred to remove these compounds by using activated carbon (AC). To design the adsorptive process the equilibrium of adsorption such as adsorption isotherm and adsorbed heat is needed.

## 4.3 Literature Review

The physisorption of aromatics on a graphitic surface has been studied thoroughly both experimentally (Avgul et al., 1958; Avgul et al., 1959; Belyakov et al., 1968; Berezin et al., 1972; Berezin et al., 1970; Carrott et al., 2000; Davis and Pierce, 1966; Isirikyan and Kiselev, 1961; Isirikyan and Kiselev, 1963; Pierce and Ewing, 1967; Pierotti and Smallwood, 1966) and theoretically (Do and Do, 2006; Matties and Hentschke, 1996a; Matties and Hentschke, 1996b; Vernov and Steele, 1991a; Vernov and Steele, 1991b); the affinity for the adsorbent being the most important criterion for better design of an adsorption system. For example AC (Lai et al., 2010; Yun et al., 1999), carbon nanotubes (Masenelli-Varlot et al., 2002; Terzyk et al., 2009), and advanced adsorbents with hexagonal pores (Morishige, 2011a; Morishige, 2011b; Wang et al., 2011) have all been the subject of investigation in the last decade. The affinity of the adsorbent for the adsorbate is characterized by the Henry constant, and has been obtained experimentally for BTX in a number of carbonaceous systems at various temperatures (Avgul et al., 1958; Berezin et al., 1972; Berezin et al., 1970; Isirikyan and Kiselev, 1961; Isirikyan and Kiselev, 1963;

Kiselev et al., 1979). These authors have shown that the order of affinity is  $B < T < X$ , due to the methyl groups attached to the benzene ring that augment the interaction with the surface. Although xylene is the strongest adsorbate on this basis, there are conflicting reports in the literature that the adsorption capacity for benzene is the highest (among BTX) in some activated carbons (Lai et al., 2010; Wang et al., 2004; Yun and Choi, 1997) but is the lowest in others (Yun et al., 1999). This raises questions about the affinity and packing of BTX in a confined space. Although it has been reported that the surface functional group can have an effect on the packing (Haghseresht et al., 2002), we will concentrate our investigation on the effects of the confined space, in terms of its size and curvature, on the packing of BTX using a grand canonical Monte Carlo (GCMC) simulation. Simulation of benzene adsorption on a graphite surface has been studied previously (Klomkliang et al., 2012). On the other hand, there are no reports in the literature of simulation of toluene and xylene adsorption on a graphite surface, and we will therefore study their adsorption on a planar graphite surface first to establish suitable potential models and then investigate the effects of confinement on adsorption on toluene and xylene.

#### **4.4 Simulation**

The conventional grand canonical Monte Carlo (GCMC) simulation is used in this chapter. As have been seen in our previous work (Klomkliang et al., 2012), the adsorptions of benzene on GTCB by assuming the graphite surface as an atomistic and a structure-less models were in good agreement with each other and described the experimental data really well. In order to save CPU time, therefore, we consider solid surface as a structure-less model with infinitely long length in this chapter. The box



length was more than 10 times the collision diameter ( $100 \text{ \AA} \times 100 \text{ \AA} \times 100 \text{ \AA}$  for open surface,  $100 \text{ \AA} \times 100 \text{ \AA} \times L_z$  for slit pores and  $100 \text{ \AA} \times \pi R^2$  for cylindrical pores), and the cut-off radius was half the box length.

## 4.5 Results and discussion

### 4.5.1 Adsorption on Graphitized Surface

Figure 4.1a and 4.1b shows the simulation results and the experimental data for adsorption isotherms and isosteric heats of benzene and toluene on GTCB at 293 K. The experimental data were taken from Avgul et al. (Avgul et al., 1959) and Isirikyan and Kiselev (Isirikyan and Kiselev, 1961). Good agreement between simulation and experiment can be achieved for loadings of  $10 \mu\text{mol/m}^2$  for benzene and  $8 \mu\text{mol/m}^2$  for toluene, when a binary interaction parameter  $k_{sf}$  of -0.12 and -0.06 was set for benzene and toluene, respectively, and a surface mediation factor,  $F$ , of 0.90. When we used the OPLS-AA model to account the effects of dipole moment for toluene, we found that the dipole has no significant effect as seen in Figure 4.1c, where the isotherms simulated with the OPLS-AA and the TraPPE-UA are essentially the same.

Unfortunately, the experimental data for xylene adsorption on a graphite surface are not available in the literature, we can only study xylene adsorption with molecular simulation. To compare the adsorption performance of BTX on a graphite surface with the same basis of potential models, we have therefore carried out simulations without introducing the binary interaction parameter or surface mediation.

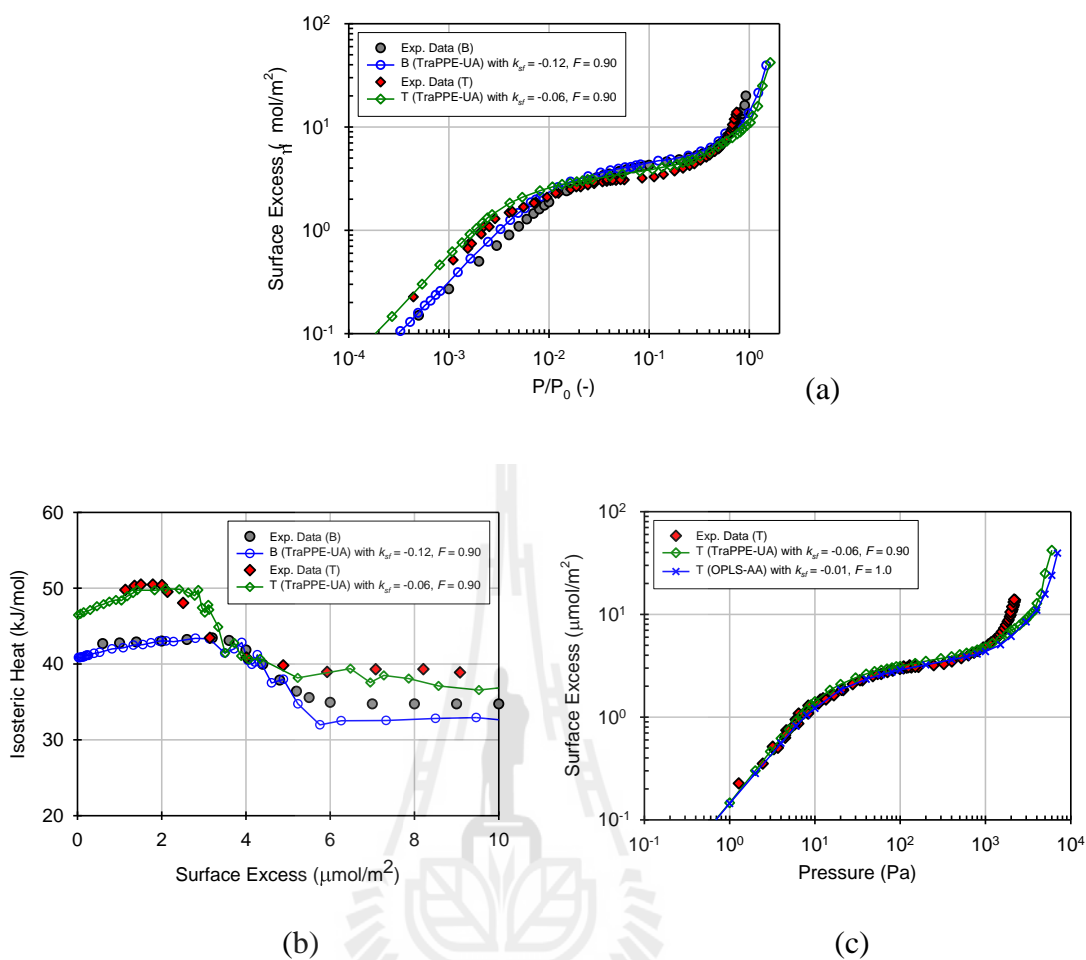


**Figure 4.1** (a) Adsorption isotherms and (b) isosteric heats of benzene and toluene on GTCB at 293 K using the TraPPE-UA model and the adjustment parameters,  $k_{sf}$  and the surface mediation factor  $F$  as described in the text. (c) Toluene adsorption isotherms on GTCB at 293 K obtained from the TraPPE-UA and OPLS-AA models. The simulations are compared with experimental data from Avgul's group (Avgul et al., 1959) and Isirikyan and Kiselev (Isirikyan and Kiselev, 1961).  $k_{sf}$  is the binary interaction parameter.

Figure 4.2a shows the simulated isotherms of BTX adsorption on a graphite surface at 298 K as surface excess ( $\mu\text{mol}/\text{m}^2$ ) as a function of relative pressure,  $P/P_0$ . Since different adsorbates have different saturation vapour pressure and the driving force for adsorption is the reduced pressure, where  $P_0$  is the simulated saturation vapour pressure (2, 6, and 20 kPa, for benzene, toluene and xylene, respectively) (Wick et al., 2002). It is seen that the order of the affinity towards the graphite surface is  $B < T < X$ , which is expected because of the stronger dispersion interaction from the additional methyl groups. Interestingly, at loadings greater than  $3 \mu\text{mol}/\text{m}^2$  which is close to the monolayer coverage concentration of toluene ( $4.30 \mu\text{mol}/\text{m}^2$ ) and xylene ( $3.61 \mu\text{mol}/\text{m}^2$ ) as listed in Table 4.1, the adsorptive capacity of benzene, expressed in mole per surface area, becomes greater than those of the other two adsorbates. This result comes about because benzene has a smaller molar volume than the other two adsorptives. If we express the isotherms as mass excess per unit surface area versus reduced pressure, as shown in Figure 4.2b, we observe the expected order of adsorption capacity for a given reduced pressure, that is  $B < T < X$ .

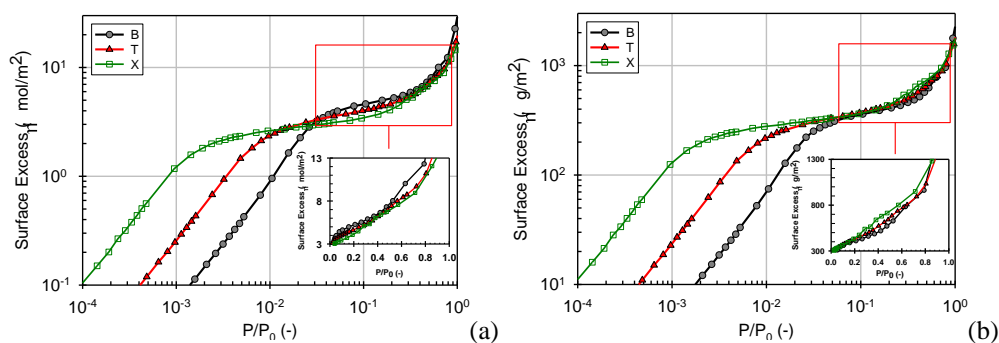


**Figure 4.2** Adsorption isotherms of BTX on GTCB at 298 K using the TraPPE-UA model without adjusting  $k_{sf}$  and  $F$ . (a) Surface excess per mole vs relative pressure; (b) surface excess per unit mass vs relative pressure .

**Table 4.1** Monolayer coverage concentration of BTX adsorption on GTCB at 298 K

adsorbate	monolayer coverage concentration ( $\mu\text{mol}/\text{m}^2$ )*
B	5.22
T	4.30
X	3.61

\* The monolayer concentration is defined as the number of molecules in the first layer ( $z < 6 \text{ \AA}$ ) at the completion of the first layer.

The isosteric heat of BTX adsorption on a graphite surface at 298 K is shown in Figure 4.3. At zero loading, the isosteric heats of benzene, toluene, and xylene are 36, 43, and 51 kJ/mol, respectively, which is in agreement with the calorimetric data of Kiselev et al. (Kiselev et al., 1979), that the zero loading-isosteric heat is in the order  $B < T < X$ , and is consistent with the order of the Henry constant. The isosteric heat versus loading curve is typical of adsorbates that have stronger fluid-solid interaction compared to fluid-fluid interaction, and the order of heat at any loadings is the same as that at zero loading.

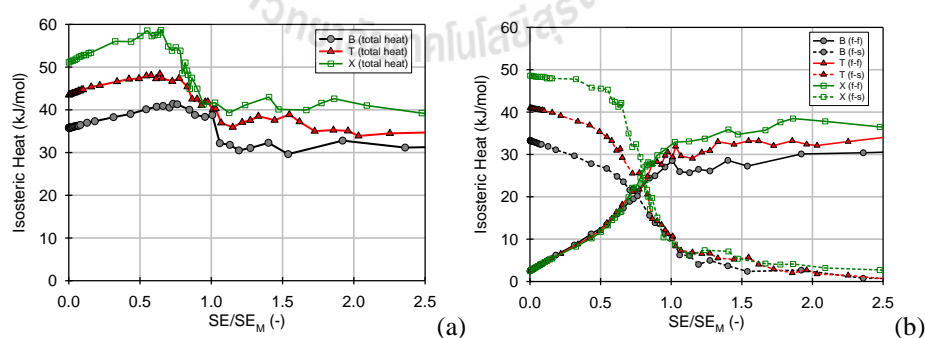


**Figure 4.3** Isosteric heats of BTX on GTCB at 298 K using the TraPPE-UA model without adjusting  $k_{yf}$  and  $F$ . (a) Total isosteric heat. (b) fluid-fluid and fluid-solid isosteric heats.  $SE$  is surface excess at any loadings.  $SE_M$  is monolayer coverage concentration.

The local density distribution versus the distance from the surface to the centre of the ring is shown in Figure 4.4 for BTX adsorption on a graphite surface. There are two overlapped peaks in the monolayer region; the main peak at 3.5 Å corresponds to molecules parallel to the plane of the surface and a minor peak at 4.5 Å corresponds to non-parallel configurations with their ring centres shifted further away from the surface to maximize the quadrupolar interaction between adsorbate molecules (Klomkliang et al., 2012). Interestingly the magnitude of the major and minor peaks is in order:  $B < T < X$  and  $B > T > X$ , respectively because the stronger interaction of the methyl groups with the surface acts against this trend.

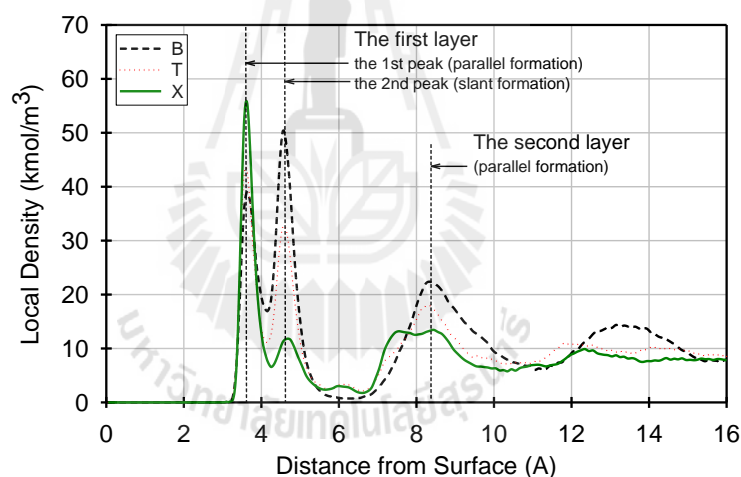


**Figure 4.4** Local density distributions as a function of distance from a graphite surface to the centre of a benzene ring in BTX at 298 K and a loading of  $20 \mu\text{mol}/\text{m}^2$  using the TraPPE-UA model without adjusting  $k_{sf}$  and  $F$ .

#### 4.5.2 Adsorption on Graphitic Pores

Adsorption and desorption isotherms of BTX in a  $20 \text{ \AA}$  graphitic slit-pore at 298 K are shown in Figure 4.5. As expected the adsorption affinities at low loadings

follow the same order as for an open graphite surface (i.e.  $B < T < X$ ) because the enhancement in the adsorption potential in a confined space works equally for all adsorbates. However, when the pore is completely filled with adsorbate, benzene has a higher capacity than toluene and xylene. The pore densities are calculated as moles per unit accessible volume (the accessible pore volume is listed in Table 4.2), and even though benzene has the highest accessible pore volume its pore density is still greater than those of toluene and xylene. This is tantamount to saying that the packing is more efficient for benzene than for aromatics with side chains. If we express the adsorptive capacity in terms of mass of adsorbate per unit accessible volume (Figure 4.5b), the order of the capacity at high loadings is opposite to when it is expressed in terms of moles ( $B < T < X$ ). This conclusion remains valid for pores having width greater than 12 Å. However, for ultra-micropores smaller than 12 Å, the order for the capacity by mole and mass at low loadings remains the same as that for pores whose widths are greater than 12 Å ( $B < T < X$ ), but the opposite is observed at high loadings ( $B > T > X$ ). This can be explained by the fact that only one layer can be accommodated in these ultra-micropores and the accessible pore volume of benzene is much greater than that of toluene and xylene (see Table 4.2).

The pore density discussed so far is based on the accessible pore volume, and gives the density of the adsorbed phase that occupies the accessible volume. However, experimental measurements are reported in the literature as the amount adsorbed per unit mass of the adsorbent.

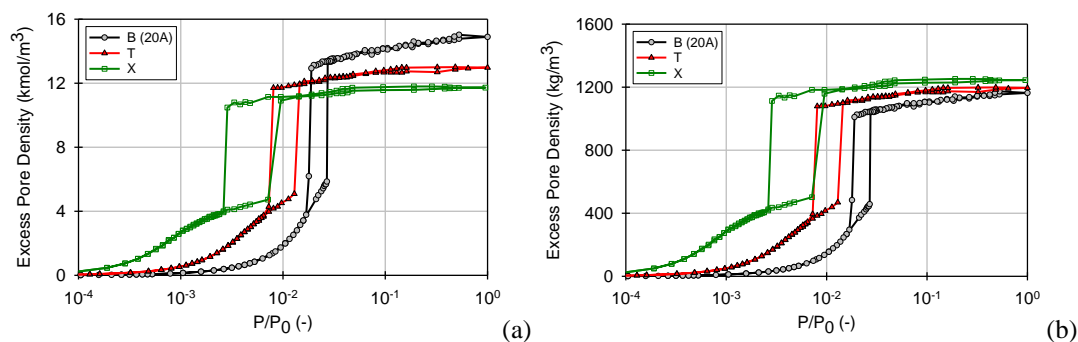


**Figure 4.5** Adsorption/desorption isotherms of BTX at 298 K using the TraPPE-UA model without adjusting  $k_{sf}$  and  $F$  on graphitized slit-pore width of 20 Å. (a) Pore density per mole vs relative pressure; (b) pore density per unit mass vs relative pressure. The pore density is based on accessible pore volume.

**Table 4.2** Pore volume at different physical pore widths of slit-pore

Physical pore width (nm)	$V_{acc}$ (nm <sup>3</sup> ) <sup>a</sup>			$V_{phy}$ (nm <sup>3</sup> ) <sup>b</sup>	$V_{He}$ (nm <sup>3</sup> ) <sup>c</sup>
	B	T	X		
0.8	5.52	3.93	3.30	80.00	70.15
1.0	24.70	19.55	15.82	100.00	89.11
1.2	44.05	38.79	33.70	120.00	97.17
1.6	83.65	78.40	72.90	160.00	138.36
2.0	123.63	118.44	113.00	200.00	179.09
3.0	223.86	218.10	212.79	300.00	281.60

<sup>a</sup> The accessible pore volume is defined as the volume accessible to the centre of a particle at zero loading and is determined by the Monte Carlo method of integration (Do et al., 2008).

<sup>b</sup> The physical pore volume is defined as the volume that occupy the distance between the plane passing through the centres of carbon atoms of the outermost layer of one wall and the corresponding plane of the opposite wall (Do et al., 2008).

<sup>c</sup> The pore volume is determined by helium adsorbed in the pore using GCMC at 1atm and room temperature.

Wang et al. (Wang et al., 2004) and Lai et al. (Lai et al., 2010) measured benzene and toluene adsorption on an activated carbon at 298 K, and observed that the adsorption capacity of toluene (mg of adsorbate/g of activated carbon) at high loadings ( $P/P_0 > 0.03$ ) was lower than benzene. On the other hand, Yun et al. (Yun et al., 1998) and Lillo-Ródenas et al. (Lillo-Rodenas et al., 2006) found that benzene adsorption capacity (by mole) was lower than that of toluene at low loadings ( $P/P_0 < 0.03$ ), but becomes greater when  $P/P_0 > 0.03$ .

To make a direct comparison between the simulation results and the experimental data, the simulation results are expressed either as molar concentrations or as mass per unit physical volume of the pore since, for a given porosity of the solid, the physical volume is proportional to the mass of the solid adsorbent. Figure 4.6 shows the simulated isotherms for BTX in terms of mole or mass per unit physical volume (the physical volumes are listed in Table 4.2). It is seen that the pore density per mole or per unit mass for BTX at low loadings follows the order  $B < T < X$ , while at high loadings the order is reversed, i.e.  $B > T > X$ , in agreement with the experimental data (Lai et al., 2010; Lillo-Rodenas et al., 2006; Wang et al., 2004; Yun et al., 1998).



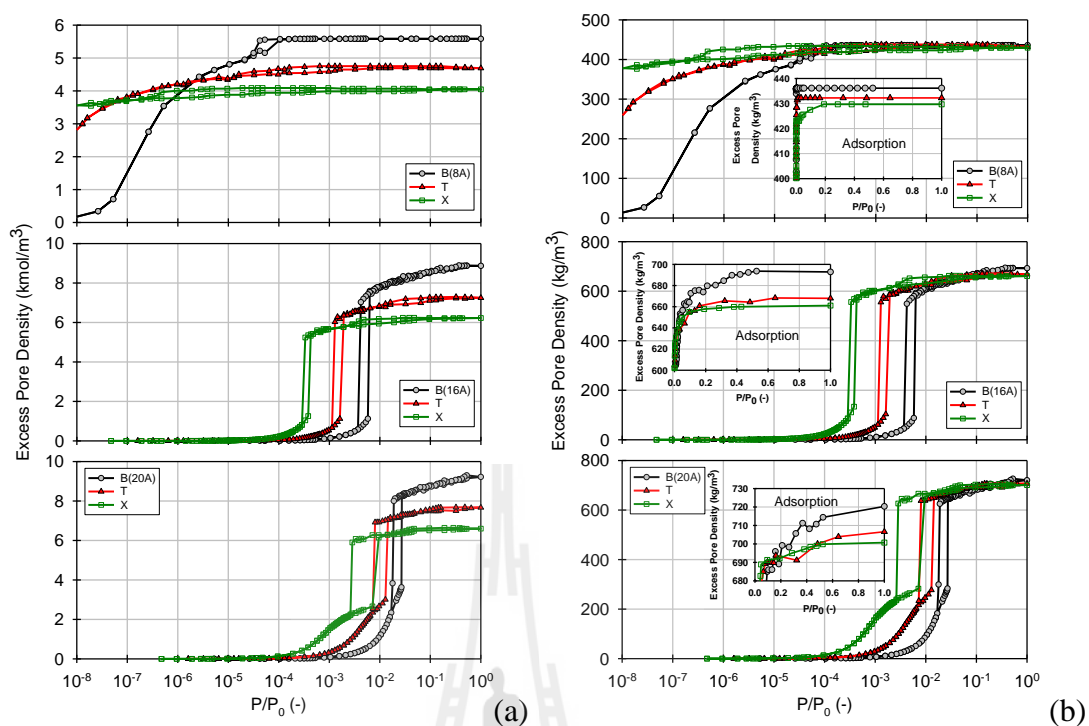


**Figure 4.6** Adsorption/desorption isotherms for BTX at 298 K on graphitized slit-pores of 8, 16 and 20 Å width. (a) Pore density per mole vs  $P/P_0$ ; (b) pore density per unit mass vs relative pressure. The pore density is based on the physical pore volume.

The single particle density distributions at  $P/P_0 = 1.0$ , plotted against distance from one of the pore walls to the centre of the benzene ring, are shown in Figure 4.7 for three pore sizes. In the 8 Å pore there is only one peak since the adsorbates are constrained to adopt a parallel configuration. In the 10 Å pore most molecules adopt a vertical orientation, but it is notable that, as on the plane surface, the proportion of parallel to inclined molecules decreases in the order BTX, showing that the molecule-surface interaction is stronger than the molecule-molecule interaction. The 12 Å pore, wide enough to accommodate two layers and therefore

shows two distinct peaks in the local density distribution. For pores in which more than two layers can be accommodated, there are more than two peaks in the local density distribution. The two peaks closest to the pore walls corresponding to the first layer are subdivided into two parts with the more distant minor peaks corresponding to molecules with orientations inclined to the surface, as previously noted for adsorption on a flat graphite surface (Figure 4.4) (Klomkliang et al., 2012).

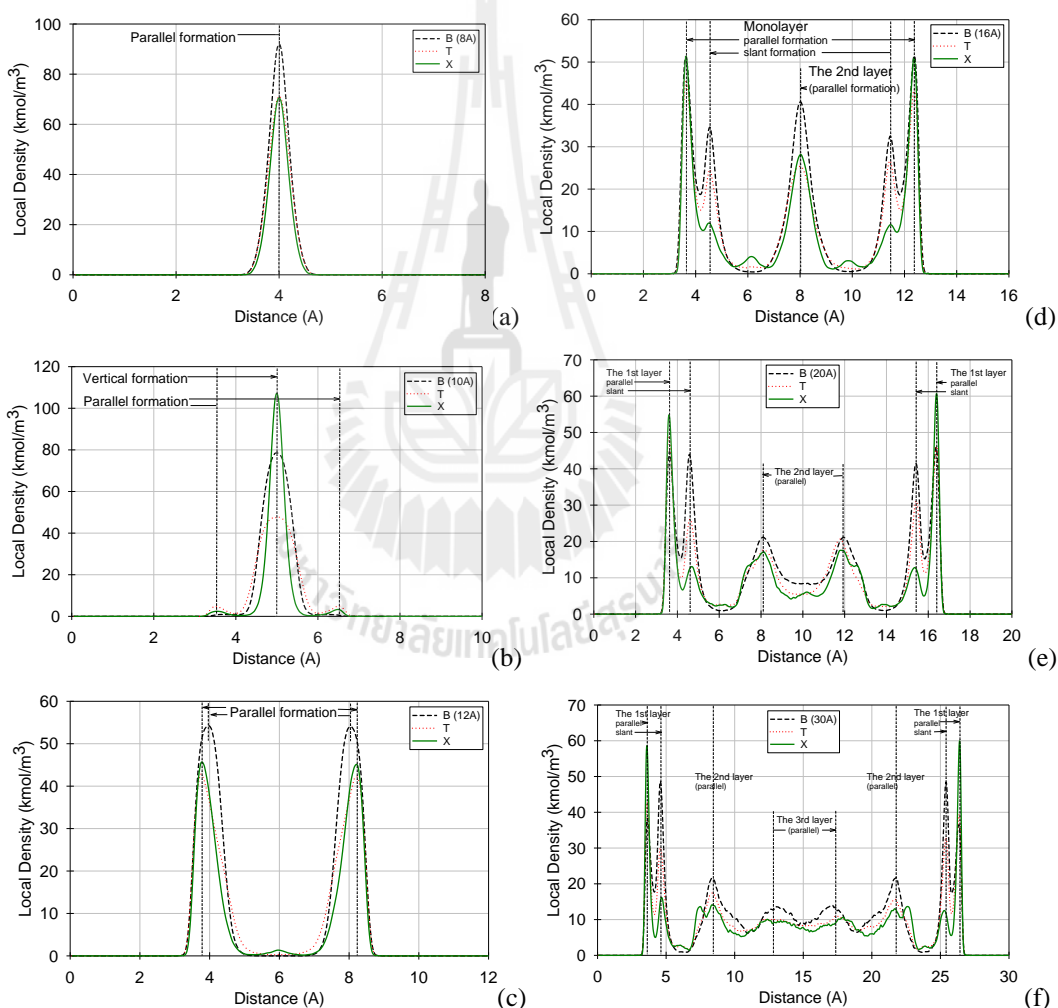


**Figure 4.7** Local density distributions as a function of distance from a pore wall to the centre of benzene ring for BTX at 298 K and  $P/P_0 = 1.0$  on graphitized slit-pore width range between 8 and 30 Å.

To understand better the orientation of BTX in a confined space, we presented in Figures 4.8 and 4.9 the orientation density distributions and corresponding snapshots for 8 and 20 Å pores, respectively. For 8 Å pore, most molecules are parallel to the pore surface because the pore is too small to allow other orientations. However, for 20 Å pore there are two peaks associated with the layers close to the pore wall, one peak occurs at 3.5 Å and the other at 4.5 Å. The first peak at 3.5 Å is associated with molecules parallel to the surface ( $\theta = 0$ , which  $\theta$  is defined as the angle between the normal vector of the benzene ring ( $\mathbf{n}$ ) and the vertical  $z$  axis), while the second peak at 4.5 Å for those exhibiting a slant configuration to the surface.

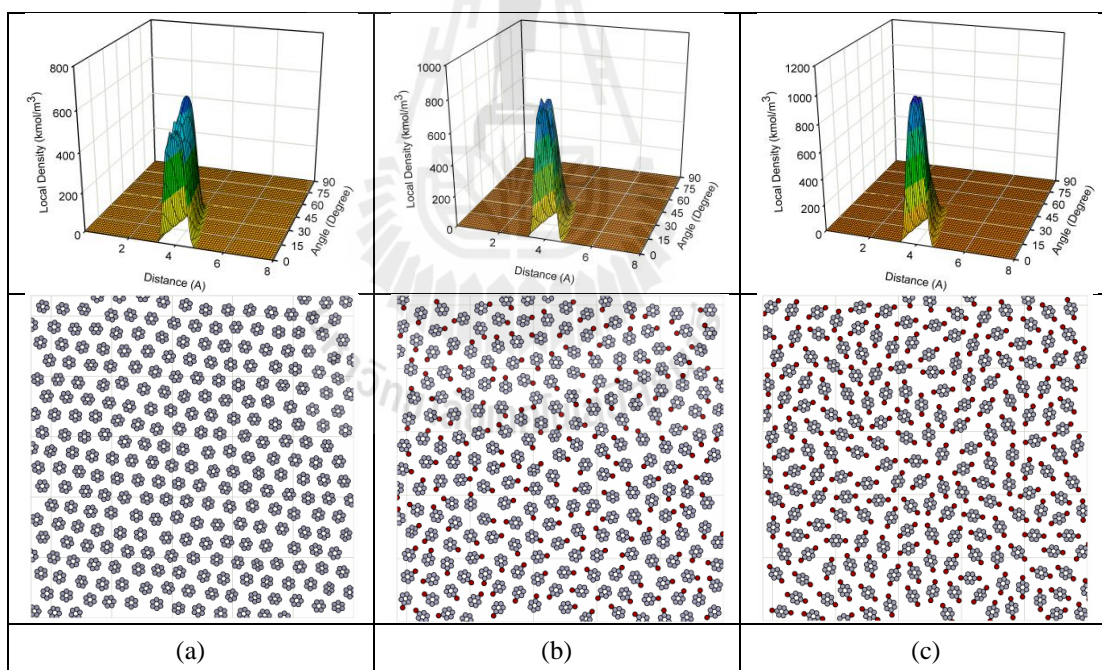


**Figure 4.8** Local density distributions as a function of distance from a pore wall to the centre of the benzene ring and the angle  $\theta$  (3D) and top view of the snapshot of molecules adsorbed of BTX at 298 K and  $P/P_0 = 1.0$  on graphitized slit-pore width of 8 Å; (a) B, (b) T, and (c) X.

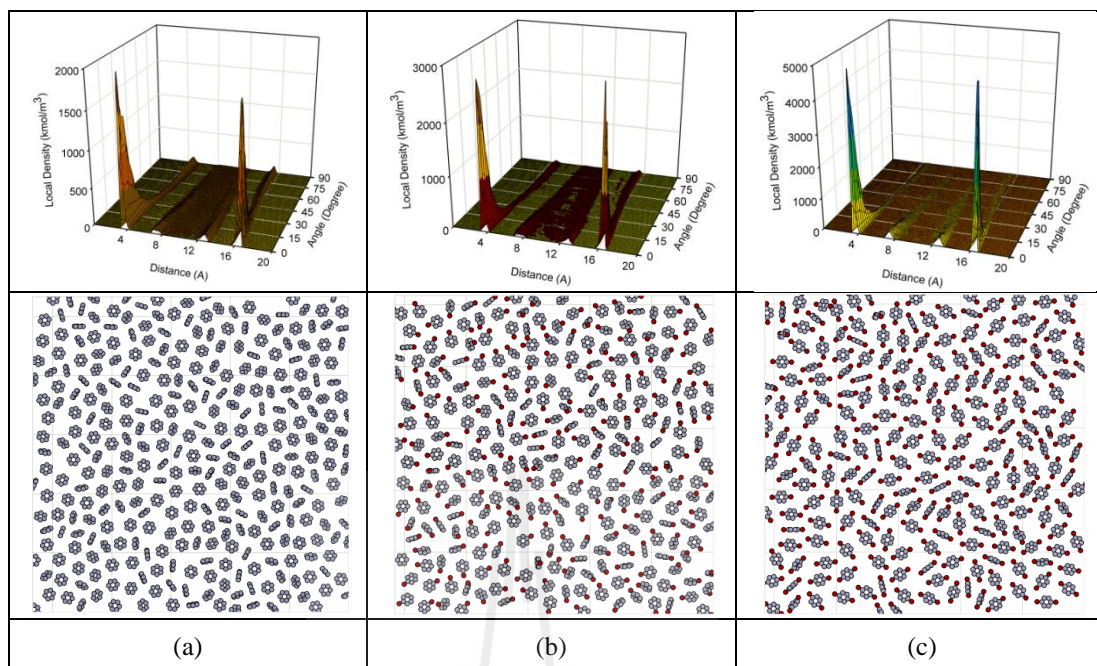


**Figure 4.9** Local density distributions as a function of distance from a pore wall to the centre of the benzene ring and the angle  $\theta$  (3D) and top view of the snapshot of molecules adsorbed for monolayer of BTX at 298 K and  $P/P_0 = 1.0$  on graphitized slit-pore width of 20 Å; (a) B, (b) T, and (c) X.

To examine the effects of pore curvature, we present, in Figure 4.10, the BTX adsorption isotherms for cylindrical pores at 298 K. The order of adsorption affinity in a cylindrical pore is the same that for a surface and slit-pore and demonstrates that the packing order is not affected by the surface curvature. To understand better the packing at high loadings, we present in Figure 4.11 the local density distribution and the snapshot for BTX at  $P/P_0 = 1$  in a pore of 30 Å diameter. We observed that the two peaks corresponding to the first layer are associated with molecules having a parallel orientation and those having other orientations, similar to what seen earlier with slit-pore.

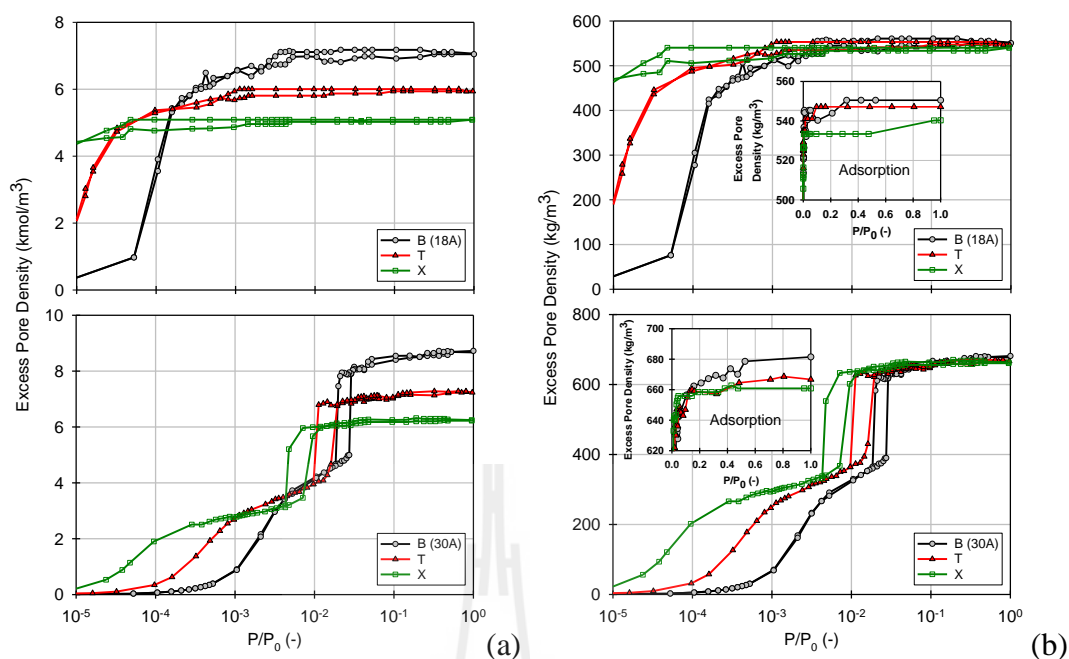


**Figure 4.10** Adsorption/desorption isotherms for BTX at 298 K on graphitized cylindrical pore width range between 18 and 30 Å. (a) Pore density per mole vs relative pressure; (b) pore density per unit mass vs relative pressure. The pore density is based on physical pore volume.

## 4.6 Conclusions

We have presented computer simulations of adsorption and desorption of BTX on a graphite surface and in slit and cylindrical pores with different pore sizes at 298K to investigate the adsorption affinity at zero loading and the adsorption capacity at high loadings. It was found that the side chains (methyl group) on the aromatics ring increase the affinity in the order benzene < toluene < xylene but decrease the capacity at high loadings (benzene > toluene > xylene).

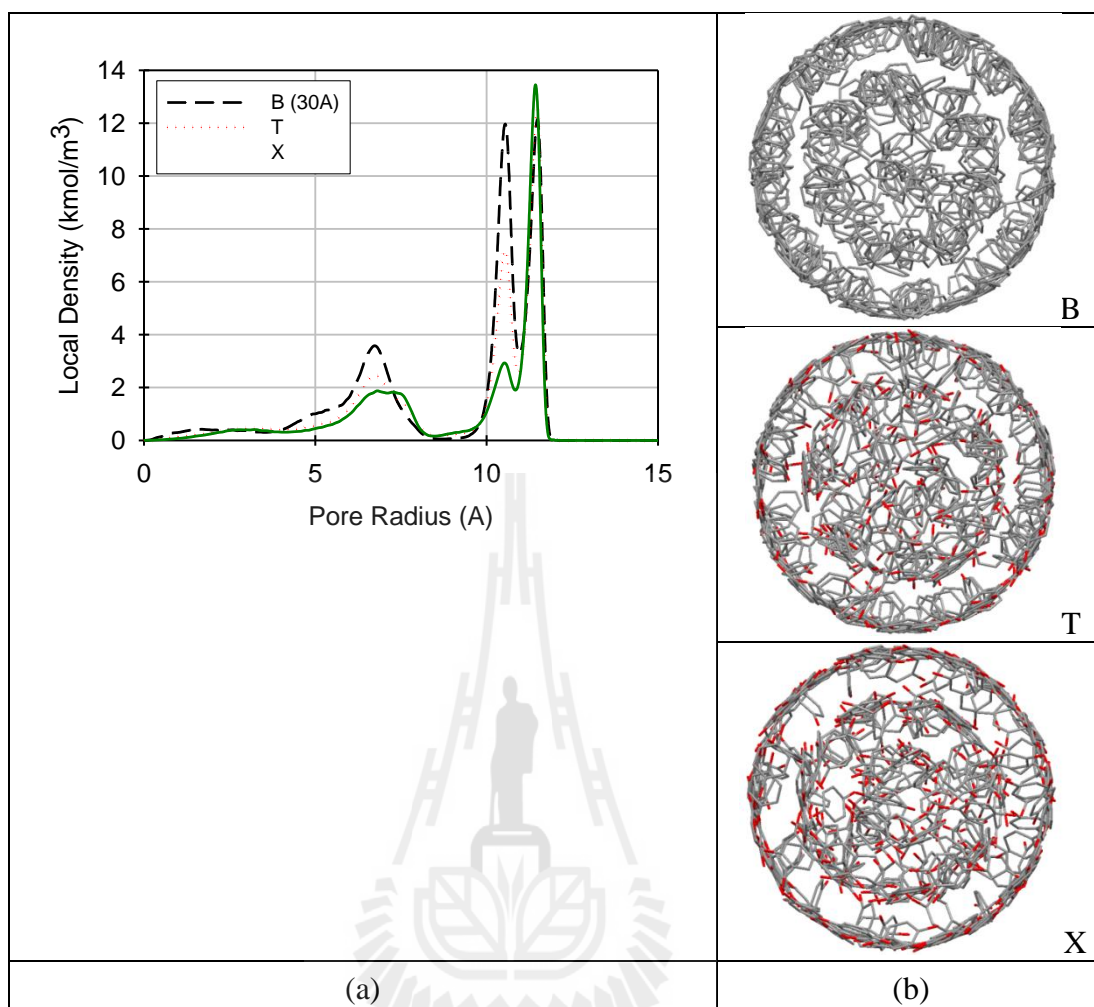


**Figure 4.11** (a) Local density distributions as a function of distance from a pore wall to the centre of benzene ring and (b) snapshots of molecules adsorbed of BTX at 298 K and  $P/P_0$  of 1.0 using the TraPPE-UA model without adjusting  $k_{sf}$  and  $F$  on graphitized cylindrical pore width of 30 Å.

## 4.7 References

Avgul, N.N., Berezin, G.I., Kiselev, A.V. and Korolev, A.Y. (1958). Heat of adsorption of hydrocarbons by carbon blacks of different degrees of graphitization. **Kolloidnyi Zhurnal**. 20: 298-304.

- Avgul, N.N., Berezin, G.I., Kiselev, A.V. and Lygina, I.A. (1959). Heats of adsorption of toluene and various isoparaffins and naphthenes on graphitized carbon black. **Russian Chemical Bulletin**. 8: 764-773.
- Belyakov, L.D., Kiselev, A.V. and Kovaleva, N.V. (1968). Gas-chromatographic determination of isotherms and heats of adsorption of water, benzene and methanol vapours on graphitised carbon black. **Russian Journal of Physical Chemistry**. 42(9): 1204-1208.
- Berezin, G.I., Kiselev, A.V., Sagatelyan, R.T. and Sinitsyn, V.A. (1972). A thermodynamic evaluation of the state of the benzene and ethanol on a homogeneous surface of a nonspecific adsorbent. **Journal of Colloid and Interface Science**. 38: 335-340.
- Berezin, G.I., Kiselev, A.V. and Sinitsyn, V.A. (1970). Adsorption of benzene and n-hexane on graphitised carbon black. **Russian Journal of Physical Chemistry**. 44: 408-411.
- Carrott, P.J.M., Carrott, M., Cansado, I.P.P. and Nabais, J.M.V. (2000). Reference data for the adsorption of benzene on carbon materials. **Carbon**. 38: 465-474.
- Davis, B.W. and Pierce, C. (1966). A study of stepwise adsorption. **The Journal of Physical Chemistry**. 70: 1051-1058.
- Do, D.D. and Do, H.D. (2006). Adsorption of benzene on graphitized thermal carbon black: Reduction of the quadrupole moment in the adsorbed phase. **Langmuir**. 22: 1121-1128.
- Do, D.D., Herrera, L.F. and Do, H.D. (2008). A new method to determine pore size and its volume distribution of porous solids having known atomistic configuration. **Journal of Colloid and Interface Science**. 328: 110-119.

- Haghseresht, F., Finnerty, J.J., Nouri, S. and Lu, G.Q. (2002). Adsorption of aromatic compounds onto activated carbons: Effects of the orientation of the adsorbates. **Langmuir**. 18: 6193-6200.
- Isirikyan, A.A. and Kiselev, A.V. (1961). The absolute adsorption isotherms of vapors of nitrogen, benzene and n-hexane, and the heats of adsorption of benzene and n-hexane on graphitized carbon blacks. I. Graphitized thermal blacks. **The Journal of Physical Chemistry**. 65: 601-607.
- Isirikyan, A.A. and Kiselev, A.V. (1963). Isotherms and heats of adsorption of nitrogen, benzene, and n-hexane vapours on graphitised carbon blacks. III. Thermodynamic quantities. **Russian Journal of Physical Chemistry**. 37: 957-961.
- Kiselev, A.V., Poshkus, D.P. and Grumadas, A.J. (1979). Statistical molecular calculation of thermodynamic parameters of adsorption of aromatic-hydrocarbons on graphite. 2. Polymethyl and mono-alkyl benzenes. **Journal of the Chemical Society-Faraday Transactions I**. 75: 1288-1300.
- Klomkliang, N., Do, D.D., Nicholson, D., Tangsathitkulchai, C. and Wongkoblaph, A. (2012). Multilayer adsorption of benzene on graphitised thermal carbon black: The importance of quadrupole and explicit hydrogen in the potential model. **Chemical Engineering Science**. 69: 472-482.
- Lai, M.H., Shih, Y.L., Chen, Y.H., Shu, S.H. and Chung, T.W. (2010). Equilibrium isotherms of the adsorption of pyrolysis gases from polymer products. **Journal of Chemical and Engineering Data**. 55: 723-727.



- Lillo-Rodenas, M.A., Fletcher, A.J., Thomas, K.M., Cazorla-Amoros, D. and Linares-Solano, A. (2006). Competitive adsorption of a benzene-toluene mixture on activated carbons at low concentration. **Carbon**. 44: 1455-1463.
- Masenelli-Varlot, K., McRae, E. and Dupont-Pavlovsky, N. (2002). Comparative adsorption of simple molecules on carbon nanotubes: Dependence of the adsorption properties on the nanotube morphology. **Applied Surface Science**. 196: 209-215.
- Matties, M.A. and Hentschke, R. (1996a). Molecular dynamics simulation of benzene on graphite. 1. Phase behavior of an adsorbed monolayer. **Langmuir**. 12: 2495-2500.
- Matties, M.A. and Hentschke, R. (1996b). Molecular dynamics simulation of benzene on graphite. 2. Phase behavior of adsorbed multilayers. **Langmuir**. 12: 2501-2504.
- Morishige, K. (2011a). Freezing and melting of Kr in hexagonally shaped pores of turbostratic carbon: Lack of hysteresis between freezing and melting. **Journal of Physical Chemistry C**. 115: 2720-2726.
- Morishige, K. (2011b). Layer-by-layer freezing of Kr confined in hexagonal pores with crystalline carbon walls. **Journal of Physical Chemistry C**. 115: 12158-12162.
- Pierce, C. and Ewing, B. (1967). Localized adsorption on graphite surfaces. **Journal of Physical Chemistry**. 71: 3408-3413.
- Pierotti, R.A. and Smallwood, R.E. (1966). The adsorption of benzene on homogeneous substrates. **Journal of Colloid and Interface Science**. 22: 469-481.

- Terzyk, A.P., Gauden, P.A., Furmaniak, S., Wesolowski, R.P., Harris, P.J.F. and Kowalczyk, P. (2009). Adsorption from aqueous solutions on opened carbon nanotubes-organic compounds speed up delivery of water from inside. **Physical Chemistry Chemical Physics**. 11: 9341-9345.
- Vernov, A. and Steele, W.A. (1991a). Computer-simulations of benzene adsorbed on graphite. 1. 85 K. **Langmuir**. 7: 3110-3117.
- Vernov, A. and Steele, W.A. (1991b). Computer-simulations of benzene adsorbed on graphite. 2. 298 K. **Langmuir**. 7: 2817-2820.
- Wang, C.M., Chang, K.S., Chung, T.W. and Wu, H.D. (2004). Adsorption equilibria of aromatic compounds on activated carbon, silica gel, and 13X zeolite. **Journal of Chemical and Engineering Data**. 49: 527-531.
- Wang, Y., Nguyen, P.T.M., Sakao, N., Horikawa, T., Do, D.D., Morishige, K. and Nicholson, D. (2011). Characterization of a new solid having graphitic hexagonal pores with a GCMC technique. **Journal of Physical Chemistry C**. 115: 13361-13372.
- Wick, C.D., Siepmann, J.I., Klotz, W.L. and Schure, M.R. (2002). Temperature effects on the retention of n-alkanes and arenes in helium-squalane gas-liquid chromatography: Experiment and molecular simulation. **Journal of Chromatography A**. 954: 181-190.
- Yun, J.H. and Choi, D.K. (1997). Adsorption isotherms of benzene and methylbenzene vapors on activated carbon. **Journal of Chemical and Engineering Data**. 42: 894-896.
- Yun, J.H., Choi, D.K. and Kim, S.H. (1999). Equilibria and dynamics for mixed vapors of BTX in an activated carbon bed. **AIChE. Journal**. 45: 751-760.

Yun, J.H., Hwang, K.Y. and Choi, D.K. (1998). Adsorption of benzene and toluene vapors on activated carbon fiber at 298, 323, and 348 K. **Journal of Chemical and Engineering Data**. 43: 843-845.



# CHAPTER V

## HYSTERESIS AND EQUILIBRIUM TRANSITION OF ARGON AND BENZENE ADSORPTIONS IN FINITE SLIT PORES

### 5.1 Abstract

*Bin* grand canonical Monte Carlo (*Bin*-GCMC) is compared with conventional GCMC in a comprehensive investigation of the effect of simulation method for the description of the adsorption-desorption hysteresis of argon and benzene in graphitic slit pores. To study the equilibrium phase transition, we applied the Mid-Density scheme and show how pore width, length and adsorption temperature affect the equilibrium transition. It was found that the desorption branch becomes closer to the equilibrium transition as the pore length is increased, while its relative position between the adsorption and desorption segments of the hysteresis loop is rather insensitive to pore width and temperature. This is distinctly different from a previous study of cylindrical pores where the equilibrium transition is closer to the adsorption segment of the hysteresis loop as the pore size is increased (Liu et al., 2012).

### 5.2 Introduction

Adsorptions of fluid in a simple solid model have been initially implemented to more understand those in a more complex solid model as well as in a real material. Adsorption in simple mesopores (for example open ended cylindrical pores) always

exhibits hysteresis when temperature is less than the critical hysteresis temperature and pore size is greater than a critical value (Morishige, 2008; Morishige and Tateishi, 2003). The characteristics of the hysteresis loop depend on the material examined, the adsorbate and the temperature (Kruk and Jaroniec, 2003; Morishige, 2008; Morishige and Tateishi, 2003). The equilibrium phase transition (vapor-liquid transition) in the hysteresis loop can be found for these systems by using the Mid-Density scheme (Liu et al., 2012; Liu et al., 2011). Understanding such confinement of fluids is of crucial interest for both fundamental research and potential applications.

### 5.3 Literature Review

To investigate hysteresis, the recently proposed a *Bin* Monte Carlo scheme (Fan et al., 2011) in which sampling has been shown to be 2 to 3 times more efficient than in conventional Monte Carlo, being especially advantageous when the system is very dense. Furthermore this method gives more reproducible and reliable adsorption and desorption branches, from which the recently introduced Mid-Density scheme (Liu et al., 2012; Liu et al., 2011) can be applied to obtain the equilibrium transition. *Bin*-MC has been successfully applied to give a much better description of the spike in the heat curve versus loading for argon, nitrogen and methane adsorption on graphite (Fan et al., 2012) than had been previously achieved by other simulation methods. *Bin*-MC has also been applied to study adsorption in mesopores, and it was found that the hysteresis loop obtained with this method is larger than that obtained with conventional MC (Fan et al., 2011), but that study has so far been restricted to a single pore size and argon adsorbate.

The Mid-Density scheme (Liu et al., 2012; Liu et al., 2011) was suggested as an alternative to more complex methods such as gauge cell Monte Carlo (Neimark et al., 2003; Neimark and Vishnyakov, 2000; Puibasset, 2010; Vishnyakov and Neimark, 2001; Vishnyakov and Neimark, 2003), the grand thermodynamic potential (Rowley et al., 1975; Walton and Quirke, 1989) or thermodynamic integration (Peterson and Gubbins, 1987; Peterson et al., 1988) to determine the equilibrium phase transition in pores. This method has been used to study the equilibrium phase transition of argon adsorbed in graphitic pores at 87.3 K, and the results were shown to be in excellent agreement with the more demanding gauge cell method (Liu et al., 2012; Liu et al., 2011).

In this chapter, we use *Bin*-GCMC to study the hysteresis loop of argon and benzene in graphitic slit pores. The effect of changing the acceptance ratio for displacement (and rotation, in the case of benzene) on the adsorption isotherms has been examined for both GCMC and *Bin*-GCMC schemes. We then apply the Mid-Density scheme in sequential *Bin*-CMC and *Bin*-GCMC simulations to investigate the equilibrium phase transition.

## 5.4 Simulation

The pore walls of slit pores are assumed to be composed of layers of constant surface density. The fluid-solid interaction energy for a slit-pore of infinite extent was calculated with the Steele 10-4-3 equation (Steele, 1973), and for slits with a finite length in one direction, bulk gas was placed at both ends of the pore as shown in Figure 5.1 and the Bojan-Steele equation (Bojan and Steele, 1988; Bojan and Steele,

1989; Bojan and Steele, 1993) was used to calculate the fluid-solid potential energy (see section 2.5.3 in CHAPTER II).

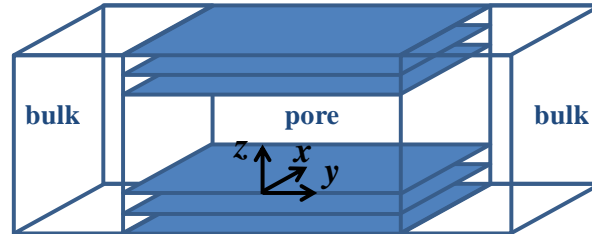


**Figure 5.1** Schematic diagram of a slit-pore of finite length in the  $y$ -direction; the pore is connected to the bulk gas phase at each end in the  $y$ -direction. Periodic boundary conditions are applied in the  $x$ -direction

To simulate the adsorption isotherm we used the conventional GCMC scheme (Allen and Tildesley, 1987), and the *Bin*-GCMC scheme (Fan et al., 2011). The box length was more than 10 times the collision diameter for pores of infinite extent in the  $x$ - and  $y$ -directions, parallel to the pore walls, and the cut-off radius was taken to be half of the box length. The number of configurations generated for both GCMC and *Bin*-GCMC was  $5 \times 10^7$  for both equilibration and sampling. For *Bin*-MC, the box was divided into bins in the  $z$ -direction and the bin width was 0.2 nm approximately controlled by the pore width.

The acceptance ratio for the displacement move is calculated at the end of each cycle as follows (for cycle  $i$ )

$$Ratio_{\text{acpt}, i} = \frac{N_{\text{acpt}, i}}{N_{\text{move}, i}} \quad (5.1)$$

where  $N_{\text{move}, i}$  and  $N_{\text{accept}, i}$  are number of attempted moves and number of successful moves, respectively, that accumulate from zero to the cycle  $i$ . The initial maximum displacement lengths were half the box length in the  $x$ - or  $y$ -direction and half the bin thickness in the  $z$ -direction for every bin. The maximum displacement lengths were updated every cycle. When the acceptance ratio was greater than the set value the maximum displacement length was increased by 1.05, otherwise it was decreased by 0.95.

## 5.5 Results and Discussion

### 5.5.1 Acceptance Ratio for Ar Adsorption on a Surface and in an Infinitely Long Slit-Pore

Conventional GCMC and the *Bin*-GCMC simulations were made at 87.3 K, in slit pores of width 10 nm (taken to be equivalent to an open graphite surface) and 2 nm. Two values of the acceptance ratio recommended in the literature: 0.20 and 0.50 (Mountain and Thirumalai, 1994) were tested. The acceptance ratio and choice of simulation scheme do not affect the isotherm or the isosteric heat for the open surface, as shown in Figures 5.2 and 5.3. However, for slit pores there is a significant difference between the simulation results obtained with the two simulation schemes, especially in the dense regions (Figure 5.4). The sampling is most effective when an acceptance ratio of 0.20 was used with the *Bin*-GCMC scheme, while the two schemes (GCMC and *Bin*-GCMC) fail to provide good sampling when the acceptance ratio is 0.50. Our finding that the 0.20 acceptance ratio is more efficient is in agreement with the conclusions of Mountain and Thirumalai (Mountain and Thirumalai, 1994).



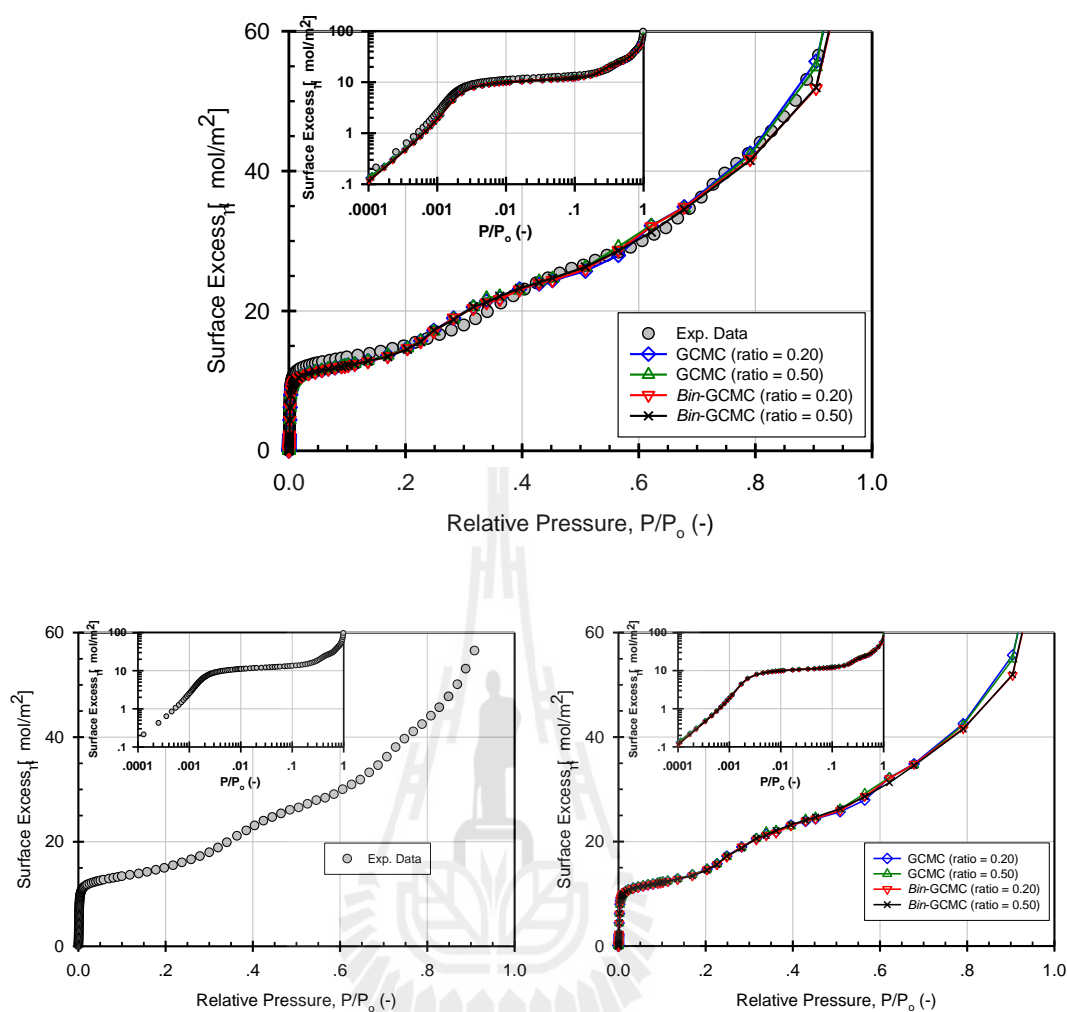


**Figure 5.2** Ar adsorption isotherms on graphitized thermal carbon black (GTCB) at 87.3 K: comparison between GCMC and *Bin*-GCMC schemes with different displacement/acceptance ratios; the experimental data are taken from Avgul and Kiselev, 1970. The saturation vapour pressures of 101.300 and 88.500 kPa are taken from the experimental data and the simulation, respectively (Do and Do, 2005).

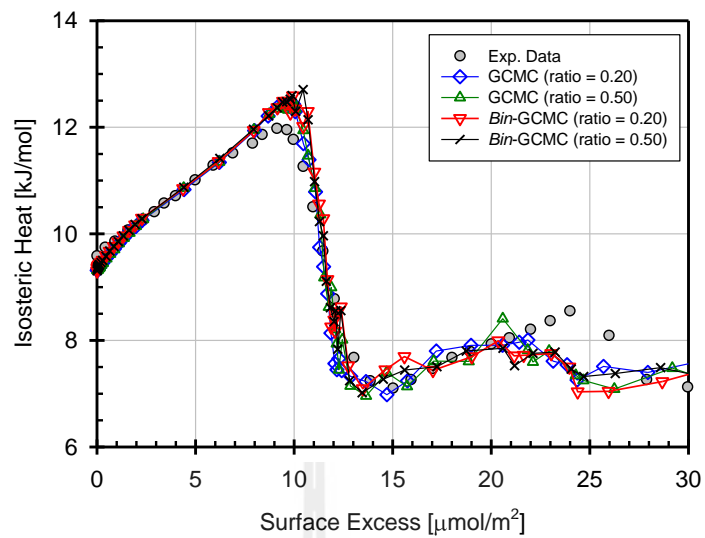


**Figure 5.3** Isosteric heats of Ar adsorption on GTCB at 87.3 K comparison between GCMC and *Bin*-GCMC schemes at different displacement acceptance ratios; the experimental data is taken from Avgul and Kiselev (1970).

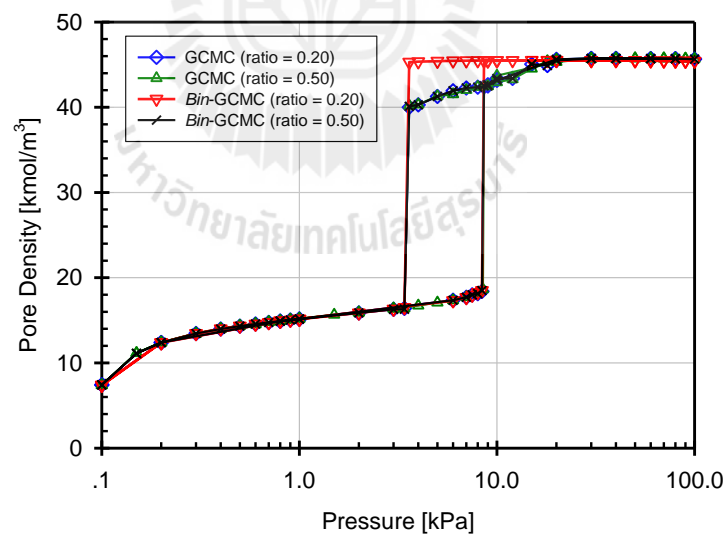


**Figure 5.4** Ar adsorption-desorption isotherms in infinitely long slit-pore of width 2 nm at 87.3 K: comparison between GCMC and *Bin*-GCMC schemes at different displacement/acceptance ratios.

### 5.5.2 GCMC and *Bin*-GCMC Simulations for Benzene on Surface and in an Infinitely Long Slit-Pore

In these simulations, we used an acceptance ratio of 0.20 and investigated the effects of the simulation scheme on benzene (TraPPE-EH model for benzene is used in this work) adsorption at 293 K on a graphite surface and in a 3 nm slit pore at 298 K. The adsorption isotherms on an open graphite surface obtained with the two schemes are the same (Figure 5.5a), implying that sampling is equally effective with either method, as was found for argon.

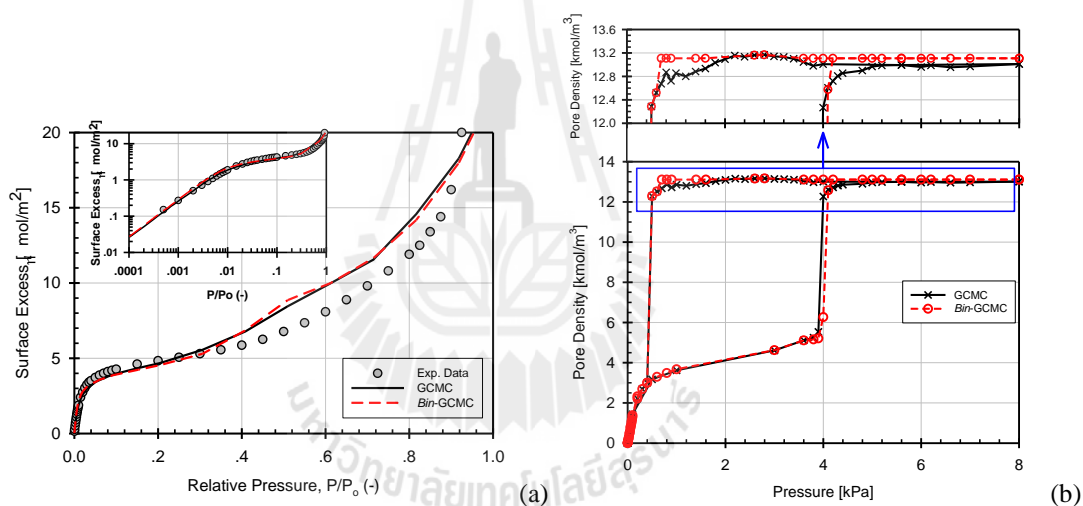


**Figure 5.5** (a)  $C_6H_6$  adsorption isotherms on GTCB at 293 K and (b)  $C_6H_6$  adsorption-desorption isotherms in an infinitely long slit-pore of width of 3 nm at 298 K comparing the GCMC and *Bin*-GCMC schemes. The  $P_0$  of 10.052 and 9.800 kPa are taken from the experimental data and simulation, respectively (Isirikyan and Kiselev, 1961; Rai and Siepmann, 2007).

However, in slit pores there are differences between the two schemes and, like argon, the sampling for benzene adsorption is more efficient with the *Bin*-GCMC scheme and the 0.20 acceptance ratio. The effectiveness of the *Bin*-GCMC lies in the fact that the probabilities of insertion and deletion are based on local densities, rather than the overall average density used in conventional MC. It is interesting to note that the desorption branch obtained with conventional GCMC shows an increase in loading when pressure is decreased (see the inset in Figure 5.5b) this is contrary to the second law of thermodynamics and is not observed with *Bin*-GCMC.

### 5.5.3 Simulations with the Mid-Density Scheme

The Mid-Density scheme was applied to determine the equilibrium phase transition in slit pores, using both conventional Monte Carlo and *Bin*-Monte Carlo simulations. We denote the Mid-Density scheme using conventional MC as “CMC+GCMC”, and the results from these simulations for argon adsorption in an infinitely long slit pore of width 2 nm at 87.3 K are shown in Figure 5.6a. The coexistence pressure was found to be 5.6 kPa.

The Mid-Density scheme used with the *Bin*-MC is denoted as “*Bin*-CMC+*Bin*-GCMC” and the results are shown in Figure 5.6b. The coexistence pressure is the same as that obtained with the “CMC+GCMC” scheme, despite the differences in the two hysteresis loops; particularly the desorption branch prior to evaporation, where the *Bin*-MC results give a higher density. A similar observation was made by Liu and co-workers. (Liu et al., 2011), who examined the effects of changing the number of MC cycles on the hysteresis loop. There the area of the hysteresis loop was found to decrease when the number of cycles was increased from

10,000 to 100,000, but the equilibrium transition pressures for the different cycle numbers were the same.

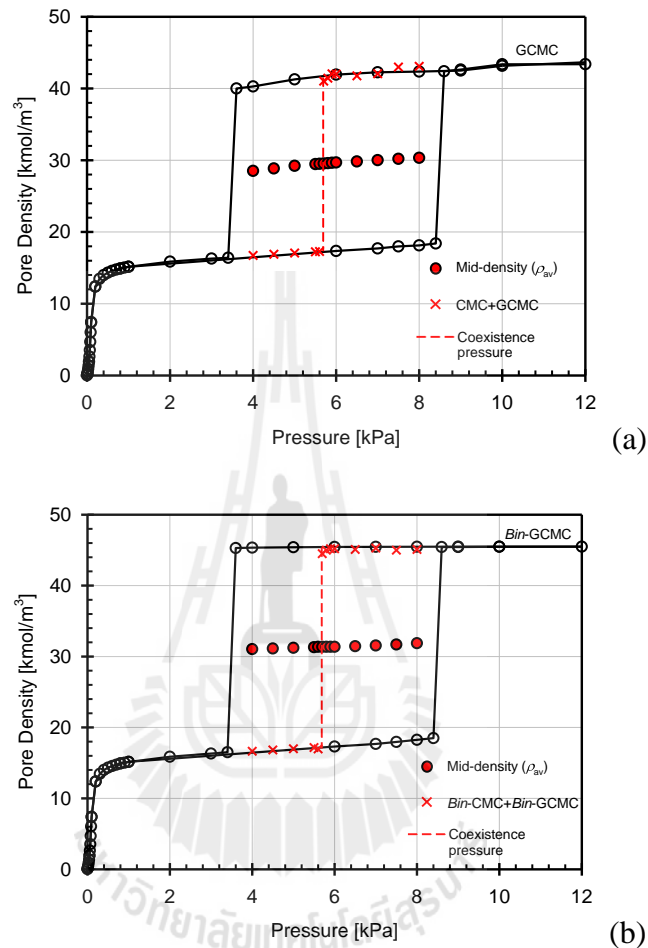


**Figure 5.6** (a) GCMC adsorption-desorption isotherm of Ar and showing the equilibrium phase transition obtained by the Mid-Density scheme using CMC+GCMC and (b) *Bin*-GCMC adsorption and desorption isotherms for Ar and the equilibrium phase transition obtained by the Mid-Density scheme using *Bin*-CMC+*Bin*-GCMC in an infinitely long slit-pore of width 2 nm at 87.3 K. Vertical dashed lines show the equilibrium transition.

#### 5.5.4 The Effect of Pore Width

*Bin*-GCMC simulations for argon adsorption at 87.3 K in infinitely long slit pores of 2 nm, 3 nm and 3.6 nm width are shown in Figure 5.7a. The condensation and evaporation pressures were found to increase with pore size, but the latter increases less, resulting in a larger hysteresis loop. The same general trend in the change in position and area of the hysteresis loop was found for benzene at 298 K as shown in Figure 5.7b.

The equilibrium phase transitions obtained using *Bin*-CMC+*Bin*-GCMC, are shown as dashed lines in Figure 5.7. The equilibrium transition is in approximately the same relative position between the vertical segments of the adsorption and desorption branches for all pore widths. This differs from previous results for infinitely long cylindrical pores, where the equilibrium transition shifts closer to the adsorption segment as pore size increases (Liu et al., 2012). The results from the Mid-Density simulations are in very close agreement with those from the gauge cell method (Liu et al., 2011) which adds further support to our claim that the two methods are equivalent.

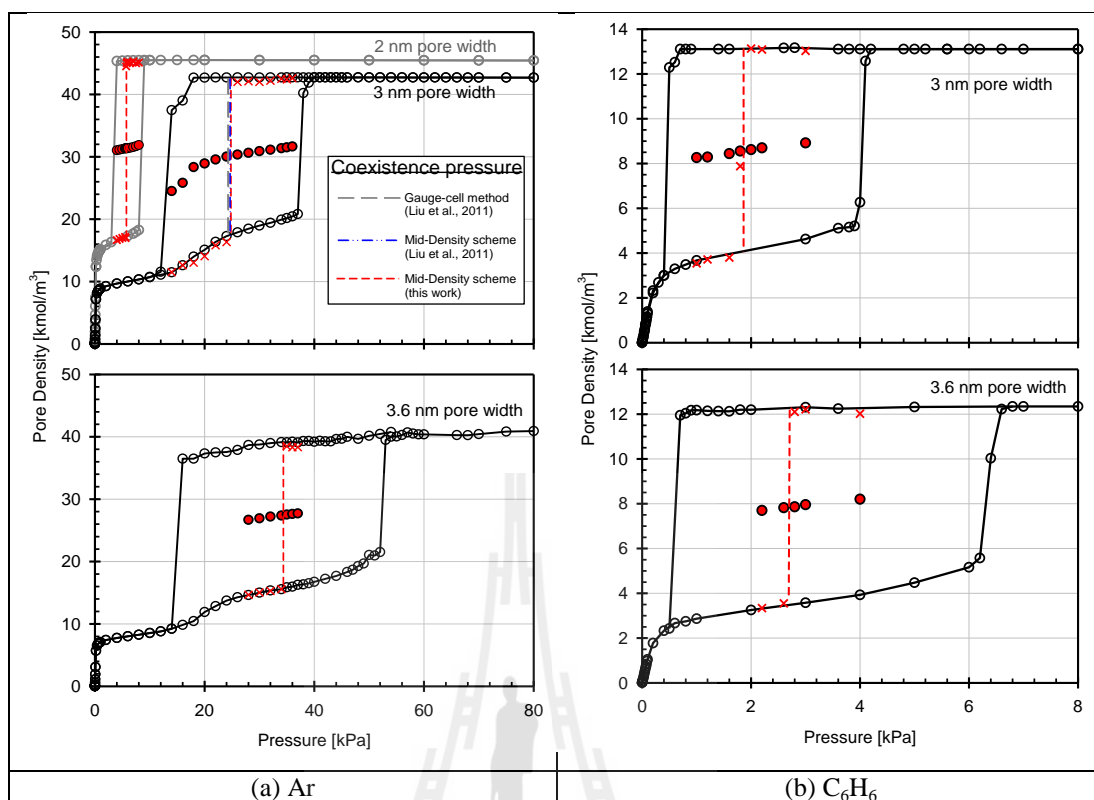


**Figure 5.7** *Bin*-GCMC adsorption-desorption isotherms of (a) Ar at 87.3 K and (b) C<sub>6</sub>H<sub>6</sub> at 298 K, and the equilibrium phase transition obtained by the Mid-Density scheme using *Bin*-CMC+*Bin*-GCMC in an infinitely long slit-pore of different pore widths. The coexistence pressure of Ar in the 3 nm pore is compared with results obtained by the gauge-cell method and Mid-Density scheme from Liu and co-workers (Liu et al., 2011). Vertical dashed lines show the equilibrium phase transition.

### 5.5.5 The Effect of Pore Length

Understanding of hysteresis for pores of infinite extent does not truly reflect the practical situations where desorption begins from a meniscus separating the liquid condensate and the gas, rather than from cavitation within the pore that leads to

an instant evaporation of an infinite column of liquid-like condensate in pores of infinite extent. The evaporation pressure for “cavitation” is always less than the desorption pressure observed experimentally, and proceeds by a mechanism in which the menisci recede from the ends of the pore to its interior. To observe this type of process in simulation, we considered finite pores in contact with the bulk gas at each end. The simulation results are shown in Figures 5.8a and 5.8b for argon and benzene, respectively. As was found for infinitely long pores, the adsorption mechanism starts with layering of molecules on the pore walls, followed by a steep condensation once the remaining core is small enough to induce it via fluid-fluid interactions. The condensation pressure is higher than in the corresponding infinitely long pore because the solid-fluid interactions are weaker, due to the absence of adsorbent atoms beyond the pore ends. The desorption process, on the other hand, proceeds by the retreat of the meniscus into the pore interior, resulting in a loss of adsorbate which is reflected in a decrease in density along the desorption branch as pressure is decreased. The liquid bridge in the middle of the pore becomes smaller as pressure is reduced and instantly evaporates when it is no longer thick enough to remain stable through mutual fluid-fluid interactions. The evaporation pressure is higher than in the infinitely long pore of the same width and therefore in closer accord with experimental observation.

Using the Mid-Density scheme, we determined the pressure of the equilibrium phase transition (shown in Figures 5.8 as red dashed lines), and observe that when the pore length is less than twice the pore width, the phase transition is discontinuous. When the pore length is greater than four times the pore width, the equilibrium transition becomes continuous, but is discontinuous again when the pore



length is infinite. The discontinuous transition in an infinitely long pore is a consequence of the absence of menisci at the pore ends and formation of cavities, followed by evaporation of molecules from the inner core. The discontinuous transition occurs in very short pores because the two menisci enclose a liquid lens that becomes unstable as explained above.

Figures 5.9 and 5.10 show snapshots of argon and benzene in finite 3nm pores at a density  $\rho_{av}^*$ , defined in Figure 5.8. These snapshots were obtained at the end of the *Bin*-CMC simulation (first half of the Mid-Density scheme). The adsorbate at the equilibrium transition has gas-like and liquid-like regions, separated by cylindrical interfaces. In the gas-like regions there are two adsorbed layers for argon but only one for benzene, which suggests that the adsorbed film of one/two layers is in equilibrium with the liquid condensate in the pore. It is interesting that the thickness of this adsorbed layer is independent of pore size, implying that the liquid bridge is larger in larger pores. The molecular configuration at the equilibrium transition is distinctly different from that at the metastable desorption branch where there are two conical interfaces, as seen in Figure 5.11, which are not as stable as the cylindrical interfaces observed at the equilibrium transition.

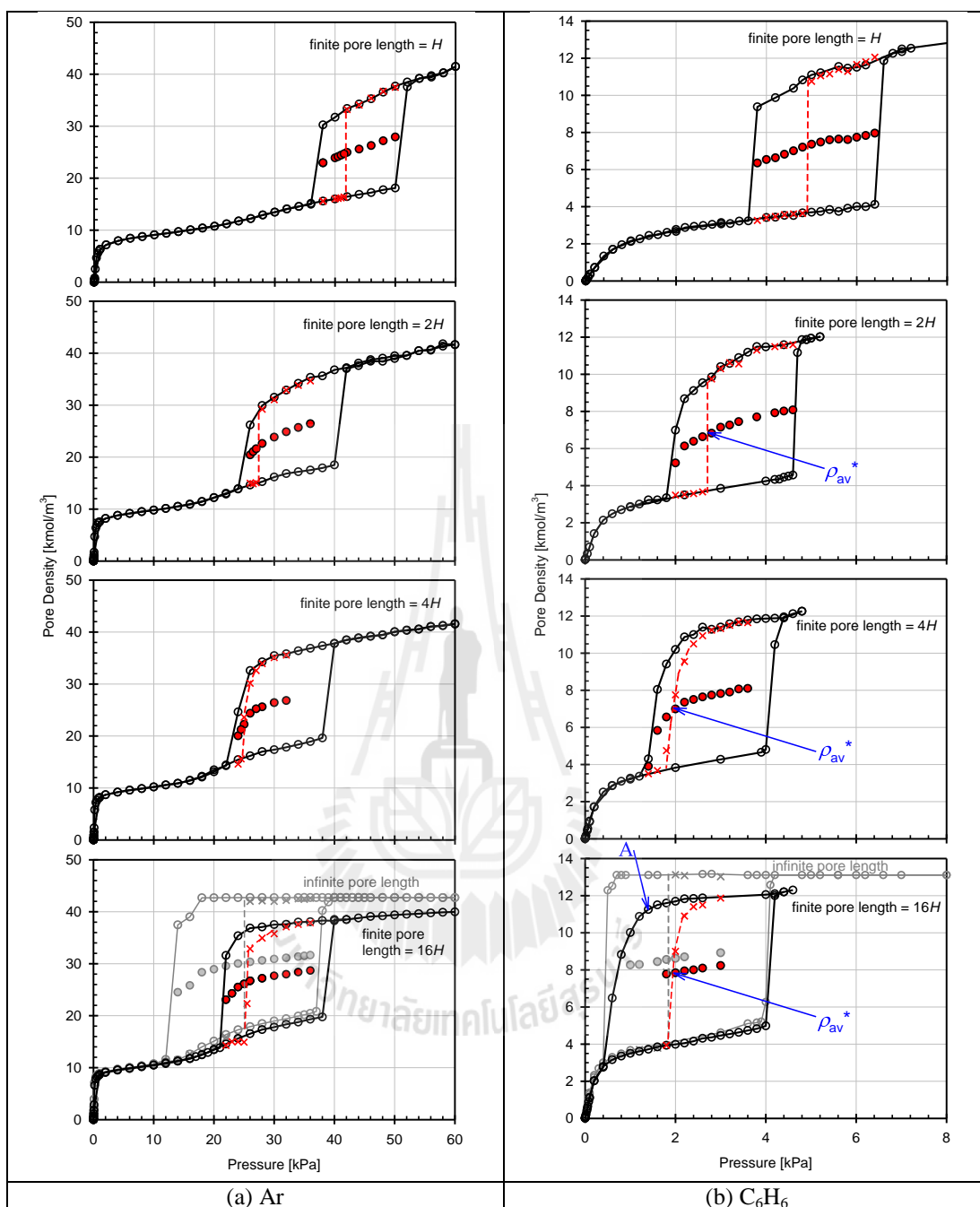


**Figure 5.8** *Bin*-GCMC adsorption-desorption isotherms for (a) Ar at 87.3 K and (b) C<sub>6</sub>H<sub>6</sub> at 298 K, and the equilibrium phase transition obtained by the Mid-Density scheme using *Bin*-CMC+*Bin*-GCMC in a finite slit-pore of width 3 nm with different pore lengths expressed in units of  $H$  the pore width. Dashed lines with crosses show the equilibrium phase transition.

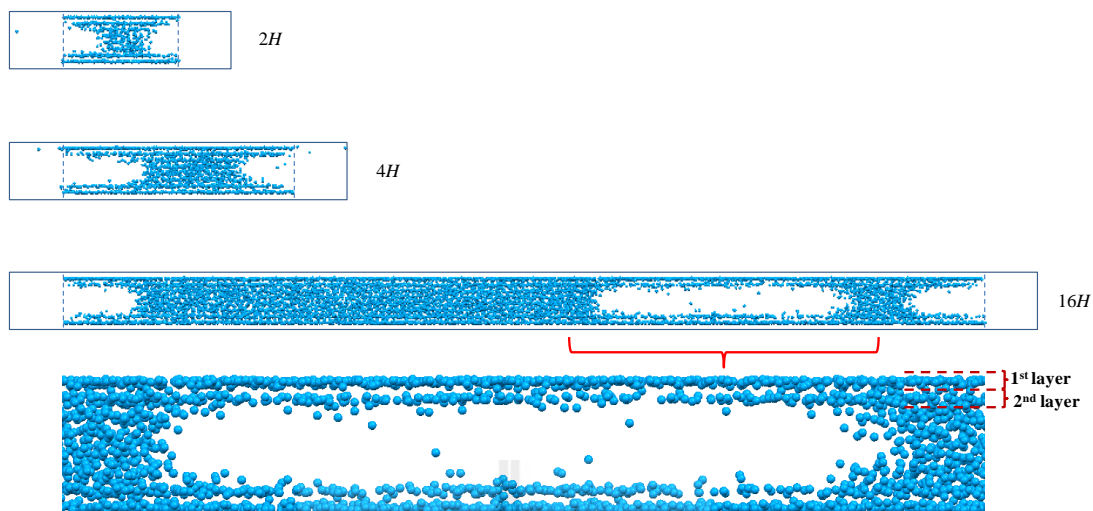


**Figure 5.9** Snapshots from *Bin*-CMC of Ar at the mid-density  $\rho_{av}^*$  and 87.3 K in pores of 3 nm width with lengths from 2 to 16 times the pore width ( $H$ ).

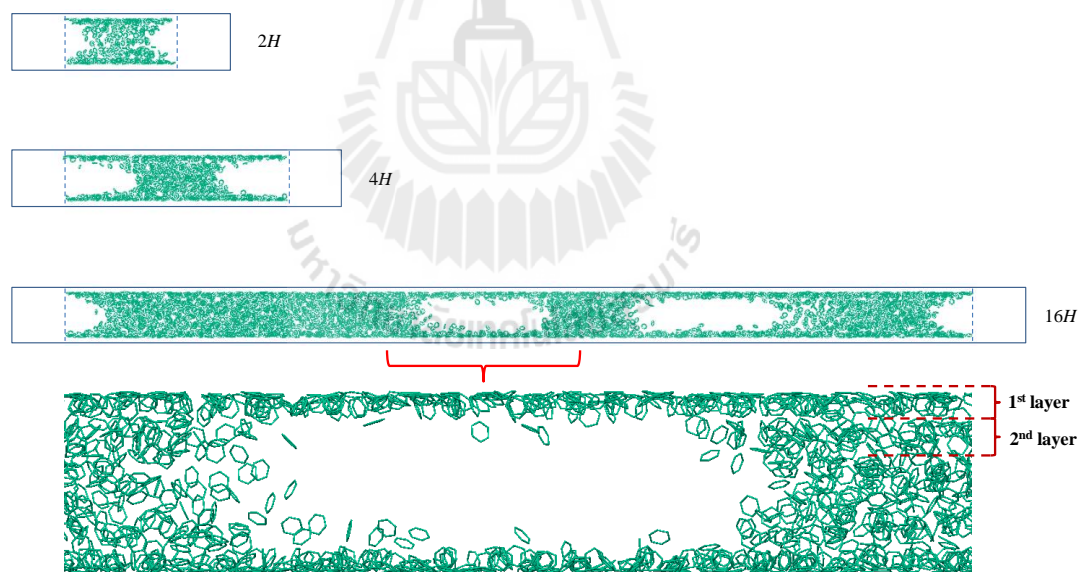


**Figure 5.10** Snapshots from *Bin*-CMC of  $C_6H_6$  at the mid-density  $\rho_{av}^*$  and 298 K in pores of 3 nm width with lengths from 2 to 16 times the pore width ( $H$ ).

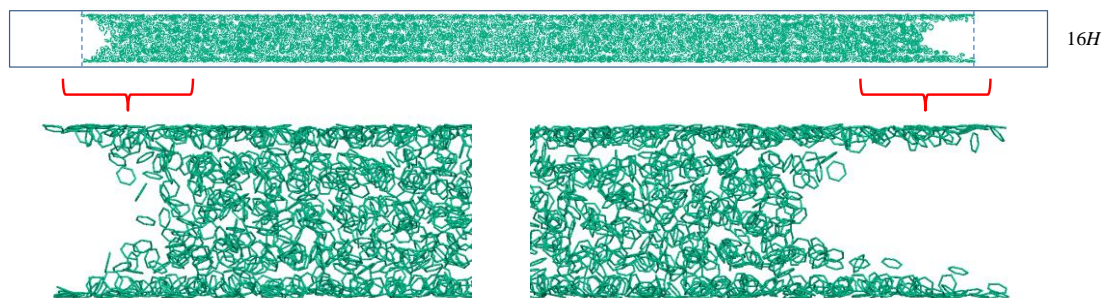


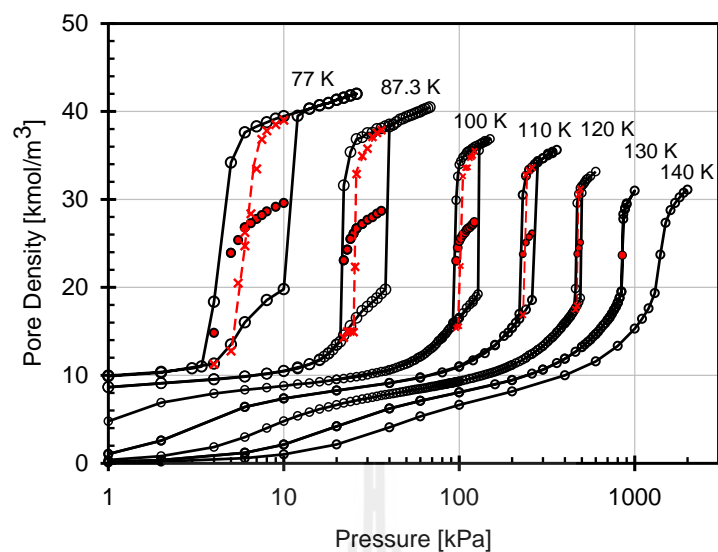
**Figure 5.11** Snapshot of  $C_6H_6$  at the metastable desorption branch corresponding to point A in Figure 5.8b.

### 5.5.6 The Effect of Temperature

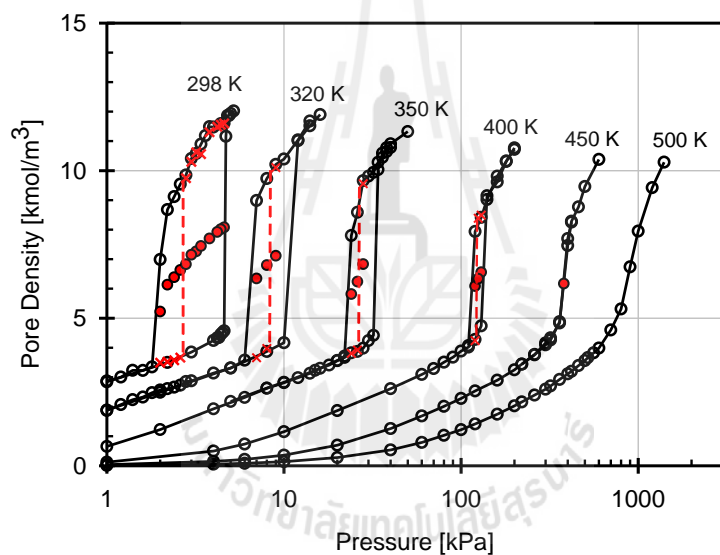
Finally, we investigated the effects of temperature on the hysteresis loop and the equilibrium phase transition of argon and benzene adsorption in finite 3 nm slit pores (Figure 5.12). As temperature is increased, we observe the following:

(1) The hysteresis loop becomes smaller and disappears at the critical hysteresis temperature, which is lower than the pore critical temperature. (2) The equilibrium transition moves closer to the desorption branch but not that significant. (3) When the pore length is less than four times the pore width the equilibrium transition is always discontinuous, irrespective of temperature. In Figure 5.13 we show snapshots of argon

adsorption as a function of temperature at the equilibrium state. A pore length of  $16H$  was used in order to ensure that we can capture the nucleation state at high temperatures despite the high thermal motion. In the range from 77 K to 110 K there are two liquid bridges of unequal length and one cavity. As temperature is increased, the cavity becomes larger and the small liquid bridge becomes larger while the large liquid bridge becomes smaller and both lose definition because of the greater thermal motion.



(a) Ar

(b) C<sub>6</sub>H<sub>6</sub>

**Figure 5.12** *Bin*-GCMC adsorption-desorption isotherms for (a) Ar in pores of length 48 nm and width 3 nm and (b) C<sub>6</sub>H<sub>6</sub> in pores of length 6 nm, and the equilibrium phase transition obtained by the Mid-Density scheme using *Bin*-CMC+*Bin*-GCMC at different temperatures. Dashed with crosses indicate the equilibrium phase transition.



**Figure 5.13** Snapshots from *Bin-CMC* of Ar at the mid-density  $\rho_{av}^*$  in pores of width 3 nm with length 16 times the pore width.

## 5.6 Conclusions

We have used conventional GCMC and the new *Bin-GCMC* techniques, to study adsorption and desorption isotherms of argon and benzene in graphitic slit-pores at 87.3 K and ambient temperatures, respectively. We find that the *Bin-GCMC*, with an acceptance ratio of 0.20, is superior to conventional GCMC. The Mid-Density scheme using a combined *Bin-CMC* and *Bin-GCMC* is effective and efficient in determining the equilibrium transition and the results are in excellent agreement with gauge cell simulations. We find that the desorption branch is closer to the equilibrium transition as the pore length is increased, while the relative position of the equilibrium transition against the adsorption and desorption segments of the hysteresis loop is insensitive to pore width and temperature, but differs from the relative position previously found for cylindrical pores.

## 5.7 References

- Allen, M.P. and Tildesley, T.P. (1987). Computer simulation of liquids. **Japanese Journal of Applied Physics Part 2-Letters**. 35: L405-L407.
- Avgul, N.N. and Kliselev, A.V. (1970). Physical adsorption of gases and vapor on graphitized carbon blacks. **Chemistry and Physics of Carbon**. 6: 1-124.
- Bojan, M.J. and Steele, W.A. (1988). Computer simulation of physisorption on a heterogeneous surface. **Surface Science**. 199: L395-L402.
- Bojan, M.J. and Steele, W.A. (1989). Computer-simulation of physisorbed Kr on a heterogeneous surface. **Langmuir**. 5: 625-633.
- Bojan, M.J. and Steele, W.A. (1993). Computer-simulation of physical adsorption on stepped surfaces. **Langmuir**. 9: 2569-2575.
- Do, D.D. and Do, H.D. (2005). Effects of potential models in the vapor-liquid equilibria and adsorption of simple gases on graphitized thermal carbon black. **Fluid Phase Equilibria**. 236: 169-177.
- Fan, C.Y., Do, D.D. and Nicholson, D. (2011). New Monte Carlo simulation of adsorption of gases on surfaces and in pores: A concept of multibins. **Journal of Physical Chemistry B**. 115: 10509-10517.
- Fan, C.Y., Razak, M.A., Do, D.D. and Nicholson, D. (2012). On the identification of the sharp spike in the heat curve for Argon, nitrogen, and methane adsorption on graphite: Reconciliation between computer simulation and experiments. **Journal of Physical Chemistry C**. 116: 953-962.

- Isirikyan, A.A. and Kiselev, A.V. (1961). The absolute adsorption isotherms of vapors of nitrogen, benzene and n-hexane, and the heats of adsorption of benzene and n-hexane on graphitized carbon blacks. I. Graphitized thermal blacks. **The Journal of Physical Chemistry**. 65: 601-607.
- Kruk, M. and Jaroniec, M. (2003). Argon adsorption at 77 K as a useful tool for the elucidation of pore connectivity in ordered materials with large cage-like mesopores. **Chemistry of Materials**. 15: 2942-2949.
- Liu, Z.J., Do, D.D. and Nicholson, D. (2012). A thermodynamic study of the Mid-Density scheme to determine the equilibrium phase transition in cylindrical pores. **Molecular Simulation**. 38: 189-199.
- Liu, Z.J., Herrera, L., Nguyen, V.T., Do, D.D. and Nicholson, D. (2011). A Monte Carlo scheme based on Mid-Density in a hysteresis loop to determine equilibrium phase transition. **Molecular Simulation**. 37: 932-939.
- Morishige, K. (2008). Adsorption hysteresis in ordered mesoporous silicas. **Adsorption**. 14: 157-163.
- Morishige, K. and Tateishi, N. (2003). Adsorption hysteresis in ink-bottle pore. **Journal of Chemical Physics**. 119: 2301-2306.
- Mountain, R.D. and Thirumalai, D. (1994). Quantitative measure of efficiency of Monte-Carlo simulations. **Physica A**. 210: 453-460.
- Neimark, A.V., Ravikovitch, P.I. and Vishnyakov, A. (2003). Bridging scales from molecular simulations to classical thermodynamics: Density functional theory of capillary condensation in nanopores. **Journal of Physics: Condensed Matter**. 15: 347-365.



- Neimark, A.V. and Vishnyakov, A. (2000). Gauge cell method for simulation studies of phase transitions in confined systems. **Physical Review E**. 62: 4611-4622.
- Peterson, B.K. and Gubbins, K.E. (1987). Phase-transitions in a cylindrical pore: Grand canonical Monte-Carlo, mean field-theory and the kelvin equation. **Molecular Physics**. 62: 215-226.
- Peterson, B.K., Gubbins, K.E., Heffelfinger, G.S., Marconi, U.M.B. and Vanswol, F. (1988). Lennard-Jones fluids in cylindrical pores: Nonlocal theory and computer-simulation. **Journal of Chemical Physics**. 88: 6487-6500.
- Puibasset, J. (2010). Counting metastable states within the adsorption/desorption hysteresis loop: A molecular simulation study of confinement in heterogeneous pores. **Journal of Chemical Physics**. 133: 104701-104714.
- Rai, N. and Siepmann, J.I. (2007). Transferable potentials for phase equilibria. 9. Explicit hydrogen description of benzene and five-membered and six-membered heterocyclic aromatic compounds. **Journal of Physical Chemistry B**. 111: 10790-10799.
- Rowley, L.A., Nicholson, D. and Parsonage, N.G. (1975). Monte-Carlo grand canonical ensemble calculation in a gas-liquid transition region for 12-6 argon. **Journal of Computational Physics**. 17: 401-414.
- Steele, W.A. (1973). Physical interaction of gases with crystalline solids. 1. Gas-solid energies and properties of isolated adsorbed atoms. **Surface Science**. 36: 317-352.
- Vishnyakov, A. and Neimark, A.V. (2001). Studies of liquid-vapor equilibria, criticality, and spinodal transitions in nanopores by the gauge cell Monte Carlo simulation method. **Journal of Physical Chemistry B**. 105: 7009-7020.

Vishnyakov, A. and Neimark, A.V. (2003). Nucleation of liquid bridges and bubbles in nanoscale capillaries. **Journal of Chemical Physics**. 119: 9755-9764.

Walton, J.P.R.B. and Quirke, N. (1989). Capillary condensation: A molecular simulation study. **Molecular Simulation**. 2: 361-391.



# CHAPTER VI

## HYSTERESIS AND EQUILIBRIUM TRANSITION OF ARGON IN SLIT-SHAPED INK-BOTTLE PORES

### 6.1 Abstract

*Bin* Grand Canonical Monte Carlo (*Bin*-GCMC) simulation was carried out to study adsorption-desorption of argon at 87.3 K in a model of ink-bottle mesoporous solid in order to investigate the interplay between the pore blocking process controlled by the evaporation through the pore mouth via the meniscus separating the adsorbate and the bulk gas surroundings and the cavitation process governed by the instability of the stretched fluid (with a decrease in pressure) in the cavity. The evaporation mechanism switches from the pore blocking to the cavitation when the size of the pore neck is decreased, and it is relatively insensitive to the neck length under conditions where cavitation is the controlling mechanism. For isotherms with a hysteresis loop, we applied the Mid-Density scheme to determine the equilibrium branch, and we have found that unlike the ideal case of simple pores of constant size and infinite extent in length where the equilibrium transition is vertical the equilibrium branch of an ink-bottle pore has three distinct sub-branches within the hysteresis loop. The first sub-branch is sharp but continuous and it is close to the desorption branch (which is typical for a pore with two open ends); this is associated with the equilibrium state in the neck. The third sub-branch is much sharper and it is close to the adsorption branch (which is typical for either a pore with one end closed

or a closed pore), and it is associated with the equilibrium state of the cavity. The second sub-branch, connecting the other two sub-branches, is gradual. The domains of these three sub-branches depend on the system parameters: the sizes of the cavity and the neck and their respective lengths.

## 6.2 Introduction

The behaviour of fluids confined within porous materials is significantly different from that of the bulk. In particular, fluids confined in mesopores exhibit the phase transition characteristic quantities (capillary condensation and evaporation). The other type of phase transition is vapour-liquid transition (the equilibrium phase transition) which occurs within the hysteresis loop. The characteristics of the hysteresis loop and the equilibrium phase transition (vapour-liquid transition) depend on the material examined, the adsorbate and the temperature (Kruk and Jaroniec, 2003; Morishige, 2008; Morishige and Tateishi, 2003). Thus, for a given adsorbate and temperature, the adsorption and desorption branches of the isotherm depend on the material properties: the pore size distribution, the pore shape and the connectivity (Fan et al., 2011b; Grant and Jaroniec, 2012; Horikawa et al., 2004; Lu and Schüth, 2005; Lu and Schüth, 2006; Nguyen et al., 2011; Rasmussen et al., 2010; Reichenbach et al., 2011). The existence of the hysteresis is attributed to the metastable states of the adsorbed layer along the adsorption branch and the metastable state of the liquid condensates along the desorption branch (Neimark and Vishnyakov, 2000). Understanding such fluid in network pores can be extended to more understand the calculation of reliable pore sizes from the adsorption data which is complicated

since the pore of disordered materials deviate from ideal pores as assumed in many models computing pore size distributions.

### **6.3 Literature Review**

The practical mesoporous materials such as activated carbon, porous glass and silica gel consist of interconnected networks of pores of varying shape, curvature, and size. Due to the complexity of pore networks, the adsorption and desorption isotherms having either a singly or doubly hysteresis loop are observed experimentally (Grosman and Ortega, 2008; Kruk and Jaroniec, 2003; Lu and Schüth, 2005; Morishige et al., 2006; Morishige and Yasuki, 2010; Morishige and Yoshida, 2010; Rasmussen et al., 2010; Ravikovitch and Neimark, 2002; Reichenbach et al., 2011; Rigby and Fletcher, 2004), and the two-step hysteresis depends on the pore size distribution, adsorbate and temperature (Grosman and Ortega, 2011; Liu et al., 2008; Morishige and Ito, 2002; Morishige et al., 2006; Morishige and Tateishi, 2003; Morishige et al., 2003; Morishige and Yoshida, 2010; Reichenbach et al., 2011; Sahu et al., 2009). The two steps in adsorption and desorption branches causing by two different pore size distribution, when the two pore size distributions became less different from disappearing of one, the hysteresis loop exhibited one stage (Liu et al., 2008; Sahu et al., 2009). The adsorption step at lower pressure is indicated capillary condensation in narrower pore while the condensation at higher pressure is associated in the wider pore. Similarly, desorption step at higher and lower pressures are indicated the evaporation in wider and narrower pores, respectively. In the desorption step, there are two mechanisms can be observed, evaporation as a receding meniscus and cavitation when pressure is decreased. The evaporation as a receding of meniscus

can be occurred in such as a single pore with both ends contacting to the gas bulk phase, a single pore closed one end, two connected pores with both ends contacting to the gas bulk phase, and/or ink-bottle pore. The desorption step induced by a meniscus shows a knee shape while the desorption step by cavitation is much steeper. Pore blocking and cavitation behaviours are found in a network porous material as an ink-bottle pore. The pore blocking is observed with evaporation as a receding of meniscus in the pore neck when the pore neck size is greater than the critical size and the pore body is still filled full with adsorbate. When the neck width is smaller the cavitation induced by evaporation is occurred, the liquid-like in the cavity (pore body) is evaporated while the neck pore remains filled by condensed liquid that induced a vapour bubble happened in the cavity. In addition, evidence from experimental work proposed by Morishige (Morishige et al., 2006) was strongly suggested that the desorption mechanism was altered from pore blocking to cavitation with increasing temperature. In a given temperature, the pore blocking and cavitation is depended on adsorbate in a corresponding material, for example, argon adsorbed onto a porous glass at 77 K was observed pore blocking where was not observed that for nitrogen in the same material and temperature, while the cavitation was found in the case of nitrogen adsorbed (Reichenbach et al., 2011). In order to explain the hysteresis by pore blocking and cavitation, different simple models on the level of single ink-bottle pores have been developed (Cohan, 1944; Fan et al., 2011b; Libby and Monson, 2004; Nguyen et al., 2011; Rasmussen et al., 2012; Sarkisov and Monson, 2001; Vishnyakov and Neimark, 2003a).

The recently proposed *Bin* Monte Carlo scheme (Fan et al., 2011a) would be used to investigate the hysteresis loop because of its better sampling than the

conventional Monte Carlo scheme (Norman and Filinov, 1969), especially when the system is very dense. This gives us more reproducible and reliable adsorption and desorption branches, from which the Mid-Density scheme can be applied to obtain the equilibrium transition. The Mid-Density scheme introduced recently (Liu et al., 2012; Liu et al., 2011) was suggested as an alternative to more complex methods such as the gauge cell Monte Carlo method (Jorge and Seaton, 2002; Neimark et al., 2003; Neimark and Vishnyakov, 2000; Puibasset, 2010; Vishnyakov and Neimark, 2001; Vishnyakov and Neimark, 2003b) and the grand thermodynamic potential (Rowley et al., 1975) or by a thermodynamic integration (Peterson and Gubbins, 1987; Peterson et al., 1988) to determine equilibrium phase transition in pores. An example of the application of the Mid-Density scheme is the study of equilibrium phase transition of argon adsorption in graphitic pores at 87.3 K, and the results were in good agreement with the more demanding gauge cell method (Liu et al., 2011). As we have known the equilibrium phase transition in confined space is difficult to measure and so far can be made only for a limited class of materials such as MCM-41 and controlled porous glasses but can investigate theoretically and has been mostly done so far in a single pore such as slit pore, cylindrical pore, and spherical pore (Jorge and Seaton, 2002; Kierlik et al., 2002; Liu et al., 2012; Liu et al., 2011; Neimark et al., 2003; Neimark and Vishnyakov, 2000; Puibasset, 2010; Vishnyakov and Neimark, 2001; Vishnyakov and Neimark, 2003a; Vishnyakov and Neimark, 2003b). Most studies were focused on infinite pore and it had been found that the equilibrium transition in an infinite pore extended in length was the first-order transition (Jorge and Seaton, 2002; Liu et al., 2011; Neimark et al., 2003; Neimark and Vishnyakov, 2000) while the equilibrium transition in a finite pore had been studied in a few papers and the

second-order transition (continuous) was observed due to the molecules in the mouth interacts with the gas bulk phase (very weak interaction) and the molecules further in the pore resulting the meniscus happened in the mouth (Liu et al., 2012). As we have seen, the equilibrium phase transition in slit-shape ink-bottle pores has not been investigated.

In the present work, we perform the *Bin*-GCMC simulation of capillary condensation and desorption in slit-shaped ink-bottle pores. We confirm two mechanisms of spontaneous evaporation from the cavity, the cavitation induced desorption and the pore blocking controlled desorption. The equilibrium phase transition in the pores exhibiting the pore blocking and the cavitation is determined using the Mid-Density scheme (*Bin*-CMC+*Bin*-GCMC).

## 6.4 Simulation

The fluid-solid interaction energy for a slit-pore of infinite length is calculated with the 10-4-3 Steele equation (Steele, 1973), while for slits of finite length in one direction, we modelled a slit pore with bulk gases at both ends as shown in Figure 6.1. There are four solid models studied in this work; the first solid model is a simple slit-pore model where both ends are exposed to gas reservoir, the second solid model is a slit-pore where one end is closed and other end is exposed to gas reservoir, the third solid model is a connected pores exposed to gas bulk phase at both ends, and the last model is an ink-bottle pore exposed to gas reservoir at the end of neck side. We used Bojan-Steele equation (Bojan and Steele, 1988; Bojan and Steele, 1989; Bojan and Steele, 1993) to calculate the fluid-solid potential energy (see section 2.5.3 in



CHAPTER II) for solid having finite length in one direction ( $y$ -direction) where the spacing between the two adjacent graphite layer is 0.34 nm.

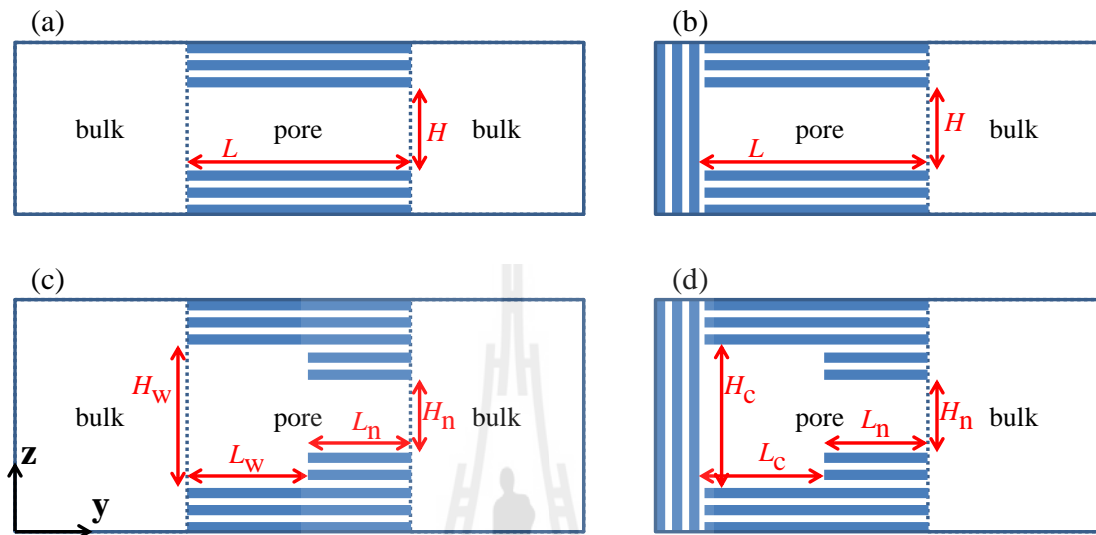
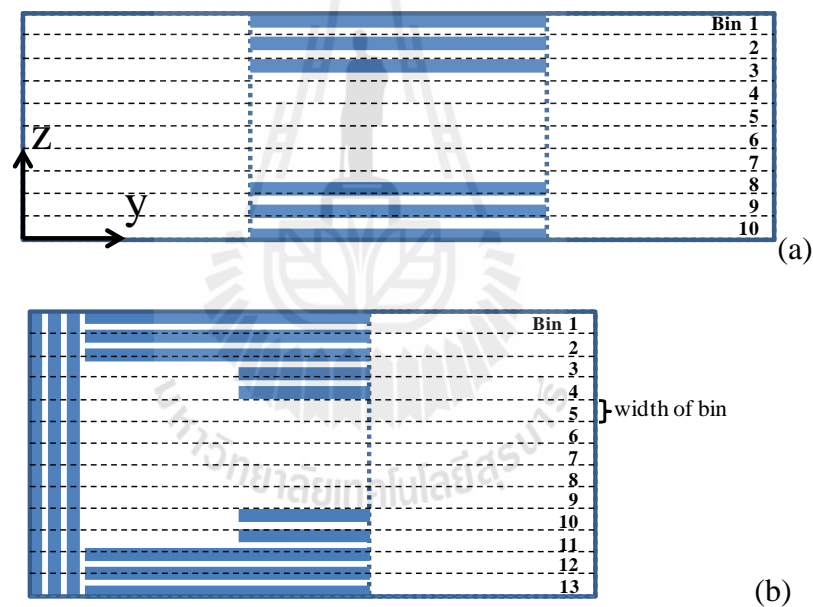


Figure 6.1 Schematic diagrams of a slit-shaped pores of finite length in the  $y$ -direction; the pore is connected to the bulk gas phase at two ends in the  $y$ -direction. Periodic boundary conditions are applied in the  $x$ -direction. (a) Finite simple slit pore, (b) finite slit pore with one closed end, (c) two connected pores exposed to bulk, and (d) ink-bottle pore (one cavity with one neck)

To simulate the adsorption isotherm we used the *Bin*-GCMC scheme (Fan et al., 2011a), which is described in section 2.7.1 of CHAPTER II. We construct the simulation box into bins having the length of bins parallel into  $y$ -direction for all pores, for example in the case of simple slit-pore and ink-bottle pore as shown in Figure 6.2, the width of bins in  $z$ -direction is equally and approximately of 0.2 nm depending on the width of simulation box controlled by the width of adsorbed pore. For the simple slit-pore exposed to reservoir at both ends, the length of bins in

y-direction is parallel to the length of solids which is the same direction of adsorbed layers that can gain the efficiency of the *Bin* concept at high dens phase. For pore closed end, it seems to divide the bin being the length of bins parallel to solid length in z-direction. But in this work, the pore length is significantly greater than its width; therefore, adsorbate would be dominated to form the adsorbed layer parallel to the pore length in y-direction. The amount adsorbed at the end of solid contacting to gas reservoir to form surface adsorption is very small; therefore, the direction of constructed bin in Figure 6.2 has no significance.



**Figure 6.2** Division of bins in simulation box, for example, (a) there are 10 bins with equal size for a simple slit-pore and (b) there are 13 bins with equal size for an ink-bottle pore. The number of bins depended on the width of simulation box which we evaluate the width in z-direction of bins approximately of 0.2 nm and equally.

## 6.5 Results and Discussion

### 6.5.1 Simple Slit Pores

The simulation results of the adsorption-desorption isotherms of 3 nm finite slit pore of length 10 nm and 3 nm slit pore of infinite in extent (i.e. periodic boundary conditions are imposed) are shown in Figure 6.3.

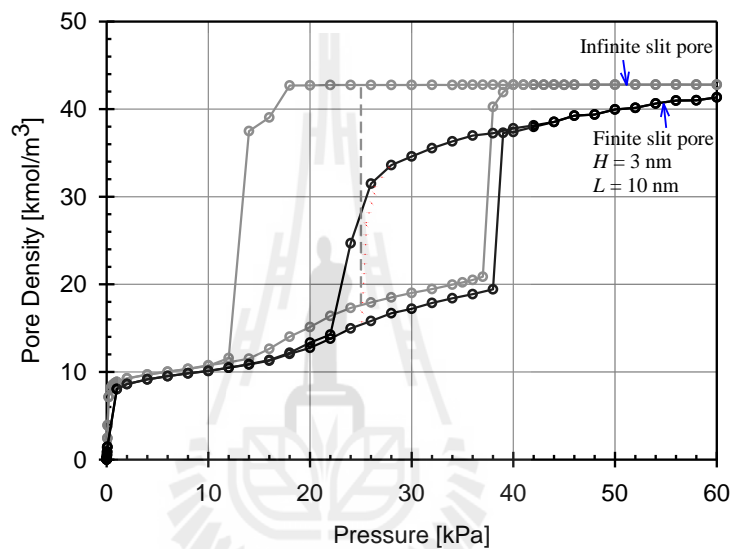


**Figure 6.3** Adsorption and desorption isotherms of argon in infinite and finite pores at 87.3 K. The vertical dash line indicates the equilibrium phase transition in infinite pore. The dotted line indicates the equilibrium phase transition in finite pore (both end exposed to gas reservoir).

Because it is more difficult to evaporate an infinite column of liquid condensate in the pore of infinite extent than the finite liquid condensate in the finite pore, the desorption pressure for the infinite pore is lower than that for the finite pore, resulting a very large hysteresis loop for the infinite pore. It is known that the pore of infinite length does not describe experimental data because the evaporation

mechanism is purely by the stretching of the fluid until it becomes unstable (cavitation; at the liquid spinodal point), while in finite pores the mechanism of evaporation is due to two simultaneous processes: the receding of the menisci from the pore mouth to the interior and the stretching the fluid in the pore interior. Another distinct difference between the infinite pore and the finite pore is that in the former the desorption branch (prior to evaporation) only decreases slightly due to the stretching of the fluid as pressure is decreased (i.e. the average distance between two fluid molecules is slightly larger) while in the finite pore the capacity along the desorption branch decreases a lot more, due to the combined loss of mass at the pore mouth, resulting from the receding of the menisci to the pore interior, and the stretching of the fluid. The receding of the menisci is due to the fact that molecules at the gas-liquid interface are pulled towards the liquid-like region (cohesive forces) rather than towards the gas-like region as seen in Figure 6.4.

#### **6.5.1.1 Equilibrium Transition**

The equilibrium phase transition in an infinite slit pore is first order (shown as the vertical dashed line in Figure 6.3); on the other hand the equilibrium branch for the finite length pore is sharp but continuous (second-order) and it is close to the desorption branch. Interestingly, we observed that the equilibrium branches for the infinite pore and finite pore are fairly close to each other. The reason why the equilibrium branch for the finite length pore is close to the desorption branch is because of the balance between the receding of the gas-liquid interface, which is maintained at equilibrium, and the stretching of the fluid interior which is under a metastable state.

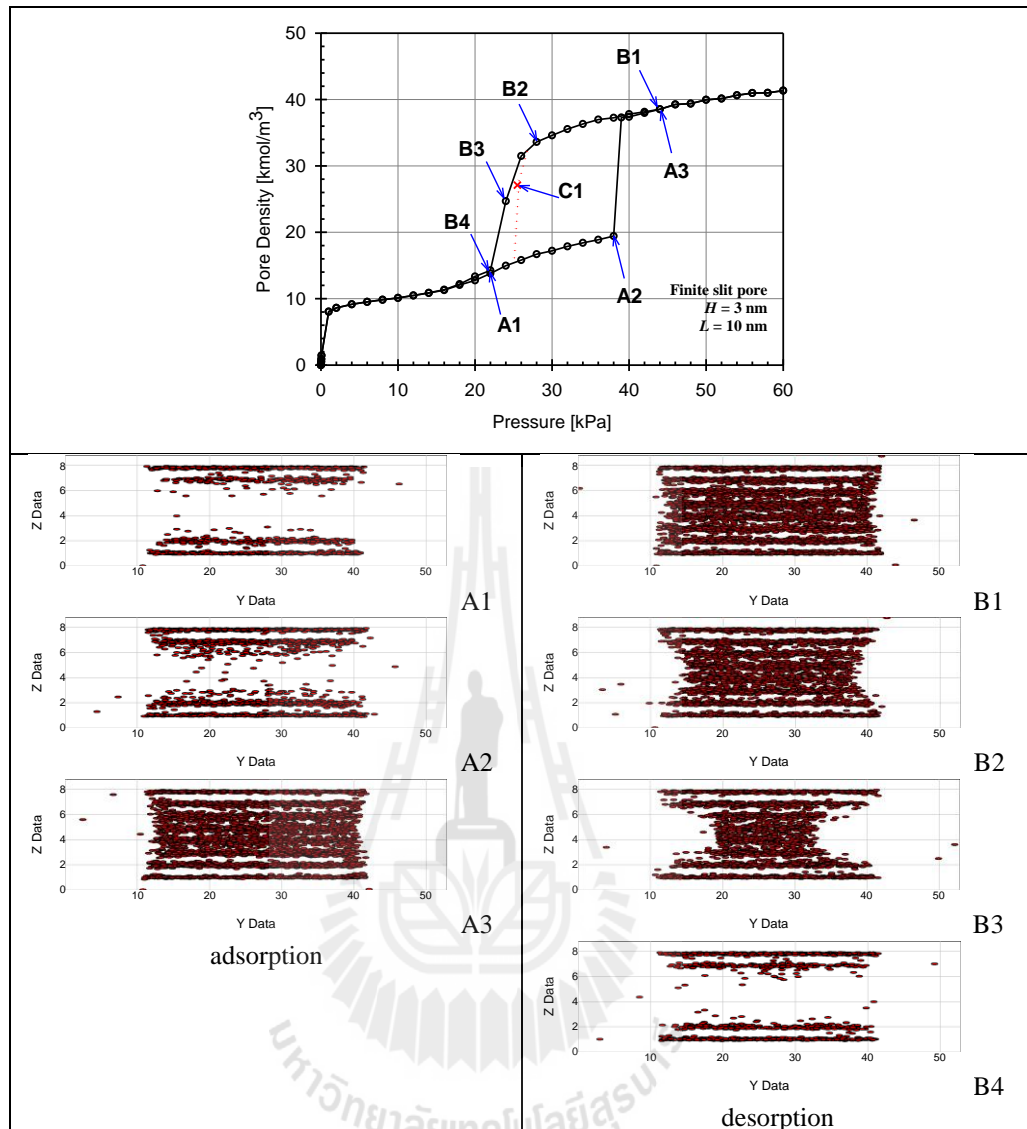


**Figure 6.4** Snapshot of argon along adsorption and desorption branches in finite slit pore at 87.3 K for 3 nm pore width and 10 nm pore length.

The snapshot of the equilibrium branch for the 10 nm length finite pore is shown in Figure 6.5. For this short length, we observe a single liquid bridge in the middle of the pore, while for longer pores two liquid bridges are formed with an existence of a cavity in the middle. This has been observed in our previous work (Klomklang et al., 2012) with 48 nm length pore.

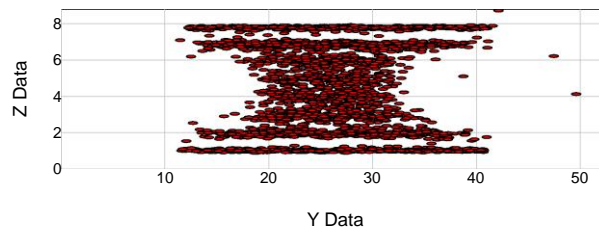


**Figure 6.5** Snapshot of argon at the equilibrium phase transition state (point C1 in Figure 6.4) output from the Mid-Density scheme at 87.3 K for 3.0 nm pore width and 10 nm pore length.

### 6.5.2 Finite Slit Pore with One Closed End

The adsorption and desorption isotherms of argon at 87.3 K for a 10 nm length pore of 3 nm width closed at one end are shown in Figure 6.6. Also shown in the same figure, for comparison, is the isotherm of an open ended pore of the same width.

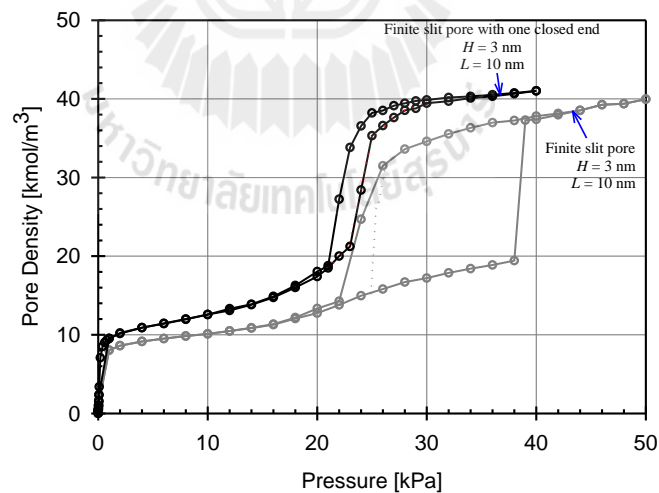


**Figure 6.6** Adsorption and desorption isotherms of argon in finite slit pore (both ends are exposed to gas reservoir) and finite slit pore with one closed end at 87.3 K. The dotted line along the cross symbol indicates the equilibrium phase transition in the pores.

The closed end has a higher adsorption affinity than the walls along the pore, and adsorption will follow a mechanism involving two simultaneous processes: the progression of a gas-liquid interface from the closed end towards the pore mouth and the build up of layer on the pore wall, with the former being the dominating one because of the greater fluid-fluid interactions, resulting from the concave curvature from the gas-like side (a fluid molecule interacts with more neighbours at the gas-liquid interface than at the pore walls). Because of this mechanism the adsorption branch does not have a sharp jump in density as in the case of open ended pore, but rather it exhibits a gradual increase with pressure. Upon desorption, the process is reverse to what we just described for adsorption, but the liquid-like region can be maintained in a metastable state because of the cohesive force (especially at low temperatures), resulting a hysteresis but its size is much smaller than the loop observed with a comparable pore (same width and length) with two open ends. The extent of the metastability is less for larger pores, and we expect the loop is smaller for larger pores of the same length and for shorter pores of the same size. The snapshots of the closed end 3nm pore having 10nm length are shown in Figure 6.7. It is seen that adsorption starts with layering on the pore walls including the closed end, followed by the formation of a meniscus at the closed end and its progression towards the pore mouth as pressure is increased.

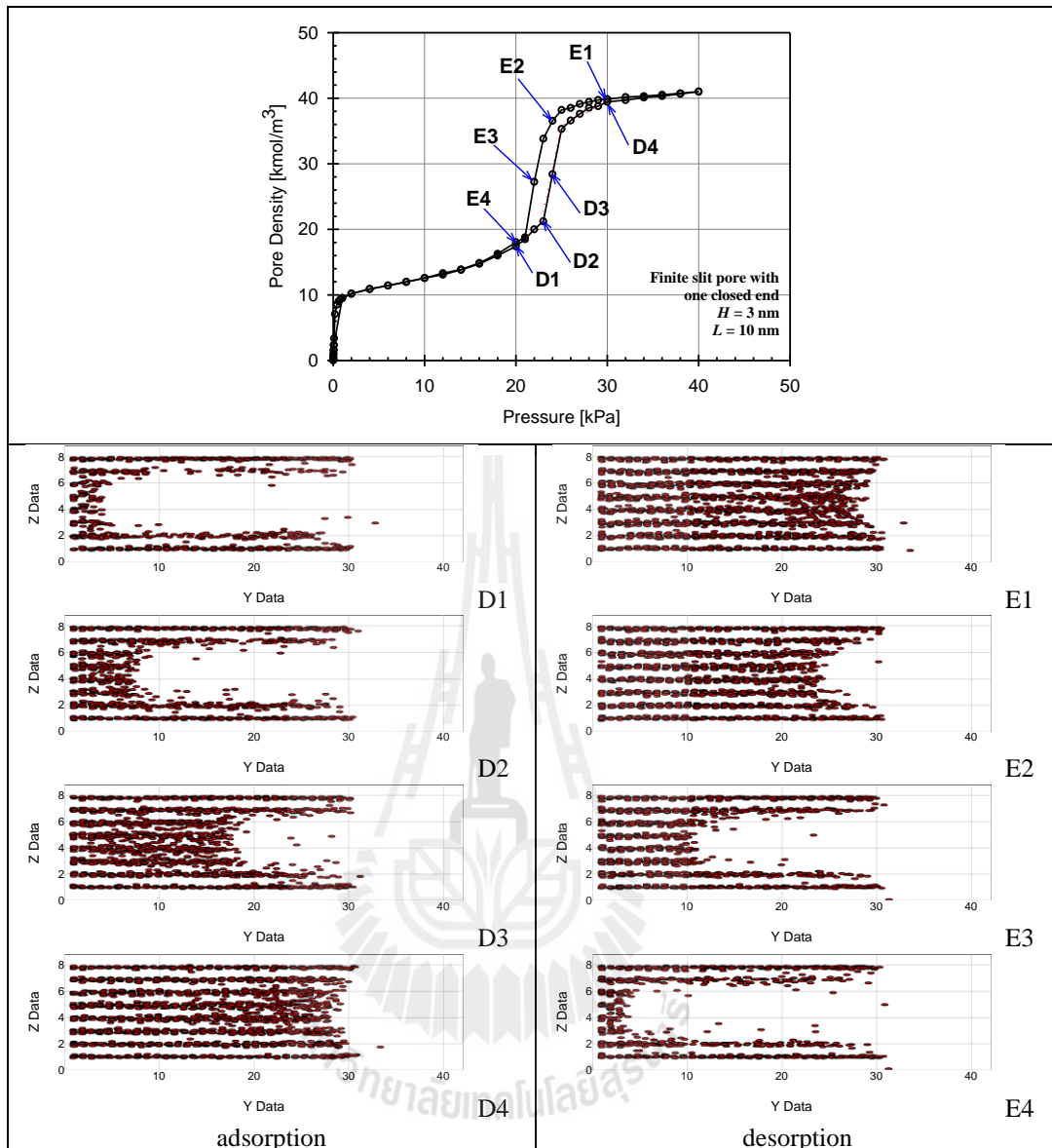


**Figure 6.7** Snapshot of argon along adsorption and desorption branches in slit pore with one closed end at 87.3 K for 3 nm pore width and 10 nm pore length.

### 6.5.2.1 Equilibrium Transition

The equilibrium phase transition for closed end pore is shown as the dotted line in Figure 6.6. The equilibrium phase transition coincides exactly with the adsorption branch of the hysteresis loop, and this is different from an open



ended pore for which the equilibrium transition is closer to the desorption branch (see Figure 6.3, and for direct comparison we also include the results of the open ended pore in Figure 6.6). This supports both arguments that were put forwarded in the literature about which branch is the equilibrium branch.

### 6.5.3 Two Connected Pores Exposed to Bulk

For a connected pore exposed to the bulk surrounding at both ends, we consider the case where the widths of the two sections of the pore are larger than the critical hysteresis pore width so that a hysteresis loop can be observed for both of them if they are unconnected. We shall consider two cases: (1) these widths are close to each other; (2) the widths are very different. In the first case, the capillary condensation in this connected pore occurs in one step (the top graph of Figure 6.8) because when condensation starts in the narrow section it will quickly spread to the larger section of the pore (an avalanche effect). However, upon desorption from a completely filled pore we observe a two-stage desorption, which is resulted from the receding of the meniscus from both ends of the pore, with the receding from the larger end being faster with the reduction in pressure. Therefore, the first stage of desorption is due to the emptying of the larger section through the larger end of the pore, and the second stage of desorption is due to the emptying of the narrow section through both ends because the larger section is now essentially empty.

However, in the second case where the widths of the two sections of a connected pore are very different we observed two steps in the adsorption branch of the isotherm. The first step is the capillary condensation (of course followed from the molecular layering) of the narrower section of the pore. After the narrower section has been filled, adsorption continues in the larger section which now behaves like a closed

end pore; one end is closed by the liquid condensate in the narrower section and the other end remains opened to the bulk surrounding (see the snapshots in Figure 6.9). Because of this closed end, adsorption in the wider section is progressed via movement (towards the pore mouth) of the meniscus formed at the junction of the two sections, and therefore the adsorption is gradual as seen in the bottom graph of Figure 6.8. Upon desorption from a completely filled pore, like the first case, we also observe a two-stage desorption, and the mechanism is the same as that described earlier for the first case.

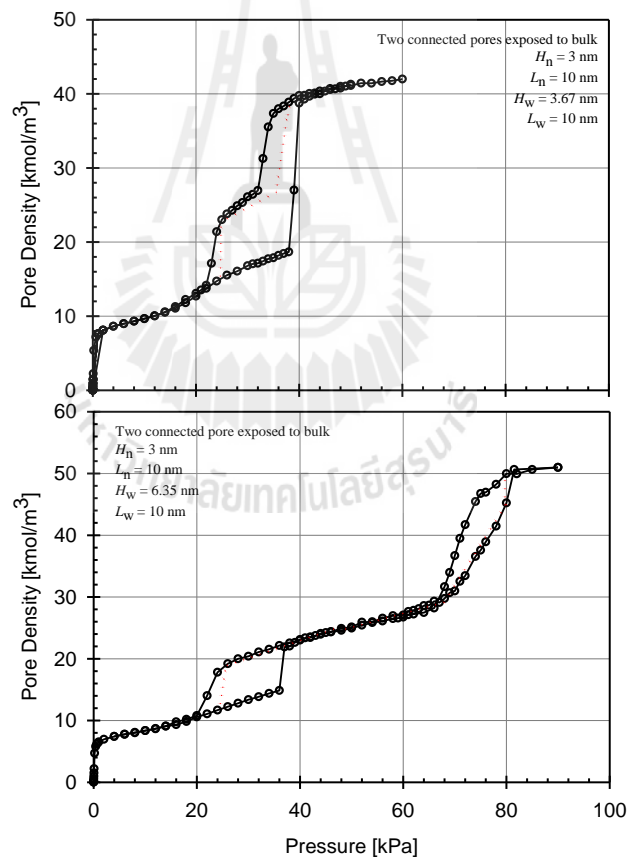


**Figure 6.8** Adsorption and desorption isotherms of argon in the two connected pores exposed to bulk at 87.3 K. The dotted line is the equilibrium phase transition in the pores.

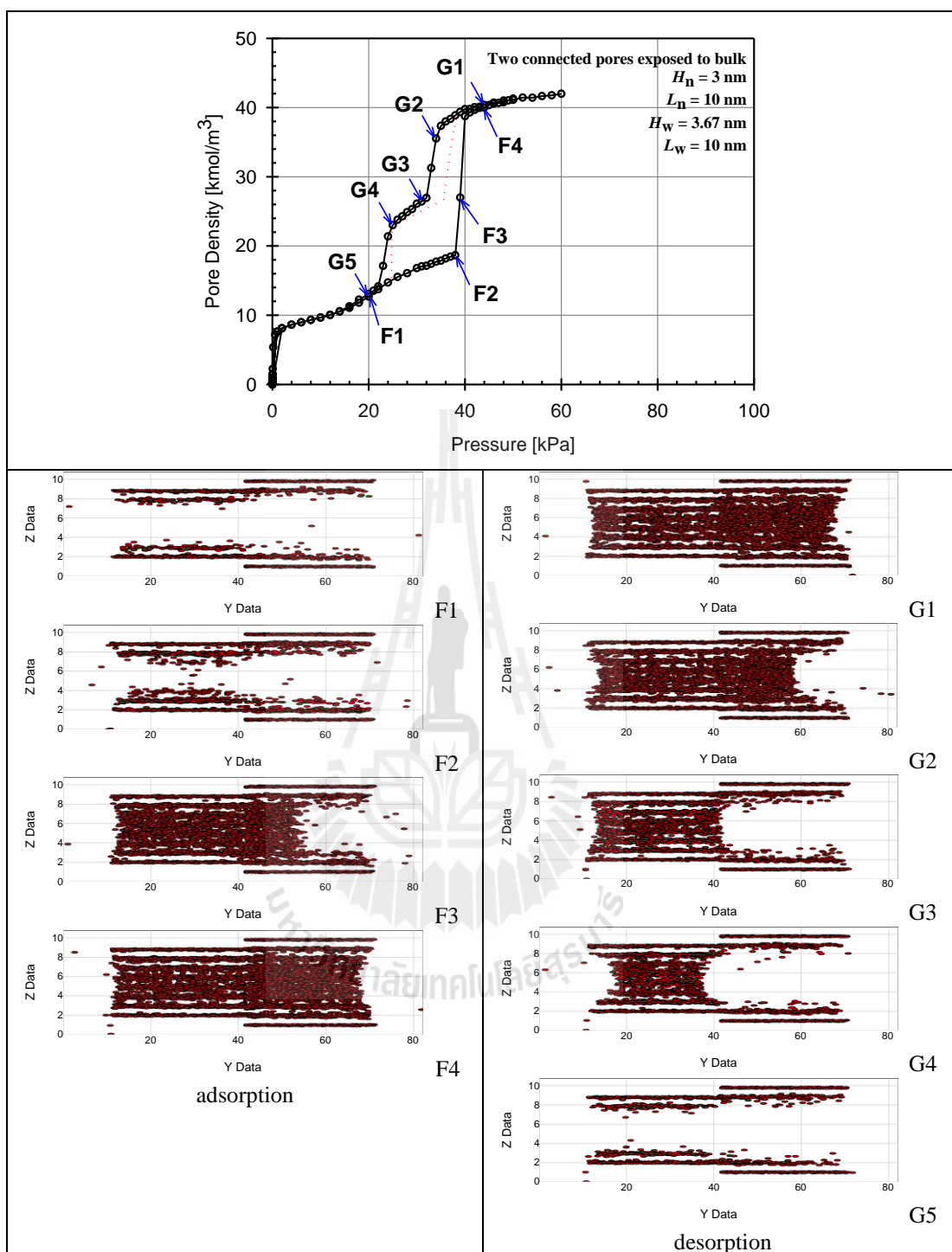


**Figure 6.9** Snapshot of argon along the adsorption and desorption branches output from the Bin-GCMC at 87.3 K for the two connected pores exposed to bulk. Desorption by receding of pressure as menisci is investigated.

### 6.5.3.1 Equilibrium Transition

The equilibrium phase transition is shown as the dotted line in Figure 6.8. Unlike the simple pores dealt with earlier, the equilibrium branch of a connected pore exhibits a two-stage behaviour. The first is second-order like, and it is close to the desorption branch and is associated with the equilibrium in the narrower section of the pore. This is so because the adsorption and desorption of this narrow section behave exactly the same as an independent pore with both ends opened to the surrounding gases (see Section 6.5.1). The second stage is sharper, and it is close to the adsorption branch of the hysteresis loop. This stage is associated with the wider section of the pore because the adsorption and desorption of this section is similar to an independent pore with one end closed, whose detailed behaviour has been discussed in Section 6.5.2.

We have explained the two distinct stages of the equilibrium transition, which are associated with the two sections of the pore. They occur over two different pressure ranges, and there exists an equilibrium branch that connects these two stages. For the ease of explanation, we shall call this branch the connecting equilibrium transition. When the sizes of the two sections are not very different, this connecting equilibrium transition is between the adsorption and desorption branches of the hysteresis loop (top graph of Figure 6.8). However, when they are very different, this transition is spanning along the desorption branch of the first hysteresis loop and the adsorption branch of the second hysteresis loop. The middle portion of this transition is spanning along the stable states of the isotherm (bottom graph of Figure 6.8).

We show in Figure 6.10 the snapshots at the equilibrium phase transition for the case where the sizes of the narrow and wide sections are not very different. The snapshots of the connecting equilibrium at the points H1 and H2 show that the system evolves at the junction of the two sections. The snapshots of the equilibrium transition in the wider section of the pore (points H3 and H4) show the molecules are building up the liquid bridge in the wider pore. It is worthwhile to study the snapshots of the metastable state (point G3) and the equilibrium transition at the same density (point H2) as shown in Figure 6.10. Although the topology of these two snapshots is the same, the difference between these two states lies in the distribution of molecules in the pore.

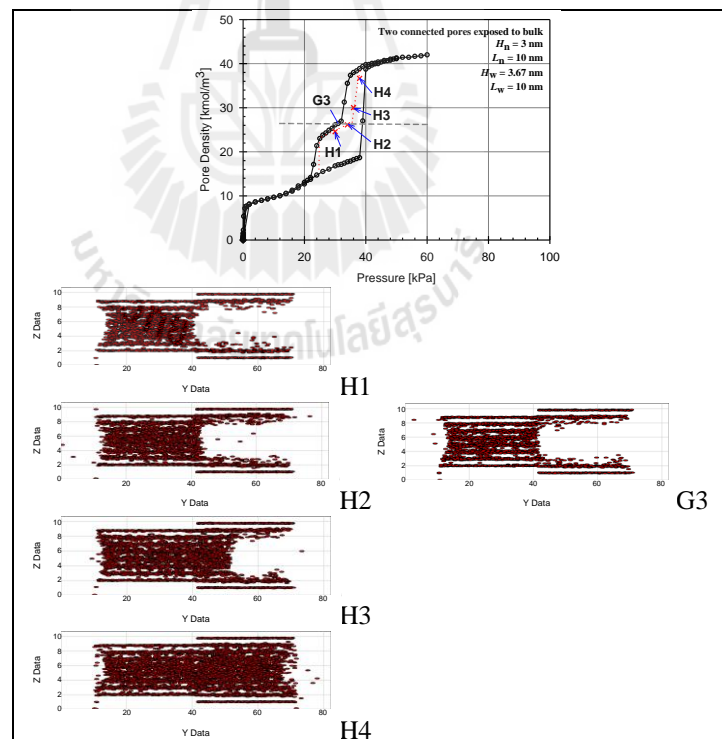


**Figure 6.10** Snapshot of argon at the equilibrium phase transition state output from the Mid-Density scheme at 87.3 K for the two connected pores exposed to bulk.

#### **6.5.4 Ink-Bottle Pore**

We next consider the case of an ink-bottle pore where a cavity is connected to the surroundings via a neck smaller in size. This ink-bottle pore is the classic example for the discussion of the phenomena of cavitation and pore blocking in the literature.

##### **6.5.4.1 Pore Blocking**

First we investigate the case where the desorption is controlled by pore blocking, we choose the neck size to be greater than a critical size, above which we have pore blocking while below which we have cavitation. This critical size is known to be a function of temperature and adsorbate (Cohan, 1944; Libby and Monson, 2004; Morishige and Ito, 2002; Morishige and Yasuki, 2010; Morishige and Yoshida, 2010; Rasmussen et al., 2012; Sarkisov and Monson, 2001). This is shown in Figure 6.11 (top graph) with an ink-bottle pore whose cavity size is 4.34 nm and neck size is 3 nm. The lengths of the cavity and the neck are 10 nm.

The adsorption branch of the isotherm shows two steps, the first of which is the capillary condensation in the neck and the second step is associated with the growth of the adsorbed layer in the cavity followed by a condensation when the gas-like core is sufficiently small (this is known in the literature as the delay condensation). Upon decreasing pressure from a completely filled pore, we observe a gradual change in the density with a decrease of pressure, followed by a sharp evaporation. This desorption is facilitated with the presence of a meniscus starting at the mouth of the neck and its receding into the pore interior until all the liquid condensate has been removed. Further decrease in pressure would result in the removal of molecules from the adsorbed layer.

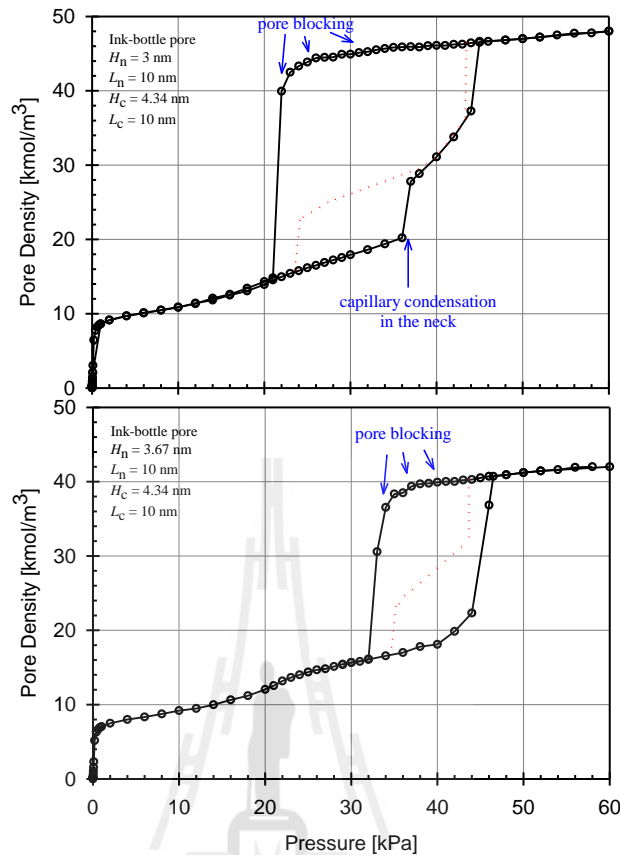


**Figure 6.11** Adsorption and desorption isotherms of argon in the ink-bottle pore at 87.3 K. The dotted line is the equilibrium phase transition in the pores.

When the neck size is increased from 3 nm to 3.67 nm (the cavity size remains the same at 4.34 nm), the two-stage condensation observed earlier when the sizes of the cavity and the neck are different becomes an one-stage condensation (bottom graph of Figure 6.11) because the sizes of the neck and the cavity are very close to each other. The mechanism of this pore is very similar to that for the case of the closed end pore discussed in Section 6.5.2, that is after some layers have been built up on the pore walls adsorption proceeds via the movement of a meniscus from the closed end towards the pore mouth. Upon desorption from a completely filled pore, the process is reverse to adsorption, but it is delayed because

of the metastability of the liquid condensate. We support this case with the snapshots in Figure 6.12.

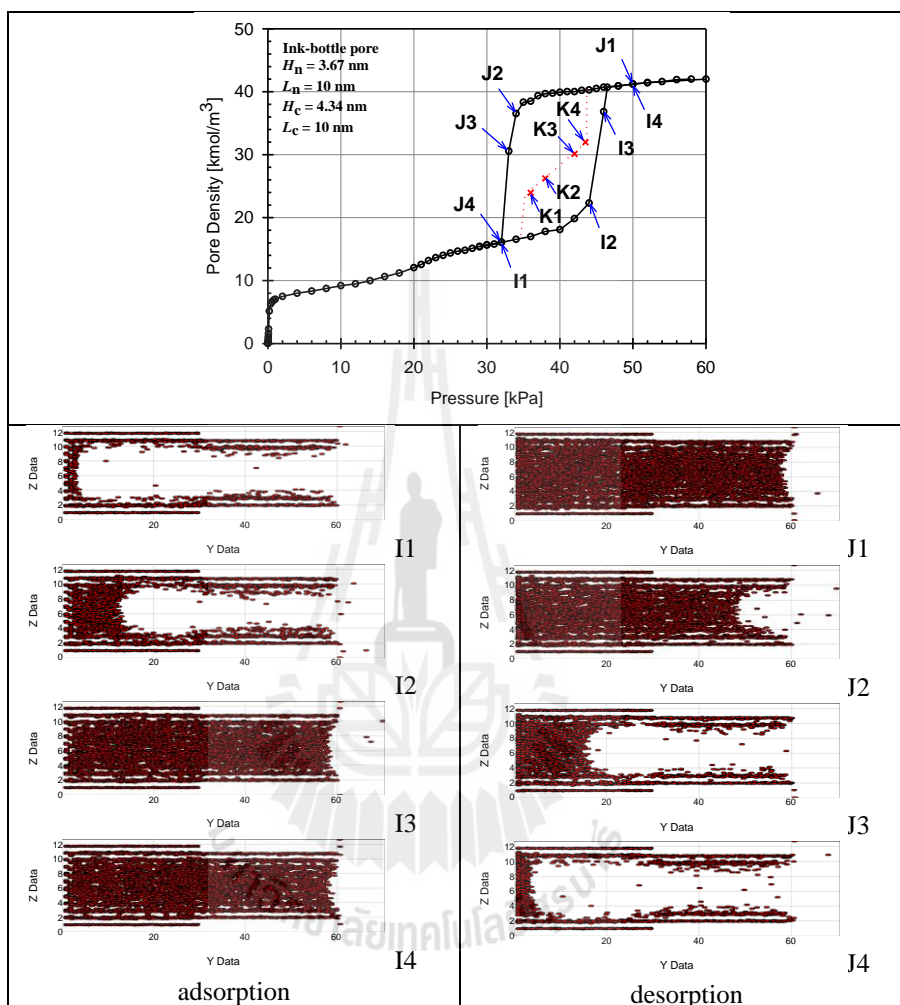


**Figure 6.12** Snapshot of argon along the adsorption and desorption branches output from the *Bin*-GCMC at 87.3 K for the ink-bottle pore corresponding to Figure 6.11 (bottom graph). Pore blocking is investigated.

### 6.5.4.2 Cavitation

When the neck is small enough (smaller than a critical size, which is a function of temperature and adsorbate) the evaporation proceeds via a



cavitation mechanism. For an ink-bottle pore with one neck with the sizes of the cavity and the neck being 4.34 nm and 2.33 nm, respectively and the lengths of the cavity and the neck are 10 nm each, the adsorption isotherm is shown in the top panel of Figure 6.13. Two distinct hysteresis loops are detected, associated with the neck and the cavity. Adsorption occurs with initial molecular layering on the pore walls, followed by the condensation of the neck (resulted in the first jump in the adsorption branch), and once the neck has been completely filled the process is proceeded with further build up of mass via the movement of the two menisci in the cavity; one is from the closed end and the other is from the junction between the filled neck and the cavity. Once the gas-like core of the cavity is small enough, condensation in the cavity occurs, resulting in the second jump in the adsorption branch. Once the pore has been completely filled, desorption occurs on the reduction in pressure. We see desorption occurs in two stages, the first of which is due to the cavitation in the cavity, resulted from the stretching of the fluid beyond its stability limit, while the second stage is due to the receding of the two menisci in the neck. Since the cavitation pressure of the cavity is greater than the evaporation pressure of the neck, the desorption branch exhibits a two-stage behaviour.

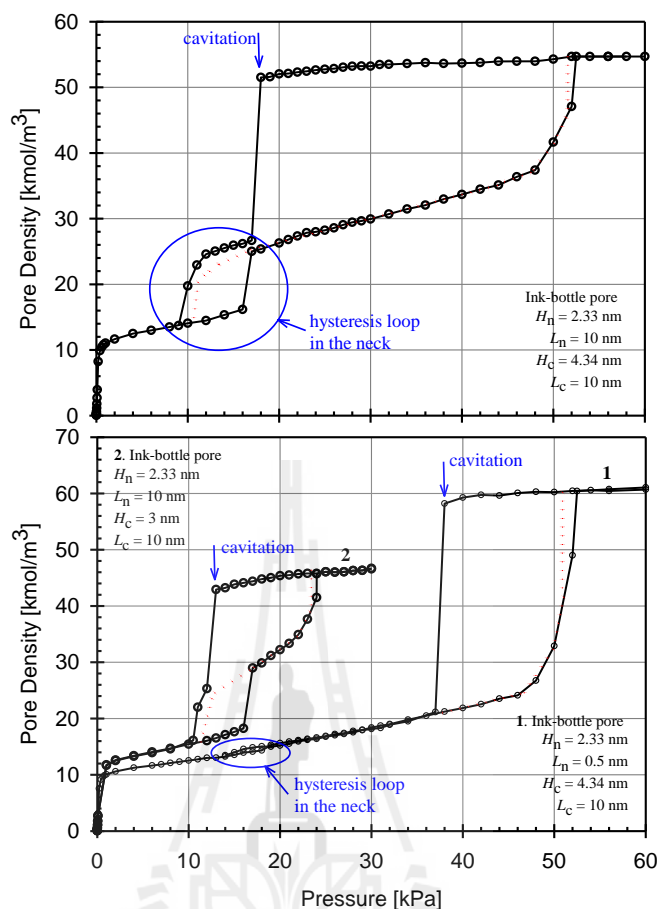


**Figure 6.13** Adsorption and desorption isotherms of argon in the ink-bottle pore at 87.3 K. The dotted line along the cross symbol indicates the equilibrium phase transition in the pores. The square symbol indicates the desorption scanning curve. The cross symbol indicates the output from the Mid-Density scheme (*Bin-CMC+Bin-GCMC*). The equilibrium transition in pores having cavitation.

In Figure 6.14 we show snapshots of adsorption and desorption cycles, where cavitation of the fluid in the cavity can be seen. One feature that should be noted is the size of the bubble just after the cavitation and the size of the gas-like core just before the condensation in the cavity. The former is much

greater and this is due to the metastability of the liquid condensate in the cavity before the cavitation.

The effects of the neck length on the desorption behaviour where cavitation is the mechanism evaporation can be studied in the bottom graphs of Figure 6.13. The neck length is reduced to 0.5 nm, which is a very short neck, compared to the long neck of 10 nm in the top graph of Figure 6.13, and the other dimensions are kept the same. Because the neck is so short, its capacity is negligible and the hysteresis associated with the neck is also almost invisible. The adsorption branch associated with the cavity is the same as before because the cavity dimensions are the same as those used in the top graph of Figure 6.13. Once the pore has been filled completely, the desorption starts when pressure is decreased. The desorption branch before the evaporation changes only slightly because of the stretching of the fluid, and once the evaporation occurs, we have a cavitation in the cavity as shown by snapshots in Figure 6.15 (points R1 and R2) and the cavitation pressure is much greater than the cavitation pressure observed with the case where the neck length is long. This interesting feature shows that the common belief that the cavitation is a fluid property is not correct, but rather it can depend on the length of the neck, as we just showed, and also on the size of the cavity. We shall show the latter now.

Let us consider the pore with the neck size and cavity size of 2.33 nm and 3 nm, respectively. The lengths of these sections are 10 nm each. The isotherm is shown as the plot 2 in the bottom graph of Figure 6.13. In this case, the sizes of the neck and the cavity are not very different. Adsorption follows a two-stage behaviour, the first of which is due to the condensation of the neck and the other is

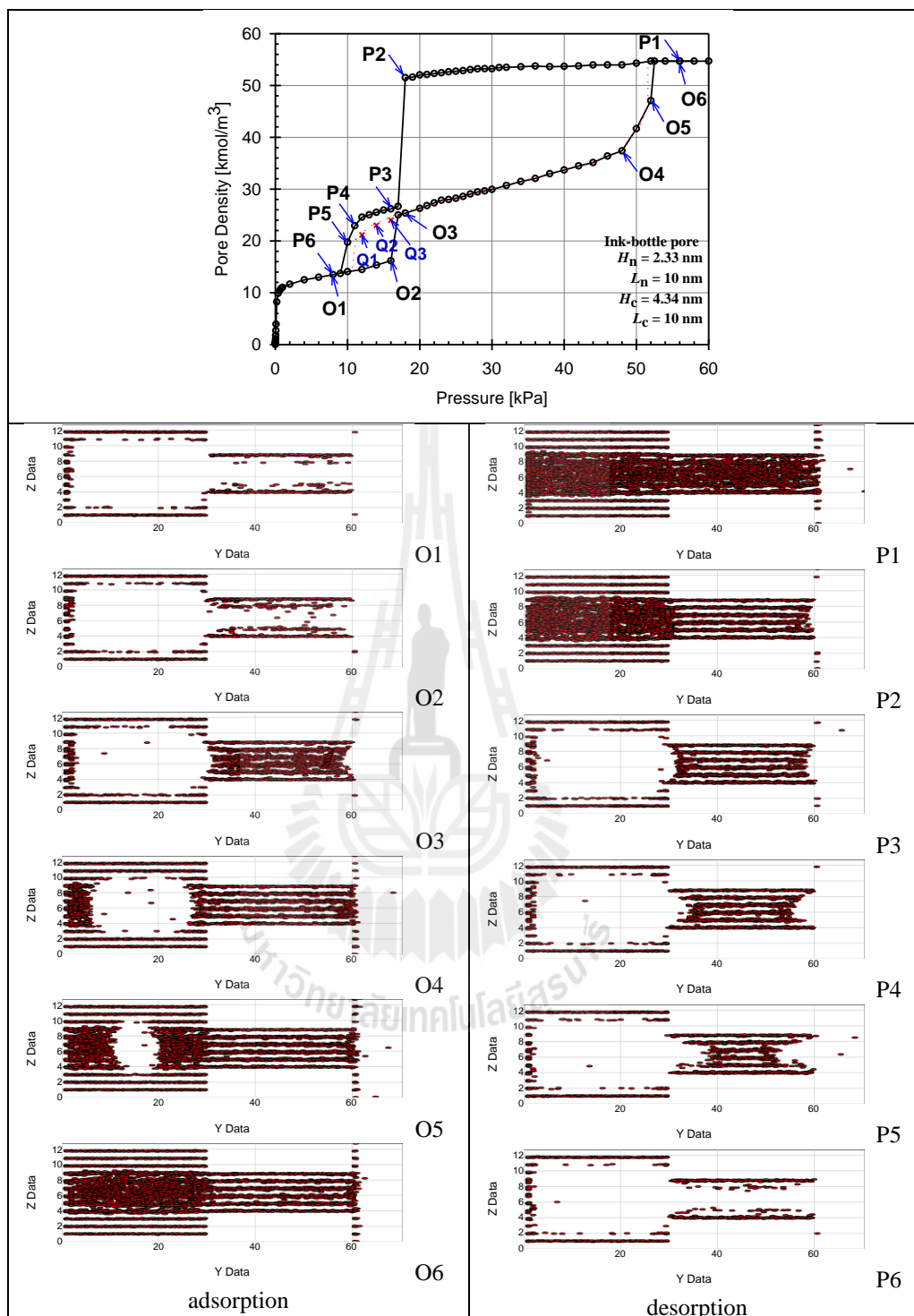


**Figure 6.14** Snapshot of argon along the adsorption and desorption branches output from the *Bin*-GCMC at 87.3 K for the ink-bottle pore corresponding to top graph of Figure 6.12. Cavitation is investigated.

associated with the cavity. Once the pore has been filled, the desorption occurs in a single stage with a small shoulder. This is due to the cavitation of the fluid in the cavity, followed almost immediately with the evaporation of the neck as shown by snapshots in Figure 6.15 (points S1 and S2) because the sizes of the neck and cavity are not too different. Like the case of very short neck, we see that the cavitation pressure is lower than that for the case when the size of cavity is large. Thus, we have shown two cases to show that the cavitation pressure is not just only the property of the fluid, but also on the dimensions of the neck and the cavity as well.

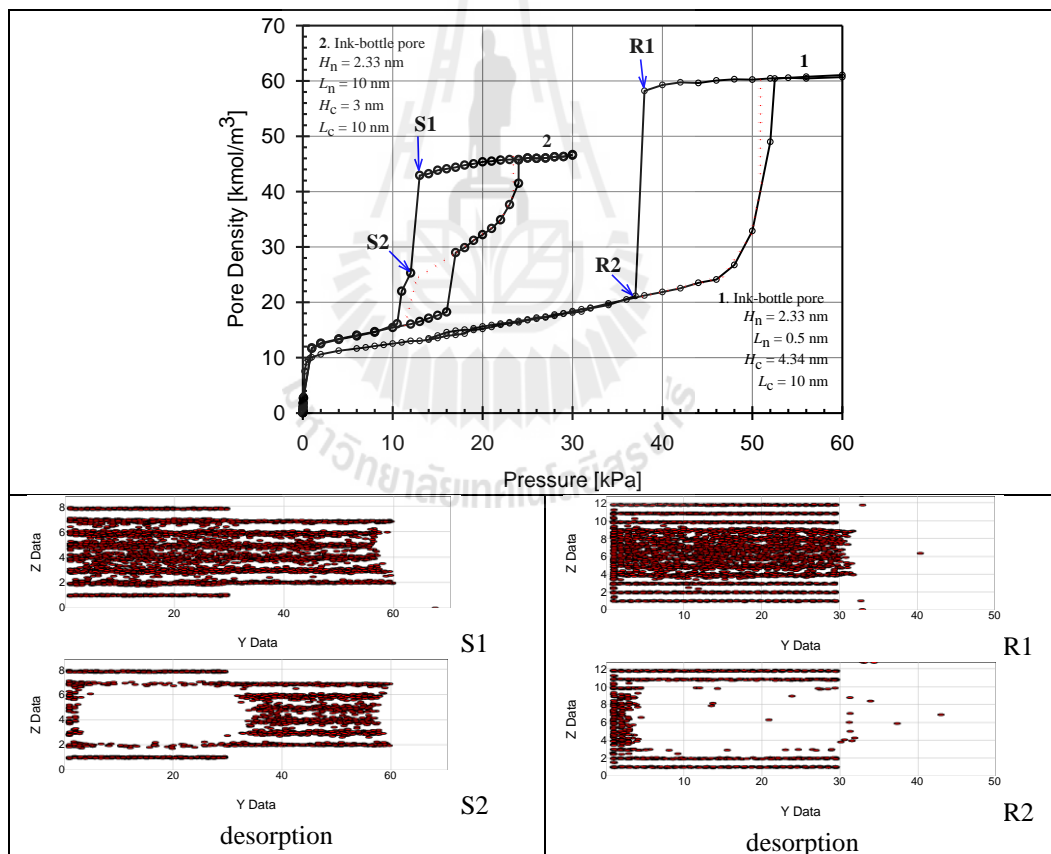


**Figure 6.15** Snapshot of argon along the desorption branches output from the *Bin*-GCMC at 87.3 K for the ink-bottle pore corresponding to bottom graph of Figure 6.13. Cavitation is investigated.

### 6.5.4.3 Equilibrium Transition

With the Mid-Density scheme we determined the equilibrium transition in the ink-bottle pore where the pore blocking is the mechanism for desorption. This transition is shown as dotted line in Figure 6.11. It is seen that the equilibrium transition associated with the neck is similar to an independent pore having the same size as the neck and opened at both ends, that is it is close to the desorption branch. On the other hand, the equilibrium transition associated with the cavity is essentially very close to the adsorption branch, which is similar to a single pore with closed end discussed in Section 6.5.2.

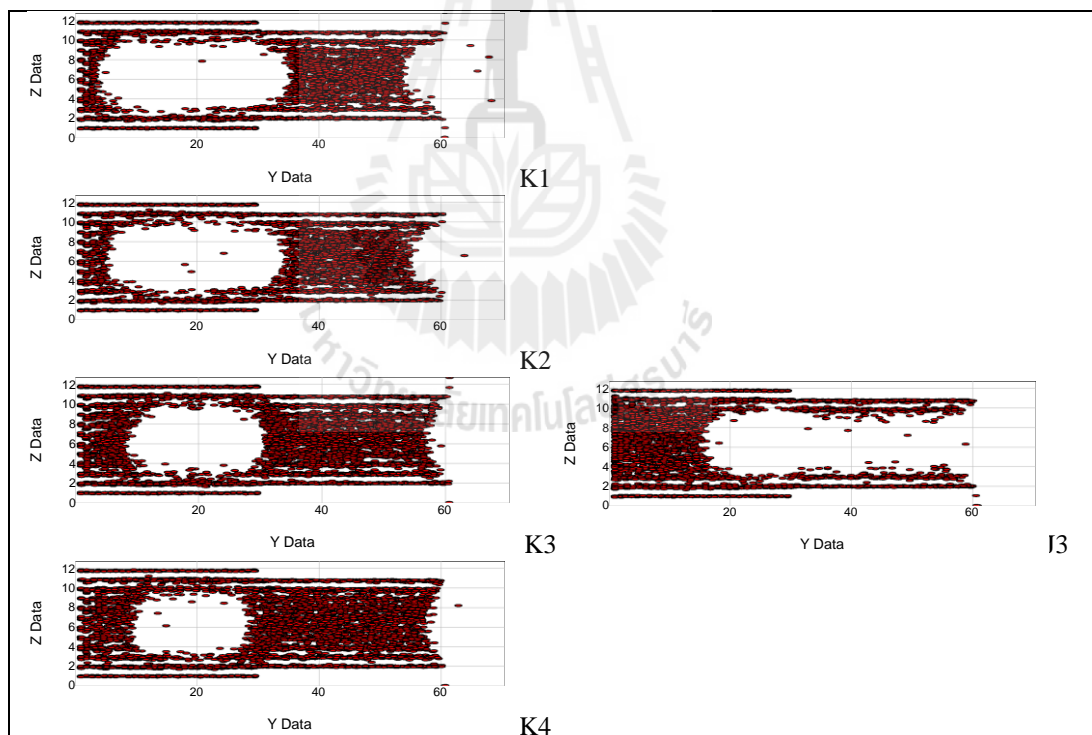


**Figure 6.16** Snapshot of argon at the equilibrium phase transition state (point K1-K4 in Figure 6.12) output from the Mid-Density scheme at 87.3 K for the ink-bottle pore.

Let us now explore the snapshots of the stable equilibrium transition, shown in Figure 6.16. The snapshots of the metastable states of adsorption and desorption branches have been shown in Figure 6.12, where we see the movement of the meniscus towards the pore mouth for adsorption branch and the receding towards the closed end for desorption. On the other hand, the equilibrium transition shows the appearance of a bubble in the cavity to form three menisci; one at the closed end and two in the neck. Thus the system is stable when we have a bubble in the cavity and the neck is relatively full. The penalty for the presence of additional interfaces (of the bubble) comes from the lower energy of the dense fluid in the neck. Upon further reduction in pressure we see the movement of the last two menisci into the interior of the neck, as is the case for an independent pore with two open ends. The stability of bubble, stabilized by the full neck, is also seen with the connecting equilibrium transition between the two equilibrium transitions associated with the neck and the cavity, as seen in the snapshots of Figure 6.17.

The equilibrium transitions in the pore where cavitation is the evaporation mechanism are indicated as dotted line in Figure 6.13, and the snapshots of the equilibrium transition are shown in Figure 6.18. It is interesting to see that the equilibrium transition in the pore having cavitation is similar to the pore for which pore blocking is the mechanism for desorption, suggesting that equilibrium is achieved when a bubble is formed so that molecules could be relocated in the region where the solid-fluid interactions and fluid-fluid interactions are greater, which they provide the stabilization force for maintaining the interfaces of the bubble.

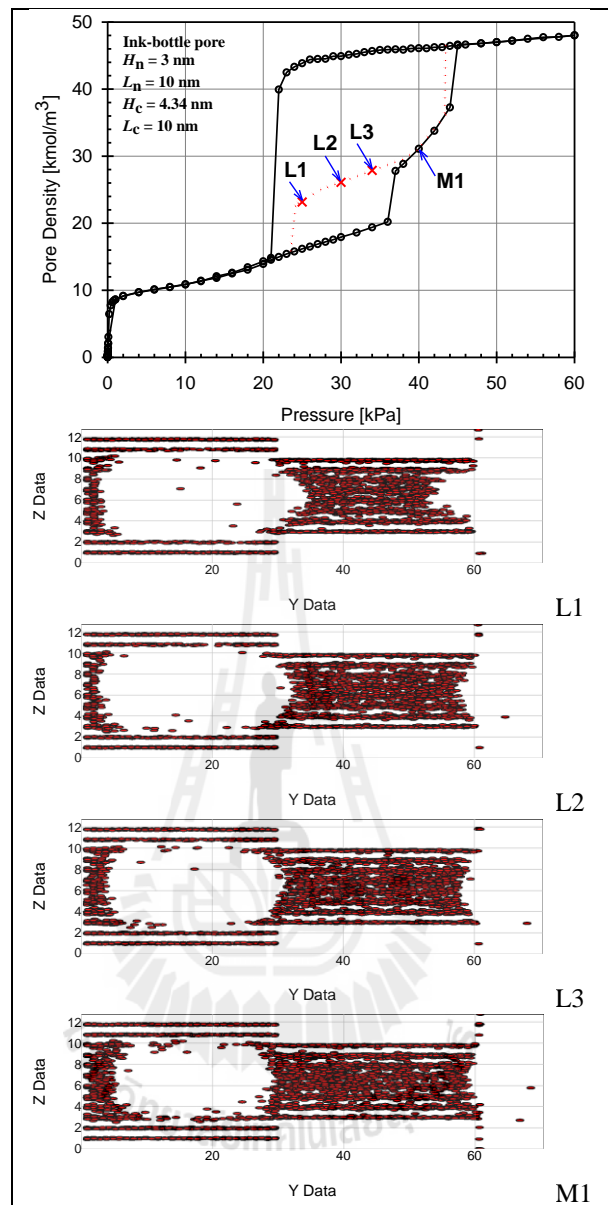


**Figure 6.17** Snapshot of argon at the equilibrium phase transition state output from the Mid-Density scheme at 87.3 K for the ink-bottle pore corresponding to top graph of Figure 6.11.



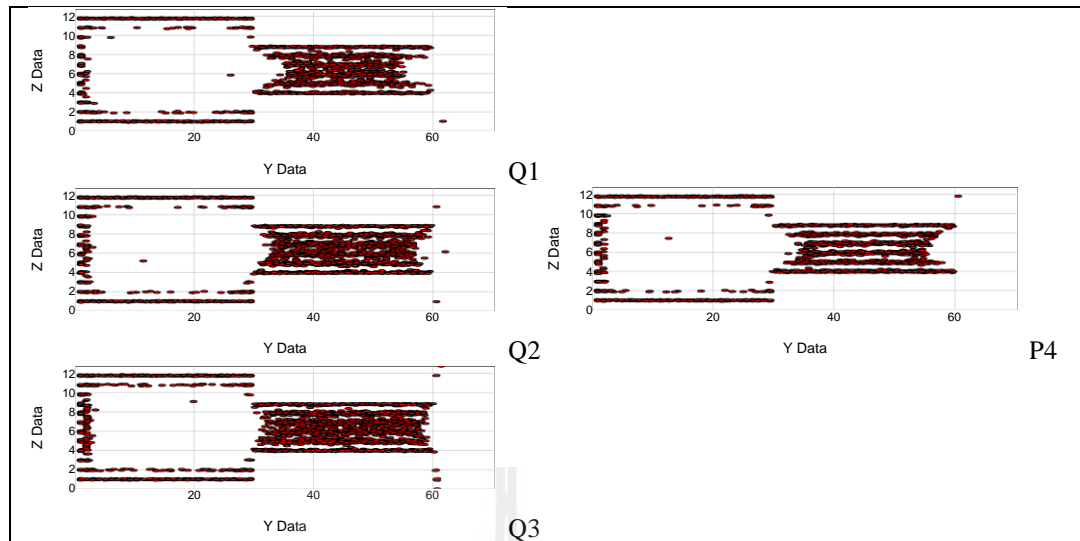


**Figure 6.18** Snapshot of argon at the equilibrium phase transition state (point Q1-Q3 in Figure 6.14) output from the Mid-Density scheme at 87.3 K for the ink-bottle pore.

## 6.6 Conclusions

We have investigated the pore blocking and the cavitation mechanisms in desorption from ink-bottle pores using the *Bin*-GCMC. These mechanisms are dictated by the size of the neck, and are somewhat insensitive to the neck length. When the neck size is smaller than some critical value, cavitation is the dominant mechanism; otherwise pore blocking is the mechanism for evaporation. A feature to distinguish these mechanisms is the manner in which the desorption branch behaves prior to complete evaporation. When cavitation is the controlling mechanism in evaporation, the desorption branch only decreases gradually before a sharp evaporation, while it decreases more when pore blocking is the controlling mechanism and it exhibits a knee shape prior to evaporation.

The equilibrium transition in various ink-bottle pores is determined using the Mid-Density scheme, and we found that it has three stages: the first stage is associated with the neck and is close to the desorption branch, the last stage is associated with the cavity and is very close to the adsorption branch, and the second stage joining the other two stages and it falls between the adsorption and desorption branches.

## 6.7 References

- Bojan, M.J. and Steele, W.A. (1988). Computer simulation of physisorption on a heterogeneous surface. **Surface Science**. 199: L395-L402.
- Bojan, M.J. and Steele, W.A. (1989). Computer-simulation of physisorbed Kr on a heterogeneous surface. **Langmuir**. 5: 625-633.
- Bojan, M.J. and Steele, W.A. (1993). Computer-simulation of physical adsorption on stepped surfaces. **Langmuir**, 9: 2569-2575.
- Cohan, L.H. (1944). Hysteresis and the capillary theory of adsorption of vapors. **Journal of the American Chemical Society**. 66: 98-105.
- Fan, C.Y., Do, D.D. and Nicholson, D. (2011a). New Monte Carlo simulation of adsorption of gases on surfaces and in pores: A concept of multibins. **Journal of Physical Chemistry B**. 115: 10509-10517.
- Fan, C.Y., Do, D.D. and Nicholson, D. (2011b). On the cavitation and pore blocking in slit-shaped ink-bottle pores. **Langmuir**. 27: 3511-3526.
- Grant, S.M. and Jaroniec, M. (2012). Effect of cosolvent organic molecules on the adsorption and structural properties of soft-templated ordered mesoporous alumina. **Journal of Colloid and Interface Science**. 367: 129-134.

- Grosman, A. and Ortega, C. (2008). Capillary condensation in porous materials. hysteresis and interaction mechanism without pore blocking/percolation process. **Langmuir**. 24: 3977-3986.
- Grosman, A. and Ortega, C. (2011). Cavitation in metastable fluids confined to linear mesopores. **Langmuir**. 27: 2364-2374.
- Horikawa, T., Hayashi, J. and Muroyama, K. (2004). Controllability of pore characteristics of resorcinol-formaldehyde carbon aerogel. **Carbon**. 42: 1625-1633.
- Jorge, M. and Seaton, N.A. (2002). Molecular simulation of phase coexistence in adsorption in porous solids. **Molecular Physics**. 100: 3803-3815.
- Kierlik, E., Monson, P.A., Rosinberg, M.L. and Tarjus, G. (2002). Adsorption hysteresis and capillary condensation in disordered porous solids: A density functional study. **Journal of Physics: Condensed Matter**. 14: 9295-9315.
- Klomkliang, N., Do, D.D. and Nicholson, D. (2012). Affinity and packing of benzene, Toluene, and p-xylene adsorption on a graphitic surface and in Pores. **Industrial & Engineering Chemistry Research**. 51: 5320-5329.
- Kruk, M. and Jaroniec, M. (2003). Argon adsorption at 77 K as a useful tool for the elucidation of pore connectivity in ordered materials with large cage-like mesopores. **Chemistry of Materials**. 15: 2942-2949.
- Libby, B. and Monson, P.A. (2004). Adsorption/desorption hysteresis in ink-bottle pores: A density functional theory and Monte Carlo simulation study. **Langmuir**. 20: 4289-4294.

- Liu, J., Zhang, L., Yang, Q. and Li, C. (2008). Structural control of mesoporous silicas with large nanopores in a mild buffer solution. **Microporous and Mesoporous Materials**. 116: 330-338.
- Liu, Z.J., Do, D.D. and Nicholson, D. (2012). A thermodynamic study of the Mid-Density scheme to determine the equilibrium phase transition in cylindrical pores. **Molecular Simulation**. 38: 189-199.
- Liu, Z.J., Herrera, L., Nguyen, V.T., Do, D.D. and Nicholson, D. (2011). A Monte Carlo scheme based on Mid-Density in a hysteresis loop to determine equilibrium phase transition. **Molecular Simulation**. 37: 932-939.
- Lu, A.-H. and Schüth, F. (2005). Nanocasting pathways to create ordered mesoporous solids. **Comptes Rendus Chimie**. 8: 609-620.
- Lu, A.H. and Schüth, F. (2006). Nanocasting: A versatile strategy for creating nanostructured porous materials. **Advanced Materials**. 18: 1793-1805.
- Morishige, K. (2008). Adsorption hysteresis in ordered mesoporous silicas. **Adsorption**. 14: 157-163.
- Morishige, K. and Ito, M. (2002). Capillary condensation of nitrogen in MCM-41 and SBA-15. **Journal of Chemical Physics**. 117: 8036-8041.
- Morishige, K., Tateishi, M., Hirose, F. and Aramaki, K. (2006). Change in desorption mechanism from pore blocking to cavitation with temperature for nitrogen in ordered silica with cagelike pores. **Langmuir**. 22: 9220-9224.
- Morishige, K. and Tateishi, N. (2003). Adsorption hysteresis in ink-bottle pore. **Journal of Chemical Physics**. 119: 2301-2306.

- Morishige, K., Tateishi, N. and Fukuma, S. (2003). Capillary condensation of nitrogen in MCM-48 and SBA-16. **The Journal of Physical Chemistry B.** 107: 5177-5181.
- Morishige, K. and Yasuki, T. (2010). Large-pore cagelike silica with necks of molecular dimensions. **The Journal of Physical Chemistry C.** 114: 10910-10916.
- Morishige, K. and Yoshida, K. (2010). Neck size of ordered cage-type mesoporous silica FDU-12 and origin of gradual desorption. **The Journal of Physical Chemistry C.** 114: 7095-7101.
- Neimark, A.V., Ravikovitch, P.I. and Vishnyakov, A. (2003). Bridging scales from molecular simulations to classical thermodynamics: Density functional theory of capillary condensation in nanopores. **Journal of Physics: Condensed Matter.** 15: 347-365.
- Neimark, A.V. and Vishnyakov, A. (2000). Gauge cell method for simulation studies of phase transitions in confined systems. **Physical Review E.** 62: 4611-4622.
- Nguyen, P.T.M., Do, D.D. and Nicholson, D. (2011). On the cavitation and pore blocking in cylindrical pores with simple connectivity. **Journal of Physical Chemistry B.** 115: 12160-12172.
- Norman, G.E. and Filinov, V.S. (1969). Investigations of phase transitions by a Monte-Carlo method. **High Temperature,** 7: 216-&.
- Peterson, B.K. and Gubbins, K.E. (1987). Phase-transitions in a cylindrical pore: Grand canonical Monte-Carlo, mean field-theory and the Kelvin equation. **Molecular Physics,** 62: 215-226.

- Peterson, B.K., Gubbins, K.E., Heffelfinger, G.S., Marconi, U.M.B. and Vanswol, F. (1988). Lennard-Jones fluids in cylindrical pores: Nonlocal theory and computer-simulation. **Journal of Chemical Physics**. 88: 6487-6500.
- Puibasset, J. (2010). Counting metastable states within the adsorption/desorption hysteresis loop: A molecular simulation study of confinement in heterogeneous pores. **Journal of Chemical Physics**. 133: 104701-104714.
- Rasmussen, C.J., Gor, G.Y. and Neimark, A.V. (2012). Monte Carlo simulation of cavitation in pores with nonwetting defects. **Langmuir**. 28: 4702-4711.
- Rasmussen, C.J., Vishnyakov, A., Thommes, M., Smarsly, B.M., Kleitz, F. and Neimark, A.V. (2010). Cavitation in metastable liquid nitrogen confined to nanoscale pores. **Langmuir**. 26: 10147-10157.
- Ravikovitch, P.I. and Neimark, A.V. (2002). Experimental confirmation of different mechanisms of evaporation from ink-bottle type pores: Equilibrium, pore blocking, and cavitation. **Langmuir**. 18: 9830-9837.
- Reichenbach, C., Kalies, G., Enke, D. and Klank, D. (2011). Cavitation and pore blocking in nanoporous glasses. **Langmuir**. 27: 10699-10704.
- Rigby, S.P. and Fletcher, R.S. (2004). Experimental evidence for pore blocking as the mechanism for nitrogen sorption hysteresis in a mesoporous material. **The Journal of Physical Chemistry B**. 108: 4690-4695.
- Rowley, L.A., Nicholson, D. and Parsonage, N.G. (1975). Monte-Carlo grand canonical ensemble calculation in a gas-liquid transition region for 12-6 argon. **Journal of Computational Physics**. 17: 401-414.

- Sahu, D.R., Hong, L.Y., Wang, S.-C. and Huang, J.-L. (2009). Synthesis, analysis and characterization of ordered mesoporous TiO<sub>2</sub>/SBA-15 matrix: Effect of calcination temperature. **Microporous and Mesoporous Materials**. 117: 640-649.
- Sarkisov, L. and Monson, P.A. (2001). Modeling of adsorption and desorption in pores of simple geometry using molecular dynamics. **Langmuir**. 17: 7600-7604.
- Steele, W.A. (1973). Physical interaction of gases with crystalline solids. 1. Gas-solid energies and properties of isolated adsorbed atoms. **Surface Science**. 36: 317-352.
- Vishnyakov, A. and Neimark, A.V. (2001). Studies of liquid-vapor equilibria, criticality, and spinodal transitions in nanopores by the gauge cell Monte Carlo simulation method. **Journal of Physical Chemistry B**. 105: 7009-7020.
- Vishnyakov, A. and Neimark, A.V. (2003a). Monte Carlo simulation test of pore blocking effects. **Langmuir**. 19: 3240-3247.
- Vishnyakov, A. and Neimark, A.V. (2003b). Nucleation of liquid bridges and bubbles in nanoscale capillaries. **Journal of Chemical Physics**. 119: 9755-9764.

# CHAPTER VII

## ADSORPTION OF WATER IN ACTIVATED CARBON AND BOTTLE PORE MODEL

### 7.1 Abstract

Water adsorption in a coconut shell-based activated carbon prepared in our laboratory was measured at temperature range 278-303 K using an Intelligent Gravimetric Analyser. The simulation results were obtained using a grand canonical Monte Carlo (GCMC) method, and the TIP4P/2005 water potential model is used in this study. We have found that the isotherm as a function of relative pressure shows an unusual behavior at temperatures lower than 293 and 278 K for experimental and simulation studies, respectively. If the temperature is greater than that point, the water uptake in activated carbon increase by decreasing temperature as expected because of energy of motion. In contrast, when temperatures decrease lower than that temperature, the adsorption decreases with a decrease in temperature, which is in opposite to what thermodynamics suggests. This unusual behavior is explained qualitatively by using GCMC simulation, suggesting that water adsorption in carbon could be affected strongly by the metastable state and the slow kinetics of cluster formation at low temperatures. The simulation of water adsorption in an ink bottle pore model is investigating and it is found that the pore blockage is observed while the pore blockage cannot be found in the case of non-polar fluid of argon.



## 7.2 Introduction

Activated carbon can be manufactured from a wide variety of raw materials. The predominant qualification is that the raw material should have a high percentage of carbon content. Commonly used raw materials are coal, wood, peat, coconut shell, and petroleum coke, etc. The process of converting the raw material into the finished adsorbent may be divided into chemical and thermal process. Furthermore, the end product may be granular, palletized or powder.

It is known that the adsorption behavior of activated carbons cannot be determined by their specific surface area or pore size distribution alone. The porous structure of the carbon determines its adsorption capacity, while its surface functional groups affect its interaction with polar and non-polar adsorbates. The existence of surface functional groups on carbons, such as carboxyl, phenol, lactone, and acid anhydride, has been postulated as constituting the source of surface acidity. Morimoto and Miura (Miura and Morimoto, 1986; Miura and Morimoto, 1988; Miura and Morimoto, 1991; Miura and Morimoto, 1994; Morimoto and Miura, 1985; Morimoto and Miura, 1986) had prepared surface oxide of graphite surface using heat treatment and found that lactone and carboxyl groups were not detected while phenol and carbonyl groups can be detected at heat treatment higher than 973 K. The oxide surface of graphite was used to measure water vapor adsorption at 283, 291 and 298 K. The uptake as a function of pressure at low temperatures was higher than that at high temperatures.

### 7.3 Literature Review

Water adsorption isotherm in an activated carbon at different temperatures was mostly presented in the range of 293 to 303 K (Harding et al., 1998; Liu and Monson, 2006; Ohba et al., 2004a; Ohba et al., 2004b; Salame and Bandosz, 1998), and it was found that the water vapor uptake at low temperatures was higher than that at high temperatures (either plotted water uptake versus pressure or relative pressure). This is due to the energy motion of molecules in the pore. The adsorption isotherm of water at temperatures less than room temperature was presented by Salame and Bandosz (Salame and Bandosz, 1998). The water uptake was plotted as a function of pressure and found that the uptake was ordered as  $283 > 288 > 293$  K. When the data from Salame and Bandosz (Salame and Bandosz, 1998) are plotted as the uptake as a function of relative pressure and have found that the uptake at 288 K is still higher than that of at 293 K while the uptake at 283 K is slightly lower than that of 293 K. However, Kim and co-workers (Kim et al., 2009) measured water vapor adsorption in single-wall carbon nanotubes including activated carbons at temperature range of 278-308 K, and they found that the water uptake at different temperatures was ordered as  $278 < 293 < 308$  K (plotted as water uptake versus relative pressure) which is different from what Salame and Bandosz found. This is due to the strong interaction of water-water and the weak interaction of water-adsorbent which accounted for this unusual behavior and the amount of surface functional groups is also affected (Müller and Gubbins, 1998; Müller et al., 1996). The unusual temperature dependence of water adsorbed into hydrophilic porous solid is difficult to explain experimentally. Therefore the investigation of the unusual behavior of water adsorption at low temperatures with other methods is still a challenging issue for scientists and

engineers. Molecular simulation has been used to investigate adsorbate adsorption especially Monte Carlo (MC) simulation. This is due to the fact that MC allows us to probe the microscopic picture and fluid-fluid or fluid-solid interactions. The adsorption is controlled by a number of parameters such as fluid-fluid interaction, relative contribution from dispersion interaction and hydrogen bonding, fluid-solid interaction hydrophilic or hydrophobic nature of the surface, pore geometries, and operating conditions including temperature and pressure. The adsorption of water in graphite pores does not take place at low pressures due to the loss of water-water hydrogen bonds when adsorbed on the surface from the bulk fluid; the adsorption occurs at higher pressures by capillary condensation (Müller et al., 1996; Striolo et al., 2005; Wongkoblaph and Do, 2007). The adsorption of water in heterogeneity graphite pores by introducing polar groups on to the surface shows different behavior (Jorge et al., 2002; McCallum et al., 1998; Müller et al., 1996; Wongkoblaph and Do, 2007). The loss of water-water hydrogen bonds in graphitic pores is compensated by the ability of water molecules to form hydrogen bonds with the surface sites in activated carbon pores.

In this work, we prepare coconut shell-based activate carbon in a fixed bed reactor by using heat treatment. The adsorption of water vapor into the activated carbon is measured at temperature range from 278 to 303 K. The behavior of water adsorption at different temperatures is described qualitatively by molecular simulation. Furthermore, water adsorption in a bottle pore model is investigated by using GCMC simulation.

## 7.4 Simulation

The model of slit-pore with a structure-less surface coupled with introduced surface functional group is investigated. The interaction between this kind of solid model and adsorbate is calculated from the summation of the continuous surface and functional group on the surface by using Steele 10-4-3 equation and LJ 12-6 plus Coulombic force, respectively with the adsorbate. To describe theoretically and qualitatively water adsorption on activated carbon having some amount of functional groups on the surface, it is no matter what kind and how amount of the surface functional groups is. The only type of functional group considered in this study is phenol. This is modeled with a single LJ site at the oxygen a distance  $C_a-O$  perpendicular to the carbon surface, positive charges on the surface ( $C_a$ ) and hydrogen atom (H) and negative charge at the oxygen atom (O). A side projection of the functional group used in this study is presented in Figure 7.1a and the distance from the surface to the hydrogen charge is 0.17 nm. The parameters for phenol group have been taken from potential model for phenol molecule (Mooney et al., 1998) and are given in Table 7.1. The LJ interaction parameters between fluid molecules and functional group are calculated using Lrentz-Berthelot mixing rule. In this study nine functional groups are placed on the bottom surface and other nine are placed on the upper surface of the pore with opposite position. The angle of phenol group are fixed and allocated in the same direction. The simulations in this thesis used the configuration presented in Figure 7.1b. The periodic boundary conditions are applied in  $x$  and  $y$  directions.

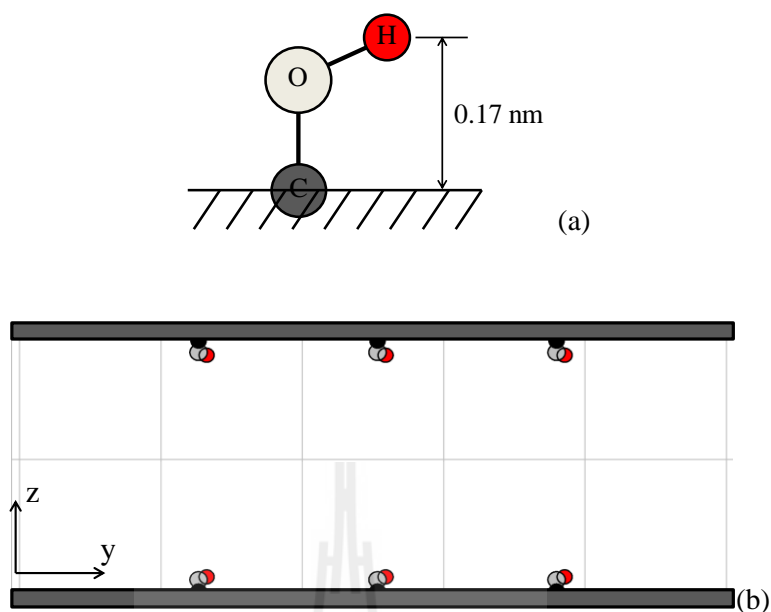


**Figure 7.1** (a) Side view of surface functional group of phenol used in simulation and (b) functional group configuration.

**Table 7.1** Potential model parameters of surface functional group

group	$\sigma$ (nm)	$\epsilon/k_B$ (K)	$q$ (e)
$C_a$	-	-	+0.20
O	0.307	78.2	-0.64
H	-	-	+0.44
$C_a$ -O	0.1364 nm		
O-H	0.096 nm		
$\angle C_aOH$	110.5°		

$C_a$  is carbon located in plane of graphene sheet

## 7.5 Experimental Work

### 7.5.1 Preparation of Activated Carbon

Activated carbons were prepared from dried coconut shell; one-step procedure was used to produce activated carbon as shown in Figure 7.2. Preparation

of coconut shell activated carbons was as follows. The pre-dried coconut shell was crushed and sieved to obtain a sample fraction with the average screen size of 0.841 to 0.594 mm (20×30 mesh) and then carbonized in a horizontal steel tube furnace at 873 K for 1 hour under a constant flow of nitrogen 100 ml/min. Next, the char was activated in the same tube furnace under a constant flow of carbon dioxide and nitrogen of 100 and 100 ml/min, respectively at 1,273 K for 1 hour. Then the system was cooled down to room temperature under nitrogen atmosphere.

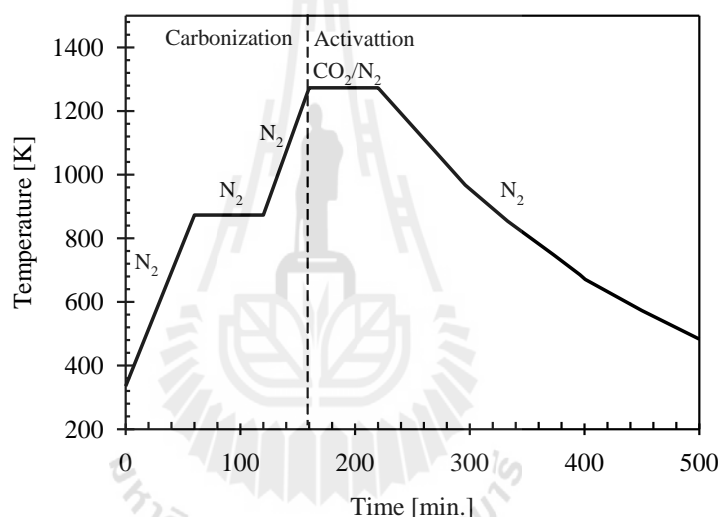


**Figure 7.2** Thermal histories during the preparation of activated carbon (one-step method)

## 7.5.2 Characterization of Activated Carbon

### 7.5.2.1 BET Surface Area and Pore Size Distribution

The sample was characterized for the structural porous properties by N<sub>2</sub> adsorption at 77 K using an automated adsorption apparatus (ASAP 2010 Micromeritics). In this experiment, 200 mg of sample was used; the system was degassed at 573 K under vacuum for 12 hours under nitrogen flow and then the

adsorption isotherm for nitrogen at 77 K was measured. The BET surface area ( $S_{\text{BET}}$ ) and the total pore volume were calculated from the nitrogen adsorption isotherms. Pore size distribution of carbon was also determined by the application of the density functional theory (DFT) to the isotherm data.

#### **7.5.2.2 Boehm Titration**

Procedures for the analysis of oxygen functional group follow those established by Boehm (Boehm, 1994). The activated carbon sample was first dried in an oven (378 K) for 24 hours. Then 100 ml of an alkali solution (0.1 N  $\text{NaHCO}_3$ ,  $\text{Na}_2\text{CO}_3$ , or  $\text{NaOH}$ ) and strong acid (0.1 N  $\text{HCl}$ ) were added to test tubes containing a given amount of the activated carbon sample (1 g). The samples were constantly mixed over a vibrator (140 rpm) at 298 K for 24 hours. A given amount of the supernatant (20 ml) was then drawn from the test tubes and back titrated with  $\text{HCl}$  (0.1 N) and  $\text{NaOH}$  (0.1 N) solutions. The concentrations of various functional groups were determined by the residual bases after back titration as described by Boehm (Boehm, 1994).

#### **7.5.3 Water Adsorption Measurement**

The apparatus used for both water vapor adsorption and sorption kinetics studies is an Intelligent Gravimetric Analyser (IGA) supplied by Hiden Analytical Ltd. The IGA instrument allows the adsorption and desorption isotherms and the corresponding kinetics of adsorption or desorption at each pressure step to be determined. The system consists of a fully computerized microbalance, which automatically measures the weight of carbon sample as a function of time, at a specified water vapor pressure and temperature under computer control. Prior to the measurements, the adsorbent is outgassed until a constant weight is achieved at a

pressure of  $10^{-6}$  mbar and the temperature of 423 K. About 100 mg of carbon sample will be loaded for each run. HPLC grade water is used as adsorbate, and dissolved gases are removed by repeated evacuation and vapor equilibration cycles of the liquid supply side of the vapor reservoir. The vapour pressure is gradually increased, over a period of 30 seconds, to prevent disruption of the microbalance, until the desired value is achieved. Pressure transducer, in the range 0-10 kPa (accurate to 0.02% of the full scale), is used to monitor the pressure of water vapour in the system. A pressure step is maintained constant during relaxation with the help of inlet/outlet control valves with high-resolution stepper motors. Pressure steps in the range of  $P/P_0$  values 0-0.95 are used to obtain the equilibrium isotherm. The weight change as a function of time is analyzed in real-time with a computer algorithm in order to predict the equilibrium. After the equilibrium is established, the vapor pressure is increased to the next set pressure value, and the subsequent uptake is measured until equilibrium is re-established. The increase in weight due to adsorbate uptake for each pressure step is used to calculate the kinetic parameters for adsorption. The errors in the fitted rate constants are typically smaller than 2% of the value. The sample temperature is constantly monitored throughout the duration of the experiment, and the variation is found to be  $\pm 0.05$  K.

## **7.6 Experimental Data and Simulation Results**

### **7.6.1 Porous Characterizations of Activated Carbon**

The adsorbed amount versus relative pressure ( $P/P_0$ ) for  $N_2$  adsorption at 77 K is presented in Figure 7.3, the adsorption isotherm shows type I isotherm showing that the adsorbent is dominated by microporous structure. The porous



properties of activated carbon are presented in Table 7.2. It is seen that the BET surface area is 1,120 m<sup>2</sup>/g of AC, the micropore volume is 0.50 cm<sup>3</sup>/g of AC, while the mesopore is 0.08 cm<sup>3</sup>/g of AC. The chemical properties are also listed in Table 7.2 by Boehm titration method. The total base and acid concentration on the carbon surface are of 1.14 and 0.30 mmol/g of AC, respectively. For total acid, carboxyl group is not detected, while phenol and lactonic groups can be detected and the amount of phenol is greater than that of lactonic groups. This is in a good agreement with experimental work of Morimoto and Miura (Miura and Morimoto, 1986; Miura and Morimoto, 1988; Miura and Morimoto, 1991; Miura and Morimoto, 1994; Morimoto and Miura, 1985; Morimoto and Miura, 1986) that lactone and carboxyl groups were not detected while phenol and carbonyl groups were detected at heat treatment higher than 973 K. In our work, the heat treatment is controlled at 1,273 K and lactonic group can be detected but the amount is relatively low (0.07 mmol/g of AC). Because the bond of C–C<sub>a</sub> of carboxyl group (C<sub>a</sub>–COOH) is weaker than the bond of O–C<sub>a</sub> of phenol (C<sub>a</sub>–OH) group, thus it can be destroyed at high temperatures (>1,273 K). When the graphene sheet is activated at high temperatures the hexagonal shape between carbon atoms is destroyed, thus it is difficult to form the lactonic group. The basic group is detected which is the bond kind of C<sub>a</sub>=O. This is due to the gases agent used are only N<sub>2</sub> and CO<sub>2</sub>.

**Table 7.2** Physical properties and Boehm titration results of activated carbon

physical properties			chemical properties				
$S_{\text{BET}}$	$V_{\text{mic}}$	$V_{\text{T}}$	total base	total acid	carboxyl	phenol	lactonic
(m <sup>2</sup> /g)	(cm <sup>3</sup> /g)	(cm <sup>3</sup> /g)	(mmol/g)	(mmol/g)	(mmol/g)	(mmol/g)	(mmol/g)
1,120	0.50	0.58	1.1379	0.3014	0	0.2314	0.0700

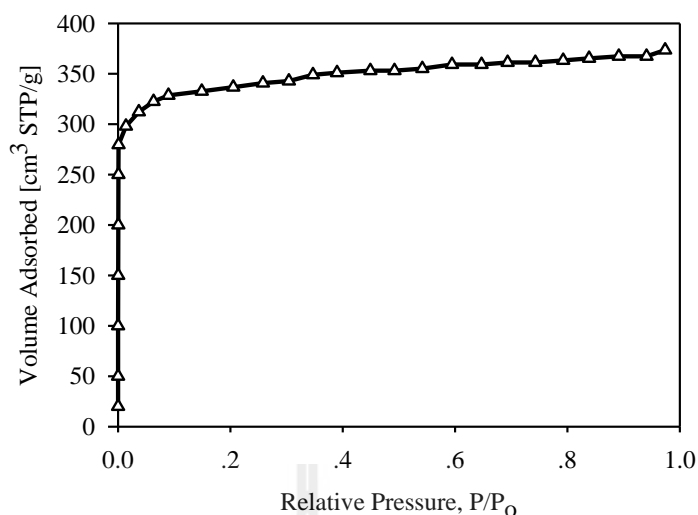


**Figure 7.3**  $\text{N}_2$  Adsorption isotherms at 77 K on the activated carbon.

### 7.6.2 Adsorption of Water in Activated Carbon

The experimental data for water vapor adsorption in the prepared activated carbon at different temperatures are presented in Figure 7.4. The experimental isotherms obtained for AC at 293 and 303 K show a gradual increase in slope at relative pressures ( $P/P_0$ ) lower than 0.3, after which the isotherm increases dramatically, and then it increases with a decreasing rate, which is the typical behavior observed in micropore sizes for activated carbons. The water uptake at 303 K is lower than that at 293 K which is normally observed for water adsorption in that the amount adsorbed decreases when the temperature is increased. This is due to that water adsorption is an exothermic system. However the interesting behavior is observed for water adsorption isotherm at 278 K which is closed to the melting point of water, the water uptake at this temperature increases gradually and is lower than those at higher temperatures that is opposite to that we have discussed above. This

unusual behavior will be described theoretically by using the GCMC simulation in the next section.

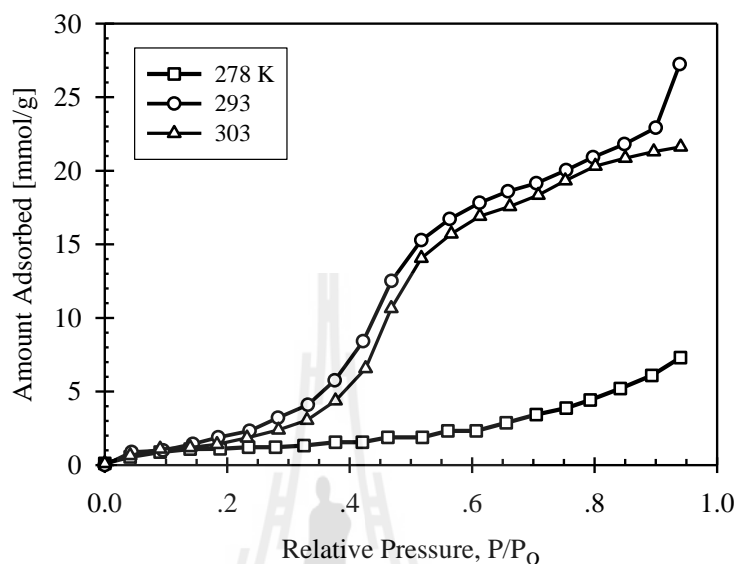


**Figure 7.4** Water vapor adsorption isotherms in the original and modified activated carbons at different temperatures obtained from IGA.

### 7.6.3 Simulation Results for Water Adsorption

The infinite slit pore model with functional groups located on its wall surfaces and the TIP4P/2005 are used in this study. As mentioned above the unusual temperature dependence of water is found in the range close to the melting point of water, we shall list its parameters in Table 7.3 to compare the parameter obtained by the potential model used in this work and experiment.

**Table 7.3** Melting points of water and the water potential model

model	melting point (K)	reference
Experiment	273.15	
TIP4P/2005	252.1	(Abascal and Vega, 2005)

We present in Figure 7.5 the adsorption of water in a slit-pore with phenol groups on the surface at different temperatures. The melting and boiling points of TIP4P/2005 water model is 252.2 and 401 K, respectively (Abascal and Vega, 2005), therefore the temperature used in this study is varied from 253 to 293 K. We see that if temperatures are greater than 278 K, the water uptake decreases by increasing temperatures which is consistent with experimental work when temperature is greater than 293 K. Like the experimental work, the unusual temperature dependence for water adsorption is observed when simulation temperatures are less than 278 K where the pore density decreases with temperatures and the insignificant adsorbed amount occurred at the melting point of the model. In the range of temperatures lower than 278 K, the isosteric heat of water adsorption at low loading at lower temperature (T253K) is greater than that at higher temperature (T273K) which is similar to those observed for physical adsorption. This is due to the contribution of fluid-solid interaction as one can see from Figure 7.6, the fluid-solid interaction at 253 K (FS253K) is greater than that at 273 K (FS273K). However, when the relative pressures increase, the total isosteric heat at both temperatures becomes close to the heat of liquefaction. The fluid-solid interaction contributed to isosteric heat is greater than the contribution of fluid-fluid interaction, because at low adsorption loading, water molecules initially adsorbed at the functional groups and this leads to the greater fluid-solid interaction, after that the opposite is true. While the FS253K is still greater than the FS273, but heat of adsorption at both temperatures are close to each other. Therefore water molecules adapt themselves to have the adsorbed heat close to the heat of liquefaction by decreasing the fluid-fluid interaction. The low interaction of fluid-fluid causes the low capacity adsorbed at temperatures lower than

278 K. At temperatures greater than 278 K, water molecules are nucleated around the functional groups, and the water clusters grow in all directions but predominantly in the direction perpendicular to the pore wall. However, at 253 K, water cluster grows across the pore forming a bridge which prevents water molecules entering the pore interior.

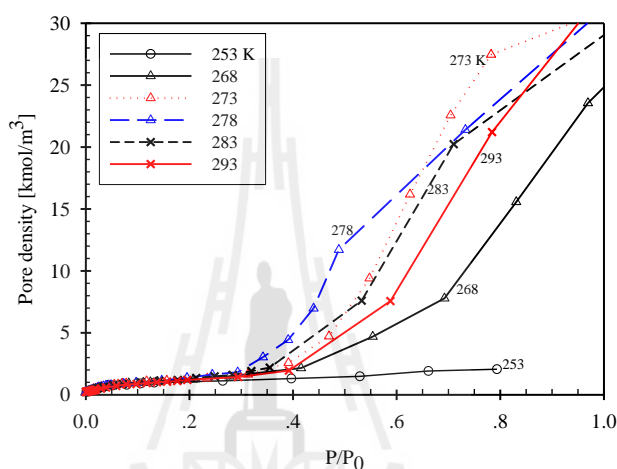


**Figure 7.5** Adsorption isotherms of water at different temperatures in slit-pore of 3 nm width with hydrophilic surface obtained from GCMC.

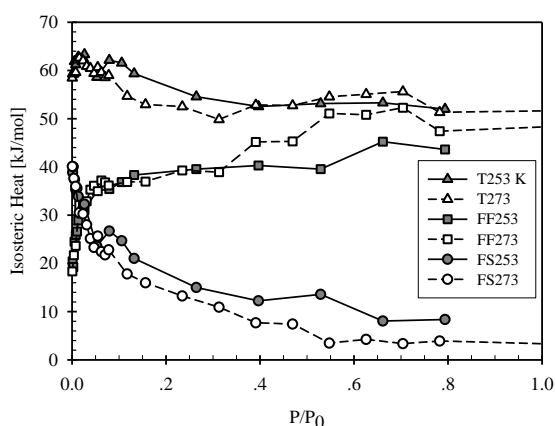


**Figure 7.6** Isothermic heat of water adsorption in 3 nm width of slit-pore with introducing phenol group on the solid surface.

Figure 7.7 shows snapshot of water adsorption in slit-pore with hydrophilic surface. Because the position and angle of functional groups are in the same manner, water molecules begin to be adsorbed to construct hydrogen bond with oxygen atom of phenol groups. Interestingly, the interaction between hydrogen atom of TIP4P/2005 water model and oxygen atom of phenol is more favorable than other hydrogen bond between hydrogen atom of phenol and oxygen atom of the TIP4P/2005 water.

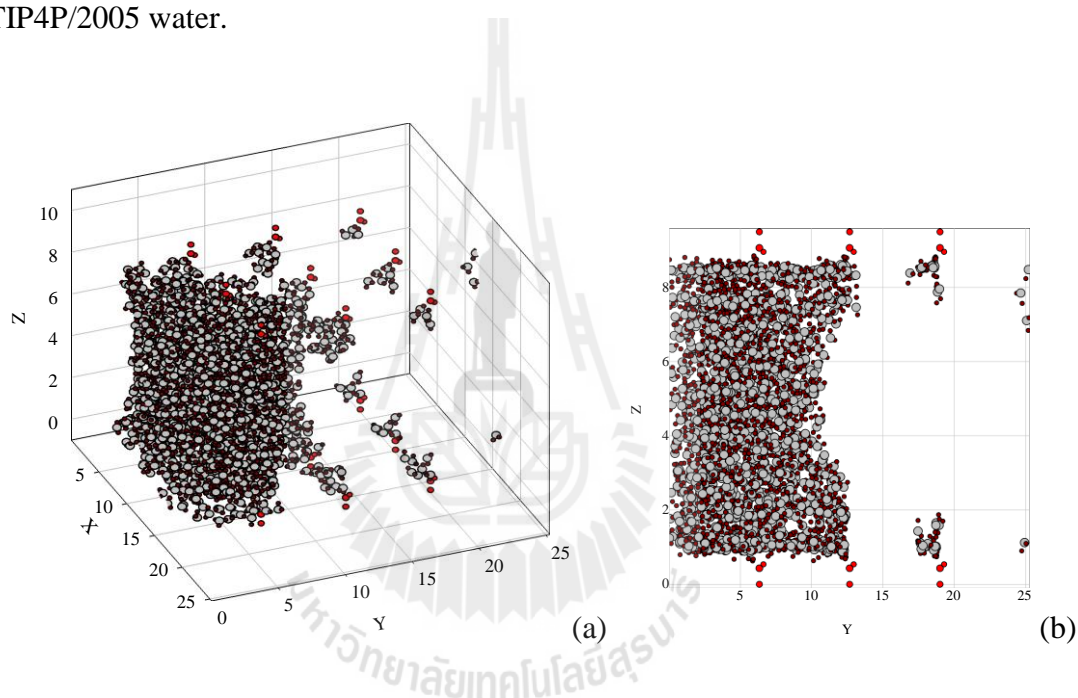


**Figure 7.7** Snapshot of water onto slit-pore of 3 nm width with hydrophilic surface; (a)  $x$ - $y$ - $z$  plane and (b)  $y$ - $z$  plane. All of carbon, oxygen and hydrogen atoms of phenol group are indicated in red. Oxygen and hydrogen atoms of water molecule are indicated in gray and black, respectively.

#### 7.6.4 Water Adsorption in an Ink Bottle Pore at 298 K

Having seen the adsorption isotherms of water in heterogeneous slit pore without connectivity, now turn to the other morphology of solid model. Water

adsorption in the bottle pore at 298 K and argon adsorption in the same pore model at 87.3 K are shown in Figure 7.8a. The adsorption of water in graphitic bottle pore does not take place at pressures lower than 4.5 kPa due to the weaker interaction between water molecule and carbon surface. When pressures increase, water molecule starts to adsorb at the pore neck by creating the cluster, after that water cluster is spread out and moves to the cavity starting from the connecting pore to the bottom of the larger pore as shown in Figure 7.8a, point A. At pressures lower than point A, the pore bottom is unfilled by water molecules. We call this phenomenon as pore blockage. Water initially adsorbs in the neck because the potential interaction of fluid-solid is stronger than elsewhere. The cluster of water is formed in the neck and then it grows in the direction perpendicular to the pore wall with increasing pressures. This is due to the stronger interaction between water molecules as shown in Figure 7.9. When the pressures increase, the capillary condensation of water molecules occur as shown in Figure 7.8a at point B and C, water molecules fill full in both pore neck and cavity. However, the pore blockage is not found in the case of non-polar fluid as argon adsorption in the corresponding solid at 87.3 K as shown in Figure 7.8b. For more information, we have presented it in CHAPTER VI. Unlike water adsorption, argon starts to adsorb at the carbon surfaces for the pore neck, the cavity and the bottom of larger pore to form the monolayer. When pressures increase the layering phenomenon is observed especially at the pore neck following by the capillary condensation as shown in Figure 7.8b at point D, E and F. The condensation of adsorbed phase at the pore neck blocked argon molecules entering the larger pore and this leads to the cavitation observed in the larger pore.

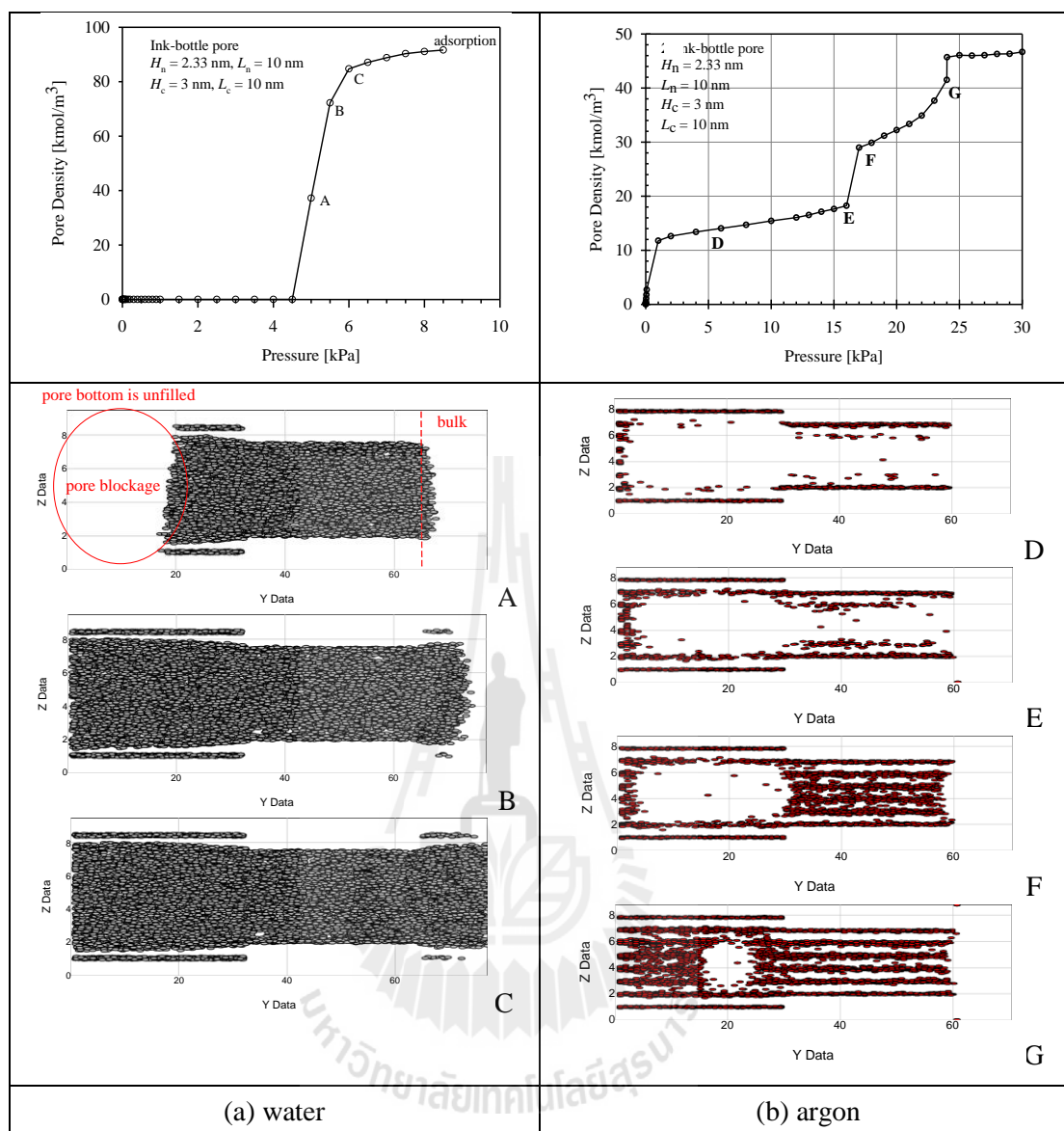


**Figure 7.8** Adsorption isotherm and snapshot onto a bottle-pore of (a) water at 298 K and (b) argon at 87.3 K. The snapshots of water are located only for oxygen atom.



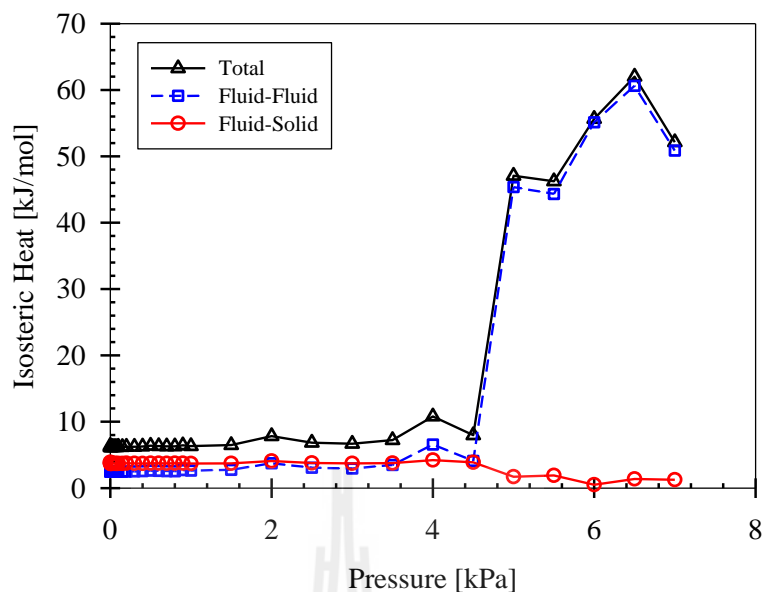


**Figure 7.9** Isostatic heat of water in the bottle pore at 298 K

## 7.7 Conclusions

We have prepared coconut shell-based activated carbon by heat treatment in a fixed-bed reactor. Water vapor adsorption isotherm is measured in the range from 278 to 303 K. In the range of 293 to 303 K, the water uptake at high temperatures is lower than that at low temperatures as expected. The unusual behavior is found when temperature is less than 293 K. The uptake at low temperatures is lower than that at high temperatures. We have used GCMC to explain this unusual behavior and found that water molecules exhibit themselves to balance the potential interaction between the fluid-fluid and fluid-solid interactions to have the adsorbed heat closed to the heat of liquefaction. The fluid-solid interaction at low temperatures in this low range is relatively strong; this causes the fluid-fluid interaction having a low value. The other unusual behavior for water has been found for adsorption in bottle-pore, this unusual behavior is called pore blockage which is not found for non-polar fluid

like argon. The later unusual observation has been found in this work because of the strong interaction between water-water and the weak interaction of water and porous carbon.

## 7.8 References

- Abascal, J.L.F. and Vega, C. (2005). A general purpose model for the condensed phases of water: TIP4P/2005. **The Journal of Chemical Physics**. 123: 234505.
- Boehm, H.P. (1994). Some aspects of the surface chemistry of carbon blacks and other carbons. **Carbon**. 32: 759-769.
- Harding, A.W., Foley, N.J., Norman, P.R., Francis, D.C. and Thomas, K.M. (1998). Diffusion barriers in the kinetics of water vapor adsorption/desorption on activated carbons. **Langmuir**. 14: 3858-3864.
- Jorge, M., Schumacher, C. and Seaton, N.A. (2002). Simulation study of the effect of the chemical heterogeneity of activated carbon on water adsorption. **Langmuir**. 18: 9296-9306.
- Kim, P., Meyer, H.M. and Agnihotri, S. (2009). Effect of surface oxygen and temperature on external and micropore adsorption of water in single-walled carbon nanotubes by gravimetric and spectroscopic experiments. **The Journal of Physical Chemistry C**. 113: 12109-12117.
- Liu, J.C. and Monson, P.A. (2006). Monte Carlo simulation study of water adsorption in activated carbon. **Industrial & Engineering Chemistry Research**. 45: 5649-5656.

- McCallum, C.L., Bandosz, T.J., McGrother, S.C., Müller, E.A. and Gubbins, K.E. (1998). A molecular model for adsorption of water on activated carbon: comparison of simulation and experiment. **Langmuir**. 15: 533-544.
- Miura, K. and Morimoto, T. (1986). Adsorption sites for water on graphite. 3. Effect of oxidation treatment of sample. **Langmuir**. 2: 824-828.
- Miura, K. and Morimoto, T. (1988). Adsorption sites for water on graphite. 4. Chemisorption of water on graphite at room temperature. **Langmuir**. 4: 1283-1288.
- Miura, K. and Morimoto, T. (1991). Adsorption sites for water on graphite. 5. Effect of hydrogen-treatment of graphite. **Langmuir**. 7: 374-379.
- Miura, K. and Morimoto, T. (1994). Adsorption sites for water on graphite. 6. Effect of ozone treatment of sample. **Langmuir**. 10: 807-811.
- Mooney, D.A., Müller-Plathe, F. and Kremer, K. (1998). Simulation studies for liquid phenol: Properties evaluated and tested over a range of temperatures. **Chemical Physics Letters**. 294: 135-142.
- Morimoto, T. and Miura, K. (1985). Adsorption sites for water on graphite. 1. Effect of high-temperature treatment of sample. **Langmuir**. 1: 658-662.
- Morimoto, T. and Miura, K. (1986). Adsorption sites for water on graphite. 2. Effect of autoclave treatment of sample. **Langmuir**, 2: 43-46.
- Müller, E.A. and Gubbins, K.E. (1998). Molecular simulation study of hydrophilic and hydrophobic behavior of activated carbon surfaces. **Carbon**. 36: 1433-1438.

- Müller, E.A., Rull, L.F., Vega, L.F. and Gubbins, K.E. (1996). Adsorption of water on activated carbons: A molecular simulation study. **The Journal of Physical Chemistry**. 100: 1189-1196.
- Ohba, T., Kanoh, H. and Kaneko, K. (2004a). Affinity transformation from hydrophilicity to hydrophobicity of water molecules on the basis of adsorption of water in graphitic nanopores. **Journal of the American Chemical Society**. 126: 1560-1562.
- Ohba, T., Kanoh, H. and Kaneko, K. (2004b). Cluster-growth-induced water adsorption in hydrophobic carbon nanopores. **The Journal of Physical Chemistry B**. 108: 14964-14969.
- Salame, I.I. and Bandosz, T.J. (1998). Experimental study of water adsorption on activated carbons. **Langmuir**. 15: 587-593.
- Striolo, A., Gubbins, K.E., Gruszkiewicz, M.S., Cole, D.R., Simonson, J.M., Chialvo, A.A., Cummings, P.T., Burchell, T.D. and More, K.L. (2005). Effect of temperature on the adsorption of water in porous carbons. **Langmuir**. 21: 9457-9467.
- Wongkoblap, A. and Do, D.D. (2007). Adsorption of water in finite length carbon slit pore: Comparison between computer simulation and experiment. **The Journal of Physical Chemistry B**. 111: 13949-13956.

## CHAPTER VIII

### CONCLUSIONS AND RECOMMENDATIONS

#### 8.1 Conclusions

We have presented a molecular simulation to study the effects of pore morphology on the adsorption of fluid in porous carbons. The outcome of this study will be an important and complementary role to the experiment in achieving a fundamental understanding of the relationship between the structural and geometrical properties of porous carbons and adsorption of fluid. This understanding is crucial to developing rational design principles to characterize these materials for specific applications.

##### 8.1.1 Benzene, Toluene and Xylene on Graphitic Surface and in Pores

Conventional pore structures slit and cylindrical pores is first investigated in this thesis to demonstrate the adsorption affinity and packing of hazardous organic compounds such as benzene, toluene and xylene (BTX) which is difficult to study experimentally. It is found that the order of adsorption affinity in a cylindrical pore is the same as that for a surface and slit-pore ( $B < T < X$ ) and the packing order is not affected by the surface curvature ( $B > T > X$ ). The molecular orientation in either graphitic slit or cylindrical pores is the same saying that most benzene molecules in the first layer adopt an orientation parallel to the solid surface but there are minor populations having slant and vertical orientations. While, in the second and higher layers adsorbed the orientations are similar to in the first layer but the ratio of molecules associated slant and vertical formation to parallel to the solid

surface became higher. This is emphasized for a pore that can pack more than two layers if the porous carbon can pack only one layer the orientation is depended on the pore width, most molecules may orientate themselves as slant or vertical orientation to the solid surface.

### **8.1.2 Hysteresis and Equilibrium Transition of Argon and Benzene in Slit-Shaped Ink-Bottle Pores**

Slit-shaped ink-bottle pores consisting of simple slit-pore, single slit-pore closed at one end, two pores connected and bottle-pore with a cavity connected to one neck are used in this part. All of the pores considered in this part are of a finite length and are connected to a bulk reservoir so that they mimic real materials for which confined fluid is always in contact with the external gas phase. Adsorption and desorption of non-polar fluid of argon and benzene in the pores are investigated by using *Bin*-GCMC as well as the equilibrium transition in the pores is determined by using the Mid-Density scheme. Observations in the case of argon and benzene are consistent qualitatively. The hysteresis loop in infinite and finite pores are different the desorption branch in the hysteresis loop region is kept constant while that for finite pore is slightly decreased with reducing of pressure as a receding of menisci from the mouth to the interior. Moreover, in simple slit-pore, we found that the desorption branch is closer to the equilibrium transition as the pore length is increased, while the relative position of the equilibrium transition against the adsorption and desorption segments of the hysteresis loop is insensitive to pore width and temperature. The adsorption-desorption and equilibrium transition in connected pore are interesting to understand adsorption in network pore, especially pore blocking and cavitation in the pores. These mechanisms are dictated by the size of the

neck, and are somewhat insensitive to the neck length. When the neck size is smaller than some critical value, cavitation is the dominant mechanism; otherwise pore blocking is the mechanism for evaporation. A feature to distinguish these mechanisms is the manner in which the desorption branch behaves prior to complete evaporation. When cavitation is the controlling mechanism in evaporation, the desorption branch only decreases gradually before a sharp evaporation, while it decreases more when pore blocking is the controlling mechanism and it exhibits a knee shape prior to evaporation. The equilibrium transition in pores having pore blocking and cavitation is determined. We found that it has three stages; the first stage is exhibited second-order like transition indicated in the neck and closed to desorption branch. The third stage is associated with the cavity exhibited as first-order transition and closed to adsorption branch. The second stage joining the other two stages and it falls between the adsorption and desorption branches.

### **8.1.3 Water Adsorption in Activated Carbon and Bottle Pore Model**

In the final part, the adsorption of water in porous carbons is studied experimentally and theoretically. The adsorption behavior of water on activated carbon and bottle-pore model is qualitatively different from that of simple fluid of argon. This major difference comes from two sources: (i) for water the fluid-fluid interaction is much more strongly attractive than the interaction of water with the carbon surface, in contrast to the situation for simpler fluids, where the reverse is the case, and (ii) the adsorption behavior for water is largely controlled by the formation of hydrogen bonds with oxygenated groups on the surface. For graphitic carbon, for which surface chemical groups have been removed, there is almost no adsorption at low and moderate pressures; in the case of porous carbons, capillary condensation

occurs at some higher pressure. For this same carbon, simple fluid argon is adsorbed strongly at much lower pressures. For graphitic carbon with surface functional groups, simple fluid pore filling occurs via the formation of a fluid monolayer on the surface, often followed by a second and possibly further layers, prior to capillary condensation and pore filling. By contrast, water molecules are first adsorbed onto oxygenated surface sites, and these adsorbed water molecules then act as nuclei for the formation of larger water clusters; eventually these clusters connect along the surface or across the pore, and pore filling usually occurs. When the density of oxygenated sites on the surface is appreciable, the pore filling seems to occur by a continuous filling process without capillary condensation. In addition, the unusual temperature of dependence of water adsorption in activated carbon is found. The experimental data and simulated results are in good agreement qualitatively that the uptake of water in the range of temperature closed to the melting point of water is found reversibly to that in the higher range of temperature. This is due to that water molecules adapt themselves to have the adsorbed heat close to the heat of liquefaction by decreasing the fluid-fluid interaction. The other unusual observation of water is that pore blockage in bottle-pore is occurred which is not found that in the case of argon. This unusual observation of water adsorption is from two sources as mentioned above.

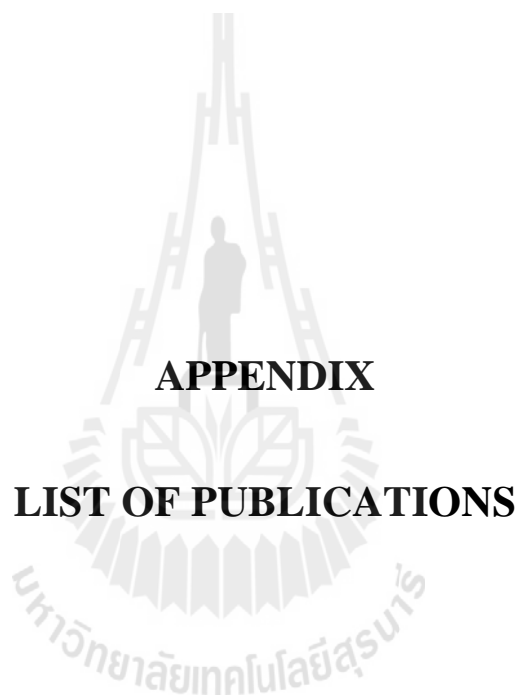
## **8.2 Recommendations for Future Work**

This thesis is focused only on pure component adsorption into porous carbons in order to investigate effects of pore morphology by using molecular simulation. The equilibrium adsorption isotherm and heat of adsorption are studied which is useful for designed applications how minimum adsorbent to be used, and how to model the



adsorber to release the heat adsorbed. The study of effects of pore morphology on fluid adsorption is advantageous to better understand for characterization of network adsorbent. However, in the reality the adsorption is mostly involved with vapor or liquid mixtures, so multi-component adsorption is interesting for our further work.





**APPENDIX**

**LIST OF PUBLICATIONS**

## List of Publications

- Klomkliang, N., Do, D.D., Nicholson, D., Tangsathitkulchai, C. and Wongkoblal, A. (2012). Multilayer adsorption of benzene on graphitized thermal carbon black: The importance of quadrupole and explicit hydrogen in the potential model. **Chemical Engineering Science**. 69: 472-482.
- Klomkliang, N., Do, D.D. and Nicholson, D. (2012). Affinity and packing of benzene, toluene, and p-xylene adsorption on a graphitic surface and in pores. **Industrial & Engineering Chemistry Research**. 51: 5320-5329.
- Klomkliang, N., Do, D.D. and Nicholson, D. (2013). On the hysteresis and equilibrium phase transition of argon and benzene adsorption in finite slit pores: Monte Carlo vs Bin-Monte Carlo. **Chemical Engineering Science**. 87: 327-337.
- Klomkliang, N., Do, D.D. and Nicholson, D. On the hysteresis and equilibrium transition in slit-shaped ink-bottle pores. (Submitted in Langmuir)
- Wongkoblal, A., Tangsathitkulchai, C., Klomkliang, N., Do, D.D. and Ngernyen, Y. Characterization of carbon nanopores with water adsorption in finite-length pore models. (Submitted in Journal of Colloid and Interface Science)
- Klomkliang, N., Do, D.D., Nicholson, D., Tangsathitkulchai, C. and Wongkoblal, A. Unusual temperature of dependence of water adsorption in porous carbon. (In preparing)

- Mus'ab Abdul Razak, Klomkliang, N., Wang, Y. and Do, D.D. The evaluation of mixing parameters in the description of hydrocarbon mixtures adsorption on graphite surface. (Submitted in Adsorption)
- Klomkliang, N., Wongkoblap, A., Tangsathitkulchai, C. and Do, D.D. (2010). Computer study for characterization of porous solid using accessible pore volume concept. **14<sup>th</sup> International ANnual Symposium on Computational Science and Engineering**, 23-26 March 2010, Mae Fah Luang University, Chiang Rai, Thailand. (Oral Presentation)
- Klomkliang, N., Do, D.D., Tangsathitkulchai, C. and Wongkoblap, A. (2012). Toluene/n-hexane mixture adsorption on graphite surface. **CHE-USDC V**, 14-16 November 2012, Chonburi, Thailand. (Oral Presentation)
- Klomkliang, N., Tangsathitkulchai, C. and Tangsathitkulchai, M. (2009). CFD simulation of acidic groups formation on activated carbon surface by air oxidation in a fluidized-bed reactor, **International Symposium of East Asian Young Scientists Follow-up Program on Environment- and Bio-Engineering**, 7-8 September 2009, Hyogo, Japan. (Poster)



## Multilayer adsorption of benzene on graphitised thermal carbon black—The importance of quadrupole and explicit hydrogen in the potential model

Nikom Klomkliang<sup>a,b</sup>, D.D. Do<sup>a,\*</sup>, D. Nicholson<sup>a</sup>, C. Tangsathitkulchai<sup>b</sup>, A. Wongkoblap<sup>b</sup>

<sup>a</sup> School of Chemical Engineering, University of Queensland, St. Lucia, Qld 4072, Australia

<sup>b</sup> School of Chemical Engineering, Suranaree University of Technology, Nakhon Ratchasima 30000, Thailand

### ARTICLE INFO

#### Article history:

Received 1 September 2011

Received in revised form

29 October 2011

Accepted 1 November 2011

Available online 11 November 2011

#### Keywords:

Adsorption

Simulation

Computation

Separation

Benzene

Graphite

### ABSTRACT

Grand Canonical Monte Carlo (GCMC) simulation was used to study multilayer adsorption of benzene on graphitised thermal carbon black over a range of temperature between 273 K and 373 K. Three potential models for benzene were compared: TraPPE-UA-9, OPLS-AA and TraPPE-EH, in order to study their capability to correctly describe the adsorption isotherms and isosteric heats. In the sub-monolayer region, there is no difference between the simulation results obtained with the three models, which all describe the experimental data well. However, in the multilayer region only the TraPPE-EH model, that includes the quadrupole moment and explicit modelling of the hydrogen, is able to describe the experimental data accurately; the other two models significantly under-predict the data. The TraPPE-EH model was then used to investigate the microscopic behaviour of the adsorbed phase: the local density distribution and the orientation of various layers, particularly the change in orientation of benzene in the first layer with increase in loading from sub-monolayer to multi-layer. It was found that the orientation of benzene molecules in the first layer is affected by the presence of molecules in the higher layers, but that most benzene molecules remain in an orientation parallel to the surface, which is favoured by the interaction with the surface, while a smaller population takes 60° and vertical orientations to the surface which maximises the entropy. The ratio of the number of molecules having parallel orientation to that having 60° and vertical orientations decreases in higher layers due to the weaker influence of the adsorbate–adsorbent interaction. Detailed study of the orientation shows that most slant and vertical molecules have two of their hydrogen atoms closer to the surface.

© 2011 Elsevier Ltd. All rights reserved.

### 1. Introduction

Benzene adsorption has been widely studied in the past because it is typical of many aromatic toxic organic compounds that are present in gas and/or liquid effluents from many chemical and petrochemical industries. Stricter environmental regulations require that aromatics need to be removed before the effluents can be safely discharged into the environment. Adsorption is among the most effective means of achieving this goal, and is the simplest process to implement. The key step in an adsorption process is the choice of a solid adsorbent, and activated carbon is often the solid of choice because the graphitic nature of the pore walls offers two distinct advantages over other solid adsorbents: it is both hydrophobic and has high atom density (greater affinity for the adsorptive). To understand the basic interaction between benzene and graphitic walls better, physisorption of benzene on a graphite (or graphitised thermal carbon black) surface has been studied both experimentally

(Avgul et al., 1958; Isirikyan and Kiselev, 1961, 1963; Berezin et al., 1970, 1972; Pierotti and Smallwood, 1966; Belyakova et al., 1968; Pierce and Ewing, 1967; Davis and Pierce, 1966) and theoretically (Vernov and Steele, 1991a, 1991b; Matties and Hentschke, 1996a, 1996b; Do and Do, 2006). The fundamental understanding of this adsorbate–adsorbent interaction is the basic step to better design of adsorption systems for benzene in pores whose walls are graphitic; for example activated carbon (Yun et al., 1999; Lai et al., 2010), carbon nanotubes (Masenelli-Varlot et al., 2002; Terzyk et al., 2009) and ordered solids with hexagonal pores (Morishige, 2011a, 2011b; Wang et al., 2011).

Early experimental studies of adsorption of benzene on graphite or graphitised thermal carbon black (GTCB) were made by Kiselev and co-workers (Avgul et al., 1958; Isirikyan and Kiselev, 1961, 1963; Berezin et al., 1970, 1972); they measured adsorption isotherms at ambient temperatures, with a volumetric apparatus and isosteric heats with a calorimetric device for a number of carbon blacks. As long as the carbon blacks were sufficiently well graphitised, the experimental data were in perfect agreement with each other because the benzene molecules form a perfect hexagonal tessellation on the graphene surface. Following this

\* Corresponding author. Tel.: + 61 7 3365 4154; fax: +61 7 3365 2789.  
E-mail address: [d.d.do@uq.edu.au](mailto:d.d.do@uq.edu.au) (D.D. Do).

early work of Kiselev, adsorption over a wider range of temperature (273–373 K), above and below the bulk freezing point of 278.7 K has been carried out by a number of workers (Pierotti and Smallwood, 1966; Belyakova et al., 1968; Pierce and Ewing, 1967; Davis and Pierce, 1966).

In recent years, with the advances of the computer simulation, molecular simulation has also been used to study benzene adsorption on graphite. Vernov and Steele (1991a, 1991b) used Monte Carlo simulation to investigate the structures and energies of benzene adsorption on graphite at 85 and 298 K. They found that the heat of adsorption was nearly constant in the sub-monolayer region, in agreement with the calorimetric data of Isirikyan and Kiselev (1961). This constant heat is attributed to cancellation between the increase in the benzene–benzene interaction and the decrease in the benzene–adsorbent interaction; which changes as the orientation of benzene molecules changes with increased loading in the sub-monolayer region. The structure of the second layer was found to be less ordered than that of the first layer, as a result of the weaker interactions of the benzene molecules in the second layer. Matties and Hentschke (1996a, 1996b) used molecular dynamics to study the structure of the benzene adsorbate in the first and higher layers on the basal plane of graphite over a wide range of temperature (60–320 K). Their results showed that ordering beyond the nearest neighbours decreases rapidly with coverage, and is virtually non-existent for second and higher layers. However, since molecular dynamics does not yield adsorption isotherms or heats their simulation results cannot be tested against experimental data. More detailed study of isotherms, heats and the structure of adsorbed benzene on graphite using grand canonical Monte Carlo (GCMC) simulation was presented by Do and Do (2006). They investigated the performance of various potential models for benzene that were available up to 2006, the united atom models TraPPE-UA-6 (Wick et al., 2000) and TraPPE-UA-9 (Wick et al., 2002) and the all atom model OPLS-AA (with 12 dispersive sites and 12 partial charges) (Jorgensen and Severance, 1990), for their suitability in correctly describing the experimental adsorption isotherm and the heat of adsorption, and found that the TraPPE-UA-9 gave the better results. From the simulation data, they found that at very low loadings, most benzene molecules adopt an orientation parallel to the surface which is the most energetically favourable position. When the loading is increased within the sub-monolayer coverage, some benzene molecules adopt a slant configuration, due to the quadrupolar interactions between benzene molecules. However, the work by Do and Do was restricted to the sub-monolayer region, and therefore a molecular simulation of benzene adsorption on GTCB beyond the first layer is desirable to assess the ability of the potential models to describe the isotherm and isosteric heat and to explore how molecules in higher layers affect the orientation of molecules in the first layer. Furthermore, a new potential model was recently proposed by Rafi and Siepmann (2007), TraPPE-EH, which includes twelve dispersive sites (carbon and hydrogen atoms) and twelve partial charges on these atoms, and it is of interest to test its capability to describe benzene adsorption. These authors compared this new model with previous potential models for benzene, and have found that this model and OPLS-AA are significantly more accurate than the 6-site model (TraPPE-UA-6) and the 9-site model (TraPPE-UA-9) for the description of vapour–liquid equilibria at 298.15 K. The OPLS-AA model performed well at 298.15 K (where it was fitted) but its performance degraded rapidly with increasing temperature. Interestingly the better models are the ones that account explicitly for the hydrogen atoms.

In this paper, we re-investigate the performance of various benzene potential models, particularly the ones that account explicitly for the hydrogen atoms, and examine whether this can describe the adsorption of benzene in the multi-layer regions, despite the small value of the well-depth of interaction energy of hydrogen atom. Physically we expect the presence of hydrogen

atoms will affect packing when loadings are high (i.e. when molecules are packed close to each other), and expect the potential models, such as TraPPE-EH and OPLS-AA to perform better in the dense adsorbed layer. We then study the structure of benzene to see whether the higher layers change the orientation of benzene molecules in the first dense layers.

## 2. Theory

### 2.1. Multisite potential model

The commonly accepted single-site Lennard Jones (LJ) 12–6 and Steele 10–4–3 potential energy equations work well for small pseudo-spherical molecules. However, for large molecules, such as benzene, single-site models are not suitable. Here we consider benzene to be a hexagonal molecule composed of at least 6 sites. For a polyatomic molecule with  $M$  LJ site centres, the potential energy of interaction between a site  $a$  on a molecule  $i$  with a site  $b$  on a molecule  $j$  can be calculated using the following LJ 12–6 equation:

$$U_{ij}^{(a,b)} = \sum_{a=1}^M \sum_{b=1}^M 4\epsilon_{ij}^{(a,b)} \left[ \left( \frac{\sigma_{ij}^{(a,b)}}{r_{ij}^{(a,b)}} \right)^{12} - \left( \frac{\sigma_{ij}^{(a,b)}}{r_{ij}^{(a,b)}} \right)^6 \right] \quad (1)$$

where  $r_{ij}^{(a,b)}$  is the separation distance between the LJ site  $a$  on molecule  $i$  and the LJ site  $b$  on molecule  $j$ ,  $\sigma_{ij}^{(a,b)}$  and  $\epsilon_{ij}^{(a,b)}$  are the cross collision diameter and the cross well-depth of the interaction energy, respectively. The cross parameters,  $\sigma_{ij}^{(a,b)}$  and  $\epsilon_{ij}^{(a,b)}$  can be determined by the Lorentz–Berthelot mixing rules:  $\sigma_{ij}^{(a,b)} = (\sigma_{ij}^{(a,a)} + \sigma_{ij}^{(b,b)})/2$  and  $\epsilon_{ij}^{(a,b)} = (\epsilon_{ij}^{(a,a)} \epsilon_{ij}^{(b,b)})^{1/2}$ . The interaction energy due to the electrostatic force between a charge  $\alpha$  on a molecule  $i$  and a charge  $\beta$  on a molecule  $j$  can be calculated from the Coulomb law of electrostatic interaction

$$U_{q\alpha q\beta}^{(\alpha,\beta)} = \sum_{\alpha=1}^{M_q} \sum_{\beta=1}^{M_q} \frac{1}{4\pi\epsilon_0} \frac{q_i^\alpha q_j^\beta}{r_{ij}^{(\alpha,\beta)}} \quad (2)$$

where  $M_q$  is the number of charges on the molecule,  $\epsilon_0$  is the permittivity of free space [ $\epsilon_0 = 10^7/(4\pi c^2) = 8.8543 \times 10^{-12} \text{ C}^2 \text{ J}^{-1} \text{ m}^{-1}$ ,  $c$  is the speed of light],  $r_{ij}^{(\alpha,\beta)}$  is the distance between two charges  $\alpha$  and  $\beta$  on molecules  $i$  and  $j$ , respectively,  $q_i^\alpha$  is the value of charge  $\alpha$  on molecule  $i$ , and  $q_j^\beta$  is the value of charge  $\beta$  on molecule  $j$ . In the present work, surface mediation is taken into account because of the surface influence on the interaction among adsorbed molecules close to the surface (Do and Do, 2006). This is done empirically by reducing the contribution of each benzene molecule in the intermolecular fluid–fluid interaction energy by a factor  $F$  whenever that molecule is in the first layer.

High-level *ab initio* quantum mechanical calculations have been computed for dimers (Zhao and Truhlar, 2005), trimers (Tauer and Sherrill, 2005) and tetramers (Tauer and Sherrill, 2005), but their applications in condensed phases and larger systems are limited because of the long computation times required. As an alternative, empirical potentials (or force fields) are generally obtained by deriving their molecular parameters and partial atomic charges from fitting simulation results to the experimental data such as the liquid density, heat of vaporisation and vapour–liquid equilibrium. Most of the general force fields, such as AMBER (Cornell et al., 1996), OPLS (Jorgensen and McDonald, 1998), and CHARMM (Feller and MacKerell, 2000), are fitted to the experimental data at ambient conditions and their application to other temperatures has not been tested, while the anisotropic OPPE force field (Contreras-Camacho et al., 2004; Ahunbay et al., 2005), and the exp-6 force field for benzene (Errington and Panagiotopoulos, 1999) are limited because the C–H bond are neglected and no electrostatic interactions are

**Table 1**  
Potential parameters of benzene for three potential models.

Model	Group	$\sigma$ (Å)	$\epsilon/k_B$ (K)	$q$ (e)
TraPPE-UA-9 (Wick et al., 2002)	CH	3.74	48.00	+2.420
	$z=0$			
	$z = \pm 0.785$ Å			
OPLS-AA (Jorgensen and Severance, 1990)	C	3.55	35.22733	-0.115
	H	2.42	15.09743	+0.115
TraPPE-EH (Rai and Siepmann, 2007)	C	3.60	30.70	-0.095
	H	2.36	25.45	+0.095

accounted for. The better empirical potential models for benzene come from the TraPPE family, TraPPE-6 (Wick et al., 2000), TraPPE-UA-9 (Wick et al., 2002) and TraPPE-EH (Rai and Siepmann, 2007). These models provide more accurate liquid and vapour densities, vapour pressures, and heats of vaporisation over a wide range of temperatures than the other models.

From an assessment of the various potential models for benzene that are currently available in the literature, we selected three models and tested them for their description of benzene adsorption on a graphite surface. The first model is TraPPE-UA-9 model with 6 Lennard–Jones sites and 3 charges that account for quadrupole moment. The 6 dispersive sites lie at the centres of the carbon atoms and the C–C bond length is 1.40 Å. The positive partial charge (+2.42e) is put at the centre of the benzene ring, and two negative partial charges (-1.21 e) are placed at a distance of 0.785 Å on both sides of the ring along a normal to the ring. The second model is the OPLS-AA model, which was proposed originally by Jorgensen and Severance (1990) and was tested by Rai and Siepmann (2007) who showed that it gives a good description of the VLE data at room temperature. This model has 12 dispersive sites and 12 partial charge sites at the centres of the carbon atoms and hydrogen atoms. The C–C and C–H bond lengths are 1.40 and 1.08 Å, respectively. Finally, the new TraPPE-EH model proposed by Rai and Siepmann is also studied in the present work. Again this model has 12 dispersive sites and 12 partial charge sites centred on the carbon and hydrogen atoms; the C–C and C–H bond lengths are 1.392 and 1.08 Å, respectively, but differ from the TraPPE-EH model in the values of the parameters. The parameters of these three models are listed in Table 1.

## 2.2. Adsorbate–adsorbent interaction energy

To calculate adsorbate–adsorbent interactions, we employ two models one of which, the GTCB surface, was modelled as a structure-less surface, and therefore the adsorbate–adsorbent potential energy can be calculated from the 10–4–3 Steele (1973) equation. For a polyatomic molecule with  $M$  LJ site centres, the interaction potential energy between molecule  $i$  and the homogeneous flat solid substrate can be calculated from

$$U_{i,s} = \sum_{a=1}^M 4\pi\epsilon_i^{(a,s)} \rho_s [\sigma_i^{(a,s)}]^2 \left[ \frac{1}{5} \left( \frac{\sigma_i^{(a,s)}}{z_i^a} \right)^{10} - \frac{1}{2} \left( \frac{\sigma_i^{(a,s)}}{z_i^a} \right)^4 - \frac{[\sigma_i^{(a,s)}]^4}{6\Delta(z_i^a + 0.61\Delta)^3} \right] \quad (3)$$

where  $z_i^a$  is the distance of site  $a$  of molecule  $i$  from the graphite surface,  $\epsilon_i^{(a,s)}$  and  $\sigma_i^{(a,s)}$  are the adsorbate–graphite interaction potential well-depth and intermolecular collision diameter respectively,  $\rho_s$  is the surface density (taken as  $0.382 \text{ \AA}^{-2}$  in this work), and  $\Delta$  is the spacing between the two adjacent graphite layers (3.354 Å). In the other model, which we call the atomistic model, the solid surface is assumed to consist of three graphene layers, and these layers are stacked on top of each other with an

interlayer spacing of 3.354 Å. The carbon–carbon bond length in a graphene layer is 1.42 Å. The interaction energy between a fluid particle and a carbon atom is calculated by the LJ 12–6 equation.

The parameters are calculated by combining the parameters for a carbon atom in graphene with the appropriate benzene parameters using the Lorentz–Berthelot mixing rules. The well-depth of interaction energy for the adsorbate–adsorbent interaction was adjusted with the binary interaction parameter,  $k_{sf}$ , to give agreement between the experimental Henry constant and GCMC simulations, where,  $\epsilon_i^{(a,s)} = (1 - k_{sf}) \sqrt{\epsilon_i^{(a,a)} \epsilon_i^{(s,s)}}$ . The molecular parameters for a carbon atom in the graphene layer are  $\sigma_i^{(s,s)} = 3.4$  Å and  $\epsilon_i^{(s,s)}/k_B = 28$  K. For the structure-less model and the atomistic model, we assume that the binary interaction parameter,  $k_{sf}$  is the same for all the interaction sites on a molecule; the values -0.120, -0.060 and -0.036 were found for TraPPE-UA-9, OPLS-AA and TraPPE-EH models, respectively. For a slit pore, the adsorbate molecule interacts with both walls, so the fluid–solid potential energy  $U_{sf}$  is calculated from

$$U_{sf} = U_{i,s}(z) + U_{i,s}(H-z) \quad (4)$$

where  $H$  is the physical pore width, defined as the distance between the plane passing through all carbon atoms in the outermost layer of one wall and the corresponding plane at the opposite wall.

## 2.3. Grand canonical Monte Carlo simulation

For modelling an open surface, we used a slit pore wide enough to behave as two independent surfaces. Long range corrections were not applied, instead we used a large simulation box whose linear dimensions were  $80 \times 80 \times 80 \text{ \AA}^3$  for the structure-less surface, while for an atomistic model of graphite, the dimensions were  $76.68 \times 78.72 \times 80 \text{ \AA}^3$  ( $L_x \times L_y \times L_z$ ). Periodic boundary conditions were applied in the  $x$  and  $y$  directions, parallel to the graphite surface, and the cut-off radius was half of the box length in both cases. The standard Metropolis sampling scheme (Allen and Tildesley, 1987) was applied. The ideal gas chemical potential was used because of the low pressures in this work. The number of cycles for an equilibration step and for statistics collection was 50,000. In each cycle, there are 1000 steps to move or rotate, insert, and delete with equal probability.

In order to compare with experimental data available in the literature, the average surface excess was calculated as

$$\Gamma_{av} = \frac{\langle N \rangle}{2L_x L_y} - \frac{\rho_b L_x L_y H}{2L_x L_y} \quad (5)$$

where  $\rho_b$  is the bulk molecular density,  $L_x$  and  $L_y$  are the box lengths in the  $x$  and  $y$  directions, respectively,  $\langle N \rangle$  is the ensemble average of the number of particles in the pore, and  $H$  is the accessible pore width.

A thermodynamic quantity of interest that can be readily obtained from the GCMC is the isosteric heat. Using the fluctuation

theory (Hill, 1956), the isosteric is calculated from (Nicholson and Parsonage, 1982)

$$q_{\text{isost}} = \frac{\langle U \rangle \langle N \rangle - \langle UN \rangle}{\langle N^2 \rangle - \langle N \rangle \langle N \rangle} + k_B T \quad (6)$$

where  $\langle \rangle$  is the ensemble average,  $N$  is the number of particles and  $U$  is the configuration energy of the system. This configuration energy can be divided into two contributions: one is due to the adsorbate interactions, and the other is due to the adsorbate-adsorbent interaction

In order to study the variation of density from the surface, the local density of the centre of mass of benzene is defined as

$$\rho(z) = \frac{\langle \Delta N_{z+\Delta z} \rangle}{L_x L_y \Delta z} \quad (7)$$

where  $\langle \Delta N_{z+\Delta z} \rangle$  is the ensemble average of the number of benzene molecules whose centres of mass are located in the segment having boundaries  $z$  and  $z+\Delta z$ . To understand the variation in the molecular orientation, we consider the orientational local density, which is calculated from (Klochko et al., 1999)

$$\rho(z, \theta) = \frac{\langle \Delta N_{z+\Delta z, \theta+\Delta \theta} \rangle}{L_x L_y \Delta z \sin \Delta \theta} \quad (8)$$

where  $\langle \Delta N_{z+\Delta z, \theta+\Delta \theta} \rangle$  is the ensemble average of the number of benzene molecules whose centres of mass are located in the segment having boundaries between  $z$  and  $z+\Delta z$  and an angle between  $\theta$  and  $\theta+\Delta \theta$ . We describe the orientation of a benzene molecule with two angles  $\theta$  and  $\phi$  as shown in Fig. 1a. The angle  $\theta$  is defined as the angle between the normal vector of benzene ring ( $\mathbf{n}$ ) and the vertical  $z$  axis, while  $\phi$  is defined as the angle between the vector passing through two adjacent carbon atoms and the horizontal surface. An angle  $\theta$  of  $0^\circ$  means that the molecule lies parallel to the pore surface and a value  $\theta$  of  $90^\circ$  means that the molecule is perpendicular to the pore surface. Due to the hexagonal shape of benzene, the range of  $\phi$  is from  $0^\circ$  to  $30^\circ$ . An angle of  $0^\circ$  means that the benzene molecule has one side parallel to the surface (Fig. 1b), and an angle of  $30^\circ$  indicates that benzene take a vertical orientation as shown in Fig. 1c. Any other angle falling between  $0^\circ$  and  $30^\circ$  are shown in Fig. 1a.

### 3. Results and discussion

#### 3.1. Adsorption at 293 K

Fig. 2 shows the simulated adsorption isotherms from the structure-less model and from the atomistic model at 293 K obtained using the TraPPE-UA-9 model in the sub-monolayer region; the results agree with the experimental data of Isirikyan and Kiselev (1961), when the surface mediation (Do and Do, 2006) is accounted for.

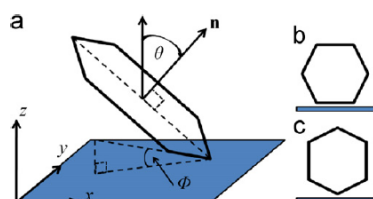


Fig. 1. Schematic showing: the two angles defining the benzene orientation on the surface (a), perpendicular benzene rotated  $0^\circ$  (b), and perpendicular benzene rotated  $30^\circ$  (c).  $\mathbf{n}$  is the normal unit vector through the benzene ring.

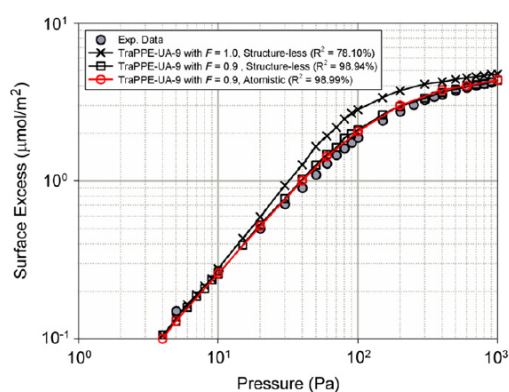


Fig. 2. Adsorption isotherm of benzene on CTGB at 293 K; comparison between the GCMC simulation results using the TraPPE-UA-9 model with and without surface mediation and experimental data from Isirikyan and Kiselev (1961).  $F$  is the surface mediation factor, and  $R^2$  is the  $R$ -squared error.

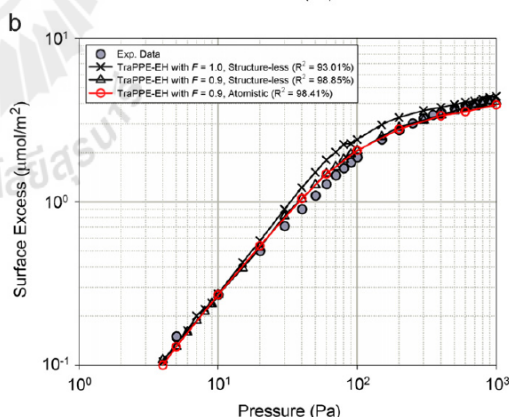
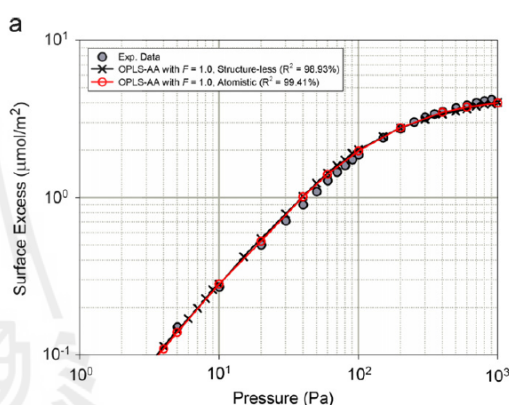


Fig. 3. Adsorption isotherm of benzene on CTGB at 293 K; comparison between the GCMC simulation results using the OPLS-AA model (a) and the TraPPE-EH model (b) with and without surface mediation and experimental data from Isirikyan and Kiselev (1961).  $F$  is the surface mediation factor.  $R^2$  is  $R$ -squared error.



The mediation of the TraPPE-UA-9 potential between the benzene molecules by 3-body interaction through the adsorbent was accounted for empirically by reducing these interactions by 10% ( $F=0.9$ ) when two benzene molecules are in the first layer, i.e. their pairwise interaction is mediated by the surface. Without mediation, the simulation results over-predict the experimental data when the first layer is close to completion. This raises the question of whether surface mediation is required when we consider the more complex OPLS-AA and TraPPE-EH potential models for benzene. The results are shown in Fig. 3, and it is interesting to see that the OPLS-AA model does not require surface mediation to describe the adsorption isotherm correctly, but this does not mean that surface mediation is not required for other surfaces. A reduction of 10% ( $F=0.9$ ) is required for the TraPPE-EH model, which is similar to the TraPPE-UA-9 model. Thus except for the difference in surface mediation, all three models give a good description of the data in the sub-monolayer region (the monolayer concentration is  $4.2 \mu\text{mol}/\text{m}^2$ ). The TraPPE-UA-9 and OPLS-AA are equally successful in describing the adsorption of benzene on a graphite surface. This is different from our earlier observation (Do and Do, 2006), and this is due to the insufficient number of cycles used in our earlier work for OPLS-AA.

Since the simulation results using the structure-less model and the atomistic model are comparable in their description of adsorption isotherm, our subsequent simulation results were obtained with the structure-less surface.

We now investigate the performance of the three potential models for their description of the multi-layer region. The simulated results are shown in Fig. 4 for a wide range of pressure over which five layers of benzene are adsorbed.

Irrespective of whether we present the results in terms of pressure or relative pressure, all potential models describe the data in the sub-monolayer region quite well, but only the TraPPE-EH model is capable of describing the data well up to five adsorbed layers of benzene. The relative pressures for the simulation results were calculated using the simulated saturation vapour pressure in the literature (Wick et al., 2002; Rai and Siepmann, 2007).

To support the statement that the TraPPE-EH potential is a better model, we tested their performance for the description of the isosteric heat. The simulation results are shown in Fig. 5, together with the experimental data obtained from the calorimetric measurements. Over the range of two layers where the heat data are available, we can draw the conclusion that the TraPPE-EH, as a whole, is the best model for the description of the isotherm and heat data as we can see from the percentage deviation in Fig. 5b.

To see the contributions of the benzene–solid and benzene–benzene interactions toward the isosteric heat, we plot these contributions in Fig. 6 as a function of loading for the TraPPE-EH model. In the sub-monolayer region, the increase in the benzene–benzene interactions compensates for the decrease in the benzene–solid interaction, resulting in a relatively constant isosteric heat in this region (although we note a modest increase of the isosteric heat in the sub-monolayer region). The benzene–adsorbent interaction diminishes in the second layer because molecules are further away from the surface, while the adsorbate interaction increases only slightly giving a constant isosteric heat, of  $35 \text{ kJ}/\text{mol}$ , compared to  $42 \text{ kJ}/\text{mol}$  in the sub-monolayer region. The isosteric heat in the second layer of  $35 \text{ kJ}/\text{mol}$  is close to the heat of liquefaction of benzene ( $34 \text{ kJ}/\text{mol}$ ), but this does not mean that the second layer is a liquid phase. The FF interaction of the second layer is less than that in the bulk liquid because each molecule has fewer neighbours, and this is only partially compensated by the small FS interaction. This is further supported when we study the structure of benzene molecules in the next section.

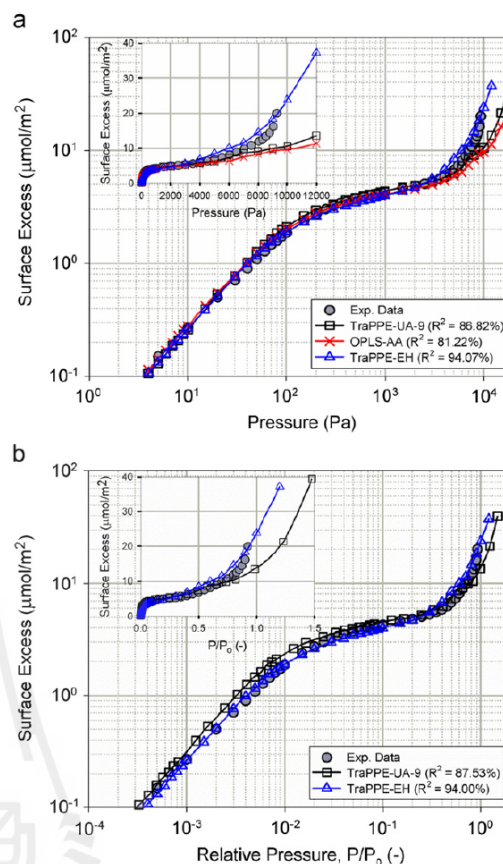


Fig. 4. Adsorption isotherm of benzene on GTCB at 293 K; comparison with the GCMC simulation results (structure-less model) using the TraPPE-UA-9 model (with  $F=0.9$ ), the OPLS-AA model (with  $F=1.0$ ), and the TraPPE-EH model (with  $F=0.9$ ); the experimental data are from Isirikyan and Kiselev (1961). Surface excess vs pressure (a) and surface excess vs relative pressure (b).  $R^2$  is R-squared error.

### 3.2. Structure of adsorbed benzene

Since the TraPPE-EH gives the best description of the isotherm and the isosteric heat of adsorption, we shall use it to study the structure of the adsorbed layer. Figs. 7–10 show the local density distributions for the centre of mass of benzene with respect to the distance from the graphite surface at 293 K.

First, we analyse the structure of benzene molecules in the sub-monolayer region, and then later show how the presence of higher layers disturbs this structure because of the FF interactions from higher layers. The chosen isotherm points are shown in the inset of Fig. 7, where A and B represent points well below the monolayer coverage and C and D are points just before and after the completion of the first layer, respectively. At points A and B, the surface is 10% and 50% covered with benzene molecules, respectively. The first layer is about  $3.44 \text{ \AA}$  from the graphite surface. At very low loadings there is a single peak indicating that all molecules have the same orientation parallel to the surface, as will be shown later. However, at point C a shoulder develops

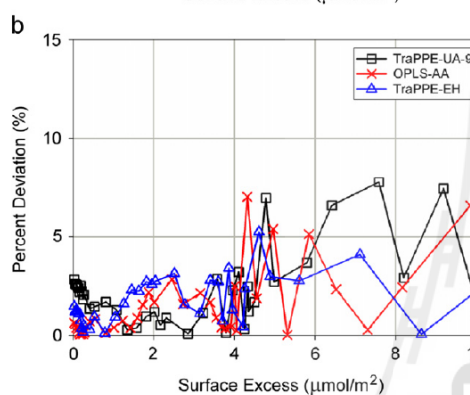
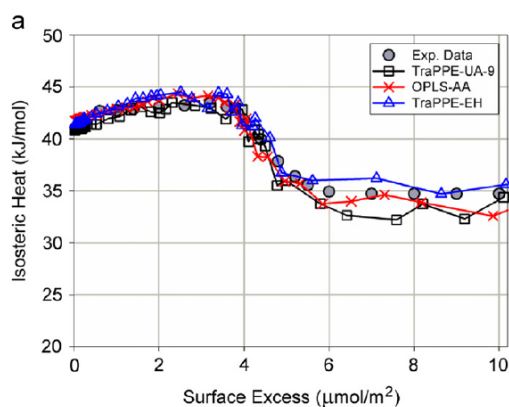


Fig. 5. Isosteric heat vs loading for benzene adsorption on GTCB at 293 K; comparison with the GCMC simulation results (structure-less model) using the TraPPE-UA-9 model ( $F=0.9$ ), the OPLS-AA model ( $F=1.0$ ), and the TraPPE-EH model ( $F=0.9$ ) (a) and their per cent deviation (b); the experimental data are from Isiriykan and Kiselev (1961).

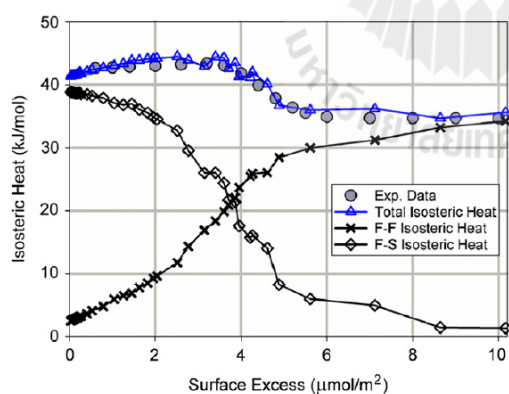


Fig. 6. Total, benzene–benzene, and benzene–solid isosteric heats vs loading for benzene adsorption on GTCB at 293 K; comparison with the GCMC simulation results (structure-less model) using the TraPPE-EH model ( $F=0.9$ ); the experimental data are from Isiriykan and Kiselev (1961).

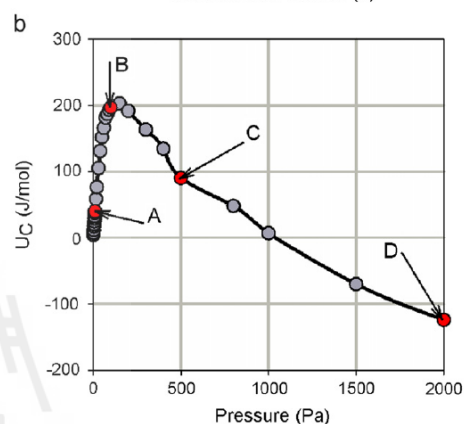
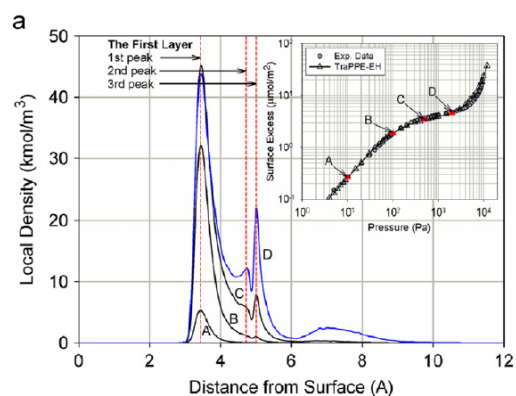


Fig. 7. Local density distribution vs distance from the graphite surface (a) and electrostatic interaction vs pressure (b) at 293 K for the TraPPE-EH model at points A, B, C, and D.

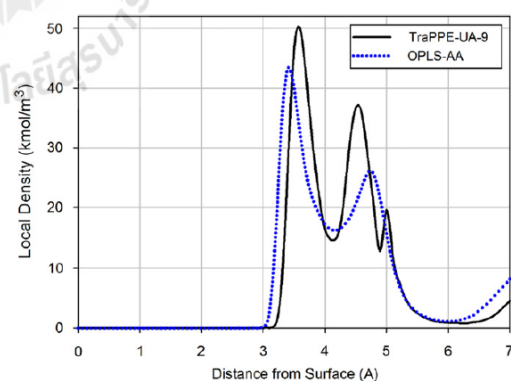


Fig. 8. Local density distribution vs distance from the graphite surface at 293 K for 10,000 Pa for the TraPPE-UA-9 model ( $F=0.9$ ) and the OPLS-AA model ( $F=1.0$ ).

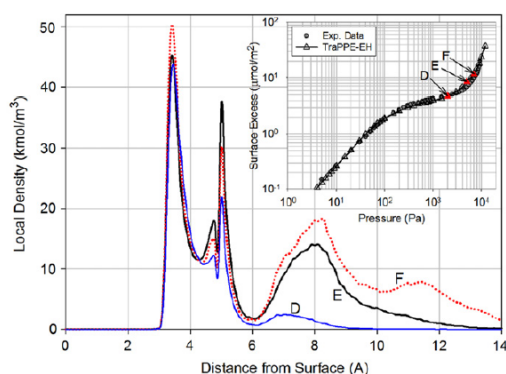


Fig. 9. Local density distribution vs distance from the graphite surface at 293 K for the TraPPE-EH model at points D, E, and F.

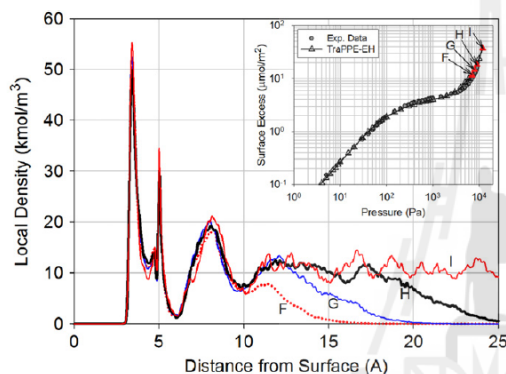


Fig. 10. Local density distribution vs distance from the graphite surface at 293 K for the TraPPE-EH model at points F, G, H, and I.

which then evolves into two minor peaks in the local density distribution at point D (Fig. 7).

These peaks do not result from the formation of another layer, but rather reflect the change in the orientation of some molecules, such that their centres of mass shift further away from the surface. These minor peaks are at 4.7 and 5 Å. The peak at 4.7 Å is associated with molecules having a slant configuration and the peak at 5 Å corresponds to those having a vertical configuration. These configurations are not energetically favoured by the fluid–solid interaction, but are favoured by the increase in the fluid–fluid interaction energy by having more benzene molecules closer to the surface. This is supported by the plot of the fluid–fluid energy contributed by the electrostatic interactions (Fig. 7b). However, it can be seen that the majority of molecules in the first layer remain parallel to the surface because the area under the first peak at 3.44 Å is still the largest. Thus at the completion of the first layer we have three configurations, parallel, slant and vertical. This interesting conclusion is slightly different from the conclusions derived from our earlier work using the TraPPE-UA-9 model (Do and Do, 2006) in that only the parallel and slant configurations were observed, with a much smaller population taking the vertical orientation (see Fig. 8). This can be attributed to the fact that the TraPPE-UA-9 model has no explicit hydrogen atoms, which occupy significant space when the packing is dense. Interestingly, although the OPLS-AA model has explicit

hydrogen atoms, it does not show vertical orientations (see dotted line in Fig. 8). However, since this model does not give an accurate description of the isotherm; we take the view that the local density distribution derived from the TraPPE-EH model is superior.

It is also interesting to observe that the minor peaks become higher when the second layer starts to form (point D), i.e. more benzene molecules in the first layer then adopt the slant and vertical configurations with the increase in the concentration of the second layer although the majority still remain in the parallel orientation.

When the loading increases from the onset of the second layer to the third layer (points D–F in the inset of Fig. 9), the positions of the major and two minor peaks of the first layer are unchanged, but the peak position of the second layer moves from 7 to 8 Å and becomes more delocalised. This is due to the presence of third layer, coupled with the thermal motion of molecules in the second layer. At point F, the third layer occurs at 11.3 Å, and we note that although the

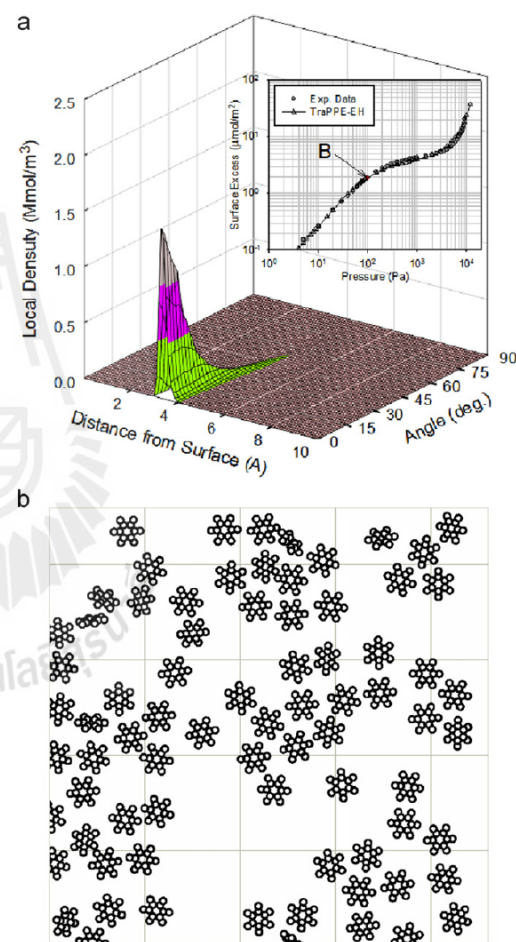


Fig. 11. Local density distribution vs distance from the surface to the centre of mass and the angle  $\theta$  (a) and top view of the snapshot of benzene molecules adsorbed on a graphite surface (b) at 293 K and point B.

positions of the minor peaks of the first layer do not change, the density of the major peak of the first layer is increased at the expense of the two minor peaks, indicating that some molecules re-orientate themselves to the energetically favoured parallel configuration. This also maximises the quadrupolar interaction if benzene molecules lie in offset positions when higher layers are present. This is shown in Fig. 7b where we show the enhancement in the electrostatic (quadrupole) interactions.

When the loading is further increased the concentration at the fourth layer distance increases (Fig. 10) (point H). The position of the first two layers remains unchanged, but the third layer becomes more diffuse. This is similar to the redistribution of the second layer when the third layer forms (at distances between 10 and 16 Å from the surface). Thus we can draw a general conclusion that the presence of a layer only affects the adjacent layer underneath. When the pressure is increased further to point I (about

6 layers are formed above the surface), the layering structure of the third and fourth layers disappears and the adsorbate has the uniform structure of a bulk liquid phase (Fig. 10).

To study in detail the orientation of molecules, the orientation density distributions versus the distance and  $\theta$  are presented in Figs. 11–14. It is seen that at very low loadings (for example, point B) benzene molecules lie flat on the surface, with a peak at zero degrees. This orientation is expected at low loadings because it is the most energetically favourable position. This observation is also supported by the snapshot as shown in Fig. 11.

When the loading is increased to point D (just after the formation of the first layer and at the onset of the second layer), we see the beginning of the formation of a second layer at 7 Å

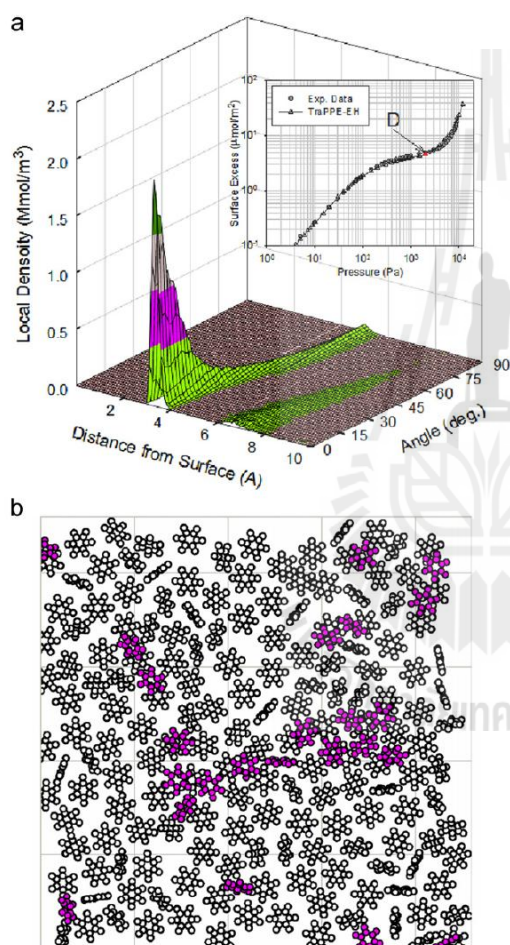


Fig. 12. Local density distribution vs distance from the surface to the centre of mass and the angle  $\theta$  (a) and top view of the snapshot of benzene molecules adsorbed on a graphite surface (molecules in purple colours are those in second layer) (b) at 293 K and point D. (For interpretation of the references to color in this figure legend, the reader is referred to the web version of this article.)

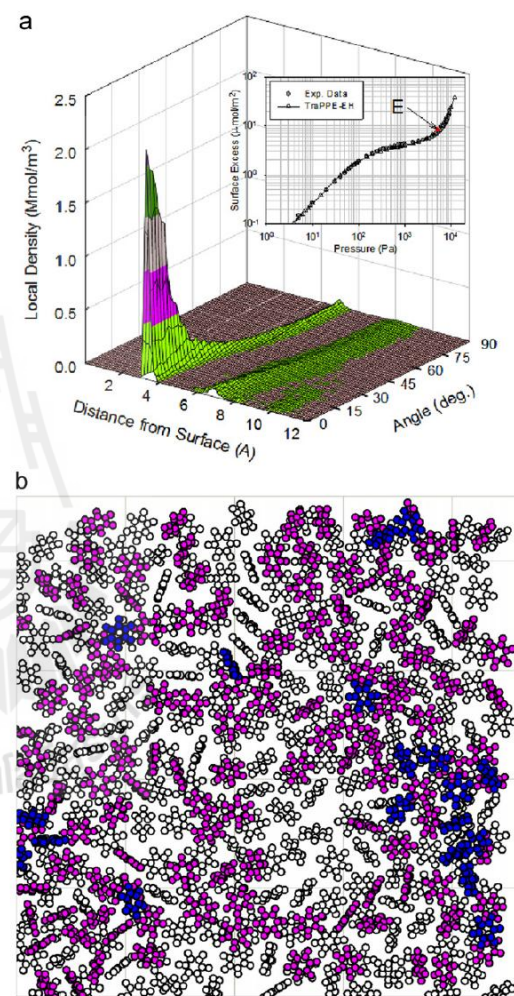


Fig. 13. Local density distribution vs distance from the surface to the centre of mass and the angle  $\theta$  (a) and top view of the snapshot of benzene molecules adsorbed on a graphite surface (molecules in purple and blue colours are those in second and third layer, respectively) (b) at 293 K and point E. (For interpretation of the references to color in this figure legend, the reader is referred to the web version of this article.)

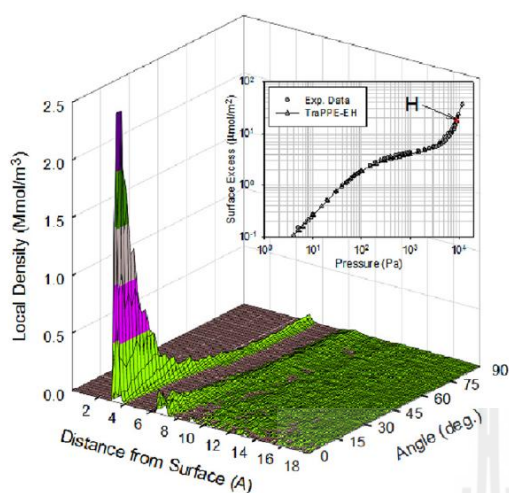


Fig. 14. Local density distribution vs distance from the surface to the centre of mass and the angle  $\theta$  at 293 K and point H.

from the surface (Fig. 12). At this coverage, most molecules in this layer are parallel to the surface, but some molecules in the first layer have orientations other than parallel, including slant and vertical orientations. It is seen that the slant peak at 4.7 Å from the surface is associated with molecules having  $\theta$  about 60° to the surface. When loading is increased to point E (Fig. 13), the second layer continues to fill but the peak shifts further away from the surface (from 7 to be 8 Å), because as molecules fill the second layer they adopt orientations away from parallel. We note that the second layer is beginning to form before the first layer is complete, and the third layer also starts before the completion of the second layer as shown by the snapshot in Fig. 13b as is usual in physical adsorption processes. When loading is increased to point H (Fig. 14), there is an adsorbate thickness equivalent to about 5 layers above the surface and there is no preference for any orientation, suggesting a liquid-like structure above the second layer.

Fig. 15 shows the orientational local density distribution as a function of distance and  $\Phi$ . The peaks J, K, and L in this figure are associated with the first layer and the two minor peaks K and L are for molecules having slant and vertical orientations where the centre of mass is further away from the surface (see the earlier discussion of Fig. 7). In Fig. 15, we see that most slant and vertical benzene molecules have  $\Phi$  equal to 0, meaning that one side of the molecule lies parallel to the surface (i.e. with two hydrogen atoms close to the surface).

### 3.3. Adsorption at wider temperature range

To further test the TraPPE-EH model description of multilayer adsorption, we have carried out simulations at 273 K (below the bulk phase triple point of 278.7 K). In Fig. 16, we compare simulation results using this model (including surface mediation with a factor  $F=0.9$ , used earlier for a temperature of 293 K) with experimental data over a range of temperatures from 273 K up to 373 K. The agreement between simulation and experiment (data of Pierotti and Smallwood (1966)) at 288 K, 303 K and 323 K, and of Belyakova et al. (1968) at 343 K and 373 K is good over the whole 50 K range. The potential model tends to slightly

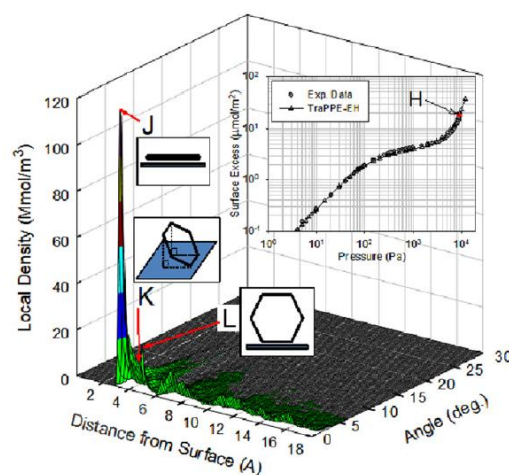


Fig. 15. Local density distribution vs distance from the surface to the centre of mass and the angle  $\Phi$  at 293 K and point H.

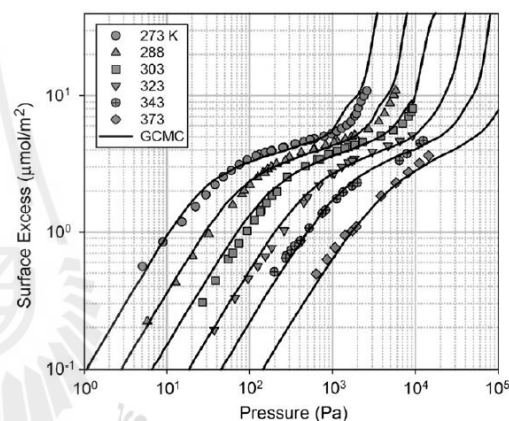


Fig. 16. Adsorption isotherms for benzene on CTCB at various temperatures; comparison between the GCMC simulation results (structure-less model) using the TraPPE-EH model with surface mediation ( $F=0.9$ ) and experimental data from Pierotti and Smallwood (1966) and Belyakova et al. (1968).

overestimate the adsorption, but there is no particular trend with temperature.

To illustrate the difference in the structure of the adsorbed film as temperature is increased, we show, in Fig. 17, the local density distributions for 273 K and 343 K. The structure of the first layer remains unchanged (although lower in density), but the structure of the second layer starts to disappear and to become more uniform and liquid-like, which can also be seen from the orientation density distributions of Figs. 18 and 19 for 343 K.

Finally, in Fig. 20, we show the temperature dependence of the isosteric heat, at 293 K and 343 K. The experimental data at 293 K are taken from Isirikyan and Kiselev (1961), and those at 343 K are from Belyakova et al. (1968). The excellent agreement between simulation and experiment reinforces our conclusion that the TraPPE-EH potential is the best model to describe the

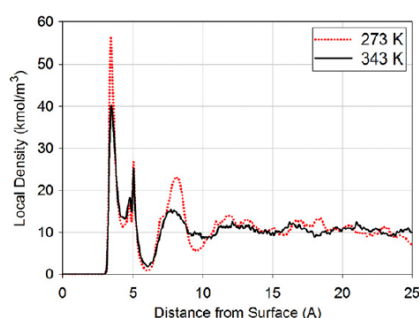


Fig. 17. Local density distribution vs distance from the graphite surface at 273 and 343 K using the TraPPE-EH model for  $30 \mu\text{mol}/\text{m}^2$ .

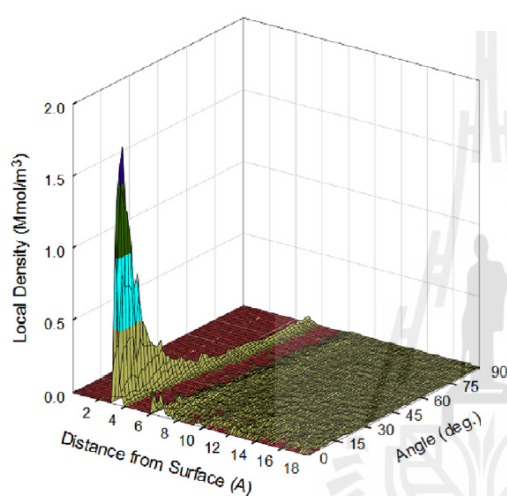


Fig. 18. Local distribution vs distance from the surface to the centre of mass and the angle  $\theta$  at 343 K for  $30 \mu\text{mol}/\text{m}^2$ .

adsorption of benzene on graphite. A weak temperature dependence of the isosteric heat is also noted in this figure.

#### 4. Conclusions

This study of benzene adsorption on a graphite surface at various temperatures in both the submonolayer and the multilayer regions provides a detailed picture of the molecular behaviour of this system. Of the various potential models for benzene tested, we have found that the TraPPE-EH model is the most suitable, and the GCMC simulation results for adsorption isotherms and isosteric heats are in excellent agreement with experimental data taken from the literature.

The GCMC simulation allows us to probe the structure of the adsorbed phase using local density distributions plots. The molecular orientation in the lower layers is influenced by the presence of molecules in higher layers. Most benzene molecules in the first layer adopt an orientations parallel to the surface plane but there are two minor populations having slant and vertical orientations. The slant orientation has an azimuthal angle of about  $60^\circ$  to the

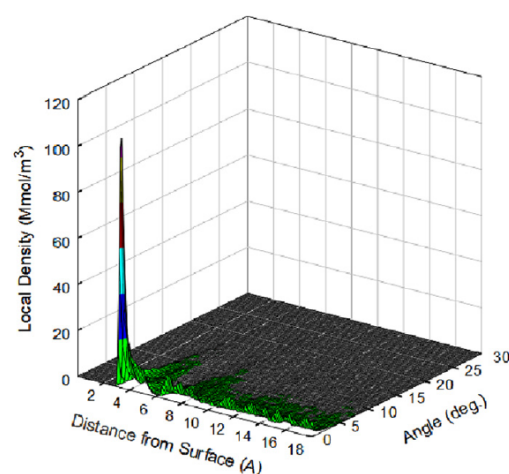


Fig. 19. Local density distribution vs distance from the surface to the centre of mass and the angle  $\phi$  at 343 K for  $30 \mu\text{mol}/\text{m}^2$ .

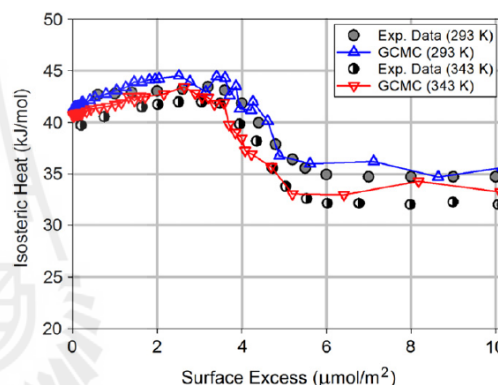


Fig. 20. Isosteric heat vs loading for benzene adsorption on GTCB at 293 K and 343 K: comparison between GCMC simulation results (structure-less model) using the TraPPE-EH model with surface mediation ( $F=0.9$ ) and experimental data from Isirikyan and Kiselev (1961) and Belyakova et al. (1968).

surface. The parallel configuration is energetically favourable in term of benzene–adsorbent interaction. The slant orientation optimises the quadrupole interactions and together with the vertical configuration is entropically favoured over the parallel orientation as temperature increases. However, the ratio of the number molecules adopting parallel orientation to that having slant and vertical orientations decreases in higher layers due to the weaker influence of the adsorbent interaction. We find that most slant and vertical molecules optimise the balance between energy and entropy when one side of the molecule lies parallel to the surface (i.e. two hydrogen atoms are closer to the surface).

#### Nomenclature

$F$	surface mediation factor (dimensionless)
$H$	physical pore width (Å)

$H'$	accessible pore width (Å)
$k_B$	Boltzmann's constant (J/K)
$k_{sf}$	binary interaction parameter (dimensionless)
$L$	length of simulation box (Å)
$N$	number of particle (dimensionless)
$q$	partial charge on the Coulombs site (e)
$q_{isost}$	isosteric heat (J/mol)
$r$	separation of interaction sites (Å)
$T$	temperature (K)
$U$	interaction energy (J)
$\epsilon$	LJ well-depth (J)
$\epsilon_0$	permittivity of a vacuum (C <sup>2</sup> /J m)
$\sigma$	LJ collision diameter (Å)
$\rho$	average local density (mol/m <sup>3</sup> )
$\rho_s$	surface density of carbon atoms (Å <sup>-2</sup> )
$\Delta$	carbon layer separation (Å)
$\Gamma$	surface adsorption (mol/m <sup>2</sup> )

### Acknowledgement

This research was made possible by the Australian Research Council and Suranaree University of Technology whose support are gratefully acknowledged. We also acknowledge the support from the Office of the Commission on Higher Education of Thailand in the form of Ph.D. scholarship to NK.

### References

- Avgul, N.N., Berzin, G.I., Kiselev, A.V., Korolev, A.A., 1958. Heat of adsorption of hydrocarbons by carbon blacks of different degrees of graphitization. *Kolloidnyi Zhurnal* 20, 298–304.
- Ahunbay, M.G., Perez-Pellitero, J., Contreras-Camacho, R.O., Teuler, J.M., Ungerer, P., Mackie, A.D., Lachet, V., 2005. Optimized intermolecular potential for aromatic hydrocarbons based on anisotropic united atoms. III. polyaromatic and naphthoaromatic hydrocarbons. *J. Phys. Chem. B* 109 (7), 2970–2976.
- Allen, M.P., Tildesley, T.P., 1987. *Computer simulation of liquids*. Clarendon, Oxford.
- Berezin, G.I., Kiselev, A.V., Sinityn, V.A., 1970. Adsorption of benzene and n-hexane on graphitized carbon black. *Russ. J. Phys. Chem.* 44 (3), 408–411.
- Berezin, G.I., Kiselev, A.V., Sagatelyan, R.T., Sinityn, V.A., 1972. A thermodynamic evaluation of the state of the benzene and ethanol on a homogeneous surface of a nonspecific adsorbent. *J. Colloid Interface Sci.* 38 (2), 335–340.
- Belyakova, L.D., Kiselev, A.V., Kovaleva, N.V., 1968. Gas-chromatographic determination of isotherms and heats of adsorption of water, benzene and methanol vapours on graphitized carbon black. *Russ. J. Phys. Chem.* 42 (9), 1204–1208.
- Cornell, W.D., Cieplak, P., Bayly, C.L., Gould, I.R., Merz Jr., K.M., Ferguson, D.M., Spellmeyer, D.C., Fox, T., Caldwell, J.W., Kollman, P.A., 1996. A second generation force field for the simulation of proteins, nucleic acids, and organic molecules (vol 117, page 5179, 1995). *J. Am. Chem. Soc.* 118 (9), 2309–2309.
- Contreras-Camacho, R.O., Ungerer, P., Boutin, A., Mackie, A.D., 2004. Optimized intermolecular potential for aromatic hydrocarbons based on anisotropic united atoms. I. Benzene. *J. Phys. Chem. B* 108 (37), 14109–14114.
- Davis, B.W., Pierce, C., 1966. A study of stepwise adsorption. *J. Phys. Chem.* 70 (4), 1051–1058.
- Do, D.D., Do, H.D., 2006. Adsorption of benzene on graphitized thermal carbon black: reduction of the quadrupole moment in the adsorbed phase. *Langmuir* 22 (3), 1121–1128.
- Errington, J.R., Panagiotopoulos, A.Z., 1999. New intermolecular potential models for benzene and cyclohexane. *J. Chem. Phys.* 111 (21), 9731–9738.
- Feller, S.E., MacKerell, A.D., 2000. An improved empirical potential energy function for molecular simulations of phospholipids. *J. Phys. Chem. B* 104 (31), 7510–7515.
- Hill, T., 1956. *Statistical Mechanics*.
- Isirikyran, A.A., Kiselev, A.V., 1961. The absolute adsorption isotherms of vapors of nitrogen, benzene and n-hexane, and the heats of adsorption of benzene and n-hexane on graphitized carbon blacks. I Graphitized thermal blacks. *J. Phys. Chem.* 65 (4), 601–607.
- Isirikyran, A.A., Kiselev, A.V., 1963. Isotherms and heats of adsorption of nitrogen, benzene, and n-hexane vapours on graphitized carbon blacks. III. thermodynamic quantities. *Russ. J. Phys. Chem.* 37 (8), 957–961.
- Jorgensen, W.L., Severance, D.L., 1990. Aromatic-aromatic interactions: free energy profiles for the benzene dimer in water, chloroform, and liquid benzene. *J. Am. Chem. Soc.* 112 (12), 4768–4774.
- Jorgensen, W.L., McDonald, N.A., 1998. Development of an all-atom force field for heterocycles. Properties of liquid pyridine and diazenes. *Theochem. J. Mol. Struct.* 424 (1–2), 145–155.
- Klochko, A.V., Brodskaya, E.N., Piotrovskaya, E.M., 1999. Computer simulations of dependence of adsorption characteristics of ethane on the size of graphite micropores. *Langmuir* 15 (2), 545–552.
- Lai, M.H., Shin, Y.L., Chen, Y.H., Shu, S.H., Chung, T.W., 2010. Equilibrium isotherms of the adsorption of pyrolysis gases from polymer products. *J. Chem. Eng. Data* 55 (2), 723–727.
- Matties, M.A., Hentschke, R., 1996a. Molecular dynamics simulation of benzene on graphite. 1. phase behavior of an adsorbed monolayer. *Langmuir* 12 (10), 2495–2500.
- Matties, M.A., Hentschke, R., 1996b. Molecular dynamics simulation of benzene on graphite. 2. Phase behavior of adsorbed multilayers. *Langmuir* 12 (10), 2501–2504.
- Masenelli-Varlot, K., McRae, E., Dupont-Pavlovsky, N., 2002. Comparative adsorption of simple molecules on carbon nanotubes-dependence of the adsorption properties on the nanotube morphology. *Appl. Surf. Sci.* 196 (1–4), 209–215.
- Morishige, K., 2011a. Freezing and melting of Kr in hexagonally shaped pores of turbostratic carbon: lack of hysteresis between freezing and melting. *J. Phys. Chem. C* 115 (6), 2720–2726.
- Morishige, K., 2011b. Layer-by-layer freezing of Kr confined in hexagonal pores with crystalline carbon walls. *J. Phys. Chem. C* 115 (24), 12158–12162.
- Nicholson, D., Parsonage, N., 1982. *Computer Simulation and the Statistical Mechanics of Adsorption*. Academic Press, London.
- Pierotti, R.A., Smallwood, R.E., 1966. The adsorption of benzene on homogeneous substrates. *J. Colloid Interface Sci.* 22 (5), 469–481.
- Pierce, C., Ewing, B., 1967. Localized adsorption on graphite surfaces. *J. Phys. Chem.* 71 (11), 3408–3413.
- Rai, N., Stepmann, J.J., 2007. Transferable potentials for phase equilibria. 9. explicit hydrogen description of benzene and five-membered and six-membered heterocyclic aromatic compounds. *J. Phys. Chem. B* 111 (36), 10790–10799.
- Steele, W.A., 1973. Physical interaction of gases with crystalline solids. I. gas-solid energies and properties of isolated adsorbed atoms. *Surf. Sci.* 36 (1), 317–352.
- Terzyk, A.P., Gauden, P.A., Furmaniak, S., Wesolowski, R.P., Harris, P.J.F., Kowalczyk, P., 2009. Adsorption from aqueous solutions on opened carbon nanotubes-organic compounds speed up delivery of water from inside. *Phys. Chem. Chem. Phys.* 11 (41), 9341–9345.
- Tauer, T.P., Sherrill, C.D., 2005. Beyond the benzene dimer: an investigation of the additivity of  $\pi$ - $\pi$  interactions. *J. Phys. Chem. A* 109 (46), 10475–10478.
- Vernov, A., Steele, W.A., 1991a. Computer-simulations of benzene adsorbed on graphite. 1. 85 K. *Langmuir* 7 (12), 3110–3117.
- Vernov, A., Steele, W.A., 1991b. Computer-simulations of benzene adsorbed on graphite 2. 298 K. *Langmuir* 7 (11), 2817–2820.
- Wang, Y., Nguyen, P.T.M., Sakao, N., Horikawa, T., Do, D.D., Morishige, K., Nicholson, D., 2011. Characterization of a new solid having graphitic hexagonal pores with a GCMC technique. *J. Phys. Chem. C* 115 (27), 13361–13372.
- Wick, C.D., Martin, M.G., Siepmann, J.I., 2000. Transferable potentials for phase equilibria. 4. united-atom description of linear and branched alkenes and alkylbenzenes. *J. Phys. Chem. B* 104 (33), 8008–8016.
- Wick, C.D., Siepmann, J.I., Klotz, W.L., Schure, M.R., 2002. Temperature effects on the retention of n-alkanes and arenes in helium-squalane gas-liquid chromatography: experiment and molecular simulation. *J. Chromatogr. A* 954 (1–2), 181–190.
- Yun, J.H., Choi, D.K., Kim, S.H., 1999. Equilibria and dynamics for mixed vapors of BTX in an activated carbon bed. *AIChE J.* 45 (4), 751–760.
- Zhao, Y., Truhlar, D.G., 2005. Multicoefficient extrapolated density functional theory studies of  $\pi$ - $\pi$  interactions: the benzene dimer. *J. Phys. Chem. A* 109 (19), 4209–4212.

## **BIOGRAPHY**

Mr. Nikom Klomkliang was born on Saturday the 6<sup>th</sup> of March 1982, in Nongbua Sub-District, Thatoom District, Surin Province of Thailand. He started his primary education at Ban Nongbua Mitraphap 85 Primary School, Nongbua Sub-District, Thatoom District, Surin Province of Thailand in 1989 where he completed his primary education in 1995. Between 1995-2001, he studied at Thatoom Prachasermwith High School, Thatoom District, Surin Province of Thailand for his secondary education. He then moved to the famous Suranaree University of Technology (SUT) for his university education. In 2005, he graduated his bachelor degree in chemical engineering from SUT. He then received scholarship for a research assistant at SUT to study for master degree in chemical engineering since 2005 where he completed the master degree in 2008. The thesis of his master degree was focused on modeling of non-linear behavior in a CSTR-separation-recycle system producing LDPE. After he finished his master degree, he continued to study his Ph.D. in chemical engineering in the same university in 2008 by receiving the support from the Office of the Commission on Higher Education of Thailand in the form of Ph.D. scholarship throughout his study. During his Ph.D. study, he received a scholarship from Japan to do experiment in Hyogo University for one month in 2009. Also he had been in the University of Queensland (UQ), Australia for one year and five months (23 November 2010 to 30 April 2012) for his research which was directly related to his Ph.D. thesis by financial support from SUT and UQ.